FACHBEREICH MATHEMATIK UND NATURWISSENSCHAFTEN
FACHGRUPPE PHYSIK
BERGISCHE UNIVERSITÄT WUPPERTAL

Measurements and searches with top quarks

Measurement of the top quark pair production cross section, the ratio of branching fractions and searches for new physics in the top quark sector with the DØ experiment

Yvonne Peters

August 2008
WUB-DIS 2008-06

Contents

1. Introduction

In 1995 the last missing member of the known families of quarks, the top quark, was discovered by the CDF and DØ experiments at the Tevatron, a proton-antiproton collider at Fermilab near Chicago. Until today, the Tevatron is the only place where top quarks can be produced.

The determination of top quark production and properties is crucial to understand the Standard Model of particle physics and beyond. The most striking property of the top quark is its mass – of the order of the mass of a gold atom and close to the electroweak scale – making the top quark not only interesting in itself but also as a window to new physics. Due to the high mass, much higher than of any other known fermion, it is expected that the top quark plays an important role in electroweak symmetry breaking, which is the most prominent candidate to explain the mass of particles. In the Standard Model, electroweak symmetry breaking is induced by one Higgs field, producing one additional physical particle, the Higgs boson. Although various searches have been performed, for example at the Large Electron Positron Collider (LEP), no evidence for the Higgs boson could yet be found in any experiment. At the Tevatron, multiple searches for the last missing particle of the Standard Model are ongoing with ever higher statistics and improved analysis techniques. The exclusion or verification of the Higgs boson can only be achieved by combining many techniques and many final states and production mechanisms. As part of this thesis, the search for Higgs bosons produced in association with a top quark pair ($t\bar{t}H$) has been performed. This channel is especially interesting for the understanding of the coupling between Higgs and the top quark.

Even though the Standard Model Higgs boson is an attractive candidate, there is no reason to believe that the electroweak symmetry breaking is induced by only one Higgs field. In many models more than one Higgs boson are expected to exist, opening even more channels to search for charged or neutral Higgs bosons. Depending on its mass, the charged Higgs boson is expected to decay either into top quarks or be the decay product of a top quark. For masses below the top quark mass, the top decay into a charged Higgs boson and a b quark can occur at a certain rate, additionally to the decays into W bosons and a b quark. The different decays of W and charged Higgs bosons can lead to deviations of the observed final number of events in certain final states with respect to the Standard Model expectation. A global search for charged Higgs bosons in top quark pair events is presented in this thesis, resulting in the most stringent limits to-date.

Besides the decay of top quarks into charged Higgs or W bosons, new physics can also show up in the quark part of the decay. While in the Standard Model the top quark decays with a rate of about 100% into a W boson and a b quark, there are models where the top quark can decay into a W boson and a non-b quark. The ratio of branching fractions in which the top quark decays into a b quark over the branching fractions in which the top quark decays into all quarks is measured as part of this thesis, yielding the most precise measurement today.

Furthermore, the Standard Model top quark pair production cross section is essential to be known precisely since the top quark pair production is the main background for $t\bar{t}H$ production and many other Higgs and beyond the Standard Model searches. However, not only the search or the test of the Standard Model itself make the precise measurement of the top quark pair production cross section interesting. As the cross section is calculated with high accuracy in perturbative QCD, a comparison of the measurement to the theory expectation yields the possibility to extract the top quark mass from the cross section measurement. Although

many dedicated techniques exist to measure the top quark mass, the extraction from the cross section represents an important complementary measurement. The latter is briefly discussed in this thesis and compared to direct top mass measurements.

The goal of this thesis is the improved understanding of the top quark sector and its use as a window to new physics. Techniques are extended and developed to measure the top quark pair production cross section simultaneously with the ratio of branching fractions, the $t\bar{t}H$ cross section or the rate with which top quarks decay into charged Higgs bosons. Some of the results are then taken to extract more information. The cross section measurement is used to extract the top quark mass, and the ratio of the top quark pair production cross sections in different final states, yielding a limit on non-Standard Model top quark decays.

2. Theory

The matter known today consists of quarks and leptons. The properties and interactions of these elementary particles are described by the Standard Model (SM) of particle physics. Although the SM predicts many phenomena it does not include gravity and does not explain dark matter nor dark energy. Several models extending the SM exist. One such model is Supersymmetry (SuSy), of which the simplest extension of the Standard Model is the Minimal Supersymmetric Standard Model (MSSM).

In this chapter a short introduction to the Standard Model is given, with special emphasise on the top quark and its production and decay. The Minimal Supersymmetric Model is described briefly with special interest on the charged Higgs boson.

2.1. The Standard Model

The Standard Model is the theory of fermionic particles and their fundamental interactions. Between fermions with spin one half, obeying the Fermi-Dirac statistics, the exchange of four fundamental forces occurs. The forces are gravitation, electromagnetic, weak and strong interaction. The inclusion of gravitation into a consistent theory with all the other forces is not yet possible. As its magnitude is by many orders smaller compared to the other three forces, gravitation can be neglected in most particle physics calculations and is not part of the Standard Model. In field theory the forces are carried by gauge bosons with integer spin, following Bose-Einstein statistics. To each fundamental interaction one or more gauge bosons are associated. Their necessity and appearance can naturally be explained in their corresponding local gauge theories [1, 2]. The four fundamental interactions together with their bosons and the particles they act upon are listed in Table 2.1.

The Standard Model contains of six types of quarks and leptons, ordered in three families. The first family includes the quarks and leptons of which the stable matter consists: up and down type quarks, electrons and electron neutrinos. Tables 2.2 and 2.3 show the different quark flavours and lepton types, their masses and electric charge. For each fermion an anti-fermion exists, having the same mass and opposite charge. In the Standard Model the neutrino mass is assumed to be zero. Although experiments show that neutrinos are not massless the assumption works for the calculations and predictions in high energy physics.

The Standard Model is based on the $SU(3)_C \times SU(2)_L \times U(1)_Y$ symmetry group, where C, L and Y refer to the colour, weak isospin and hypercharge quantum numbers.

Force	gauge boson	interacts with
gravitation	Graviton (?)	all massive particles
weak interaction	$W^{\pm}$, Z	quarks & leptons, $W^{\pm}$, Z
electromagnetic interaction	photon γ	quarks and charged leptons
strong interaction	8 gluons g	quarks & gluons

Table 2.1.: The fundamental interactions; the graviton is not yet observed

Family	Quark flavour	Mass [GeV]	Electric charge [e]
1	up (u)	0.0015 - 0.003	$2/3$
	down (d)	0.003 - 0.007	$-1/3$
2	charm (c)	1.25 ± 0.09	$2/3$
	strange (s)	0.095 ± 0.025	$-1/3$
3	top (t)	174.2 ± 3.3	$2/3$
	bottom (b)	4.2 ± 0.07	$-1/3$

Table 2.2.: Overview over the quark flavours [3]

Family	Leptons	Mass [MeV]	Electric charge [e]
1	ν_e (electron neutrino)	$< 2 \cdot 10^{-6}$ @ 95 %CL	0
	e^- (electron)	$0.51099892 \pm 0.00000004$	-1
2	ν_μ (muon neutrino)	< 0.19 @ 95 %CL	0
	μ^- (muon)	105.658369 ± 0.000009	-1
3	ν_τ (τ neutrino)	< 18.2 @ 95 %CL	0
	τ^- (tau)	$1779.99^{+0.29}_{-0.26}$	-1

Table 2.3.: Overview over the leptons [3]

2.1.1. The strong interaction and Quantum Chromodynamics

The gauge theory describing the strong interaction is the Quantum Chromodynamics (QCD). QCD is a non-abelian gauge theory based on the gauge group $SU(3)$. Local gauge invariance under colour phase transformation leads to eight massless gluons.

The strong interaction acts on colour charged particles, which are the quarks and gluons. Colour charge occurs in three flavours, called red, green and blue, and the corresponding anti-colours. In contrast to the gauge boson in QED (see section 2.1.2) the gluon itself carries colour charge, causing gluon self-coupling. If the number of quark flavours at a considered energy is not higher than 16 (see Eq. 2.1), an increase of the colour force between colour charged particles with increasing distance occurs. As a consequence quarks and gluons can not appear as free particles but only in colour-neutral objects. This behaviour is called confinement and implies that only particles that are colour-singlets can be observed directly. Two kinds of colour-singlets are observed: baryons (qqq) and mesons ($q\bar{q}$). With decreasing distance the strength of the interaction between coloured particles decreases. This leads to quasi-free coloured particles at small distances and is called asymptotic freedom.

To calculate cross sections and matrix elements, perturbative calculations in orders of the coupling constant α_s are performed. The perturbation calculation must be renormalised in order to remove ultraviolet divergencies. The formula for the coupling $\alpha_s(Q^2)$ results from renormalisation, where Q^2 is the scale of the observed process.

In first order perturbation theory $\alpha_s(Q^2)$ has the form [2]:

$$\alpha_S(Q^2) = \frac{12\pi}{(33 - 2n_f)\ln(Q^2/\Lambda^2)}\,. \tag{2.1}$$

n_f is the number of quark flavours that contribute at the considered energy and Λ is an integration constant representing the scale at which α_s diverges. The denominator in Eq. 2.1 shows that for n_f larger than 16 the sign of α_s becomes negative, which would result in a behaviour like in Quantum Electrodynamics. At present energies n_f is below this number. Furthermore, measurements of the Z boson width restrict the number of neutrinos with mass lower than the half of the Z mass to three.

At small energy scales α_s becomes large, and therefore perturbative calculations are not possible anymore. Thus, all energies below a certain threshold require non-perturbative models in order to enable a full description of observable processes.

2.1.2. The electroweak interaction and the Higgs mechanism

Historically, the gauge theory describing the electromagnetic interactions, the Quantum Electrodynamics (QED), was the first gauge theory constructed to describe particles and their interaction. QED is the simplest gauge theory, with only one gauge boson – the photon. While QED and QCD are self-consistent gauge theories, the description of the weak interaction only works properly in the unified picture of electromagnetic and weak interaction. The three gauge bosons for the weak force are massive, requiring a mechanism to explain how particles aquire their mass.

Quantum Electrodynamics

The gauge theory describing the electromagnetic interactions is Quantum Electrodynamics (QED). The QED is based on the symmetry group $U(1)$. The equation that describes a free fermion in this theory is the Dirac equation. Invariance of the equation under local gauge transformations of the group $U(1)$ leads to the photon as gauge boson and the coupling to the electric charged particles. Perturbation theory in QED is done in the coupling constant α_{QED}, which increases with increasing energy or decreasing distance. At very small energies α_{QED} is of the order of $\frac{1}{137}$, and therefore small enough to allow perturbative calculations. α_{QED} increases very slowly with increasing Q^2, enabling perturbative corrections up to high energies.

The weak interaction

While the strong interaction only acts on quarks and the electromagnetic interaction only on electrically charged particles, the weak interaction seems to occur between all quarks and leptons at first sight. Experiments have shown that weak interactions are related to the chirality of the particle. The gauge bosons of the weak interactions are the $W^{\pm}$ and the Z bosons. The $W^{\pm}$ and the Z bosons act on fermions carrying a weak isospin quantum number different from zero, and interact with each other. In contrast to the gauge bosons of QED and QCD, the gauge bosons of the weak interaction are massive, resulting in a short lifetime of the bosons and a small interaction length of the weak force. Analogous to the electric charge in QED and the colour charge in QCD, the weak interaction acts on the weak isospin. Left-handed particles appear in pairs, while right-handed ones are singlets.

The electroweak theory and the Higgs mechanism

While QCD and QED are consistent with observation, a theory of weak interaction on its own, based on $SU(2)$, is not. When requiring invariance of the Lagrangian under $SU(2)_L$ it results in two charged bosons and a neutral gauge boson W^0. The latter is not consistent with observation, as the observed weak neutral current has a right-handed component. Furthermore, the local gauge theory requires massless gauge bosons, which is not consistent with observation neither.

The unification of electromagnetic and weak interaction delivers a description that is consistent with the observed neutral current processes and the boson masses. The theory of electroweak interaction is based on the $SU(2)_L \times U(1)_Y$ symmetry group. The requirement

of invariance under local gauge transformations leads to four gauge bosons: W^1, W^2 and W^3 from the group $SU(2)_L$ and B from the group $U(1)_Y$. Since $SU(2)_L$ is a non-abelian group the three bosons from this group interact with each other.

The two bosons W^3 and B can not directly be identified with the observed Z boson and the photon. While Z is massive, the photon must remain massless, implying a strict constraint on the theory. Furthermore, experiments show that the coupling of the Z boson to charged leptons and neutrinos is different. The photon and the Z boson can be defined as a linear combination of W^3 and B:

$$Z = \cos\theta_W W^3 - \sin\theta_W B \tag{2.2}$$
$$A = \sin\theta_W W^3 + \cos\theta_W B \tag{2.3}$$

with θ_W being the weak mixing angle. θ_W is determined by the coupling constants g_W of the $SU(2)_L$ and g'_W of the $U(1)_Y$ groups:

$$\sin\theta_W = \frac{g'_W}{\sqrt{g_W^2 + {g'_W}^2}} \tag{2.4}$$

The bosons W^+ and W^- are a mixture of the gauge bosons W^1 and W^2:

$$W^\pm = \frac{1}{\sqrt{2}}(W^1 \mp iW^2)\,. \tag{2.5}$$

The Higgs mechanism The local gauge theories require massless gauge bosons. The three observed bosons $W^\pm$ and Z are massive and therefore violate the $SU(2)_L \times U(1)_Y$ gauge invariance. The Higgs mechanism [4], which introduces a spontaneous symmetry breaking, can solve this problem.

The Lagrangian of a complex scalar isospin doublet $\Phi(x) = (\Phi_+, \Phi_0)$ [5,6]

$$L = (D_\mu\Phi)^*(D^\mu\Phi) - V(\Phi^*\Phi) \tag{2.6}$$

with the potential

$$V(\Phi^*\Phi) = \lambda(\Phi^*\Phi)^2 - \mu^2\Phi^*\Phi \tag{2.7}$$

with $\lambda > 0$ and $\mu^2 > 0$, is invariant under local SU(2) gauge transformations. V is called the Higgs potential. It has its minimum at the non-zero value $\Phi = v/\sqrt{2} = \sqrt{\mu^2/2\lambda}$. The vacuum expectation value v (vev) of the neutral Higgs field Φ introduces the symmetry breaking. By setting one component of Φ to zero at the minimum (Φ_+) and expanding the other component of Φ near the minimum as $\Phi_0(x) = (v + h(x))/\sqrt{2}$ and inserting it into Eq. 2.6, mass terms for the gauge bosons and the Higgs boson appear. $h(x)$ is a non-complex field or the Higgs boson.

In order to give mass to fermions Yukawa coupling terms of the form $g_f f_L \Phi f_R$ are introduced, where f_L and f_R are left and right-handed fermions. For each fermion an own coupling g_f is introduced, resulting in the mass of the fermion of $m_f = g_f v\sqrt{2}$. g_f or m_f are thus not calculable but have to be determined experimentally.

The CKM matrix The $SU(2)_L$ gauge bosons W_1, W_2 and W_3 couple only to left-handed fermions and right-handed anti-fermions and are therefore maximal parity violating. All right-handed quarks and leptons (and left-handed anti-quarks and anti-leptons) are members of $I = 1/2$ isospin doublets, while all right-handed quarks and leptons (and left-handed

particles				I	I_3	Y	Q
leptons	$\binom{\nu_{eL}}{e_L}$	$\binom{\nu_{\mu L}}{\mu_L}$	$\binom{\nu_{\tau L}}{\tau_L}$	$\binom{1/2}{1/2}$	$\binom{1/2}{-1/2}$	$\binom{-1/2}{-1/2}$	$\binom{0}{-1}$
	e_R	μ_R	τ_R	0	0	-1	-1
quarks	$\binom{u'_L}{d'_L}$	$\binom{c'_L}{s'_L}$	$\binom{t'_L}{b'_L}$	$\binom{1/2}{1/2}$	$\binom{1/2}{-1/2}$	$\binom{1/6}{1/6}$	$\binom{2/3}{-1/3}$
	u'_R	c'_R	t'_R	0	0	2/3	2/3
	d'_R	s'_R	b'_R	0	0	-1/3	-1/3

Table 2.4.: Isospin doublets and singlets for quarks and leptons.
Flavour quantum numbers for leptons and quarks:
weak isospin I with third component I_3;
Y: hypercharge;
Q: electric charge Q=$I_3 + Y$

anti-quarks and anti-leptons) are $I = 0$ isospin singlets. The flavour quantum numbers of the SM fermions are listed in Table 2.4. The $W^{\pm}$ bosons carry an isospin value of $|I_3| = 1$, the Z boson has $I_3 = 0$.

Assuming the mass eigenstates were identical to the electroweak eigenstates, no weak transition between different quark generation would be observed. As this does not agree with observation the electroweak and mass eigenstates must be different. By modification of the quark doublets this problem can be solved. The electroweak eigenstates (u',c',t') and (d',s',b') are rotations of the mass eigenstates (u,c,t) and (d,s,b). The electroweak eigenstates differ from the mass eigenstates by a unitary transformation

$$\begin{pmatrix} d' \\ s' \\ b' \end{pmatrix} = U_d \begin{pmatrix} d \\ s \\ b \end{pmatrix} \tag{2.8}$$

and

$$\begin{pmatrix} u' \\ c' \\ t' \end{pmatrix} = U_u \begin{pmatrix} u \\ c \\ t \end{pmatrix} \tag{2.9}$$

The matrix $V = U_u^{\dagger} U_d$ is called CKM-Matrix (Cabbibo-Kobayashi-Maskawa) and is written as:

$$V = \begin{pmatrix} V_{ud} V_{us} V_{ub} \\ V_{cd} V_{cs} V_{cb} \\ V_{td} V_{ts} V_{tb} \end{pmatrix} \tag{2.10}$$

The probability of a transition from quark q_u into a quark q_d is proportional to the corresponding CKM matrix element squared: $|V_{q_u q_d}|^2$. The unitarity requirement leaves four free parameter in the matrix. Three are independent mixing angles and one is a phase, that causes the CP violation in the Standard Model.

Observation shows that neutrinos are not massless, therefore the electroweak and mass eigenstates (or flavour eigenstates) are not identical for the neutrinos either. A transformation matrix similar to the CKM matrix is introduced, called Maki-Nakagawa-Sakata (MNS) matrix [7] and connecting the electroweak eigenstates (ν_1,ν_2,ν_3) to the flavour eigenstates (ν_e,ν_μ, ν_τ).

2.1.3. The top quark

The top quark is the heaviest elementary particle known today. The top quark is interesting for several reasons. Due to its short lifetime it is the only quark where pure properties of a

free quark can be measured. Due to its high mass the top quark has the strongest coupling of all known fermions to the Higgs boson, making the consideration of processes involving the coupling of both particles interesting.

The top quark mass The mass of the fermions are free parameter in the SM. The current world average for the top quark mass [1)] is [9]

$$m_t = 172.6 \pm 0.8 \text{ (stat)} \pm 1.1 \text{ (syst) GeV}. \tag{2.11}$$

The relative uncertainty on the measurement is about 0.8% and therefore the top quark mass is measured more precisely than the mass of any other quark.

Due to the dependence of the theoretical $t\bar{t}$ cross section calculation on the top quark mass the latter can be extracted from the measurement of the top pair production cross section [10, 11]. It can directly be compared to the dedicated top mass measurements. In section 9.2 the top mass measurement from cross section will be described briefly.

The top quark production The production of the top quark can occur via strong or electroweak interaction. At the Tevatron with a centre of mass energy of 1.96 TeV, the $t\bar{t}$ pair production via strong interaction is the dominant process, while single top quark production via electroweak interaction is much weaker.

Single top quark production can occur via the s-channel $q\bar{q} \rightarrow W^+ t\bar{b}$ or the t-channel process $gq \rightarrow qt\bar{b}$. In 2006 DØ reported the first evidence for single top production [12] with a measured cross section of s- and t-channel together of $\sigma = 4.7 \pm 1.3$ pb yielding a standard deviation of 3.6 sigma from a cross section of zero. No 5 sigma observation was reported so far.

The leading order Feynman diagrams for top quark pair production are shown in Fig. 2.1. The upper diagram shows the quark-antiquark annihilation. The three bottom diagrams compose the gluon-gluon fusion.

The two incoming partons of the hard interaction, i. e. quarks or gluons, are part of the accelerated proton and antiproton. Each of the partons from the incoming proton and antiproton carry a fraction x of the (anti)proton momentum. The probability densities for a parton of type a or b to carry the momentum fraction x are described by the parton distribution functions (PDFs) $f_a^p(x, Q^2)$ and $f_b^{\bar{p}}(x, Q^2)$. Q describes the scale for the interaction. The PDFs are determined from deep inelastic scattering and other data.

The separation of the hard interaction from long distance processes is called factorisation. To separate the two pieces the factorisation scale μ is introduced.

The production of a $t\bar{t}$ pair requires at least a centre of mass energy $\sqrt{s}$ of $2m_t$ for the hard interaction. This yields a typical value for the momentum fraction x of $x \simeq \frac{2m_t}{\sqrt{s}}$. For the Tevatron this results in $x = 0.18$, while it is $x = 0.025$ for the LHC. The parton distribution functions for a scale of $Q^2 = (172.6\,\text{GeV})^2$ are shown in Fig. 2.2. Due to the different ratio of quark to gluon distribution functions for different x the composition of the processes $q\bar{q} \rightarrow t\bar{t}$ and $gg \rightarrow t\bar{t}$ depend on the centre of mass energy. At $x = 0.18$ the PDFs for quarks are much higher than for gluons, causing a contribution of about 85 % quark-antiquark annihilation and of 15 % gluon-gluon fusion to the production cross section of a top pair at the Tevatron. At the LHC, the gluon-gluon fusion dominates with about 90 %.

[1)] The latest value from August 2008 is $m_t = 172.4 \pm 0.7$ (stat) ± 1.0 (syst) GeV [8]. This value is not yet used in this thesis.

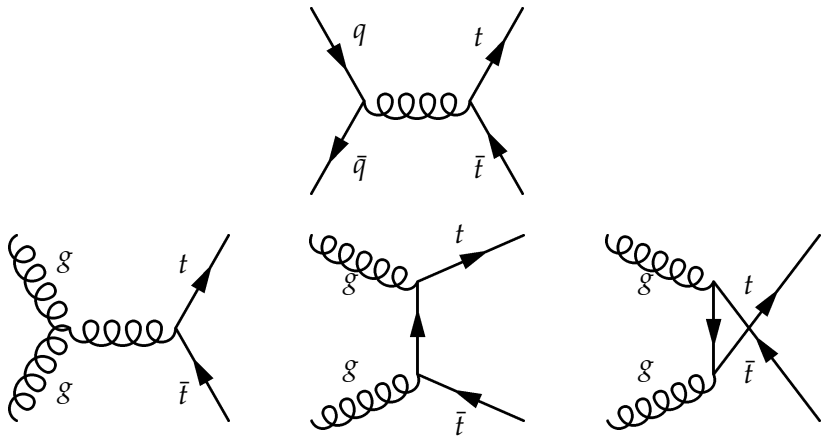

Figure 2.1.: Leading order Feynman diagrams for $t\bar{t}$ pair production at the Tevatron

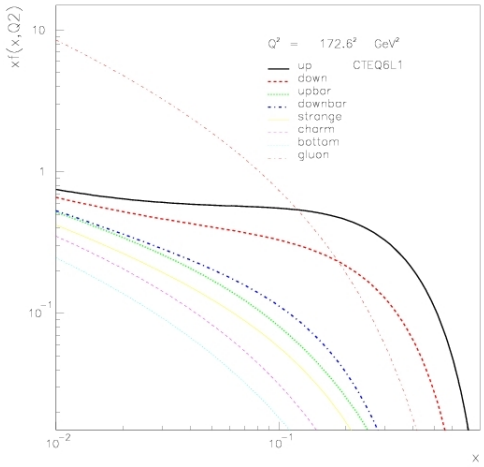

Figure 2.2.: Parton Distribution Function for quarks and the gluon of the proton [13]. The scale Q is set to the current value of the top quark mass 172.6 GeV. The CTEQ6L1 parametrisation is used.

The top quark pair production cross section can be written as [14]

$$\sigma_{t\bar{t}} = \sum_{a,b} \int dx_a dx_b f_a{}^p(x_a,\mu) f_b{}^{\bar{p}}(x_b,\mu) \hat{\sigma}^{ab\to t\bar{t}}(\hat{s}, m_t^2, x_a, x_b, \alpha_s(\mu^2), \mu^2), \tag{2.12}$$

where a and b run over all quark types and the gluons in the proton and antiproton respectively, with the partons a and b carrying a momentum fraction x_a and x_b from proton and antiproton. $\hat{s}$ is the effective centre of mass energy for the partonic process. For a top mass of 175 GeV the theoretical cross section in next-to-leading order (NLO) including additional subleading terms, next-to-next-to-next-to-leading-logarithmic (NNNLL) terms and some virtual terms, calculated by Kidonakis et al. [15] using the CTEQ6M [16] PDFs yields

$$\sigma^{p\bar{p}\to t\bar{t}+X}(m_t = 175\,\text{GeV}, \sqrt{s} = 1.96\,\text{TeV}) = 6.77 \pm 0.6\,\text{pb}^{-1}. \tag{2.13}$$

An alternative calculation was carried out by Cacciari et al., also at NLO, including resummation of leading and next-to-leading soft logarithms appearing at all orders of perturbation theory [17]. The result for the theoretical cross section agrees with

the calculation from Kidonakis et al. A new calculation from Moch and Uwer [18, 19] containing all logarithms in NNLL that are relevant for a next-to-next-to-leading order (NNLO) calculation exists, using a new CTEQ6.6 [20] PDF set, resulting in $\sigma^{p\bar{p}\to t\bar{t}+X}(m_t = 175\ GeV, \sqrt{s} = 1.96\ TeV) = 6.92 \pm 0.53\, pb^{-1}$.

The top quark decay Within the Standard Model the top quark decays via the weak interaction to a W boson and a down-type quark q ($q = d, s, b$). The rate of the decay is proportional to the CKM matrix element $|V_{tq}|^2$. Under the assumption of three fermion families and a unitary 3×3 CKM matrix the elements $|V_{tq}|$ are severely constrained. The decay $t \to W^+b$ and its charged conjugate occurs to almost 100%, with $|V_{tb}| = 0.999100^{+0.000034}_{-0.000004}$ [3].

However, in several extensions of the Standard Model the 3×3 CKM is a sub-matrix of a larger matrix and would not appear unitary. In this case the $|V_{tq}|$ elements can significantly deviate from their Standard Model values. Experimentally this can be checked with the single top quark production mode, which depends directly on $|V_{tb}|^2$, or with the ratio of branching fractions

$$R = \frac{B(t \to Wb)}{B(t \to Wq)}. \tag{2.14}$$

R can be expressed in terms of the CKM matrix elements as

$$R = \frac{|V_{tb}|^2}{|V_{td}|^2 + |V_{ts}|^2 + |V_{tb}|^2}. \tag{2.15}$$

In case of the existence of a fourth quark generation, the denominator does not change. The limits on the mass of a fourth generation quark are already larger than the top quark mass [3], therefore the top quark decays only into the quarks of the three known generations.

There are also models where the W boson from the top quark decay is replaced by other particles. For example the decay of the top quark to a charged Higgs boson is predicted in Supersymmetric models. More details about this decay possibility are given in section 2.2.4.

Assuming 100% decay of top to W boson and bottom quark the decay width of the top quark in leading order perturbation theory is $\Gamma(t \to Wb) = 1.42$ GeV for a top quark mass of 175 GeV. The lifetime $\tau_t = \hbar/\Gamma$ of the top quark is therefore very short with $\tau_t \simeq 0.5 \cdot 10^{-24}$ s. This is about ten times smaller than the characteristic time for hadronisation – i. e. the formation of hadrons from quarks – to take place.

The $t\bar{t}$ decay channels For the measurement of the top quark production and properties it is useful to define separate final states according to the final physics objects. The $t\bar{t}$ decay channels are classified according to the decay of the two W bosons from the top decays. Each of the W bosons can decay leptonically into $e\bar{\nu}_e$, $\mu\bar{\nu}_\mu$ or $\tau\bar{\nu}_\tau$ or hadronically into $u\bar{d}$ or $c\bar{s}$, or charge conjugate. Due to the three possible colour charges, the ratio of hadronic to leptonic decay modes is a factor of two.

The $t\bar{t}$ decay is separated into the following final states:

All hadronic With a probability of about 46 % both W bosons decay hadronically. Experimentally, the channel suffers from large backgrounds from multijet production.

τ+jets The τ+jets channel consists of events where one W boson decays hadronically and the other one into a hadronic decaying τ. Due to the experimental similarity between this final state and the all hadronic final state the identification of the τ is essential. The separation of the τ+jets channel and the lepton+jets final state is a convention. Especially since the reconstruction of hadronic decaying τ's is different from and more difficult than the reconstruction of electrons and muons, this convention is useful.

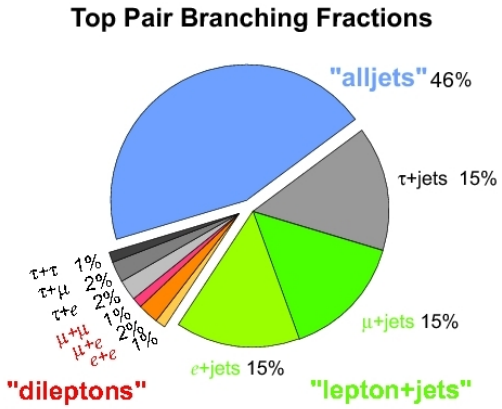

Figure 2.3.: $t\bar{t}$ decay channels and the corresponding branching ratios. The branching ratios correspond to the theoretical predictions at tree level [21].

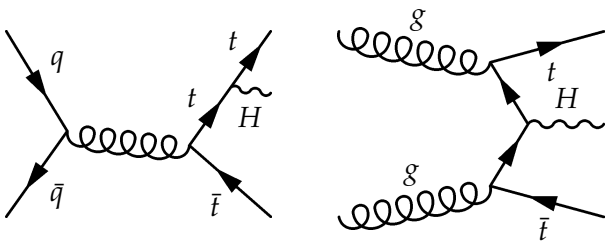

Figure 2.4.: Examples for Feynman diagrams of associated $t\bar{t}H$ porduction at the Tevatron.

Lepton+jets In the lepton+jets channel one W boson decays hadronically and the other one leptonically into an electron or muon and its corresponding neutrino. Decays of the W boson into a τ with leptonic decay of the τ are included in the lepton+jets channel. With a branching ratio of about 35 %, including the leptonic decaying τ decays the lepton+jets channel shows the best combination of large statistics and a clear signature due to the presence of a lepton.

Dilepton If both W bosons decay into electron or muon and the corresponding neutrino the channel is called dilepton channel. Decays of the W boson to τ with leptonic decay of the τ are also counted into this channel. Due to the two leptons giving a clear signature the dilepton final state is the purest of all channels. The branching fraction for this channel is about 5% only.

τ+lepton The τ+lepton channel contains the final states where one W boson decays into electron, muon or leptonic decaying τ and the other one decays into a hadronic decaying τ. The statistics of this channel is very low and the identification of the τ is essential to distinguish it from the lepton+jets channel.

In Fig. 2.3 all decay channels and the corresponding branching ratios are summarised.

The top quark and the Higgs boson

The large mass of the top quark suggests that it may play an important role in the electroweak symmetry breaking of the Standard Model. The Yukawa coupling of the Higgs boson to the top quark is expected to be of order unity.

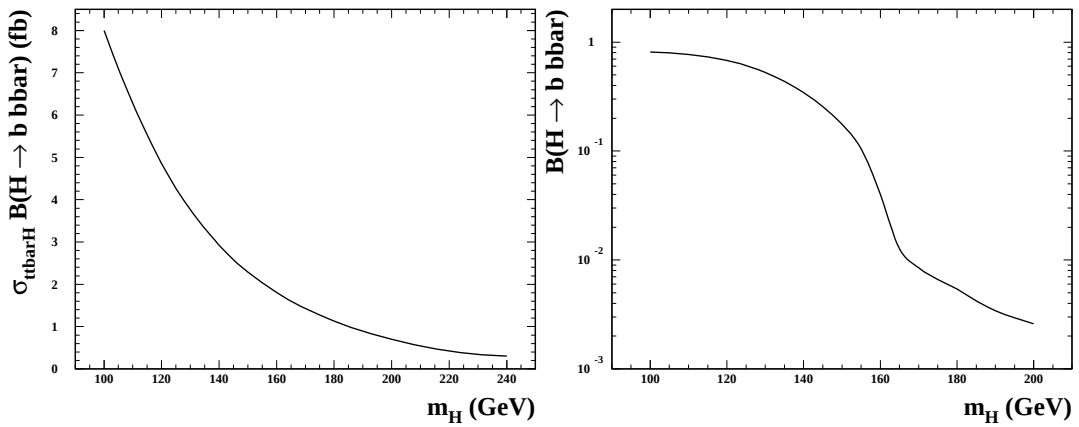

Figure 2.5.: The NLO $t\bar{t}H$ cross section (left) and the branching ratio $B(H \rightarrow b\bar{b})$ (right) in NLO including $\mathcal{O}(\alpha_s^3)$ contributions as a function of the Higgs mass. The PDF used for this calculation is CTEQ6M [16], and both the renormalisation and factorisation scales are set to $m_t + m_H/2$ [22].

The associated production of a Higgs boson with a $t\bar{t}$ pair provides direct access to the Yukawa coupling of the top quark. Figure 2.4 shows examples of Feynman diagrams for $t\bar{t}H$ production. The cross section times branching ratio at the Tevatron as function of the Higgs mass in NLO QCD calculation is shown in Fig. 2.5.

2.2. Supersymmetry, 2HDM and MSSM

Although the Standard Model of particle physics can explain many phenomena and although it was possible to predict for example the existence of the top quark, there are indications that the Standard Model is incomplete.

One imperfection of the Standard Model is the so-called fine-tuning problem [23, 24]. The Higgs mass receives large quantum corrections from all bosons and fermions it couples to, for example the ones shown in Fig. 2.6. The fermion or boson loop results in a correction to the Higgs boson self-energy that is proportional to the cut-off scale Λ and shows a quadratic divergency. From electroweak fits it is known that the Higgs mass is of the order of 100 GeV. For a cut-off scale Λ of about the Planck scale $\Lambda_P \simeq 10^{19}$ GeV the one-loop corrections to the squared Higgs mass come out to be by more than 30 orders of magnitude larger than $(100\ \text{GeV})^2$. This discrepancy would require an enormous fine-tuning of the bare Higgs mass, to get the physical Higgs mass down to $\mathcal{O}(100\ \text{GeV})$ while having large quantum corrections many orders of magnitude larger than the physical mass. Loop-corrections to the squared Higgs mass due to bosons and fermions have opposite signs. By introducing a symmetry between fermions and bosons the diverging contributions can be systematically cancelled out. Such a symmetry, relating fermions and bosons, is called Supersymmetry (SuSy).

2.2.1. The Two Higgs Doublet Model

In the Standard Model the Higgs field is chosen as a scalar doublet. This choice is the field with the minimal number of degrees of freedom needed to induce symmetry breaking in the electroweak sector. Based on theoretical arguments some general requirements and con-

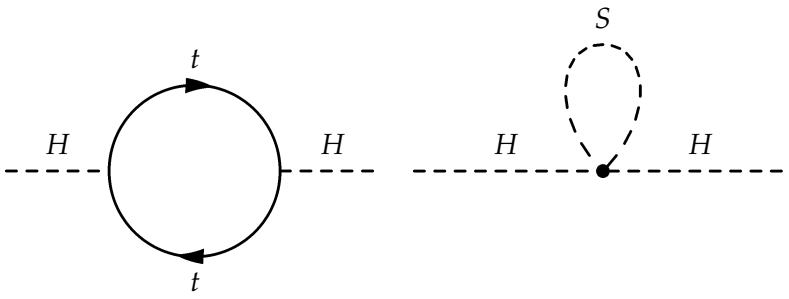

Figure 2.6.: One-loop diagrams providing quadratically divergent contributions to the Higgs mass [23].

straints can be applied on new or extended models. There are two important constraints the models have to obey [5]:

- The quantity

$$\rho = \frac{m_W^2}{m_Z^2 cos^2\theta_W} \tag{2.16}$$

  is constrained very tightly to one by experiments [25]. In case of only Higgs doublets and additional singlets included in the theory, the tree level value determined by the Higgs structure is $\rho = 1$.

- The very tight limits on flavour changing neutral currents (FCNC), which are achieved by experiments, give a second major constraint on the Higgs model. In case of only one Higgs doublet this constraint is fulfilled automatically within the theory. In case of more Higgs doublets the constraint is always fulfilled if all fermions of a given electric charge couple to one Higgs doublet only [26].

The simplest extension of the Standard Model is the two Higgs Doublet Model (2HDM) where a second complex doublet is introduced, resulting in four new fields. Each of the two complex doublets Φ_1 and Φ_2 has a vacuum expectation value v_1 and v_2. In the model a total of five physical Higgs bosons occur: a pair of charged Higgs ($H^\pm$), two neutral CP-even scalars (H^0 and h^0) and a neutral CP-odd scalar (A^0). In contrast to the Standard Model with only one complex doublet field for the Higgs, where one free parameters has to be determined, the 2HDM has six free parameters, which are the four Higgs masses, the ratio of vacuum expectation values of both Higgs doublet fields $\tan\beta = v_2/v_1$ and an angle α, which is the phase of the mass matrix for the two CP-even physical Higgs scalars, resulting in the two physical mass eigenstates h^0 and H^0. The vev or the sum of the two vev's is fixed by the W boson mass: $m_W^2 = g^2(v_1^2 + v_2^2)/2$.

The fermion coupling to the Higgs doublets is not fixed by the model. Due to the experimental constraints the fermion couplings must not allow for flavour changing neutral currents. There are two main models that satisfy this requirement:

Type I The fermions couple to only one Higgs doublet Φ_2 and are completely decoupled from Φ_1.

Type II One of the Higgs doublet, Φ_1, couples only to down-type quarks and charged leptons, while the other Higgs doublet Φ_2 couples only to up-type quarks and neutrinos.

In Supersymmetry, also in the MSSM, the Type II model of the Higgs-fermion couplings is required [5, 27].

2.2.2. Multi Higgs Doublet Models

The symmetry breaking in the electroweak sector is not restricted to one or two Higgs doublets. In general Multi Higgs Doublet Models (MHDM) several Higgs doublets are introduced [28, 29], of which the 2HDM represents the simplest one. In a general MHDM n Higgs doublets induce the spontaneous symmetry breaking. In total there are $2n$ neutral and $2n$ charged scalar fields. After subtraction of the three degrees of freedom needed for the $W^{\pm}$ and Z boson to acquire mass, this leaves $2(n-1)$ charged and $2n-1$ neutral physical observable scalars.

The Yukawa couplings to fermions require the introduction of three complex coupling constants for each of the charged scalars, arising from their mixing matrix. The interaction of the charged scalar with the fermion is proportional to the fermion mass.

The problem of the required absence of flavour changing neutral current, as discussed for the 2HDM, can in general be achieved if all fermions of a given electric charge couple to only one Higgs doublet.

2.2.3. Supersymmetry

By introducing a new symmetry connecting fermionic and bosonic states Supersymmetry [23, 24] extends the Standard Model. Each fermionic state turns into a bosonic state under a Supersymmetric transformation and vice versa. All particles are put into irreducible representations called super-multiplets. Each super-multiplet contains fermionic and bosonic states with the same quantum numbers, i. e. electric charge, colour, isospin and mass, which are super-partners of each other. Each of the super-multiplets contains the same number of fermion and boson degrees of freedom. All Standard Model fermions are arranged in chiral super-multiplets, all gauge bosons in gauge super-multiplets. As the fermions and bosons in the Standard Model carry different quantum numbers, they can not build each others super-partners, and new particles have to be introduced.

The names of the Supersymmetric partners of the fermions are constructed by putting an "s" in front of the fermion name, e. g. quarks have squarks as super-partners. For the super-partners of the gauge bosons an "ino" is appended to the boson name, e. g. the W has the super-partner Wino.

So far, no evidence for Supersymmetric particles has been found. Therefore the masses of the Supersymmetric partners must be heavier than the known particles, thus Supersymmetry must be a broken symmetry.

MSSM

In the minimal Supersymmetric model only the fields that are required to reproduce all Standard Model particles and build a consistent theory are contained. Table 2.5 shows the chiral super-multiplets together with the Higgs particles, Table 2.6 the gauge super-multiplets of the MSSM.

The Higgs boson belongs to the chiral super-multiplet. In Supersymmetry in general and the MSSM it turns out that one Higgs chiral super-multiplet is not sufficient. With only one Higgs super-multiplet a gauge anomaly would occur in the electroweak gauge symmetry.

One of the Higgs doublets (Φ_2) has hypercharge $Y = 1/2$, while the other has hypercharge $Y = -1/2$. In Supersymmetric models this leads to the requirement that one Higgs super-multiplet couples to up-type quarks only, while the other can only couple to down-type

quarks and charged leptons. This means that the Type II 2HDM Higgs sector, discussed in section 2.2.1, is realized in the MSSM.

The super-partners in Table 2.5 and 2.6 can be different from the mass eigenstates of the MSSM theory. Mixing can occur between particles with the same quantum numbers, i. e. between the electroweak gauginos and the higgsinos, and between the sets of squarks, sleptons and Higgs scalars with the same electric charge. The gluino is a colour octet fermion and can thus not mix with anything else, as the SU(3) colour symmetry has to be conserved.

In the MSSM a total of 105 new free parameters (additionally to the 18 free parameters from SM) are introduced that determine masses, mixing angles and phases of the Supersymmetric particles [27].

Names	spin 0	spin 1/2
left handed quarks and squarks	$(\tilde{u}_L \tilde{d}_L)$	$(u_L d_L)$
right handed quarks and squarks	$\tilde{u}_R, \tilde{d}_R$	u_R , d_R
left handed leptons and sleptons	$(\tilde{\nu}_L \tilde{e}_L)$	$(\nu_L e_L)$
right handed leptons and sleptons	$\tilde{e}_R$	e_R
Higgs, higgsinos H_u	$(H_u^+ H_u^0)$	$(\tilde{H}_u^+ \tilde{H}_u^0)$
Higgs, higgsinos H_d	$(H_d^0 H_d^-)$	$(\tilde{H}_d^0 \tilde{H}_d^-)$

Table 2.5.: Chiral super-multiplets in the MSSM [23]

Names	spin 1/2	spin 1
gluino and gluon	$\tilde{g}$	g
winos and W boson	$\tilde{W}^{\pm}$	$W^{\pm}$
zino and Z boson	$\tilde{Z}$	Z
photino and photon	$\tilde{\gamma}$	γ

Table 2.6.: Gauge super-multiplets in the MSSM [23]

2.2.4. The charged Higgs

Considering the 2HDM model, in total five physical Higgs bosons are introduced: h^0, H^0, A^0 and $H^{\pm}$.

Due to the Supersymmetric structure some constraints on the Higgs sector are imposed by the model. The Higgs self-interaction, for example, depends on the electroweak gauge coupling. Therefore the Higgs sector parameters depend only on two free parameters at tree level. One is usually chosen to be the ratio of vacuum expectation values of both Higgs doublet fields $\tan\beta = v_2/v_1$ and the other the mass m_A of the A^0 Higgs boson. The tree-level calculation yields then the following equations [27,30]:

$$m_{H^{\pm}}^2 = m_A^2 + m_W^2 \tag{2.17}$$

$$m_{H^0,h^0}^2 = \frac{1}{2}\left(m_A^2 + m_Z^2 \pm \sqrt{(m_A^2 + m_Z^2)^2 - 4m_Z^2 m_A^2 \cos^2 2\beta}\right) \tag{2.18}$$

$$\cos^2(\beta - \alpha) = \frac{m_{h^0}^2 (m_Z^2 - m_{h^0}^2)}{(m_{H^0}^2 + m_{h^0}^2 - m_Z^2)(m_{H^0}^2 - m_{h^0}^2)} \tag{2.19}$$

Radiative corrections can significantly change the predicted Higgs masses and the couplings. For example the mass of the h^0 depends on the top and the stop mass and the third generation squark mixing parameters due to radiative corrections.

Charged Higgs branching ratio and decay For a charged Higgs mass lower than the top quark mass the branching fraction $t \to H^+ b$ can get large. At leading order the partial decay width of $t \to H^+ b$ can be written as [5,31,32]

$$\Gamma(t \to H^+ b) = p(t \to H^+ b) \cdot \left[\left(m_t^2 \cot^2 \beta + m_b^2 \tan^2 \beta \right) \cdot \left(m_t^2 + m_b^2 - m_{H^+}^2 \right) + 4 m_t^2 m_b^2 \right] \quad (2.20)$$

with $p(t \to H^+ b)$ being a phase space factor.

The charged Higgs couplings are proportional to the fermion masses of the up- and down-type fermions. Therefore the charged Higgs predominantly decays into third generation quarks and leptons. Especially the decays of the charged Higgs boson to $c\bar{s}$, $\tau^+\nu$, $t^*\bar{b}$, W^+h^0 and W^+A^0 are considered in the following and other decay modes are neglected. For high regions of $\tan\beta$ the decay $H^+ \to \tau^+\nu$ is dominant, while for low $\tan\beta$ the decays $H^+ \to c\bar{s}$ and $H^+ \to t^*\bar{b}$ prevail, depending on the mass of the charged Higgs boson. Figure 2.7 shows $B(t \to H^+ b)$ and the branching ratio of the charged Higgs into the particles mentioned above for various charged Higgs masses. The calculations of the charged Higgs branching ratios used in this thesis are done with the program CPsuperH [33]. The Figure shows one example benchmark model from [34].

Within the MSSM, large radiative corrections from SuSy-breaking effects can lead to a suppression of $H^\pm \to \tau\nu$ compared to $H^\pm \to c\bar{s}$, even for high $\tan\beta$ [35]. Furthermore, in theories with Multi Higgs Doublet Models (MHDM) [28,29] a decay of the charged Higgs boson into quarks only is possible.

In this thesis two models are considered: One where the charged Higgs decays purely tauonic. This model is also valid in the MSSM for high $\tan\beta$. The other model assumes a leptophobic charged Higgs, completely decaying into $c\bar{s}$.

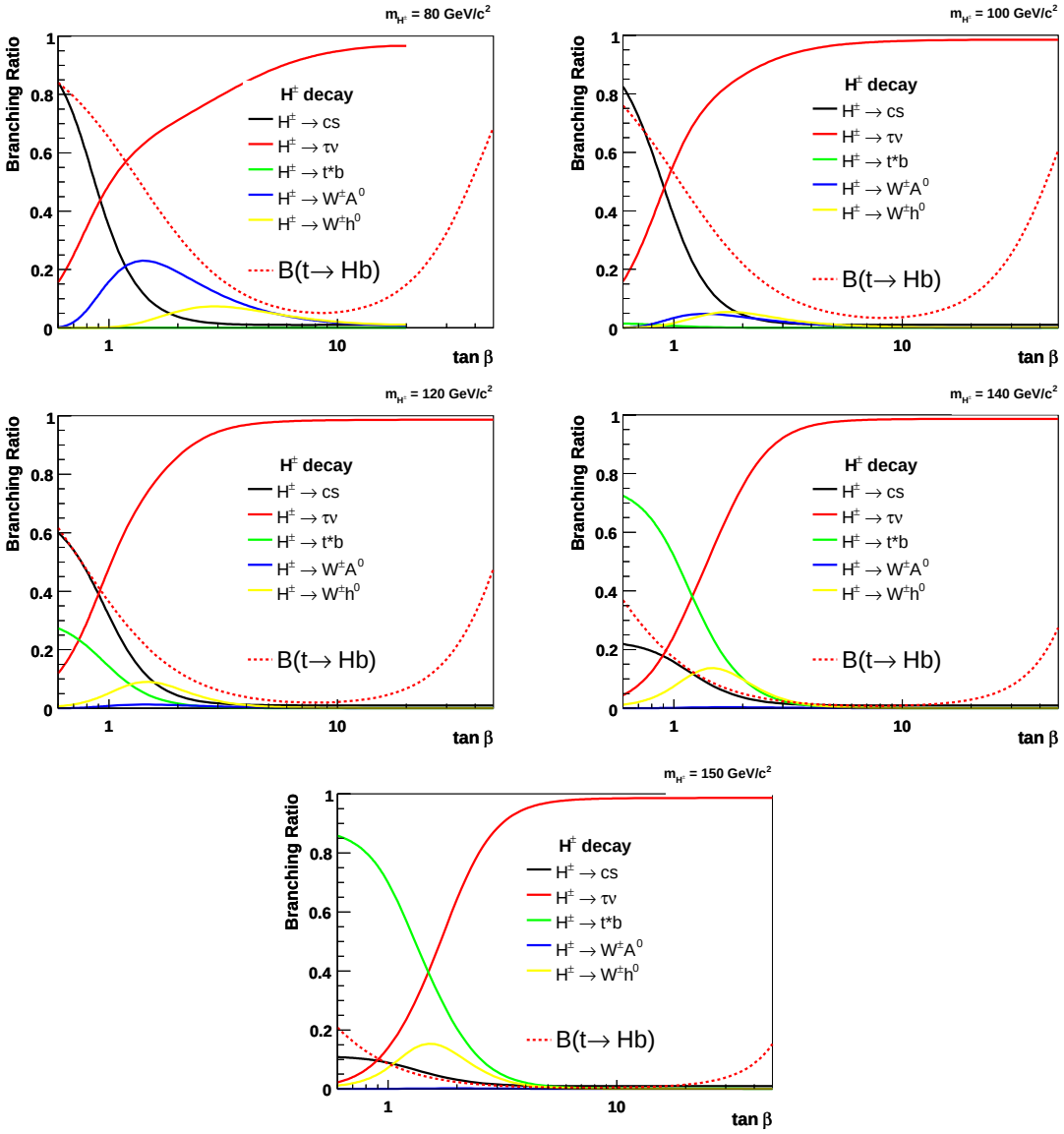

Figure 2.7.: Charged Higgs branching ratio (right) and $B(t \rightarrow H^+b)$ (left) for different charged Higgs masses. The top mass is set to 170 GeV. Benchmark model 4 from [34] is used.

3. Limit setting procedures

Besides the precise measurement of quantities like the top quark pair production cross section, the goal of many experiments is to look for the presence of new physics. If, for example, the cross section of a new, so far unknown, process is significantly different from zero, one would claim a discovery and quote the measured cross section and its uncertainty as the result. In case the measured cross section is consistent with zero an upper limit on the considered cross section is quoted as the result.

In general, there are are two problems to be considered. The first problem is the construction of the interval containing a certain fraction of the expected outcomes of the measurement – a so-called confidence region or confidence interval – or the degree of belief of a hypothesis predicting the outcome. The second, related problem is that the quantities of interest often have physical boundaries, for example a cross section should be non-negative, or a fraction is defined to lie between zero and one. If the sensitivity of a measurement of such a quantity is weak or the true value lies close to a physical boundary, the results can end up close or outside the physical boundaries. On such quantities it is useful to quote limits.

There are two common approaches to construct confidence regions and to set limits: the frequentist and the Bayesian approach [36]. For the former the Feldman-Cousins [37] and the modified frequentist approach CL_S [38] methods are commonly used. The frequentist and Bayesian approach use different interpretations of the measured quantity, and have different advantages and disadvantages.

In the Bayesian approach the hypothesis that an event occurs – or a certain value of the parameter of interest has been measured – is tested, and a measure of the degree of belief of this hypothesis is introduced. The interpretation of the probability in the frequentists approach is the relative frequency with which an event occurs when the experiment is repeated under the same conditions.

Due to the different definitions of limits in the frequentist and Bayesian approach, both can lead to different numerical results for the limits. For example, if the result is outside the physical boundary the different approaches can result in different values of the limit.

In this thesis the Feldman-Cousins method is used for the limit setting on the ratio of branching fractions R and the Bayesian and Feldman-Cousins approach are applied for the limits on the branching ratio of top quarks to charged Higgs bosons. For the search for Higgs bosons in the $t\bar{t}H$ channel, also a modified CL_S method is used. In the following, all three limit setting procedures used in this thesis are described briefly.

3.1. Bayesian limit setting

In the Bayesian approach a certain hypothesis is tested. The probability is interpreted as a measure for the degree of belief of the hypothesis. A posterior probability density $p(d(\mu)|D)$ is constructed, that describes the degree of belief that the parameter of interest μ has a certain value given the observed data D.

For the construction of the posterior probability density, a likelihood $L(D|d(\mu, \vec{\lambda}))$ is needed, that gives the probability density to observe a certain number of events D for a given μ.

$d(\mu, \vec{\lambda})$ is the number of expected events that depends on the parameter of interest μ and other parameters $\vec{\lambda}$ – for example acceptance and backgrounds. All parameters and the observed number of events D, d, μ and $\vec{\lambda}$ can be vectors – like $\vec{\lambda} = (\lambda_1, \lambda_2, \dots)$ – representing different channels, different backgrounds and different parameters.

According to Bayes theorem a probability density $p(d(\mu)|D)$ can be obtained from $L(D|d(\mu))$. This means, the likelihood can be used to get the posterior probability density:

$$p(d(\mu)|D) = \frac{\int L(D|d(\mu, \vec{\lambda}))\, \pi(\mu, \vec{\lambda}) d\vec{\lambda}}{\int\int L(D|d(\mu, \vec{\lambda}))\, \pi(\mu, \vec{\lambda})\, d\mu\, d\vec{\lambda}} \tag{3.1}$$

where $\pi(\mu, \vec{\lambda})$ is the a priori probability (or prior). The prior contains the input knowledge about the parameter of interest and the other parameters $\vec{\lambda}$. If the knowledge about the parameter μ and $\vec{\lambda}$ are independent, the prior probability can be factorised as

$$\begin{aligned} \pi(\mu, \vec{\lambda}) &= \pi(\vec{\lambda}|\mu) \cdot \pi(\mu) \\ &= \pi(\vec{\lambda}) \cdot \pi(\mu). \end{aligned} \tag{3.2}$$

For a cross section measurement the prior $\pi(\mu)$ is usually chosen as a positive, constant distribution within the physically allowed region and zero otherwise. Whether a probability distribution is flat or not depends on the observables, or metric, under study. A prior is metric dependent, i. e. the prior may be flat in p, $\log p$ or $\sqrt{p}$ for example. Usually it is not clear how to chose the prior and the dependence of the resulting limit on the choice of the prior probability distribution has to be studied [39].

The prior probability $\pi(\vec{\lambda})$ depends on the auxiliary parameters $\vec{\lambda}$ – also called nuisance parameters. The prior of the nuisance parameters is typically modelled as a multivariate Gaussian. By integrating $p(d(\mu, \vec{\lambda})|D)$ over the nuisance parameters, the dependence on the parameter of interest, μ, can be calculated as

$$p(d(\mu)|D) = \frac{\pi(\mu)}{N} \int L(D|d(\mu, \vec{\lambda}))\pi(\vec{\lambda}) d\vec{\lambda}\,, \tag{3.3}$$

where N is a normalisation factor. Here the factorisation of the prior probability is used implicitly. Usually a Monte Carlo integration is performed over the nuisance parameters as

$$p(d(\mu)|D) \simeq \frac{1}{N} \cdot \frac{\pi(\mu)}{M} \sum_{i=1}^{M} L(D|d(\mu, \vec{\lambda}_i)) \tag{3.4}$$

where M is the number of sampling points. For each sampling point, the nuisance parameters $\vec{\lambda}_i$ are chosen randomly according to the distribution given by $\pi(\vec{\lambda})$.

To obtain a Bayesian upper limit at a given Confidence Level CL (or C.L.) the equation

$$\int_{LB}^{\mu_{CL}} p(d(\mu)|D) d\mu = CL \tag{3.5}$$

has to be solved for μ_{CL}, where LB is the lower bound of the physically allowed region. LB is often zero, for example for limits on cross sections.

3.2. Frequentist limit setting with Feldman Cousins

The frequentists approach uses a different interpretation of the probability compared to the Bayesian approach. The probability is considered as the relative frequency of an outcome to occur if the process or experiment is repeated a large number of times.

Given a certain distribution of measured values x around the true value μ, a X % confidence interval can be defined. The confidence interval can be constructed in several ways. For example there are approaches following the Neyman ordering [40]. The approach introduced by Feldman and Cousins uses a construction called "the likelihood ratio ordering principle", which is described in the following.

The limit setting procedure proposed by Feldman and Cousins [37] is a frequentist approach. It uses a specific method to construct the confidence region. Usually, the decision whether to quote one-sided limits or two-sided confidence regions is done based on the result from data. This can introduce a bias on the limit or confidence interval. The main advantage of the Feldman Cousins approach is that it avoids this so-called "flip-flopping", which means that one does not have to decide whether to quote a limit or a two-sided confidence region depending on the outcome of the measurement. The construction of the confidence level bands is independent of this prior knowledge.

In general one wants to set limits on a parameter μ by measuring a parameter x. First the probability density function $p(x \mid \mu)$ has to be determined, which describes the expected distribution of the measured value x for a given true value of the parameter μ.

For the general frequentist procedure $p(x \mid \mu)$ can be considered to be known precisely for all physically allowed values of μ. The construction of $p(x \mid \mu)$ in the analyses presented in this thesis is done by generating a set of ensembles of many simulated datasets (also known as pseudo datasets) at various μ values. x is determined for each dataset, resulting in a distribution of x values for each μ. Systematic uncertainties can be incorporated into this procedure by introducing nuisance parameters that describe systematic variations and varying them in each simulated dataset [41].

Once the probability density functions are known, the confidence intervals have to be constructed. In case of Neyman the X % so-called acceptance region (x_d, x_u) is constructed by integrating $p(x \mid \mu)$ over all x values having equal or higher probability than x_d and x_u. This is done independently for each μ value.

In the Neyman case $p(x \mid \mu)$ is therefore used for the ordering that determines which area will be summed up first. Feldman and Cousins propose a different ordering scheme, with the motivation that the confidence intervals are never unphysical or empty. Instead of starting with the most probable value they calculate the so-called r_{likeli} value, which is defined as the ratio of $p(x \mid \mu)$ and $p(x \mid \mu_{\text{best}})$, where μ_{best} is the parameter value that has the maximal probability for x:

$$r_{\text{likeli}}(x) = \frac{p(x \mid \mu)}{p(x \mid \mu_{\text{best}})}. \tag{3.6}$$

The important point here is that μ_{best} is a function of x, and is required to be within the physically allowed region. The latter automatically implies the physics boundaries on the confidence level bands, resulting in either two sided or one sided intervals for μ. While the former would be a measurement of the quantity, one considers the one sided intervals as a limit.

For the calculation of the acceptance region (x_d, x_u), the probability density $p(x \mid \mu)$ is summed up starting with the x value where r_{likeli} is maximal and continuing with decreasing r_{likeli} until the set of x values chosen contains the desired confidence level X.

By definition $r_{\text{likeli}}(x) = 1$ for $\mu = \mu_{\text{best}}$ and $0 \leq r_{\text{likeli}}(x) < 1$ otherwise. When the experimental sensitivity, e.g. resolution, is different for different μ's, the ordering can be very different from the Neyman ordering. Areas with small probability can be summed up before areas with higher probabilities are considered.

Given a value x_{obs} observed in the dataset D, all values of μ, for which x_{obs} lies within the acceptance regions (x_d, x_u) build the confidence region (μ_d, μ_u) for x_{obs}. If μ_d (μ_u) is identical

with the physical boundary, the resulting one sided region builds the upper (lower) limit at X % confidence level.

3.3. Frequentist limit setting with modified frequentist confidence levels

Each procedure to determine how well a hypothesis matches to a given dataset relies on a certain test statistic, as for example a likelihood or χ^2. In the modified frequentist scheme with the CL_S method [38], the optimal solution to separate a signal hypothesis (H_S), including the prediction of signal and background (s+b), and a null hypothesis (H_0), including a background-only (b) prediction, is a likelihood ratio [42]

$$Q = \frac{p(D|H_S)}{p(D|H_0)} \tag{3.7}$$

where $p(D|H_S)$ and $p(D|H_0)$ are the probability densities of the signal (s+b) or null (b) hypothesis to match the data, respectively. The likelihood ratio in Eq. 3.7 is similar to the one in Eq. 3.6. The difference lies in the denominator, where in case of the likelihood ratio ordering of Feldman and Cousins the signal plus background hypothesis is used, but for Q only the background hypothesis. The goal of this method is to compare the probability density in case of the presence of a signal with the background-only hypothesis. This method is introduced to reduce the sensitivity to fluctuations in the background-only model.

The test statistics Q can easily be used to find the combined limit of independent channels by multiplication of all individual test statistics. For the computation a log-likelihood ratio (LLR) is defined as $\chi = -2\ln(Q)$. The LLR is monotonically increasing with the number of observed events in each channel.

The frequentistic confidence level for the signal hypothesis is given as the probability that the log-likelihood ratio of the signal hypothesis is less or equal to the one in data (χ_{obs}):

$$CL_{s+b} = P_{s+b}(\chi \leq \chi_{obs}) \tag{3.8}$$

The same quantity is defined for the null hypothesis:

$$CL_b = P_b(\chi \leq \chi_{obs}) \tag{3.9}$$

With the confidence levels in Eq. 3.8 and 3.9 the modified frequentist confidence level CL_s is calculated as

$$CL_s = CL_{s+b}/CL_b \tag{3.10}$$

For the limit calculation with the CL_s method at DØ, the `Collie` package is used [42, 43], which incorporates systematic uncertainties via nuisance parameters. In this package a technique called profile likelihood technique is build in, in which the "best-fit" model for the data is determined by adjusting the null (background only) hypothesis in a way that the probability density functions are maximised over the space of systematic uncertainties.

4. Fermilab, Tevatron and DØ

In order to study quarks, gluons and leptons and search for particles not seen before very high energies are necessary. The Fermi National Accelerator Laboratory (FNAL, or Fermilab) is located in Batavia, west of Chicago. At Fermilab, the Tevatron, a large proton-antiproton collider with a circumference of 6.4 km, reaches the current world's highest centre of mass energy (cms) of $\sqrt{s} = 1.96$ TeV. Two multi-purpose detectors, CDF and DØ, are located at collision points where the proton and antiproton beams collide.

Fermilab was founded in November 21st 1967. Many fundamental discoveries were made at Fermilab, like the discovery of the bottom quark in 1977, the discovery of the top quark in 1995 and the first direct observation of the tau neutrino in July 2000.

In 1983 the Tevatron began its operation. The CDF detector saw its first proton-antiproton collisions in 1985. The DØ detector was build later, and started data taking in 1992, during the Run I of the Tevatron. Run I lasted from 1992 to 1996 and about 125 pb^{-1} of integrated luminosity were collected by CDF and DØ with a cms of 1.8 TeV.

After Run I the detectors and accelerator were upgraded, and in spring 2001 Run II started, with a cms of 1.96 TeV. The data taking of Run II is expected to end in 2010, with 6 fb^{-1} to 9 fb^{-1} of collected data.

4.1. The Tevatron Collider

The Tevatron is the last stage of an accelerator chain for protons and antiprotons and is used to collect and collide the protons and antiprotons. The whole chain consists of a Cockcroft-Walton accelerator, a linear accelerator (LINAC), a Booster synchrotron ring, and a Main Injector and the Tevatron at the final stage. The antiprotons are produced in an additional complex. Figure 4.1 shows the accelerator chain schematically.

The whole procedure starts with the ionisation of hydrogen atoms to H^-, which are then accelerated to an energy of 750 keV in the Cockcroft-Walton. In the LINAC the H^- are further accelerated up to an energy of 400 MeV. After that the electrons are stripped off and the remaining protons are accelerated to 8 GeV in the Booster and get injected in the Main Injector. In order to produce antiprotons the protons are accelerated to 120 GeV in the Main Injector and are directed from the Main Injector on a nickel target. The antiprotons are then filtered from the end products with a magnet, and are collected and accelerated to 8 GeV in the Accumulator. After the collection of enough antiprotons the protons and antiprotons are accelerated to 150 GeV and go into the Tevatron, where each beam is accelerated to its final energy of 0.98 TeV. More details on the accelerator chain can be found in [45, 46].

In order to keep the particles on their ideal track a magnetic field of 4.2 T is needed. For this purpose superconductive dipole magnets are used, which require liquid helium for cooling to a temperature of 4.2 K.

Protons and antiprotons are accelerated in three trains, each consisting of 12 bunches. The spacing between each bunch is 396 ns, the spacing between the trains is 7 μs. Each individual bunch consists of $\mathcal{O}(10^{11})$ protons or $\mathcal{O}(10^{10})$ antiprotons. The bunches of protons and an-

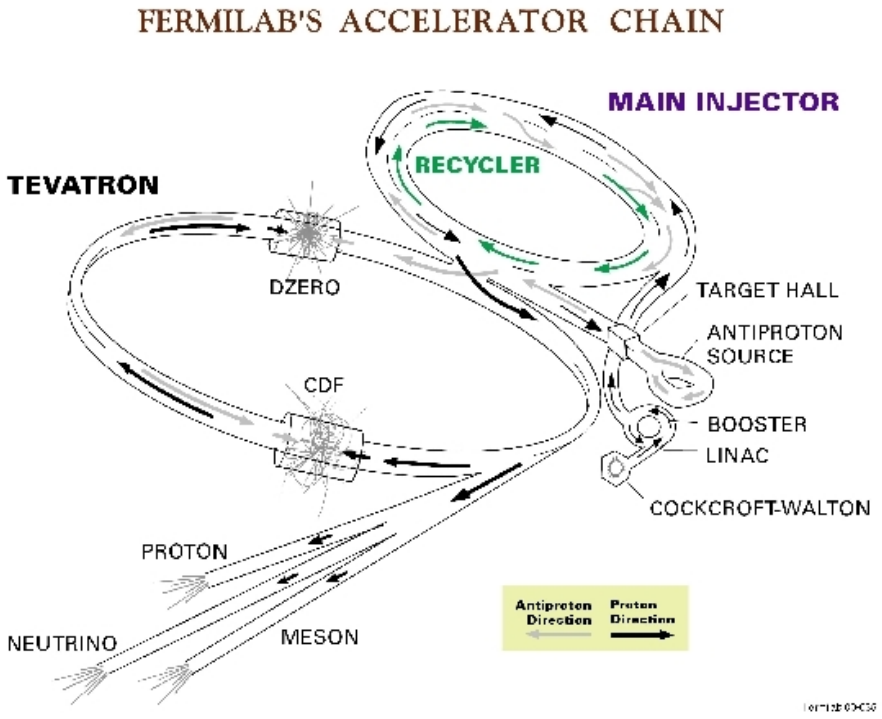

Figure 4.1.: Accelerator chain [44].

tiprotons are collided at two positions in the accelerator, namely at the detector positions of CDF and DØ.

Since 2006 the Recycler – located along the ceiling of the Main Injector Tunnel – is in use. It is used to store and accumulate antiprotons and is more effective than the Accumulator. It makes it possible to collect more antiprotons for each store, leading to higher luminosities.

4.2. The DØ Detector

The DØ detector, built around one of the bunch crossing points of the Tevatron, is a multi-purpose detector with the main goal to measure electrons, muons and jets with high precision. In Fig. 4.2 the side view of the complete DØ detector is shown.

The DØ detector has a length of 20 m, and a height of 13 m. The three main components are the tracking system, the calorimeter and the muon system, as described in detail in [48–50]. Additionally there are luminosity monitors and proton detectors (FPD) in the forward regions.

The coordinate system of the DØ detector is right-handed. The positive z axis points along the proton beam, the positive x-axis points horizontally inside the Tevatron ring, and the y-axis upwards. The transverse plane is defined by the x and y-axis. A more useful coordinate system than the Cartesian (x, y, z) coordinates is the cylindrical coordinate system with (r, ϕ, η), where

$$r = \sqrt{x^2 + y^2} \tag{4.1}$$

$$\phi = \arctan \frac{x}{y} \tag{4.2}$$

$$\eta = -\ln \tan(\frac{\theta}{2}) \tag{4.3}$$

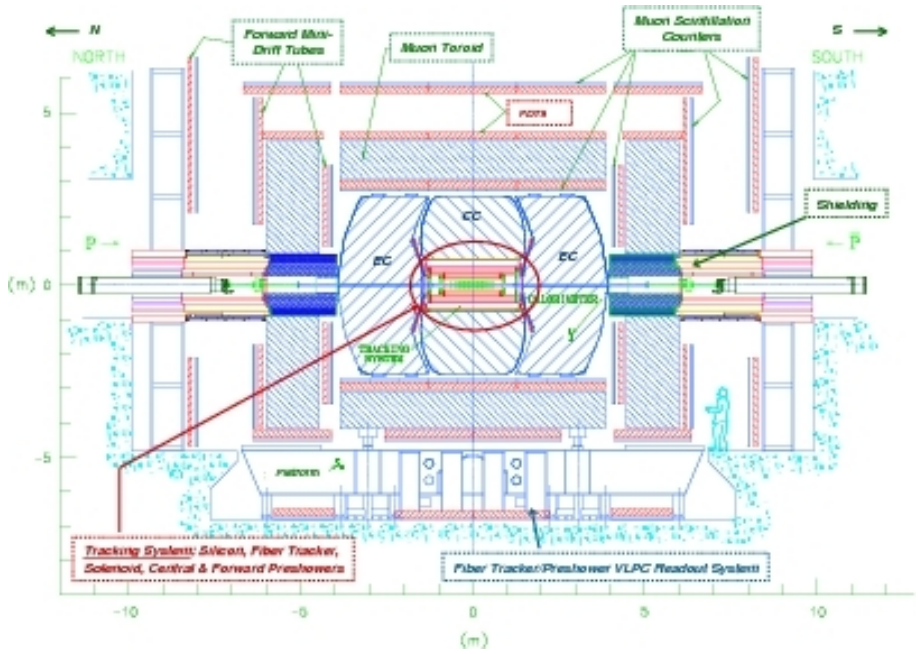

Figure 4.2.: Side view of the DØ detector [47].

with θ the azimuthal angle. η is called the pseudo-rapidity and is equal to the rapidity

$$y = \frac{1}{2}\ln\left(\frac{E + p_z}{E - p_z}\right) \tag{4.4}$$

for massless particles. Two definitions of η exist at DØ: One is to define η wrt. the centre of the detector, called detector η or η_{det}. All η in this chapter refer to the detector η. The other definition is called physics η and is defined relative to the primary vertex of the events and is typically used for reconstructed particles and will be used in the analyses chapters of this thesis. Due to the distribution of the beams and therefore the possibility of the hard interaction taking place outside the exact centre of the detector the two definitions are not identical.

4.2.1. The Tracking System

In the innermost of the detector the tracking system is situated. It consists of the silicon micro-vertex tracker (SMT) directly at the collision point, and the central fibre tracker (CFT) around the SMT. The whole tracking system is surrounded by a solenoid magnet with a magnetic field of 2 T. A schematic view of the tracking system is shown in Fig. 4.3. The magnet with a length of 2.73 m is cooled with cryostats to ensure superconductivity. Figure 4.4 shows the solenoid and its magnetic field lines. Both together, cryostat and magnet, form 1.1 radiation lengths[1)] of material. The solenoid was designed with the purpose of optimisation of the momentum resolution $\delta p_T / p_T$ and the tracking pattern recognition.

The tracking system has a momentum resolution of

$$\Delta p_T / \text{GeV} = 0.002\,(p_T / \text{GeV})^2. \tag{4.5}$$

As this resolution is much better than that for the muon system, the tracking system is also important for the measurement of muons.

[1)] The radiation length X_0 is defined as the distance, in which the energy of a particle is reduced by $1/e$ due to radiation loss.

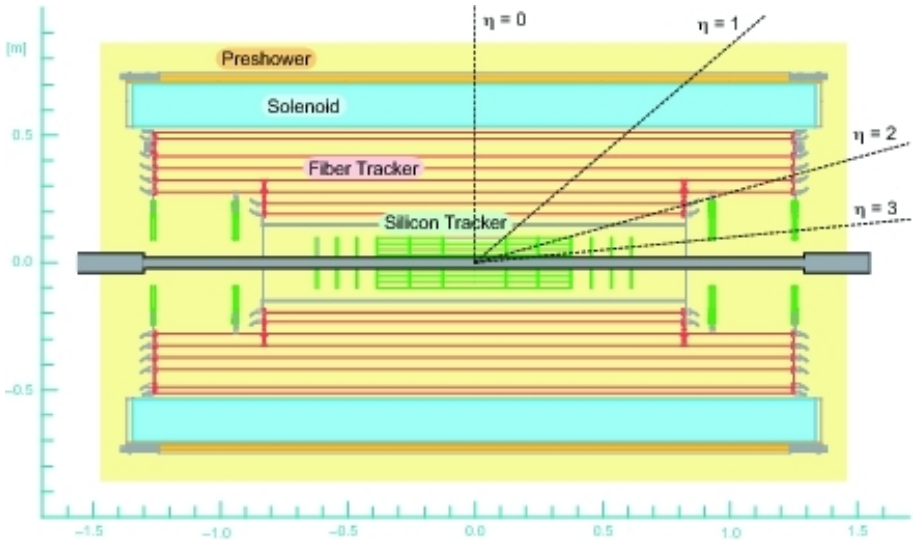

Figure 4.3.: Schematic picture of the central tracking system [51].

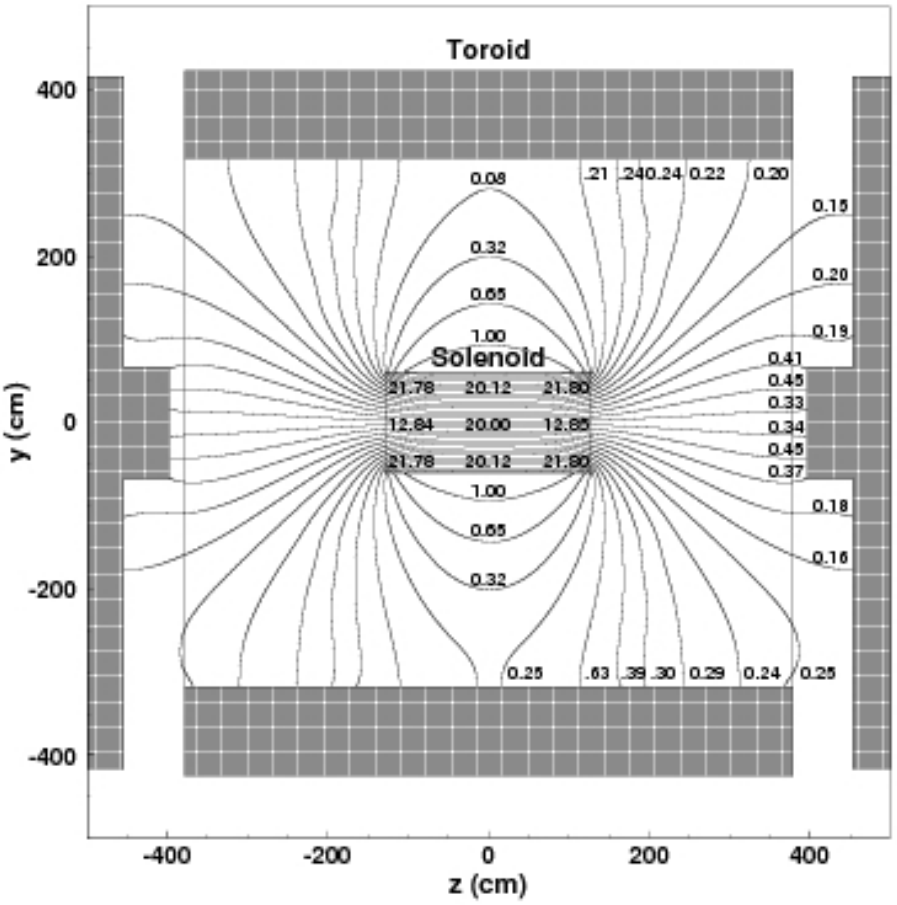

Figure 4.4.: View of the magnetic field inside the DØ detector [50].

The Silicon Microstrip Tracker

The detector component nearest to the interaction point is the silicon microstrip tracker (SMT). The purpose of the SMT is tracking and the determination of primary and secondary vertices. Secondary vertices are important for the identification of *b*-jets.

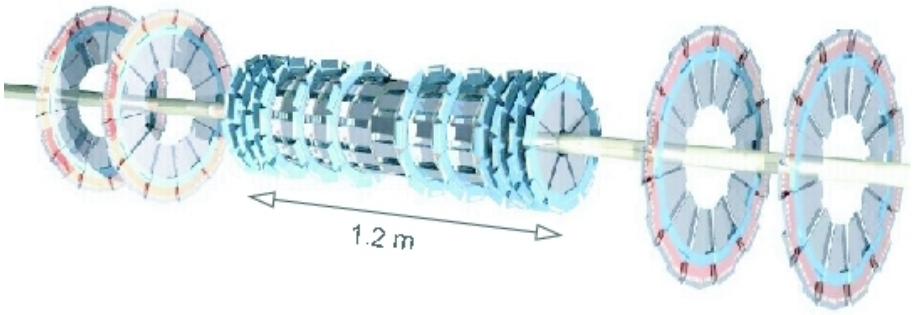

Figure 4.5.: The design of discs and barrels in the SMT [50].

The design of the SMT is shown in Fig. 4.5. It consists of six barrels and 16 discs. The main purpose of the barrel detector is to measure the r–ϕ coordinate, which is used to determine the transverse momentum of the track. The discs provide additional information in the r–z plane, yielding three dimensional information of the track.

Each barrel has four layers of silicon readouts. The silicon modules in the barrels are called ladders. The first and second layer consist of 12 ladders respectively, while the third and fourth layer have 24 ladders each. Each layer consists of two sub-layers. The central four barrels use double-sided double-metal (DSDM) detectors in layer 1 and 3. Layer 2 and 4 in all barrels use a single-sided (SS) technology. In the outermost barrels double-sided (DS) detectors are used. The DSDM sensors consist of axial and 90° stereo strips, while the DS consists of axial and stereo strips with a stereo angle of 2°. The SS detectors are axial only.

The discs that intersperse the barrels are the so-called F-discs that consist of twelve double-sided wedge-detectors. In the forward region two so-called H-discs are placed that provide tracking information for high $|\eta|$ up to $|\eta| = 3$. The H-discs consist of 24 wedges which are made of two back-to-back single-sided wedges. The discs are planar modules. The double-sided F-wedges have an effective stereo angle of 30°. The two single sided detectors of the H-wedges form together a double-sided sensor that provides an effective stereo angle of 15°.

In 2005 a new layer, called layer 0, was installed in the SMT [52]. It is now the layer closest to the interaction point and fits inside layer 1. With the new layer 0 better vertex resolution can be achieved.

The Central Fibre Tracker

Around the SMT the central fibre tracker (CFT) is arranged. The CFT covers the region $|\eta| < 1.62$ and consists of 76800 scintillating fibers mounted on eight concentric cylinders. The two innermost cylinders have a length of 1.66 m, the six outer cylinders are 2.52 m long. Every cylinder consists of a doublet layer of fibers in axial direction (axial layer) and a doublet layer of fibers with a stereo angle in ϕ of $\pm 3°$ (stereo layer). The stereo layers on the first, third, fifth and seventh cylinders are oriented in $+3°$ direction, the stereo layers on the other cylinders in the $-3°$ direction. The scintillating fibers are coupled to clear fibre waveguides which conduct the light to visible light photon counters (VLPCs) where the light signal is converted into an electric signal and is read out. Each fibre has a diameter of 835 μm and is 1.66 m or 2.52 m long. Only one end of the scintillating fibers is connected to a waveguide. The opposite end is mirrored with sputtered aluminium coating, which provides reflectivity of about 90%.

A charged particle produces about ten photoelectrons in a fibre. The VLCP have a quantum efficiency of $\geq 75\%$ and a high gain. They convert each photon to 22000 to 65000 electrons.

4.2.2. The Preshower Detector

The preshower detector is arranged around the solenoid. It consists of the central preshower detector (CPS) covering the region $|\eta| < 1.3$ and the forward preshower detector (FPS) covering $1.5 < |\eta| < 2.5$. The FPSs are located at the ends of the calorimeter. The purpose of the preshower detector is to increase the electron and photon identification as well as the background rejection.

The CPS is located around a 5.6 mm lead radiator, which corresponds to about one radiation length. Together with the $0.9X_0$ thick solenoid it forms at least two radiation length of material, increasing to four radiation lengths depending on the angle of the entering particle. The CPS consists of three layers of scintillator strips, each layer consisting of 1280 strips. Each strip is read out by two wavelength-shifting (WLS) fibers.

The two FPSs on the north and south side of the detector are mounted on the calorimeter cryostats. Both detectors consist of two layers of double planes of scintillators, separated by a 11 mm ($2X_0$) thick lead-stainless-steel absorber. The innermost layer is called MIP (minimum ionizing particle) layer, the outermost layer is called shower layer. In the MIP layer charged particles passing through the detector deposit minimum ionizing signals. In the shower layer charged particles and photons produce a shower signal.

4.2.3. The Calorimeter

The purpose of the calorimeter is to identify and to measure the energy of electrons, photons, jets and missing transverse energy. The calorimeter consists of three parts: The central calorimeter (CC) and the end calorimeters (EC) on the north (ECN) and south (ECS) side of the detector, as shown in Fig 4.6. EC and CC are absorber plates made of uranium surrounded by liquid-argon. Figure 4.7 shows the coverage of the calorimeter as well as the segmentation of the absorber plates. The CC covers the range $|\eta| < 1$ while the ECN and ECS cover the range up to $|\eta| \simeq 4$. Each of the three calorimeter parts consists of four electromagnetic layers (EM), forming the innermost calorimeter section, surrounded by three fine and one coarse hadronic layer. In order to keep the argon at a temperature around 90 K, each calorimeter part is located within a cryostat.

The absorber plates in the EM and hadronic sections of the calorimeter are different. In the EM thin plates (3 mm in CC and 4 mm in the EC) of almost pure depleted uranium are used, while the fine hadronic sections have thin uranium-nobium alloy and the coarse hadronic contains thick (46.5 mm) copper plates in the CC and stainless steel plates in the EC.

The segmentation of the fine, the coarse hadronic and the first, second and fourth layer of the electromagnetic calorimeter in the η-ϕ space is $\Delta\eta = 0.1$ and $\Delta\phi = 0.1$. As the third layer of the EM calorimeter is located at the electromagnetic shower maximum its segmentation is twice as fine in η and ϕ in order to ensure a more precise determination of the EM shower centroids.

In the central region of $\eta = 0$ the thickness of the EM calorimeter is $20.6X_0$. The hadronic calorimeter has a thickness of about 6.4 λ_A [2)].

In the EM calorimeter electromagnetic particles are completely absorbed. Hadronic jets start to shower within the EM, but the showering mainly takes place in the fine and coarse hadronic calorimeter. This gives the possibility to distinguish electromagnetic and hadronic objects. Additionally, the form of the shower is different for electromagnetic and hadronic objects.

[2)] The nuclear interaction length λ_A is defined as the distance in which the number of initial particles reduces by a factor of $1/e$.

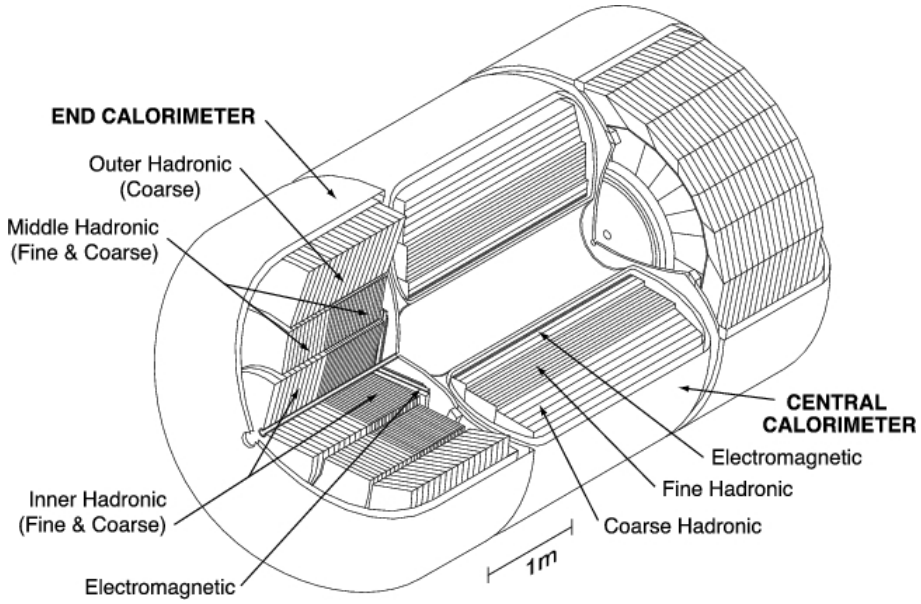

Figure 4.6.: View of the central and end calorimeters of the DØ detector [50].

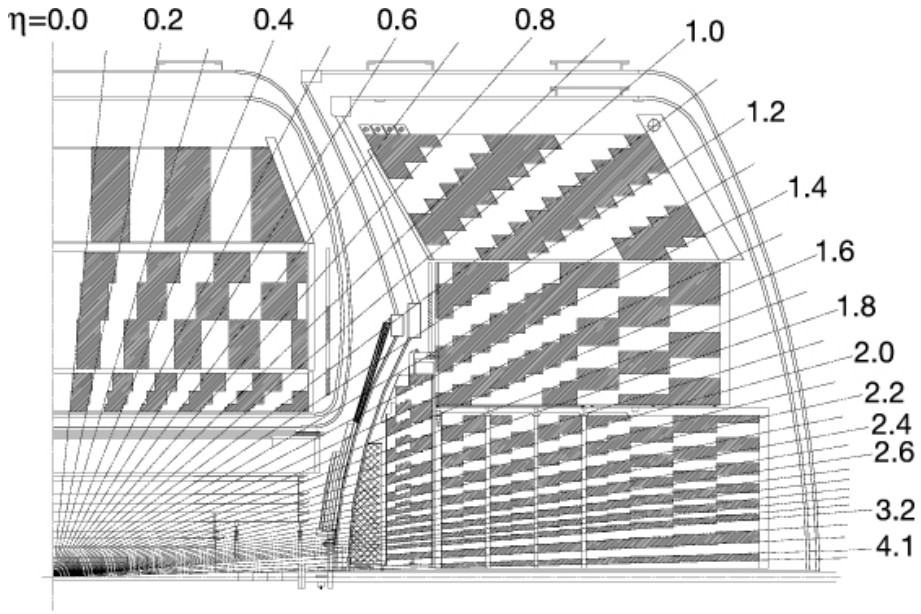

Figure 4.7.: Part of the calorimeter [50], showing the segmentation pattern and the coverage in η.

The relative uncertainty on the energy of electromagnetic and hadronic objects in the calorimeter can be parameterised as

$$\frac{\Delta E}{E} = \sqrt{\frac{S^2}{E/\mathrm{GeV}} + \frac{N^2}{E/\mathrm{GeV}^2} + C^2}. \tag{4.6}$$

where N describes instrumental effects like uranium noise and pedestal subtraction, S describes fluctuations in the deposition of energy and C stands for uncertainties in the calibra-

tion. The parameters N, C and S measured from data are listed in table 4.1. In contrast to the tracking system the energy resolution improves with increasing energy depositions.

Object	C	S [$\sqrt{\text{GeV}}$]	N [GeV]
Electrons, Photons	0.041	0.15	0.29
Jets	0.036	1.05	2.13

Table 4.1.: Energy resolution parameters [53, 54]

The Intercryostat Detector

In between the CC and the EC part of the calorimeter the Intercryostat Detector (ICD) is situated. The gap between CC and EC leads to incomplete coverage in the region $0.8 < |\eta| < 1.4$. The ICD, consisting of scintillating tiles, is attached on the surface of the end cryostats, and covers the region $1.1 < |\eta| < 1.4$. Furthermore, standard calorimeter readout cells called massless gaps are added within the central and end cryostats.

The ICD consists of 16 scintillating tiles, each covering $\Delta\eta \times \Delta\phi$ of about 0.3×0.4. Each tile consists of 12 sub-tiles covering $\Delta\eta \times \Delta\phi$ of about 0.1×0.1 each.

4.2.4. The Muon System

The outermost system of the detector is the muon system. Its purpose is to identify and measure muons. In order to have a stand-alone muon-system momentum measurement, a toroidal magnet with a magnetic field of 1.8 T is located within the muon system. The magnetic field lines are shown in Fig. 4.4.

The muon system consists of two parts: The wide angle muon system or central muon system (WAMUS) and the forward muon system (FAMUS). The central muon system covers the range up to $|\eta| \simeq 1$, the forward muon system covers $1 \leq |\eta| \leq 2$. Both systems consist of three layers, called the A, B and C layers.

In the central muon system all three layers consist of proportional drift tubes (PDTs) and scintillation counters. The A layer is placed directly around the calorimeter. The toroid magnet, surrounds the A layer, followed by the B and C layer. About 90% of the central region is covered by at least two layers, while the three layers of the PDTs cover about 55%. Each of the drift chambers in the B and C layer consists of three decks of drift cells. The PDTs in the A layer have four decks, except for the bottom A layer which also has three decks. A PDT has a size of 2.8×5.6 m^2 and is made of an aluminium tube. A typical drift chamber contains 72 (three decks) or 96 (four decks) cells, each cell being 10.1 cm wide. The electronics to read out the wires is located at the end of each drift chamber.

On the top, sides and bottom of the C layer the scintillation counters are installed. The bottom ones are called the bottom counters, the rest is called cosmic cap. The cosmic cap and bottom counters, which provide a fast timing signal, have the purpose to associate muons with a bunch crossing and help to discriminate against cosmic rays.

Additionally, so-called Aϕ scintillation counters are covering the PDTs of the A layer. The purpose of the Aϕ scintillators is to have a fast detector to reject out-of-time backscatter, to trigger on muons, and to identify muons. The timing resolution of the Aϕ counter is about 2 ns.

In the forward muon system mini drift tubes (MDTs) are used instead of the PDTs. It consists of the end toroidal magnets, the A, B and C layer of MDTs, three layers of scintillators and

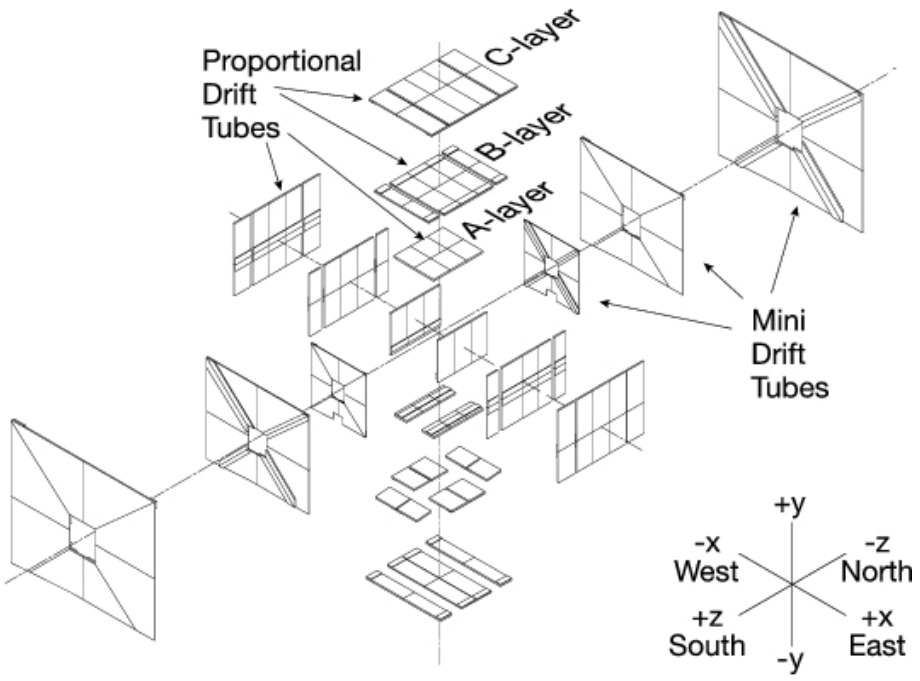

Figure 4.8.: View of the PDTs and MDTs in the muon system [50].

shielding around the beam pipe. The A layer is located inside the toroid, closest to the interaction point and consists of four planes of MDTs, which are mounted parallel to the magnetic field lines. The B and C layer are outside of the toroid and further away from the interaction region. B and C layer consist of three planes of MDTs each, which are also mounted on field lines of the magnet.

Each drift tube is made out of eight cells. Each cell covers an area of $9.4 \times 9.4\,\mathrm{mm}^2$. The trigger scintillation counters are located outside the A, B and C layer. Each of the layers of scintillation counters consists of eight parts in ϕ, each part containing 96 counters. The scintillators are designed to provide good time resolution.

A view of the PDTs and MDTs in the central and forward muon system is shown in Fig. 4.8. Figure 4.9 shows the positions of the cosmic cap, the bottom counters, the Aϕ scintillators and the trigger scintillation counters within the muon system.

The toroidal magnet's purpose is to provide a stand-alone muon-system momentum measurement, in order to allow for low p_T cutoffs in the Level 1 muon trigger, to get a better matching of muons with central detector tracks, to better reject π and K decays and to improve the momentum resolution for muons with high momentum. The polarity of the magnet is reversed regularly during data taking, in order to avoid systematic errors due to asymmetries in the detector.

In order to reduce background due to beam halo interaction in the accelerator tunnel, a shielding is installed in the tunnel. Additionally a shielding with the purpose of suppressing backgrounds due to proton and antiproton remnants interacting with the quadrupole magnets of the Tevatron is installed. The position of the shielding at the south side of the detector is shown in Fig. 4.2. .

4.2.5. The Forward Proton Detector

Protons and antiprotons scattered at small angles of about 1 mrad are measured with the forward proton detector (FPD). The FPDs are positioned along the beam line. Figure 4.10

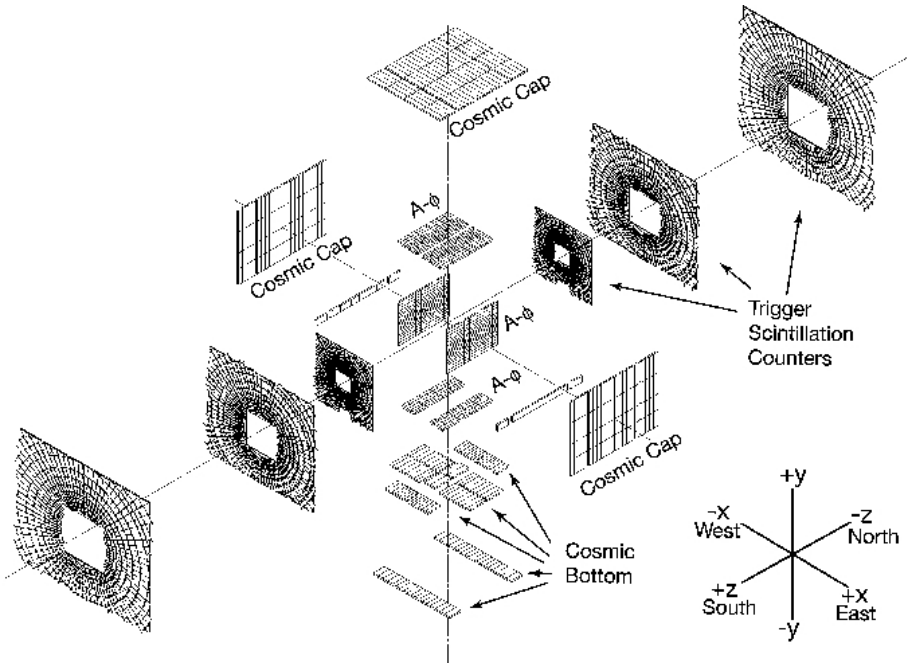

Figure 4.9.: View of the scintillation detectors of the muon system [50].

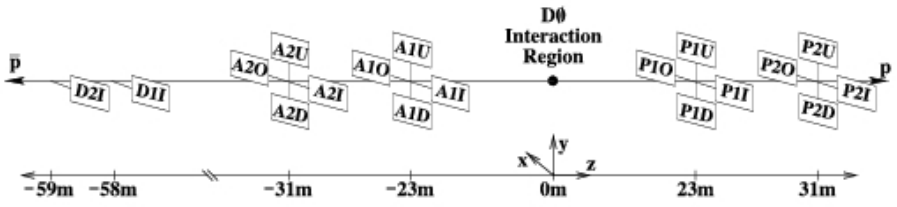

Figure 4.10.: Location of the forward proton detector [50].

shows the position of the FPDs wrt. the DØ interaction point along the beam axis.

4.2.6. The Luminosity Monitors

In order to measure the Tevatron luminosity at the DØ interaction points, luminosity monitors (LM) are located at $z = 140$ cm and $z = -140$ cm, as shown in Fig. 4.11. The LMs detect inelastic $p\bar{p}$ collisions. Each LM consists of an array of 24 plastic scintillation counters. Each counter is 15 cm long and covers $2.7 < |\eta| < 4.4$. The timing resolution of the scintillators is about 0.3 ns. The high timing resolution enables the discrimination between particles from the interaction region and the beam halos. The second purpose of the LM is to measure beam halo rates and act as fast vertex finder.

Luminosity determination

The inelastic proton-antiproton counting rate is used to determine the instantaneous luminosity [55–58]

$$\mathcal{L} = \frac{1}{\sigma_{\text{eff}}} \frac{dN}{dt} \tag{4.7}$$

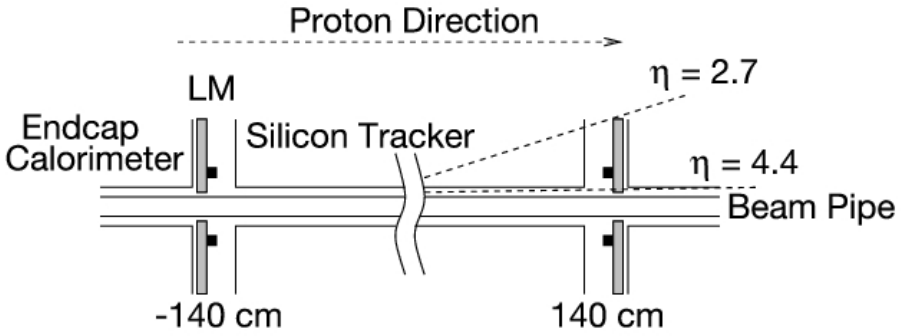

Figure 4.11.: Location of the luminosity monitors on the z-axis [50].

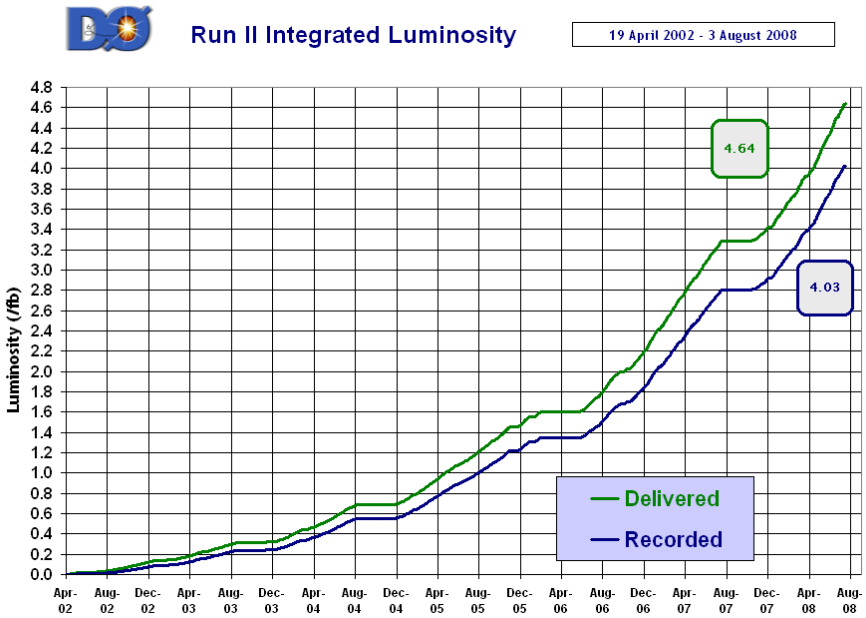

Figure 4.12.: Delivered and recorded integrated luminosity [60].

with σ_{eff} being the effective inelastic cross section measured by the LM. The effective cross section is derived from the inelastic cross section [59] $\sigma_{\text{inelastic}}(1.96\,\text{TeV}) = 60.7 \pm 2.4$ mb, but taking into account acceptance effects and the efficiency of the LM detector. In order to properly distinguish $p\bar{p}$ interactions from beam halo interactions the z coordinate of the interaction vertex is calculated from the difference in time-of-flight between the north and south part of the LM. Beam halo particles have a larger time-of-flight difference than inelastic $p\bar{p}$ collisions.

The integrated luminosity is calculated in luminosity blocks. Each luminosity block, which builds the fundamental unit of time for the luminosity measurement, is indexed by a luminosity block number (LBN). After each run or store transition (as defined in section 4.2.7) or after 60 seconds the LBN monotonically increases. The time period is chosen such that for each LBN the integrated luminosity is approximately constant.

Figure 4.12 shows the delivered and recorded integrated luminosity for DØ from the beginning of Run II up to august 2008. The difference between delivered and recorded luminosity is caused by data taking efficiencies of about $80 - 90\%$.

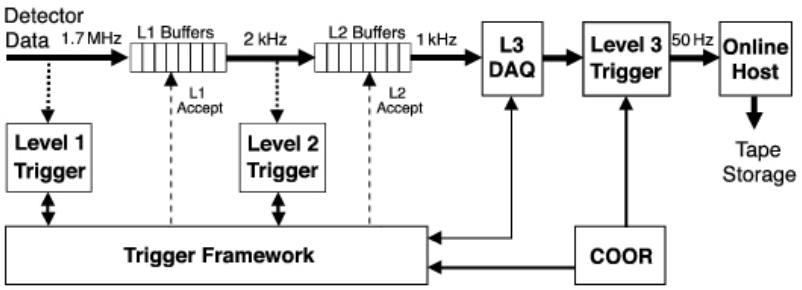

Figure 4.13.: The DØ trigger and data acquisition systems [50].

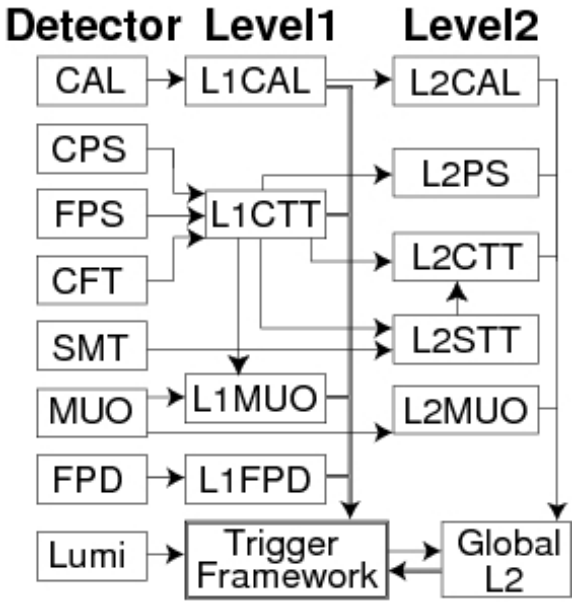

Figure 4.14.: The DØ L1 and L2 trigger system [50].

4.2.7. The Trigger System and Data Acquisition

At each collision point an interaction takes place every 369 ns, resulting in an average rate for collisions of about 2.5 MHz. The average rate with which data can be stored and reconstructed is about 50 Hz. In order to reach this rate it is necessary to preselect interesting events with the aid of triggers [50, 61, 62].

The DØ trigger system consists of three levels. The Level 1 (L1) trigger is a pure hardware trigger and uses electronic signals from separate detector components. The Level 2 (L2) trigger is a mixture of hardware and software triggers, which already use reconstructed and identified objects for the trigger decision. The Level 3 (L3) trigger is a pure software trigger, in which the event is almost fully reconstructed. Figure 4.13 shows the overview of the DØ trigger and data acquisition system. In Fig. 4.14 the L1 and L2 triggers and the communication with the trigger framework are sketched.

Level 1 trigger

The Level 1 trigger, consisting of hardware trigger elements, reduces the trigger acceptance rate to about 2 kHz. It consists of the calorimeter trigger (L1CAL), central track trigger (L1CTT) and the muon system trigger (L1Muon).

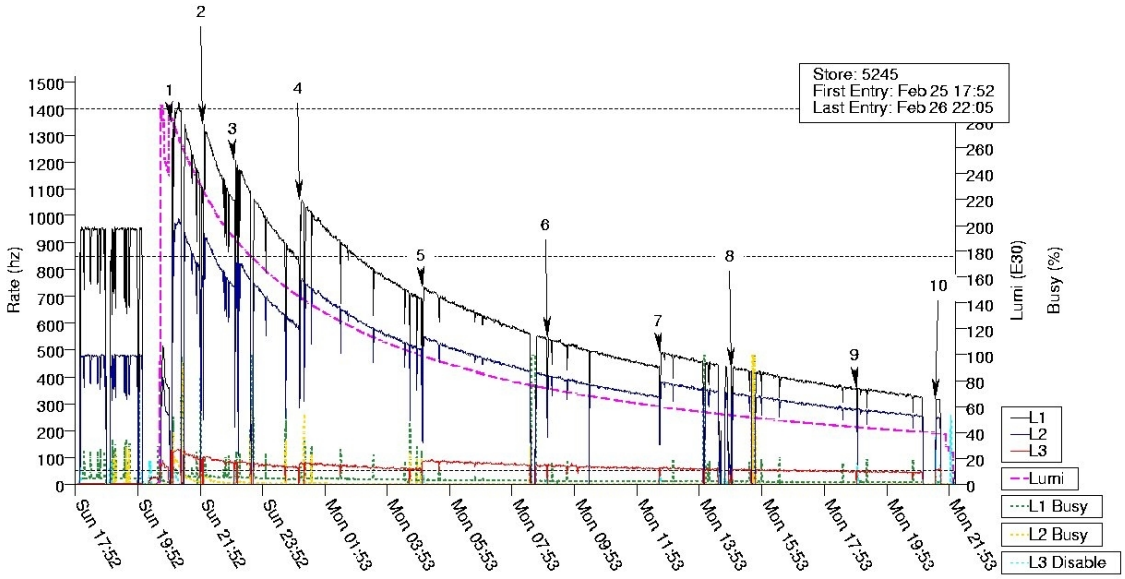

Figure 4.15.: Luminosity and rates for store 5245 [63].

The triggers from each system decide if the event is kept or not in 3.5 μs or less. The information of each trigger is then gathered together at the trigger framework (TFW) where the decision is made if the considered event is accepted or not.

Level 2 trigger

The L2 trigger consists of two stages. In the preprocessor stage the information from the subsystems are collected and the data are analysed to form physics objects. The preprocessor stage consists of the Level 2 calorimeter trigger (L2CAL), the preshower detector trigger (L2PS), the muon system trigger (L2MUO), the SMT trigger (L2STT) and the Level 2 central track trigger (L2CTT). In the global stage (L2Global) the data from across the subsystems is combined and physics objects are formed. The decision whether an event is kept or not is made within 100 μs at Level 2. The L2 trigger reduces the data rate to about 1 kHz.

Level 3 trigger

The purpose of the last trigger stage is to enrich the physics samples and reduce the rate for data writing on tape to 50 Hz. The Level 3 trigger is a fully programmable software trigger that performs a simplified event reconstruction, thus the L3 trigger decisions are based on complete physics objects and relations between them.

Stores, runs, prescales and data acquisition

Stores, runs and prescales When a store begins the instantaneous luminosity and therefore the interaction rate are high and decrease during the store. In order to keep a constant rate of 50 Hz, prescales are used, which let only a fraction $1/n$ of a certain event type pass the L1 trigger in case the trigger condition is fulfilled. Figure 4.15 shows an example for a store together with the instantaneous luminosity and the L1, L2 and L3 rates. At each run transition, the trigger configuration and prescale rates can be changed in order to adjust the trigger rates to the luminosity.

Data Acquisition Systems The transport of data from the readout crates to the farm nodes for processing is done by the primary data acquisition system (L3DAQ). The triggering and data acquisition are controlled by a coordination program (COOR) [64]. The read-out of the LM is done with a stand-alone DAQ system.

5. Object Identification

Each event recorded by the DØ detector consists of large quantities of electronic signals. Out of measured energies deposited in the calorimeter, signals of fibers in the tracking system or in the layers of the muon system and trigger informations, for example, physical objects have to be reconstructed and identified. For this purpose several high level algorithms were designed.

In the following sections the reconstruction and identification of tracks, vertices, electrons, muons, jets and missing transverse energy are described. In the end of the chapter a more detailed consideration of the identification of b-jets is given.

5.1. Tracks

When a charged particle passes through the detector, it leaves hits in the SMT or CFT. Due to the magnetic field of the solenoid the charged particle describes a curved trajectory. Clusters are built from the hits, which are used in the track reconstruction algorithms.

Two different algorithms are used to find tracks from the detector hits [65]. The Histogram Track Finder (HTF) [66] algorithm and the Alternative Algorithm [67] run sequentially. The advantage of using two algorithms is the fact that AA is better for low p_T, at high impact parameter and has a lower fake rate than HTF, whereas the HTF algorithm is more efficient for high p_T tracks. After the separate run of both algorithms the track candidates are filtered with a Kalman Filter algorithm [68].

HTF The Histogram Track Finding algorithm divides the detector into slices in the angle ϕ at the interaction point and the track curvature ρ. The slices are thus perpendicular to the magnetic field. Each pair of hits corresponds to one point in the parameter space (ϕ, ρ) represented by a 2D histogram. The idea of the algorithm is now that all pairs of hits on one track trajectory point to the same value of (ϕ, ρ). Points from different tracks result in a randomly distributed background in the parameter space. The HTF algorithm improves this method using the Hugh transform [66]. Each hit corresponds to a line in the parameter space. An intersection of different lines corresponds to candidates for tracks.

AA The Alternative Algorithm starts with the combination of any three hits in the SMT. Each track candidate is then extrapolated to the next SMT or CFT layer, and hits found within the expected region are associated to the track hypothesis if the increase in χ^2 does not exceed a threshold. In case of multiple tracks fulfilling the hypothesis and the χ^2 condition, one track candidate for each possible hit is formed. Tracks with less than three hits in the SMT are reconstructed by using the primary vertex candidates found with reconstructed tracks having at least three hits in the SMT. Any three hits in the CFT are then required to fulfil the additional condition of the track hypothesis passing near a reconstructed primary vertex.

Combination of HTF and AA and filtering of track candidates After the track finding procedure a complete set of track candidates from both algorithms are reconstructed. This list

is passed to the track fitter based on the Kalman filter algorithm [68]. The fitting procedure uses the DØ interaction propagator [69] that propagates a track in the DØ tracking system. It includes effects of interactions with detector material and propagates the uncertainties of the track. By going through the list of candidate tracks, removing ambiguities and refitting the tracks with the Kalman filter, the final track parameters with their proper uncertainties are calculated.

5.2. Vertices

The interaction and decay of particles results in a bunch of tracks that originate from one vertex. The primary vertex (PV) represents the point of the hard interaction. A precise reconstruction of the PV is essential to distinguish the objects from the hard interaction from underlaying events and to distinguish tracks from the primary and secondary vertex (SV). The latter are important for the determination of heavy flavour jets.

5.2.1. Primary Vertex

For the reconstruction of the primary vertex the so-called adaptive primary vertex algorithm [70] is applied, which is an extension of the Kalman Filter algorithm that was used before [71, 72]. The advantage of the adaptive primary vertex algorithm in contrast to the Kalman Filter is that tracks from secondary vertices, occurring in heavy flavour events, are down-weighted, reducing the bias on the sample reconstruction [73]. Another improvement with respect to the older algorithm is in the definition of a SMT fiducial region, which makes it possible to achieve high vertex reconstruction efficiencies up to high z values.

In the first step of the primary vertex fitting procedure tracks with $p_T \geq 0.5$ GeV and at least two SMT hits for tracks within the acceptance region of the SMT, the so-called SMT fiducial region, are required. Then all tracks that are within 2 cm along the beam axis are clustered with a z-clustering algorithm. For each of the z-clusters the vertex fitting is performed. After that all selected tracks within all clusters are fitted into a common vertex with the tear-down Kalman Filter algorithm, in order to determine the beam spot position. The tear-down algorithm starts by fitting one vertex with all tracks. Then the track contributing the highest χ^2 to the fitted vertex is removed iteratively. This procedure is repeated until χ^2/ndf[1)] is smaller than 10.

After the reconstruction of the beam spot the z-clusters are preselected according to their *dca* significance, defined as the distance of closest approach (*dca*, also called impact parameter) divided by its uncertainty, with respect to the reconstructed beam spot. The clusters are required to have the *dca* significance smaller than five.

At this point the reconstruction of the primary vertices starts. The algorithm is based on a tear-down Kalman filter with the extension that the errors of the contributing tracks are weighted by a sigmoidal function, according to their χ^2 contribution to the vertex. The weight is calculated as

$$\omega_i = \frac{1}{1 + e^{(\chi_i^2 - \chi_{cutoff}^2)/2T}} \tag{5.1}$$

with χ_i^2 the contribution of track i to the χ^2 of the vertex, χ_{cutoff} the distance where the weight function drops to 0.5 and T the parameter controlling the sharpness of the function. $T > 0$ allows a track to contribute to both primary and secondary vertex, but with a weight smaller than one. Only tracks with very small weights ($\omega_i < 10^{-6}$) are rejected from the fit, all other

[1)] ndf: Number of degrees of freedom

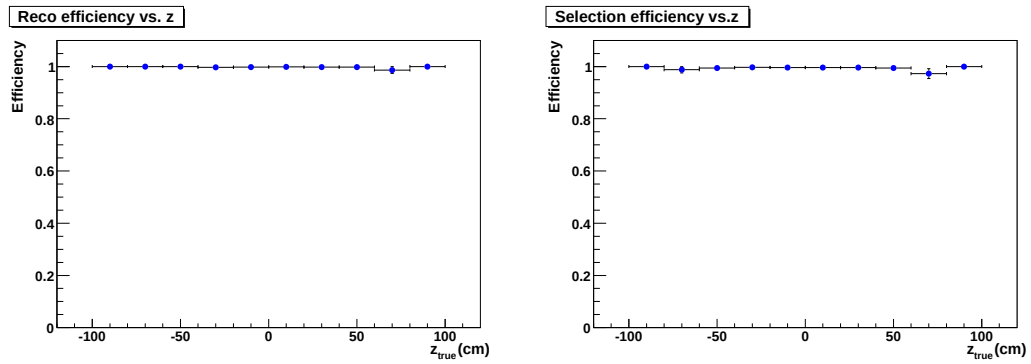

Figure 5.1.: The reconstruction (left) and selection (right) efficiency of the primary vertex in $Z \rightarrow \mu\mu$ Monte Carlo events versus the z position of the true interaction point.

tracks contribute to the vertex. The fitting procedure is iterated until the weights for all contributing tracks are stable.

With this method a list of primary vertices is reconstructed. In order to distinguish the hard scatter primary vertex from minimum bias vertices a probabilistic approach is used [72, 74]. The algorithm uses the fact that tracks from minimum bias interaction tend to have smaller transverse momenta than tracks from the hard interaction. For each track the probability to origin from a minimum bias vertex is calculated based on a $\log_{10} p_T$ distribution. For each vertex the product of the probabilities for all tracks are calculated. The vertex with the smallest probability to be a minimum bias vertex is chosen as the hard scatter primary vertex.

In order to check whether the adaptive primary vertex algorithm introduces a smaller bias on heavy flavour samples than the Kalman filter algorithm, the resolution and pull width of the reconstructed primary vertex in $t\bar{t}$ events is studied as part of this thesis. The resolution is defined as the difference of reconstructed and true x, y or z position of the hard interaction. The pull is defined as the resolution divided by the uncertainty of the reconstructed quantity. A pull width of the resulting distribution close to one indicates a realistic error estimation of the reconstruction. As shown in [73] the pull width for the adaptive primary vertex algorithm is close to one, independent of the heavy flavour content of the considered sample, which is not achieved with the Kalman filter [72]. The reconstruction and selection efficiencies are close to 100% and do not show a drop-off for large z due to the definition of the SMT fiducial region. The reconstruction efficiency, defined as the number of events where at least one primary vertex was found [2)], divided by the number of all events, is shown for an example of $Z \rightarrow \mu\mu$ Monte Carlo events in Fig. 5.1 (left). The selection efficiency, defined as the number of events where the reconstructed hard scatter vertex was found divided by the number of events with any found reconstructed vertex, is shown in Fig. 5.1 (right) for the example of $Z \rightarrow \mu\mu$ Monte Carlo events. Both efficiencies are close to 100% up to high z.

5.2.2. Secondary Vertex

Heavy hadrons traverse typically up to several millimetres in the detector before they decay. A secondary vertex, displaced from the primary vertex, can thus be used to identify heavy hadrons and tag b-jets.

[2)] A vertex was found if it fulfils the requirement that the absolute difference in reconstructed and true z position is less than 1 cm.

The reconstruction of secondary vertices [75–78] is based on the Kalman Filter algorithm and consists of four steps. First track jets are reconstructed [79], then a list of tracks is selected, the vertex finding is performed and in the end a selection of vertices is done.

Track jets and track selection The reconstruction of track jets has the advantage that the secondary vertex reconstruction is kept independent from the calorimeter reconstruction. Track jets are independent of jets from calorimeter noise and not affected by tracker-calorimeter misalignment. Furthermore the tracking system allows for the construction of three dimensional jets.

The track clustering starts with the construction of z-pre-clusters [75]. All tracks are ordered in p_T, and are added in decreasing order to z-pre-clusters if the distance of closest approach in z of track and pre-cluster is smaller than 2 cm. After pre-clusters from all tracks are built, a track selection is performed for each of the clusters. The number of SMT hits has to be at least one, $p_T > 0.5$ GeV and the distance of closest approach to the nearest vertex is required to be $|dca| < 0.2$ cm and $z_{dca} < 0.4$ cm. For each pre-cluster track jets are formed with a simple cone algorithm with $\Delta R = 0.5$. A further requirement of the seed track $p_T > 1$ GeV is applied in order to reduce the number of track jets from the underlying event.

Within each track jet tracks with a large impact parameter significance $dca/\sigma_{dca} > 3$ are selected [80]. σ_{dca} is defined as the uncertainty on the distance of closest approach. Depending on the version of the b-tagging algorithm (as discussed in section 5.7) the track criteria can vary.

Vertex reconstruction On each track jet with at least two tracks fulfilling the dca/σ_{dca} criterion, the vertex reconstruction algorithm is applied. In contrast to the primary vertex reconstruction a build-up Kalman Filter algorithm is used. This algorithm starts with the construction of seed vertices, by fitting all combinations of pairs of tracks in the track jet. On each seed vertex additional tracks are attached, if the χ^2 contribution to the vertex is below a tunable threshold. The attachment of tracks to the vertex is repeated iteratively until no more tracks can be attached. The reconstructed vertices within each track jet are allowed to share tracks. As the number of vertices per jet is an input for the Neural Network b-tagger described in more detail in section 5.7, an algorithm is implemented as part of this theses, where the sharing of tracks is avoided for the secondary vertex reconstruction [81].

An extension of the secondary vertex algorithm is a 2Pass method, that allows first to search for a vertex with tight criteria that provide vertices of high quality. In case no vertex can be found a second, looser algorithm runs on the track jet. This has the advantage of high efficiency and higher quality vertices in case the first pass finds one. The implementation of the 2Pass method into the SVT framework is part of this thesis, together with the optimisation of the secondary vertex tagger operating points. More details can be found in [81].

5.3. Electrons

The reconstruction of electrons starts from clusters in the calorimeter. All towers within a cone of $R < 0.2$ in the $\eta \times \phi$ space around a seed tower belong to a cluster. The p_T of the cluster must be larger than 1.5 GeV. The energy deposition for electrons takes place mainly in the electromagnetic (EM) calorimeter, therefore the fraction of energy E_{EM} in the EM calorimeter is required to be high. The energy fraction (f_{em}) of the cluster in the electromagnetic calorimeter over the total energy (E_{tot}) in the calorimeter is required to be

$$f_{em} = \frac{E_{EM}}{E_{tot}} > 0.9. \tag{5.2}$$

Electrons have to be isolated in $\eta \times \phi$ space from surrounding clusters. A second cone with radius $R < 0.4$ is defined. Only 15% of the total energy within the cone of $R < 0.4$ are allowed to be outside the $R < 0.2$ cone or to be non-EM energy:

$$f_{iso} = \frac{E_{tot}(R < 0.4) - E_{EM}(R < 0.2)}{E_{EM}(R < 0.2)} < 0.15. \tag{5.3}$$

Another criterion for the electron reconstruction is the shower development of the cluster in the calorimeter, which is different from hadronic objects. A 7×7 covariance matrix (H-matrix) that quantifies how similar the shower development of the cluster is to that of an electron is calculated from seven correlated variables. The variables are the deposited energy in the four EM layers, the shower energy in the EM calorimeter, the z position of the primary vertex divided by its uncertainty and the width of the shower in $r - \phi$ in the third EM layer. For the last variable the third EM layer is chosen as it has the finest granularity. The χ^2 of the H-matrix (χ^2_{hmx7}) should be small for electrons, with

$$\chi^2_{hmx7} < 50. \tag{5.4}$$

As the electron is a charged particle it leaves a track in the tracking system. At least one reconstructed track must point to each cluster within the cone $\Delta\eta \times \Delta\phi < 0.05 \times 0.05$ around the cluster in the third EM layer. For this matching χ^2_{EM-trk} is calculated, that includes the difference in ϕ and z in the EM3 layer, and also includes the squared significance of the resolution of the transverse energy of the cluster over the transverse momentum of the track E_T/p_T

$$\chi^2_{EM-trk} = (\frac{\Delta\phi}{\sigma_\phi})^2 + (\frac{\Delta z}{\sigma_z})^2 + (\frac{E_T/p_T - 1}{\sigma_{E_T/p_T}})^2 \tag{5.5}$$

$$= \chi^2_{spatial} + (\frac{E_T/p_T - 1}{\sigma_{E_T/p_T}})^2. \tag{5.6}$$

The probability $Prob(\chi^2_{EM-trk})$ is required to be larger than zero.

The criteria described so far define a "loose isolated" electron. A "tight isolated" electron has to fulfil the criteria of the "loose isolated" electron and additionally the output of an electron likelihood L_7 [82,83] must be at least 0.85. The electron likelihood is designed to discriminate true electrons from fake electron background processes. Seven variables are used as input for the electron likelihood: the electromagnetic fraction f_{em}, the H-matrix, E_T/p_T, the probability $Prob(\chi^2_{spatial})$, the z position of the distance of closest approach of the matched track to the primary vertex, the number of tracks within a cone of $\Delta R = 0.05$ around the matched track and the sum of all track p_T's in a cone of $\Delta R = 0.4$ around, but excluding, the candidate track.

5.4. Muons

The reconstruction of muons uses information from the muon system and the central tracking detectors [84], the former delivers unambiguous muon identification, the latter provides precise momentum resolution and a high efficiency of finding tracks in the whole angular acceptance region of the muon system. In each of the three layers of the muon system segments are reconstructed from the layer wire and scintillator hits. The separately reconstructed segments of the three layers are then matched together and form a "local muon". Each "local muon" that can be matched with a central track is called "central track-matched muon". Additionally information from the calorimeter can be used by looking at signatures from minimum ionising particles (MIP). The identification of muons with the "Muon Tracking in the Calorimeter" (MTC) algorithm is still under development. The current efficiency of the MTC algorithm is about 50%, which is far less efficient than all other muon signatures.

According to the number of hits and layers in the muon system and the quality of the matched track of the reconstructed muon, a classification into different muon qualities and track qualities is done [85]. The muons used for this analysis have to have the muon quality "MediumNSeg3" and track quality "medium", which fulfil the following criteria:

- $n_{seg} = 3$, which means that the "local muon" must have hits in all three layers of the muon system, i. e. the innermost A layer and the two outer B and C layers.
- The muon quality "medium", requiring at least two A layer wire hits, a A layer scintillator hit, at least two wire hits in the combined BC layer and at least one scintillator hit in the BC layer. In case of muons with less than four BC wire hits the criteria on the BC scintillator hits does not apply.
- The muon must be matched to a central track.
- The central track match must be of "medium" quality. That means the track must have a $|dca| < 0.02$ with respect to the primary vertex if the number of SMT hits is at least one, or $|dca| < 0.2$ if no SMT hits were found. The χ^2/ndf of the track fit must be smaller than four.
- A cosmic veto cut is applied. Only muons are used, for which the time of flight between the hard interaction and the A layer (t_A) and the BC layer (t_{BC}) is close to zero: $t_A < 10$ ns and $t_{BC} < 10$ ns.

In this thesis no muons from heavy hadron decays are specifically considered. Therefore an isolation cut criterion on the considered muon is applied, that requires a separation of the muon from jets. The muons passing the described criteria and having a distance in $\eta \times \phi$ space of $\Delta R > 0.5$ are called "loose isolated muons".

Muons fulfilling additionally the following two criteria are called "tight isolated muons":

- $Rat11 = Halo(0.1, 0.4)/p_{T\mu} < 0.08$, where $p_{T\mu}$ is the transverse momentum of the muon and $Halo(0.1, 0.4)$ the sum of the transverse energies of all calorimeter clusters within a hollow cone with inner radius $R_i = 0.1$ and outer radius $R_o = 0.4$ around the muon. For the calorimeter cluster only the fine hadronic and the electromagnetic calorimeter are considered.
- $Rattrk = TrkCone(0.5)/p_{T\mu} < 0.06$, where $TrkCone(0.5)$ is defined as the sum of the transverse momenta of all tracks within a cone of radius $R = 0.5$ around the muon. The transverse momentum of the muon itself is not included in the sum.

5.5. Jets and Jet Energy Scale

The hadrons in high-energy collisions show a non-isotropic distribution. This behaviour can be explained by the formation of so-called jets.

A general definition of a jet can be given as "a large amount of hadronic energy in a small angular region" [86]. The hadronisation of a parton as well as soft gluon radiation cause the production of hadrons that are concentrated around the flight direction of the original parton and build a jet. The more energetic the partons are, the tighter the final hadrons concentrate around the parton flight direction.

For a $p\bar{p}$ collision jets are formed from partons from the hard interaction, partons from initial state radiation (ISR) and from beam remnants (beam jets). All partons but the top quark fragment immediately. Therefore the precise study of jets is important to study the observable

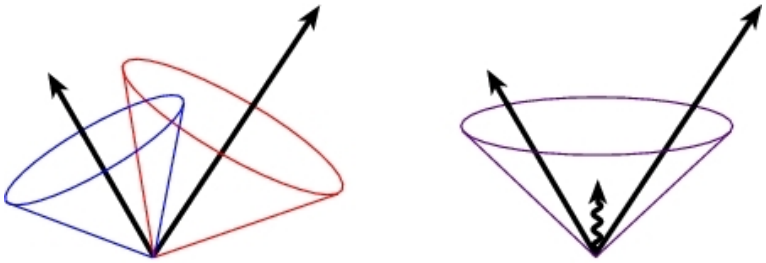

Figure 5.2.: Illustration of infrared sensitivity for cone jets. The arrows represent seed particles with the length of the arrow proportional to the energy. A soft radiated parton causes a merging of the jets [87].

kinematics and topology of the final state hadrons in order to study the fundamental properties of the related partons. To get the final jets that are used in the analyses from calorimeter or track signals the reconstruction of jets with so-called jet algorithms, the identification of good jets, the study of the resolution of the jet and the correction of the observed jet energy to the parton energies is necessary. These four parts are described in the following paragraphs.

5.5.1. Jet reconstruction

The ideal jet reconstruction algorithm has to fulfil certain theoretical and experimental criteria. The theoretical features that have to be fulfilled in order to give meaningful predictions of the jet algorithm, are

- Infrared safety: The solution of the jet algorithm should not depend on soft radiations, e. g. soft gluon radiation. Figure 5.2 shows an example of an algorithm that does not fulfil the requirement of infrared safety.

- Collinear safety: The solution of the jet algorithm should be insensitive to collinear radiations. Two possible collinear problems are shown in Fig. 5.3. In the first example the splitting of seed energy between towers does affect jet finding. With a low seed tower threshold of $E_T > 1$ GeV this problem is solved at DØ. The second example shows the problem of the algorithm being sensitive to E_T ordering of particles. In Fig. 5.3 (right) the hardest parton is split into two almost collinear partons and thus affects the jet finding.

- Invariance under boost: The interacting partons in hadron-hadron collisions have spectra of longitudinal momenta given by parton distribution functions (PDF). The centre-of-mass of the parton-parton collision system therefore moves with unknown velocity along the beam axis. All observables and reconstruction steps of the jet algorithm need to be lorentz-invariant under a boost along the beam axis.

Furthermore several experimental criteria are desired, like independence of the detector, the algorithm should minimise the resolution of smearing and angle biases and be independent of luminosity.

For the reconstruction of jets two different types of jet algorithms exist: the so-called cluster algorithms [86] and cone algorithms. The cone algorithm in general is based on the idea of associating all particles that lie within a cone of radius $\Delta R = \sqrt{(\Delta\eta)^2 + (\Delta\phi)^2}$ in $\eta \times \phi$ space. At DØ the jet reconstruction is done with the "Improved Legacy Cone Algorithm" (ILCA, or RunII Cone Algorithm) [87, 88]. In order to better reject calorimeter noise cells and

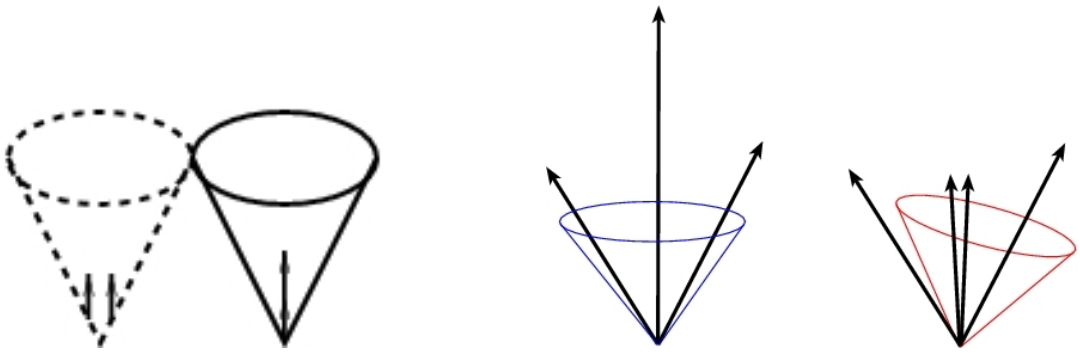

Figure 5.3.: Illustration of the collinear sensitivity for cone jets [87]. Left: The production of a seed can fail due to the splitting of energy into several calorimeter towers. Right: The E_T ordering of the seeds can cause a collinear problem.

therefore improve the jet energy scale and missing transverse energy resolution, the so-called T42 algorithm is applied additionally [89].

First the Simple Cone Algorithm [88] forms preclusters from calorimeter towers. From a list ordered in decreasing p_T the lower-E_T towers are clustered to higher E_T ones in cones with $\Delta R = 0.3$. All towers with $E_T > 0.5$ GeV can act as seeds for the pre-clustering. All preclusters with $E_T > 1$ GeV and consisting of more than one tower are considered as input to the ILCA algorithm.

The preclusters are used as seeds for the formation of "proto-jets". From the list of precluster, the algorithm uses the highest E_T precluster as seed for a new "proto-jet". Iteratively, all preclusters within a cone of $\Delta R = 0.5$ are assigned to the "proto-jet" until the E_T-weighted cone centre is found. In order to avoid sensitivity to soft radiation also stable cones around midpoints of any combination of two "proto-jets" are searched for. Finally a list of "proto-jets" from preclusters and midpoints is considered in the last step of merging and splitting. The condition that each precluster is only present in one jet is not fulfilled for the "proto-jets" formed so-far. All pairs of "proto-jets" with distance in R larger than the cone size but smaller than twice the cone size are considered. These cones get either split or merged, according to their overlapping energy. If the overlap is larger than 50% of the cone with lower energy the jets are merged. In case of smaller overlap the preclusters get assigned to the cone with the cone axis closer in $\eta \times \phi$ space. All jets with $E_T > 6$ GeV are kept for the next step of jet identification.

5.5.2. Jet identification

In order to distinguish fake jets due to calorimeter noise from physical jets, further quality criteria are applied to the jet candidates [90].

- The electromagnetic fraction is required to be $f_{em} < 0.95$. This cut helps to distinguish jets from electromagnetic particles.
- In order to suppress noise a minimum cut on f_{em} is applied. Due to the detector geometry including a gap in the EM calorimeter in the ICD region, the minimum electromagnetic fraction cut is optimised depending on detector η. The jet is required to have
  1. $f_{em} > 0.05$, or
  2. $1.3 > ||\eta_{det}| - 12.5| + \max(0.4 \times (\sigma_\eta - 0.1))$ (ICD region), or

3. $f_{em} > 0.03$ and $11.0 < |\eta_{det}| < 14.0$ (ICD region), or
4. the electromagnetic fraction is > 0.04 for forward jets with $|\eta| > 2.5$.

σ_η defines the width of the jet in η. The second and third points enable to separate narrow and wide jets, the former on which no f_{em} cut is applied.

- A cut on the energy fraction f_{ch} of the coarse hadronic calorimeter E_{ch} over the total energy ($f_{ch} = \frac{E_{ch}}{E_{tot}}$) is applied in order to remove noise dominated jets. Again the cuts are optimised depending on the detector geometry

  1. $f_{ch} < 0.4$, or
  2. $f_{ch} < 0.6$ in the region of $8.5 < |\eta_{det}| < 12.5$ where many CH layers but few material in front of them is present, and $n90 < 20$, or
  3. $f_{ch} < 0.44$ for central jets with $|\eta| < 0.8$, or
  4. $f_{ch} < 0.46$ for $1.5 < |\eta| < 2.5$, which is the end cap excluding the forward regions.

  $n90$ is defined as the number of calorimeter towers, that represent 90% of the total jet energy.

- A certain fraction of the jet energy should already be measured in the first trigger step (L1). The Level 1 ratio is defined as

$$L1_{ratio} = \frac{p_T(\text{from L1 readout})}{p_T(\text{from precision readout})} \text{ [91].} \tag{5.7}$$

  p_T(from L1 readout) is the scalar sum of the 100 hottest L1 towers within a cone of radius $\Delta R = 0.5$, p_T(from precision readout) is the vector sum of jet towers excluding the coarse hadronic layers. The requirement on the Level 1 ratio is

  1. $L1_{ratio} > 0.5$, or
  2. $L1_{ratio} > 0.35$ and $p_T < 15$ GeV in the end cap ($|\eta| > 1.4$), or
  3. $L1_{ratio} > 0.1$ and $p_T < 15$ GeV in the forward region with $|\eta| > 3.0$, or
  4. $L1_{ratio} > 0.2$ and $p_T \geq 15$ GeV in the forward region ($|\eta| > 3.0$).

5.5.3. Jet energy scale

The total energy of all calorimeter towers within a cone jet does not correspond to the sum of energy of all particles building the jet. Due to detector effects and the fixed cone radius the calorimeter jet energy can largely differ from the stable particle jet before interaction with the detector. The Jet Energy Scale (JES) tries to correct for these differences [92].

The formula for the JES correction can be written as [93]

$$E_{jet}^{ptcl} = \frac{E_{jet}^{raw} - O}{F_\eta \times R \times S} \tag{5.8}$$

with

E_{jet}^{ptcl}	:	corrected jet energy
E_{jet}^{raw}	:	uncorrected jet energy
O	:	offset energy correction
F_η	:	relative response correction
R	:	absolute response correction
S	:	showering correction

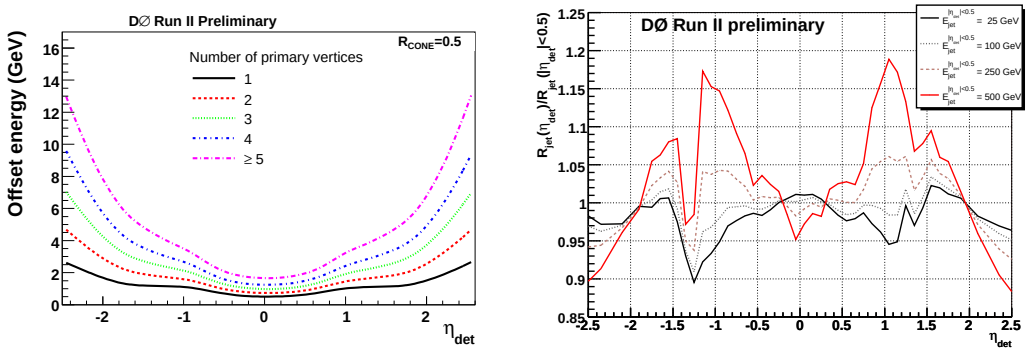

Figure 5.4.: Example plots for offset and relative response corrections [93]. Left: Offset energy dependent on η_{det} for different primary vertex multiplicities. Right: Example of relative response correction in data.

The individual components of the jet energy scale correction are derived and applied sequentially in the above order. The estimation of the corrections is done separately for data and Monte Carlo.

Starting from the raw jet energy the offset correction O is subtracted. The offset energy arises from multiple $p\bar{p}$ interactions, beam remnants, multiple parton interactions, electronics and uranium noise in the calorimeter or energy from previous collisions ("pile-up"). The offset correction is measured with minimum bias events, which are triggered by the luminosity monitor. The energy density per tower is measured depending on the number of reconstructed primary vertices in order to include the luminosity dependence in the offset energy calculation. The energy density within a jet cone ΔR is then defined as the offset energy. Figure 5.4 (left) shows the offset energy as function of η_{det} for different primary vertex multiplicities. The offset correction is measured purely from data.

After correcting for the offset the jet energy is divided by the relative response correction F_η. The relative response correction calibrates the jet energy for the fact that the response of the calorimeter is not uniform in η_{det}. Especially the ICD region and the massless gap detector region show a different response than CC and EC. For the measurement of F_η the so-called Missing Transverse Energy Projection Fraction (MPF) method is used. In the MPF method events of dijet or photon+jets samples with a tag object in the CC and the probe object in the region to be considered are used. The missing transverse momentum between tag and probe object can then be used to extract the relative response. Due to differences in the real and simulated detector, the response determination is done in data and Monte Carlo separately. Figure 5.4 (right) shows the relative response correction in data. Clear bumps in the ICD region can be seen.

Once the relative response is determined the absolute response correction R can be measured and applied to the jet energy. R corrects for example for the difference in calorimeter response of hadrons and electrons and energy loss in un-instrumented detector regions. The measurement of R is done with the MPF method applied on photon+jet events. Figure 5.5 (left) shows the absolute response correction as function of jet energy for jets with cone $R = 0.7$.

The last step is the determination and application of the shower correction S. Due to showering in the calorimeter or magnetic fields, energy belonging inside (outside) the jet is missing from (added to) the jet energy. The correction does not account for physical showering, due to gluon emission for example. S is measured in photon+jet events with exactly one primary vertex. The ratio between the jet energies at the particle level and the reconstruction level yield the showering correction. In Fig. 5.5 (right) the showering correction in data is shown.

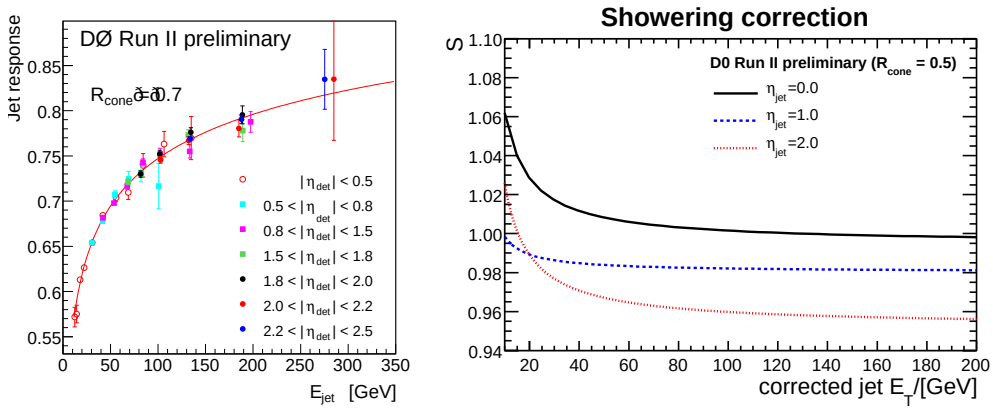

Figure 5.5.: Example plots for absolute response and showering correction [93]. Left: Example of absolute response for $R = 0.7$ in data versus the offset and relative response corrected jet energy. Right: Example of showering correction in data versus corrected transverse jet energy.

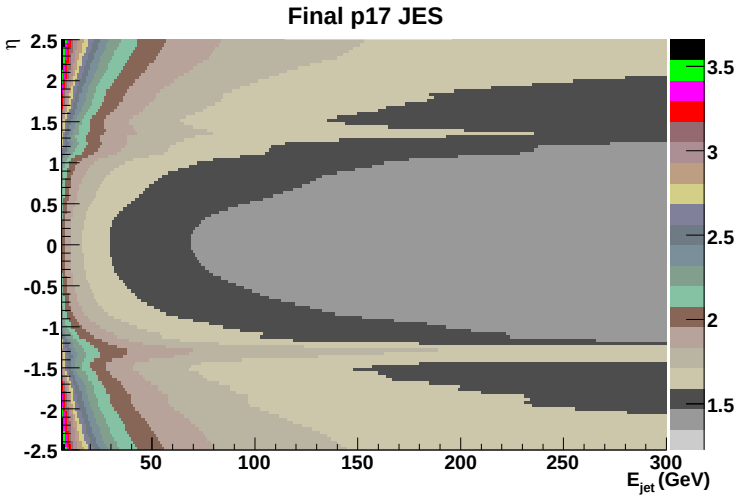

Figure 5.6.: Example plots for final p17 JES correction in Monte Carlo. The Correction is parametrised as function of η and the raw jet energy.

The uncertainty on the jet energy scale is one of the dominating systematic uncertainties on the $t\bar{t}$ cross section measurement in the l+jets channel. For the simultaneous measurement of R and the $t\bar{t}$ cross section, the "preliminary p17 JES" is applied, for the cross section combination and the search for charged Higgs the "final p17 JES" is available. A large, successful effort was made to reduce the uncertainties of the jet energy scale. Figure 5.6 shows an example for the final total jet energy scale correction depending on η and the uncorrected jet energy. Especially for small energies and in the ICD region the JES factors can get large. In Fig. 5.7 the relative uncertainty of the jet energy scale is shown as function of the raw transverse jet energy. The left plot shows the uncertainty for the preliminary, the right one for the final p17 JES. The uncertainties on the latter are reduced by about a factor of two compared to the preliminary p17 JES.

In case of reconstructed muons within the jet cone, the jet energy scale has to get a further correction for the muon and the neutrino energy.

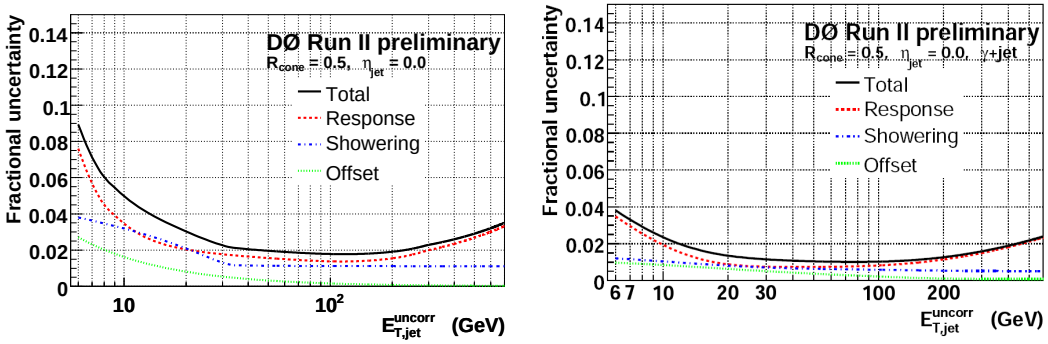

Figure 5.7.: Relative uncertainty of preliminary (left) and final (right) p17 JES correction in data as function of uncorrected transverse jet energy. For $R = 0.5$ and $\eta = 0.0$ [92, 93].

5.5.4. Jet resolution

The jet energy resolution is derived from data events [94]. The parametrisation is given in Eq. 4.6 in section 4.2.3.

In order to take into account differences between Monte Carlo and data for jet resolution, jet reconstruction efficiencies and identification efficiencies, a method called "Jet shifting, smearing and removal" (JSSR) is introduced [95, 96]. JSSR does a re-calibration, smearing and discarding of simulated jets, after which the behaviour is similar to jets in data.

5.6. Missing Transverse Energy

The weak interacting neutrinos traverse the detector without giving rise to any electronic signal. In the plane transverse to the beam axis the momentum conservation requires total E_T to be zero. The missing transverse energy $\not\!\!E_T$ can be used to identify neutrinos. The x and y components of $\not\!\!E_T$ are defined as $\not\!\!E_x = -p_x^{meas}$ and $\not\!\!E_y = -p_y^{meas}$ [92, 97]. p_x^{meas} and p_y^{meas} are the sum of the x and y components of the momenta for the electromagnetic and fine hadronic calorimeter, ICD and massless gap cells after removal of noise with the T42 algorithm [89]. The missing transverse energy has to be corrected for three components:

- The jet energy scale correction changes the balance in the transverse plane. On the electromagnetic objects the JES correction is applied before summation to $\not\!\!E_T$.
- In case of the presence of muons the missing transverse energy has to be corrected for their energy. The muon deposits a small amount of its energy in the calorimeter, which must be subtracted.
- Due to the large noise, the energy in the coarse hadronic calorimeter is not taken into account in p_x^{meas} and p_y^{meas}. The $\not\!\!E_T$ is corrected for coarse hadronic calorimeter energy belonging to the jets in the event.

5.7. Identification of b-jets

The identification of jets originating from heavy flavour partons is one of the major ingredients for the analyses in this thesis. Especially for the measurement of the ratio of branching fractions the identification of b-jets and the related uncertainties are the limiting factor.

The identification of b-jets relies on two properties that show a good discrimination power from light jets:

- About 20 % of the b-jets contain a lepton from semileptonic decay of the b quark. The Soft Lepton Tagger (SLT) relies on muons within jets.
- B hadrons have a relatively long lifetime compared to light hadrons. They travel several millimetres in the detector before they decay into other partons. The properties of the tracks from the decay particles as well as the displaced secondary vertex are the basics for different lifetime b-taggers at DØ: The counting signed impact parameter (CSIP) tagger, the jet lifetime probability (JLIP) tagger and the secondary vertex tagger (SVT). Properties from all three lifetime taggers are combined in a neural network (NN) tagger that shows better performance than each individual tagger.

The lifetime b-taggers rely on information of the tracks. Therefore it is natural to run the b-tag algorithms on track jets. As the jets used in physics analyses are calorimeter jets, an additional step is needed, where the track jets are associated to calorimeter jets. Each calorimeter jet that is matched to a track jet is called taggable. The performance of the b-tagging independent from calorimeter jets also has the advantage that the b-tagging is decoupled from noise effects in the calorimeter. Furthermore, direct performance comparisons between different b-tag algorithms are possible when considering taggable jets.

More details on taggable jets and the different b-taggers are given in the following sections.

5.7.1. Taggability and Taggability Rate Functions

A jet is defined taggable [79] if at least one track jet (see section 5.2.2) can be matched within a cone of $\Delta R \leq 0.5$ to the calorimeter jet. The track jet used for taggability has a cone size of $R = 0.5$. All tracks within the track jet must have p_T of at least 0.5 GeV, at least one SMT hit, a distance of closest approach $dca < 0.15$ cm and the z component of dca smaller than 0.4 cm.

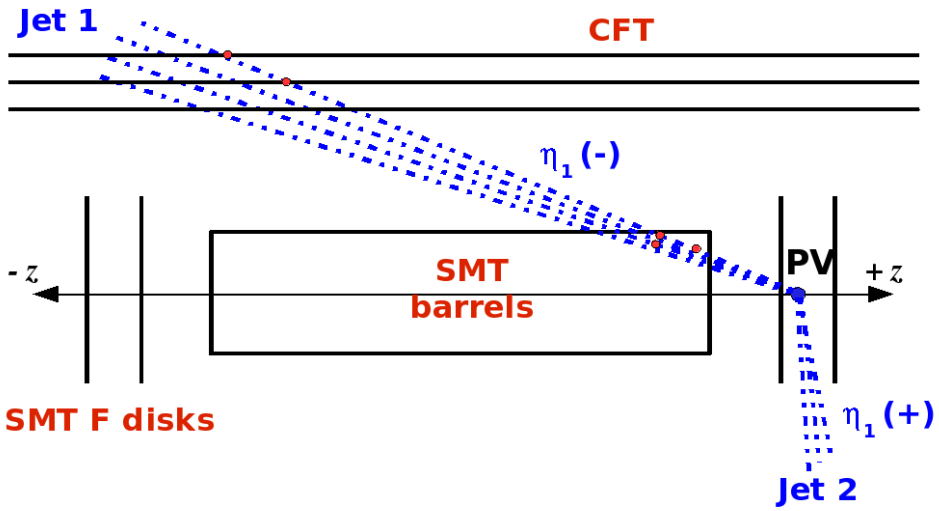

Figure 5.8.: Scheme of region dependence of taggability [98]. For jet 1 the probability that the jet is taggable is high, while the combination of jet direction and primary vertex z position causes low probability to be taggable for jet 2.

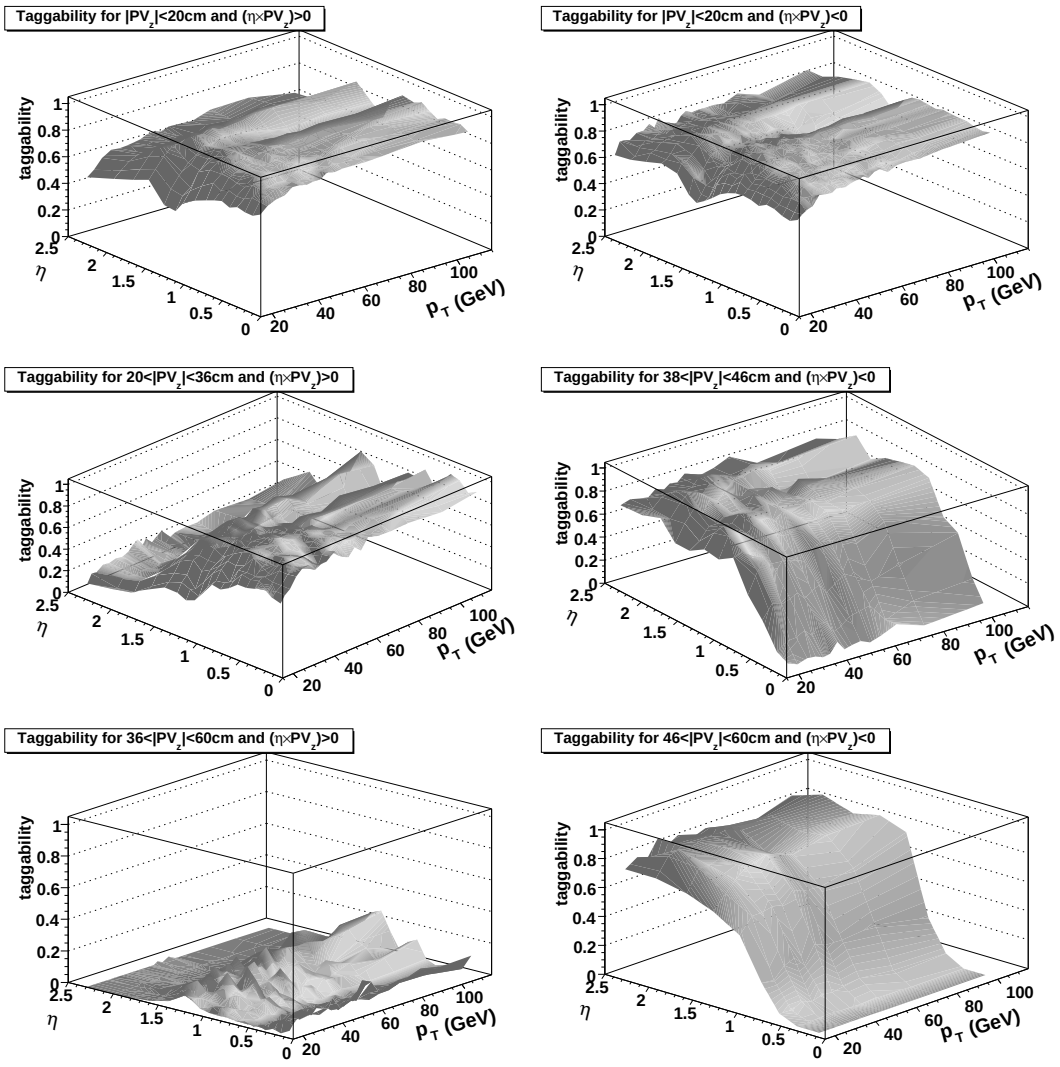

Figure 5.9.: Taggability parametrisation for the e+jets data set. The parametrisation is done separately in six regions of $|PV_z|$ and $\eta \times PV_z$.

Due to the requirement to have at least one hit in the SMT, the taggability strongly depends on the position of the primary vertex and the η of the jet. Figure 5.8 shows a sketch of two different primary vertex z (PV_z) and jet η configurations leading to high and low probability of the jet to be taggable.

The efficiency for jets to be taggable is different in data and Monte Carlo simulation, due to tracking inefficiencies and calorimeter noise effects that are not simulated properly. In order to avoid a bias, taggability is determined on data and the thus calculated parametrisation is applied on Monte Carlo. For the parametrisation the PV_z and jet η dependence is taken into account and six different Taggability Rate Functions (TaggabilityRFs) for different regions of $|PV_z|$ and $\eta \times PV_z$ are derived. In each region the probability that a jet is taggable is parametrised as function of calorimeter jet η and p_T. The taggability parametrisation is derived on the data sample that is used for the analysis in order to avoid sample dependent biases. Figure 5.9 shows the TaggabilityRF for the e+jets sample, Fig. 5.10 for the μ+jets sample. A difference between the taggability parametrisation of both samples can be seen especially in the region of $|PV_z| < 20$ cm, where the TaggabilityRF for e+jets shows dips for jets directing into the ICD region.

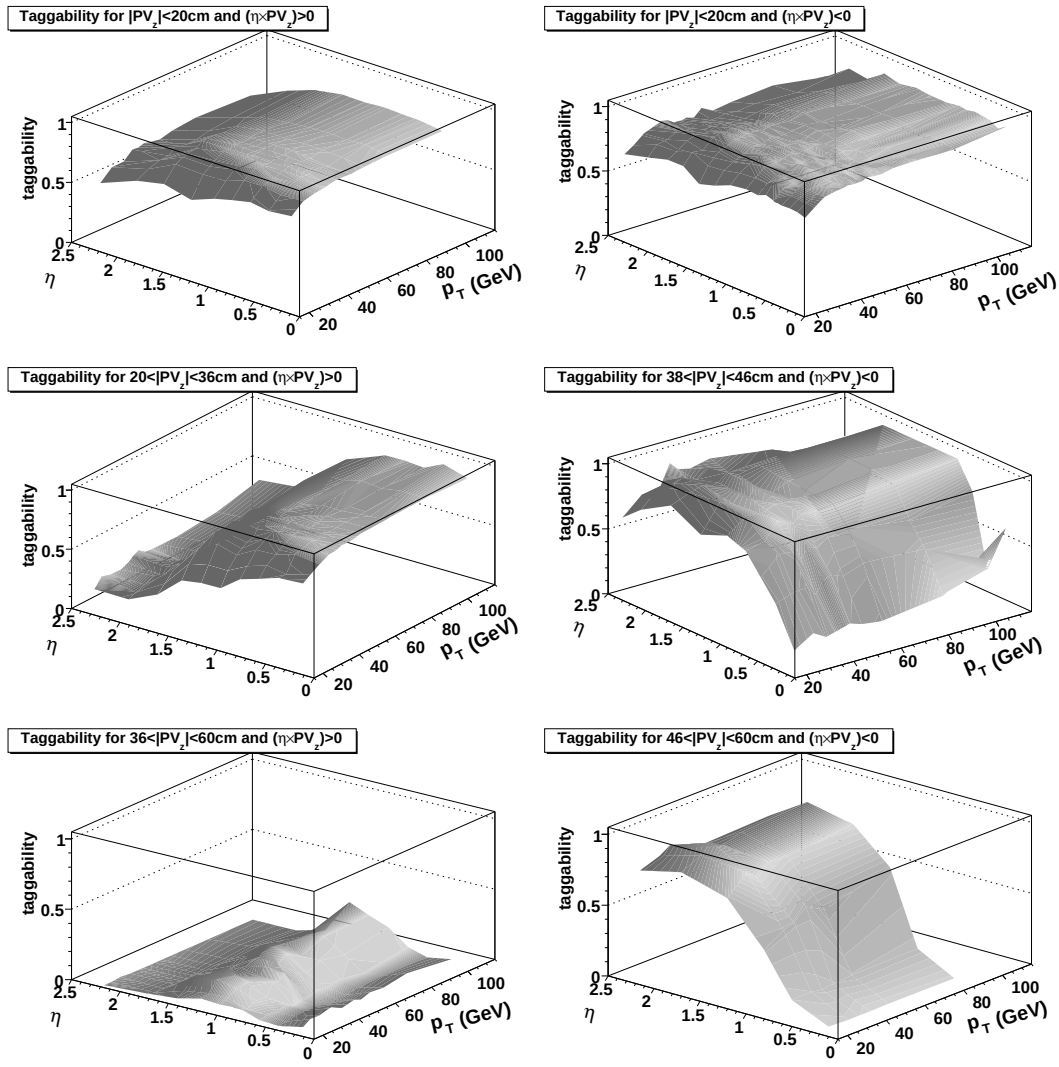

Figure 5.10.: Taggability parametrisation for the μ+jets data set. The parametrisation is done separately in six regions of $|PV_z|$ and $\eta \times PV_z$.

5.7.2. *b*-tagger and Tag Rate Functions

In the following paragraphs the different individual b-tag algorithms as well as the Neural Network tagging algorithm are described briefly. Due to differences in the tagging rate for data and Monte Carlo simulation, scale factors and Tag Rate Functions (TRF) that parametrise the b-tag efficiencies per jet have to be derived, as described at the end of this section.

Soft Lepton Tagger The Soft Lepton Tagger (SLT) [99] relies on the fact that B hadrons decay with about 10.8% probability into muons, while most light hadrons do not decay semileptonically inside the detector. A high p_T muon within the jet cone is required in order to declare the jet as b-tagged. As only a fraction of the b-jets contain a muon the SLT has a low efficiency.

Counting Signed Impact Parameter Tagger The Counting Signed Impact Parameter Tagger (CSIP) [100] is based on the fact that the charged decay products of B hadrons have an impact parameter much larger than zero with respect to the primary vertex. Additionally, the sign of the projection of the vector for the distance of closest approach onto the axis of the jet is

assigned to the track impact parameter. Tracks from b-jets show larger positive impact parameter significance than light jets. Jets with a certain number of tracks with large signed impact parameter significance are b-tagged. With a cut on p_T of the considered tracks, different tag working points can be defined. With increasing p_T a decrease in fake rate and b-tag efficiency occur. A jet is tagged if it contains at least three tracks with impact parameter significance of more than two, or two tracks with impact parameter significance greater than three.

Jet Lifetime Probability Tagger Based on the impact parameter information of the tracks the Jet Lifetime Probability Tagger (JLIP) [101] calculates a probability (jet lifetime probability P_{jet}) for each calorimeter jet to be b-tagged. P_{jet} is the probability that all tracks within the jet originate from the primary vertex. Different tag working points are defined with different cuts on P_{jet}.

Secondary Vertex Tagger The Secondary Vertex Tagger (SVT) [77, 80, 81, 102] is based on a full reconstruction of the secondary vertex described in section 5.2.2. The secondary vertex has to fulfil the following requirements:

- The χ^2/ndf for each track must be smaller than 15 when being attached to the vertex.
- The χ^2/ndf of the vertex must be smaller than 100 in order to ensure a converged fit.
- All tracks must fulfil a minimum quality requirement of at least two SMT hits, and an impact parameter with respect to the primary vertex in the transverse plane of $|dca| < 0.15$ cm and in the longitudinal plane $|z_{dca}| < 0.4$ cm.
- The maximum decay length in the $x-y$ plane (L_{xy}) must be smaller than 2.6 cm in order to remove vertices from long lived particles like Λ or K^0_S.
- Collinearity > 0.9. The vertex collinearity is defined as the normalised product of L_{xy} and the sum of the momenta of all tracks attached to the vertex. A large collinearity ensures that the momentum of the secondary vertex points back to the primary vertex.

Besides the common criteria different tag working points of the SVT are defined with additional criteria listed in Table 5.1. The superloose working point is used as input to the Neural Network tagger.

All jets with at least one vertex fulfilling the described criteria within the jet cone $\Delta R < 0.5$ are called b-tagged. Tagged jets with vertices with $L_{xy} > 0.0$ are called positive, with $L_{xy} < 0.0$ negative. As negative tagged jets originate from mis-reconstruction and resolution effects they can be used to measure the fake tag rate.

Working Point	track p_T	track dca/σ_{dca}	track χ^2/ndf	vertex $L_{xy}/\sigma_{L_{xy}}$
Tight	> 1.0 GeV	≥ 3.5	≤ 3.0	≥ 7.0
Medium	> 1.0 GeV	≥ 3.5	≤ 10.0	≥ 6.0
Loose	> 1.0 GeV	≥ 3.0	≤ 10.0	≥ 5.0
Loose_xtrack	> 0.5 GeV	≥ 3.0	≤ 10.0	≥ 5.0
Superloose	> 0.5 GeV	≥ 0.0	≤ 15.0	≥ 0.0

Table 5.1.: Tag working points of the secondary vertex tagger [81]

It should be noted that the different working point definitions of the SVT are not strict subsets of each other. Due to the selection criteria on the tracks that are used for the vertex reconstruction it is possible, that for example a tight secondary vertex can be found within a jet, but no superloose.

Neural Network Tagger The Neural Network Tagger [103, 104] combines properties of the JLIP, CSIP and SVT into one neural network output variable. The optimisation of input variables [103] results in the following variables, given in order of their rank:

- SVT_{SL} ***dls*** The most important input variable to the Neural Network is the decay length significance $dls = L_{xy}/\sigma_{L_{xy}}$ of the secondary vertex for the superloose definition. In case of several secondary vertices within the jet cone the one with the highest decay length significance is used.
- **CSIP Comb** A weighted combination of the impact parameter significance ips of the tracks. The combination consists of a sum of the number of tracks with $ips > 3$, $ips > 2$, $ips < 3$ and $ips < 2$
- **JLIP Prob** The probability P_{jet} that the jet originates from the primary vertex.
- SVT_{SL} $\boldsymbol{\chi^2/ndf}$ The χ^2/ndf of the secondary vertex for the superloose definition.
- SVT_L $\boldsymbol{N_{\text{tracks}}}$ The number of tracks associated to the secondary vertex with loose definition.
- SVT_{SL} **Mass** The invariant mass of the secondary vertex with superloose definition.
- SVT_{SL} **Num** The number of secondary vertices with superloose definition found within the jet cone.

Figure 5.11 shows the seven input variables and their performance for $b\bar{b}$ and QCD Monte Carlo events as well as for a QCD data sample. The QCD Monte Carlo is dominated by events containing no b-jets.

The jets fed into the Neural Network have to fulfil a very loose requirement to be considered as b-tagged, using the most powerful variable from each of the input taggers. Optimisation of the cuts for the maximum number of b-jets while minimising the number of fake jets results in cuts on the decay length significance of the superloose secondary vertex SVT_{SL} dls of at least 2.5, or a JLIP probability smaller than 0.02 or the CSIP combination of at least 8.

By cutting on the output of the Neural Network b-jets get selected with the NN tagger. In Fig. 5.12 the NN output of $b\bar{b}$ and QCD Monte Carlo is shown. It can clearly be seen that the $b\bar{b}$ sample peaks at an NN output of one, while the QCD sample, dominated by light jets, tends to yield lower NN values.

Different cuts on the NN output define different tag working points for the NN tagger. Table 5.2 shows the cut on the tag working point and the associated operating point name. The analyses presented in this thesis use exclusively the Neural Network tagger, as it shows the best performance of all taggers. Figure 5.13 compares the performance of the Neural Network tagger to the performance of the JLIP tagger. An improved b-tag efficiency versus fake rate can clearly be seen.

Tag Rate Functions The same problem as for taggability also holds for b-tagging: Due to insufficient simulation of tracking the b, c and mistag efficiencies in data are not described when applying the algorithm on Monte Carlo events. Therefore the b, c and mistag efficiencies have to be derived on data events. The parametrisations done in E_T and η of the jet are called tag rate functions (TRFs). All jets used in the measurement and the application of the TRF are required to be taggable.

The measurement of the b-jet TRF for data is done using muonic b-jets, which can be identified by the SLT tagger. Due to the high p_T track from the muon, the b-tag efficiency for muonic b-jets is not expected to be the same as for inclusive b-jets. Therefore a muonic b-jet and an inclusive b-jet TRF is derived on Monte Carlo.

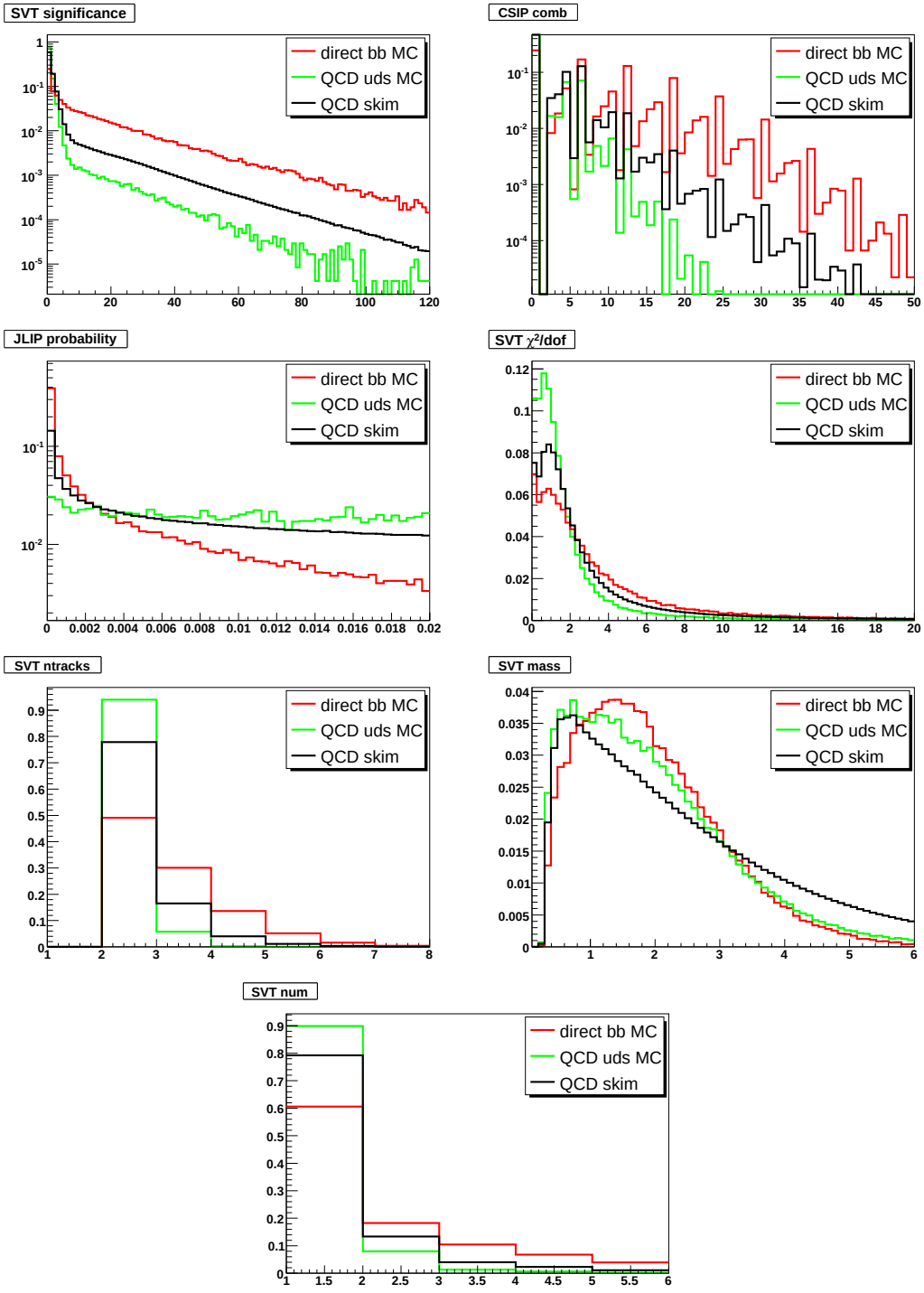

Figure 5.11.: Input variables to Neural Network tagger [104].

The measurement of the muonic b-jet TRF in data is done with a method called System8 [104, 105]. A system of eight equations with eight unknowns is constructed, where the number of tags found by two independent taggers in two samples are used. For the calculation of the muonic b-jet TRF of the NN tagger, the SLT tagger is chosen as the second tagger.

The muonic b-jet TRF is also derived in a Monte Carlo sample. By dividing the muonic b-jet TRF in data by the one in MC, a scale factor $SF_b(E_T, \eta)$ is calculated. It is assumed that the scale factor can be applied on muonic and inclusive b-jets. The inclusive b-jet TRF for data is

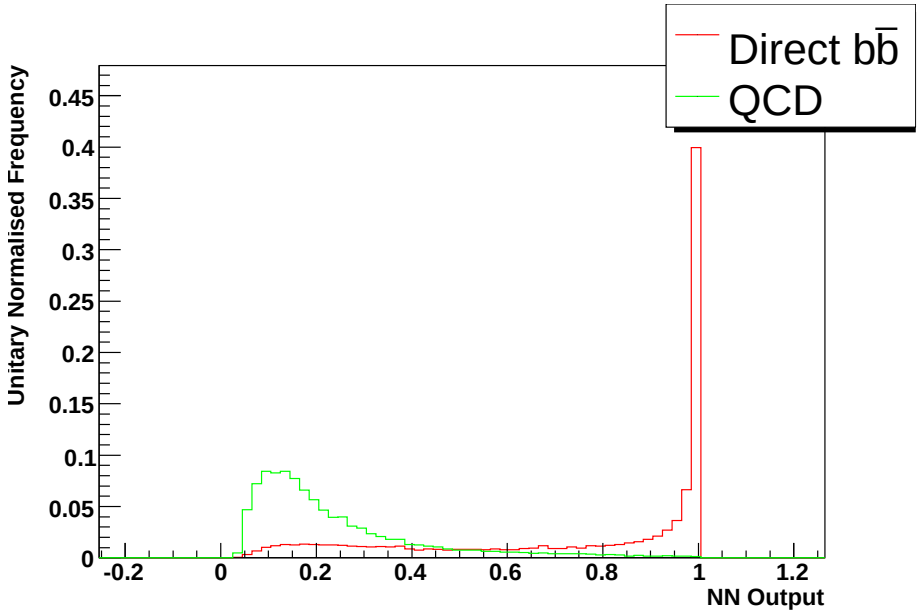

Figure 5.12.: Output of the Neural Network tagger [104].

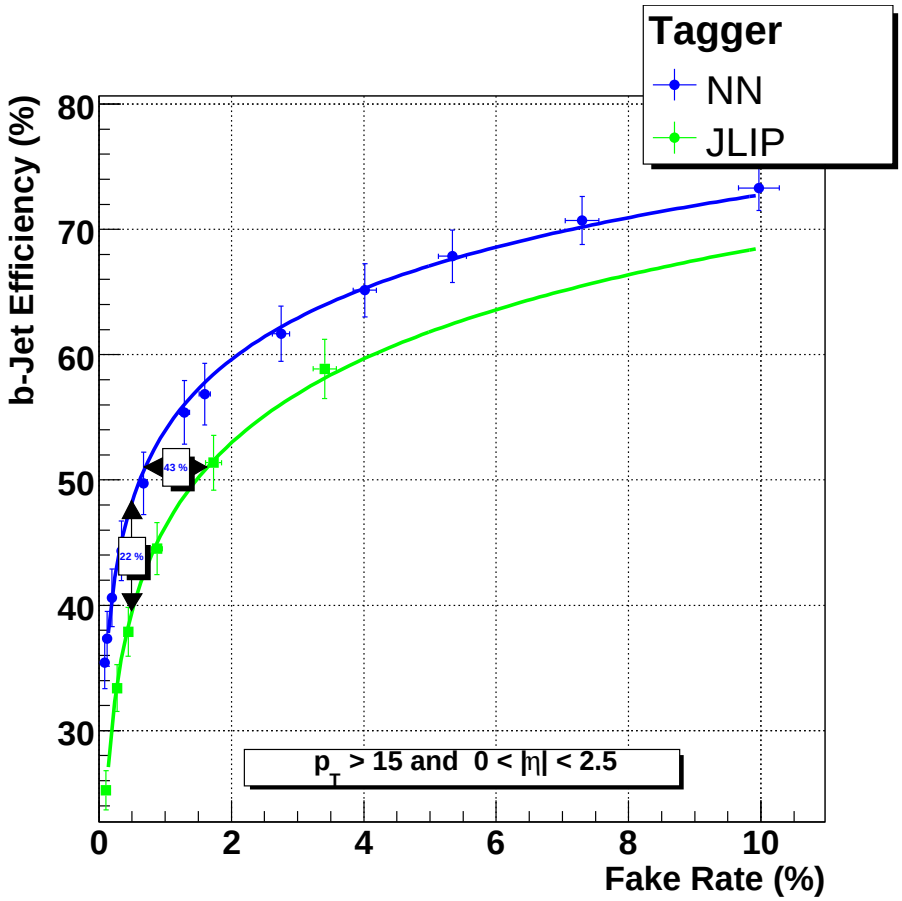

Figure 5.13.: Performance of the Neural Network tagger for jets with $p_T > 15$ GeV and $|\eta| < 2.5$ [104].

Operating Point name	NN cut
L6	> 0.1
L5	> 0.15
L4	> 0.2
L3	> 0.25
L2	> 0.325
Loose	> 0.45
oldLoose	> 0.5
Medium	> 0.65
Tight	> 0.775
VeryTight	> 0.85
UltraTight	> 0.9
MegaTight	> 0.925

Table 5.2.: Certified tag working points of the Neural Network tagger [104]

obtained by multiplication of the inclusive b-jet TRF on Monte Carlo and the scale factor SF_b:

$$\epsilon^{\text{data}}_{\text{incl}\,b}(E_T,\eta) = \epsilon^{\text{MC}}_{\text{incl}\,b}(E_T,\eta) \cdot SF_b(E_T,\eta) \tag{5.9}$$

with $\epsilon^{\text{data}}_{\text{incl}\,b}(E_T,\eta)$ the data b-TRF and $\epsilon^{\text{MC}}_{\text{incl}\,b}(E_T,\eta)$ the MC b-TRF.

In order to obtain the inclusive data c-TRF a similar procedure is used. The inclusive c-TRF on Monte Carlo is derived and multiplied with the scale factor. It is assumed that the difference in Monte Carlo to data is the same for b- and c-jets, therefore the assumption $SF_c(E_T,\eta) = SF_b(E_T,\eta)$ is made. The inclusive c-jet TRF for data is defined as

$$\epsilon^{\text{data}}_{\text{incl}\,c}(E_T,\eta) = \epsilon^{\text{MC}}_{\text{incl}\,c}(E_T,\eta) \cdot SF_b(E_T,\eta) \tag{5.10}$$

The fake or mistag rate is measured differently from the b- and c-TRF, by using negative tags (NTs). As negative tags of the input taggers originate from mis-reconstruction and resolution effects, the negative tag result of the NN can be used to measure the NN fake rate. In case all NN inputs are from negative tags within the jet, the output of the NN is defined as a negative tag result.

The fake rate derived from negative tags is supposed to be a measure of the mistag rate in positive tagged jets. Due to long lived light particles and due to contributions from b- and c-quarks in the negative tagged jets, the negative tag rate (NTR) measured in data alone does not represent a good approximation for the fake rate. In order to correct the measured NTR two additional scale factors are calculated: The SF_{hf}, which is the ratio of the light jet to the total negative tag rate, to correct for the heavy flavour contamination, and SF_{ll}, which is the ratio of the light jet positive tag rate and the light jet negative tag rate, to correct for long lived light particle decay. Both scale factors are derived on QCD Monte Carlo events, resulting in a light jet TRF:

$$\epsilon_{\text{light}}(E_T,\eta) = \epsilon_{NT}(E_T,\eta) \cdot SF_{hf}(E_T,\eta) \cdot SF_{ll}(E_T,\eta) \tag{5.11}$$

with $\epsilon_{NT}(E_T,\eta)$ denoting the NTR measured in data.

Figure 5.14 shows the b-, c- and light jet TRF and their uncertainty band for the medium NN tag working point. The b- and c-jet TRFs are parametrised in jet E_T and η. The fake tag rate is parametrised separately for the CC, ICD and EC region. Each of the three fake tag rate parametrisations is a function of E_T.

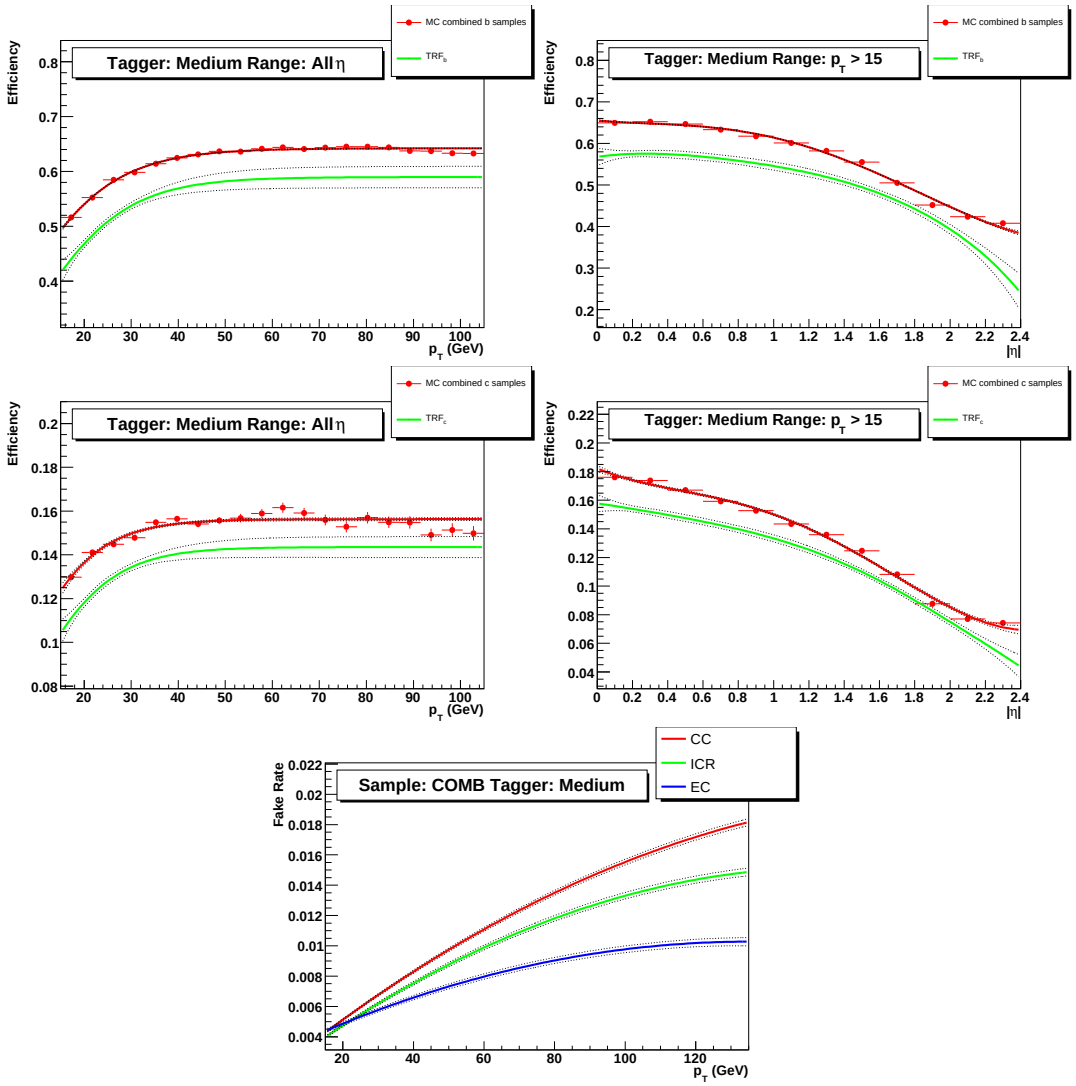

Figure 5.14.: *b*-, *c*- and light TRF for the Medium NN tagger [104].
Top: *b*-tag efficiency on Monte Carlo and *b*-TRF parametrised in E_T (left) and η (right). Middle: *c*-tag efficiency on Monte Carlo and *c*-TRF parametrised in E_T (left) and η (right). Bottom: Fake tag rate parametrised in E_T in the three η regions CC, ICD and EC.

5.7.3. Taggability and Tagging corrections

As especially the measurement of the ratio of branching fractions is very sensitive to *b*-tagging, two additional corrections that do not belong to the default TaggabilityRFs and TRFs are taken into account. One correction originates from the fact that the taggability is derived on a light flavour dominated sample. Due to track p_T and track multiplicity differences for heavy flavour jets compared to light jets a flavour correction on taggability is applied. The second correction has to be applied on gluon splitting samples like *Wbb* and *Wcc* Monte Carlo. Due to a lower *b*-quark momentum fraction of the jets from gluon splitting the common TRFs overestimate the tagging efficiency for low jet p_T. Both corrections are described in more detail in the following paragraphs.

Flavour dependence of taggability In order to correct for the difference of *b*- and *c*-jet taggability the ratio of both with respect to light jets has been measured as function of jet p_T and

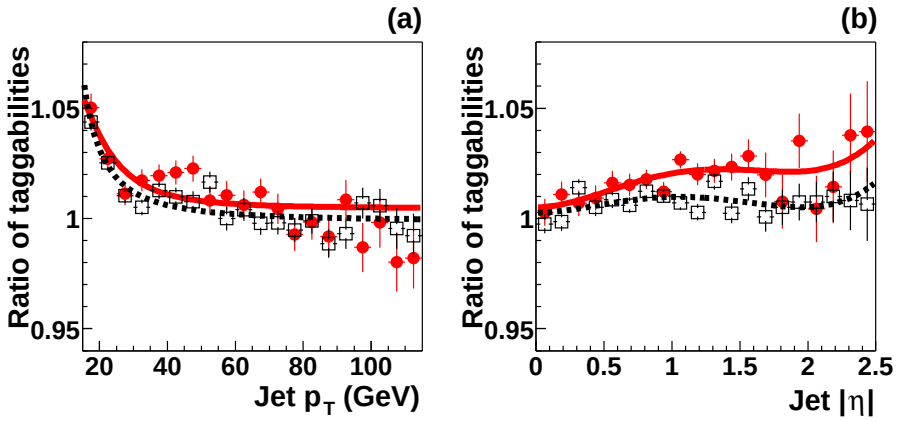

Figure 5.15.: Taggability flavour dependence corrections, parametrised in jet p_T (left) and η (right) [106]. The red full circles show the ratio of b to light jet taggability, the black open circles the jet taggability ratio for c to light jets measured in a QCD MC sample.

η in a QCD multijet MC sample [106]. Especially for low p_T jets the correction on taggability is up to 5%, as can be seen in Figure 5.15. The correction for both, the b- and c-jet taggability, require a similar correction factor. The systematic uncertainty of the flavour dependence correction is estimated by using Wbb and Wcc MC samples instead of the QCD multijet sample. The difference between the parametrisations is assigned as uncertainty.

Gluon splitting sample TRF correction Due to differences in the fraction of energy carried by b-quarks or c-quarks in jets from gluon splitting, the TRFs overshoot the b-tag or c-tag efficiency. Especially for low p_T jets the effect is not negligible. In order to derive a correction factor the efficiency of direct tagging and application of the TRF on b-jets in a Wbb MC sample and c-jets in a Wcc MC sample are compared [107]. Direct tagging means that the b-tagger is applied on MC in the same way as on data. Events with at least one jet with $p_T > 15$ GeV are used for the study. The correction factor c is then calculated as

$$c(p_T) = \frac{\epsilon_{dir} \cdot SF_b(E_T, \eta)}{\epsilon_{TRF}(E_T, \eta) \cdot \epsilon_{\text{taggability}}} \tag{5.12}$$

with ϵ_{dir} the b- (c-)tag efficiency for direct tagging, $SF_b(E_T, \eta)$ the scale factor to correct the tagging efficiency in MC to data, $\epsilon_{TRF}(E_T, \eta)$ the b- (c-)tag efficiency from TRF and $\epsilon_{\text{taggability}}$ the efficiency for directly applied taggability. The last factor is applied in order to cancel out effects due to differences in directly applied taggability and TaggabilityRFs.

Figure 5.16 shows the p_T dependent b- and c-tag efficiency for applied direct tagging and TRF with the medium tag working point on the Wbb and Wcc MC sample as well as the derived correction factors for b- and c-tag efficiencies. A correction factor smaller than one for low p_T can clearly be seen.

It should be noted that the denominator of c is independent of the choice of b-fragmentation in the MC sample, whereas the numerator depends on the b-fragmentation. Therefore the correction factor depends on the chosen fragmentation parameters, as discussed in section 6.3.1.

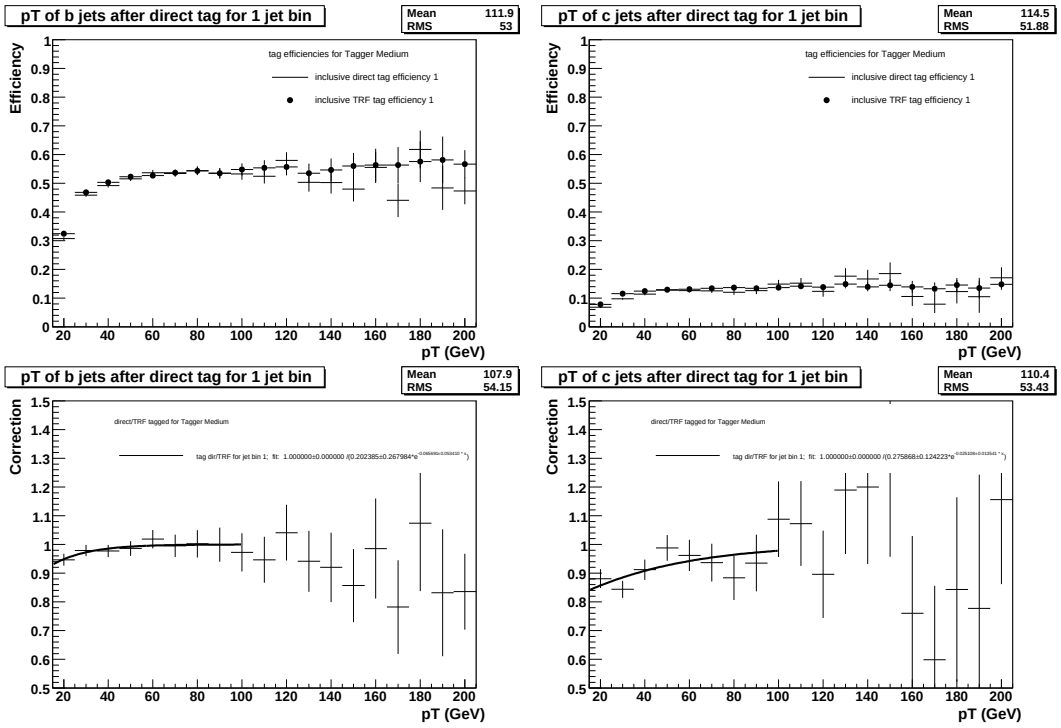

Figure 5.16.: *Wbb* and *Wcc* TRF correction factors. Upper plots: tag efficiencies; Lower plots: correction factor. Left: *Wbb* and *b*-tagging; Right: *Wcc* and *c*-tagging. More plots can be found in Ref. [107].

6. Data, Monte Carlo and Correction Factors

The measurements and searches in the top sector require the simulation of $t\bar{t}$ signal and background samples and the comparisons of the prediction with the data. The data samples are required to fulfil several conditions to ensure good quality. For a realistic description of all detector effects, the generated samples have to undergo detector simulations and require additional Monte Carlo to data correction factors and reweightings. In this chapter the used data sample, the Monte Carlo simulation and the weights and scale factors are described briefly.

6.1. Data sample

The raw data are reconstructed with the DØ reconstruction software D0reco. All hits, energies and trigger informations are analysed by D0reco. The tracks, calorimeter clusters and missing energy are reconstructed with the algorithms described in chapter 5.

For part of this thesis the data collected between August 2002 and December 2005 is used. For the cross section combination and the charged Higgs part further data are included, covering the time from August 2002 to April 2006, referred to as full Run IIa dataset. In the following the trigger requirements, the integrated luminosity for the data sample and the data quality requirements are presented.

6.1.1. Data Quality

In order to ensure good quality of the data used for analysis a basic data quality selection is applied. A whole run or luminosity block (see section 4) can be taken out if it is declared as bad. For each part of the detector, i. e. SMT, CFT, calorimeter and muon system, a run can be declared as "bad" according to the status during data taking. The information about the status of the run is stored in the Offline Run Quality Database. All runs are required to have none of the sub-detector systems declared as "bad".

Depending on the triggers used for the analysis a list of bad luminosity blocks is created based on certain calorimeter information that is checked per luminosity block. Events belonging to the bad luminosity blocks are discarded. Luminosity blocks are declared as bad if, for example, in about 20 consecutive luminosity blocks the average missing transverse energy is significantly different from zero. In that case all 20 luminosity blocks are declared as bad.

There are additional calorimeter noise patterns, for which single events are discarded. This includes for example events, where a ring of energy in ϕ occurs based on grounding problems, or where for all crates a synchronous shift in the pedestals occur.

In case of calorimeter noise that occurs on an event-by-event basis, the events get a calorimeter flag and are removed from the analysis. These events can not be excluded from the luminosity calculation. Therefore a data quality efficiency correction has to be applied on Monte Carlo events [108]. A more detailed description of the data quality efficiency correction will be given at the end of this chapter.

6.1.2. Trigger

In order to enrich the data sample with events that have jets and at least one lepton in the final state, electron plus jets (e+jets) and muon plus jets (μ+jets) triggers are required. Different trigger requirements lead to slightly different values for the integrated luminosity in the e+jets and μ+jets channels. Due to an increased instantaneous luminosity and optimisation of the trigger conditions, the trigger requirements and algorithms have changed during the time of data taking. The different trigger conditions applied during one period of data taking are put in so-called trigger lists. More details on the triggers used in this thesis can be found in [109].

Electron plus jets channel The trigger for the e+jets channel requires at least one electron and at least two jet candidates. Table 6.1 shows the trigger list version, the corresponding trigger, and the integrated luminosity for data with good quality. From trigger list version $V8$ to $V11$ the trigger EM15_2JT15 was used, starting from trigger list version $V12$ the trigger E1_SHT15_2J20, E1_SHT15_2J_J25 or E1_SHT15_2J_J30 is required. All of the trigger lists require an electromagnetic (EM) object with transverse energy E_T larger than a certain threshold between 10 and 20 GeV on Level 1, an EM object with high E_T on Level 2 and at least two jets with E_T larger than 15 or 20 GeV on Level 3. The requirements are optimised to enrich the data with events containing an electron and jets with high momentum, corresponding to a simplified and very loose selection of $t\bar{t}$ events in the e+jets channel. More information on the individual trigger lists are given in Appendix A.

Triggerlist Version	Trigger name	Integrated luminosity [pb^{-1}]
V8.0 - V9.0	EM15_2JT15	23.49
V9.0 - V10.0	EM15_2JT15	24.96
V10.0 - V11.0	EM15_2JT15	9.81
V11.0 - V12.0	EM15_2JT15	63.40
V12.0 - V13.0	E1_SHT15_2J20	227.80
V13.0 - V13.3	E1_SHT15_2J_J25	55.22
V13.3 - V14.0	E1_SHT15_2J_J30	298.94
V14.0 - V15.0	E1_SHT15_2J_J25	334.20
TOTAL		1037.82

Table 6.1.: Integrated luminosity collected with the e+jets trigger and the trigger list version. For the full Run IIa dataset.

Table 6.1 lists the dataset from August 2002 to April 2006. For the dataset from August 2002 to December 2005 the same triggers and trigger lists were used. The integrated luminosity for the latter set is 912.55 pb^{-1} in the e+jets channel. The breakoff of trigger lists for the subset of data is shown in Table 8.1 in section 8.

Muon plus jets channel For the μ+jets channel the trigger requirement is at least one muon and at least one jet candidate. In Table 6.2 the trigger list version, the corresponding trigger, and the integrated luminosity for data with good quality are listed. From trigger list version $V8$ to $V11$ the trigger MU_JT20_L2M0 was used. For trigger list version $V12$,the trigger MU_JT25_L2M0 has been applied. In later version the triggers MUJ2_JT25, MUJ2_JT25_LM3, MUJ2_JT30_LM3, MUJ1_JT25_ILM3 and MUJ1_JT35_LM3 were used. All trigger lists have in common, that on Level 1 one muon trigger based on scintillator or wires and one calorimeter jet trigger tower are required to fulfil E_T of larger than 3 or 5 GeV (depending on the trigger

list), a muon with medium quality on Level 2 and at least one jet with high E_T on Level 3. A more detailed description on the individual trigger lists is given in Appendix A.

Triggerlist Version	Trigger name	Integrated luminosity [pb^{-1}]
V8.0 - V9.0	MU_JT20_L2M0	24.79
V9.0 - V10.0	MU_JT20_L2M0	25.00
V10.0 - V11.0	MU_JT20_L2M0	10.70
V11.0 - V12.0	MU_JT20_L2M0	65.83
V12.0 - V13.0	MU_JT25_L2M0	231.63
V13.0 - V13.2	MUJ2_JT25	31.84
V13.2 - V13.3	MUJ2_JT25_LM3	16.10
V13.3 - V14.0	MUJ2_JT30_LM3	255.94
V14.0 - V14.2	MUJ1_JT25_LM3	0.01
V14.2 - V14.3	MUJ1_JT25_ILM3	21.89
V14.3 - V15.0	MUJ1_JT35_LM3	312.55
TOTAL		996.27

Table 6.2.: Integrated luminosity collected with the μ+jets trigger and the trigger list version. For the full Run IIa dataset.

For the dataset from August 2002 to December 2005 the same triggers and trigger lists were used. The integrated luminosity for that set is 871.34 pb^{-1} in the μ+jets channel. The breakoff of trigger lists for this subset of data is shown in Table 8.2 in section 8.

6.2. Monte Carlo simulation

In order to study the composition of the data sample, a simulation of the different signal and background contributions is important. The simulation of different processes in inelastic particle collisions is done with Monte Carlo event generators. A Monte Carlo generator combines perturbative theoretical calculations with phenomenological models for different parts of an event, as described in the following.

Event simulation The simulation of an event in high energy physics can be separated into different steps. Figure 6.1 shows the scheme of an event in e^+e^- collisions and the more complicated structure of an event in $p\bar{p}$ collisions.

The simulation starts with the hard interaction. Two constituents of the colliding beams interact with each other. The hard interaction is calculated with perturbative quantum field theory. While in an e^+e^- collision the initial state is clearly defined by the two leptons, the initial particles in $p\bar{p}$ collisions radiate further partons, e. g. gluon radiation from quarks or gluon self-couplings take place. As can be seen in Fig 6.1, the radiation of gluons from the hard interacting particles and the colour charged initial state leads to a more complex event structure in $p\bar{p}$ than in e^+e^- collisions.

In the event simulation the radiation of particles from final particles of the hard interaction is separated from the radiation before the hard interaction. The radiation of photons and gluons from final particles of the hard interaction is called Final State Radiation (FSR). The beam particles can radiate photons and gluons before the hard interaction takes place, which is called Initial State Radiation (ISR). Both ISR and FSR can be calculated perturbatively.

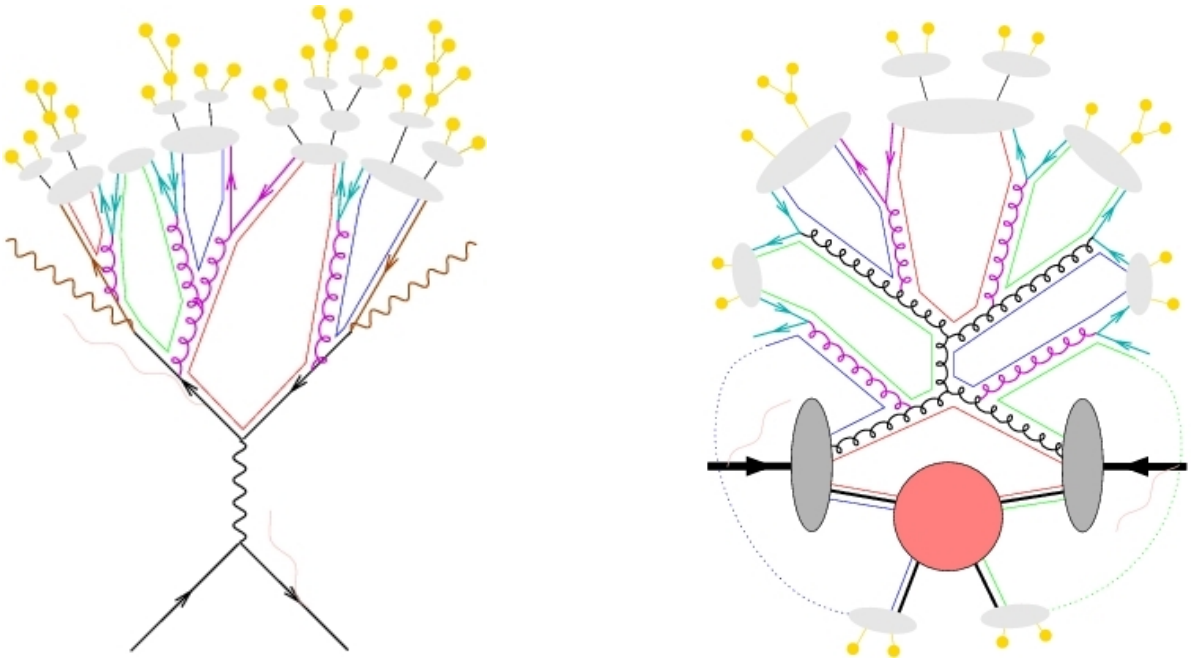

Figure 6.1.: Schematic picture of an event in e^+e^- (left) and $p\bar{p}$ (right) collisions [110].

The initial particles from hard interaction, FSR and ISR radiate further quarks and gluons. There are different methods for the simulation of this perturbative step, like the parton shower and the colour dipole ansatz.

Once energies of about 1 GeV are reached, the fragmentation of quarks and gluons into hadrons takes place. Phenomenological models are necessary for the description of the hadronisation. All models have free parameters that need to be measured in order to properly describe the fragmentation process. The most commonly used Monte Carlo generators use either the string fragmentation model as used in PYTHIA [111], or cluster fragmentation, as realized in the HERWIG event generator [112]. In the last step the instable hadrons decay into stable final particles that can be identified in the detector.

Monte Carlo generators Different models for the event simulation are combined in different Monte Carlo generators. The generation of signal and background events in this thesis is mainly done with the PYTHIA [113] and ALPGEN [114] event generators. For the generation of single top quark events the CompHEP-SingleTOP [115] generator is used. The simulation uses the parton distribution functions at leading order, CTEQ6L1, via the LHAPDF package [116].

The PYTHIA generator uses the parton showering for the modelling of initial and final state radiation. The hadronisation is done with a string fragmentation model. In the ALPGEN event generator only the hard interaction is calculated. The outcome of ALPGEN is put into PYTHIA where the parton shower and fragmentation are simulated. In ALPGEN extra jets are calculated with additional Feynman diagrams. As also in a parton shower extra jets can be created, a mechanism to avoid double counting has to be applied in case PYTHIA and ALPGEN are combined. In ALPGEN the so-called MLM matching [117] is implemented. For different parton multiplicities individual samples are generated separately. After the parton shower a jet cone algorithm is applied to the final partons and the jets are matched to the partons from the matrix element. In case the jet and parton multiplicity does not match or the assignment of jets and partons does not work, the event is rejected. In order to take into account the

relative cross sections for each separately generated parton multiplicity a weight is assigned to the different events [118].

Detector simulation The Monte Carlo generators simulate charged and neutral particles. The real data do not contain the particles themselves but objects in the detector, e. g. energy depositions in the calorimeter. In order to compare generated events to data the simulation of the Monte Carlo particles with the detector material and the resulting electronic signals is necessary.

The interaction of the particles with the DØ detector is simulated with D0gstar [119], which is based on GEANT [120], a software package designed to describe the passage of elementary particles through matter. With D0gstar the energy depositions in the active detector parts are determined. The D0gstar output is then passed to D0SIM [121], that simulates the electronic signals and the pile-up[1)] of additional minimum bias interactions. Alternatively to the simulation of minimum bias interactions with Monte Carlo, real zero bias[2)] data can be prepared with D0Raw2Sim, and then be used as pile-up by D0SIM. In the Monte Carlo used in this thesis the pile-up comes from real zero bias data. The output of D0SIM is in the same format as the output from real data. It is then treated by the same reconstruction software as the data events.

The one thing that is not simulated are the triggers that are used to select the data. The probability for a trigger to fire is measured in data and parametrised as function of lepton and jet p_T, η or ϕ. The parametrisations are applied on each Monte Carlo event. The efficiency for all leptons and jets to pass the trigger conditions is calculated and combined into a probability for the event to pass the trigger conditions.

More information on the preparation of Monte Carlo events can be found at DØ's Monte Carlo web page [122].

6.3. Monte Carlo to Data correction factors and reweightings

The events generated with Monte Carlo and passed through detector simulation do not reproduce the data perfectly. Therefore several Monte Carlo correction factors have to be applied. There are two main types of corrections:

- Corrections of the Monte Carlo: The Monte Carlo generators use leading order matrix elements for the hard interactions. Higher order corrections can result in differences in the cross section but also in the shape of the resulting distributions. Moreover, certain settings for different parameters, for example the parameters used for the fragmentation model in PYTHIA, can result in different shapes of the sensitive observables, depending on the setting. Another effect can be that the overlaid zero bias events, that are used to include effects from pile-up, are depending on the luminosity of the considered data. All of these effects require a reweighting of the Monte Carlo events according to certain reference distributions. The normalisation of the number of considered events does not change due to this class of corrections.

- Corrections of Monte Carlo to Data: Due to imperfect simulation of the tracking system the efficiency to reconstruct a lepton, for example, is different in data and Monte Carlo events. A correction factor has to be applied to correct the identification in Monte Carlo events to reflect the one in data. Additionally, trigger efficiencies are not simulated in

[1)] pile-up describes the energy from previous bunch crossings that remain in the detector
[2)] zero bias events are recorded with no trigger requirement

Monte Carlo. This has to be taken into account by applying a probability to each event to pass the trigger requirements. The efficiency for each trigger as function of lepton and jet p_T and η or ϕ is measured in data.

In the following the different correction factors and reweightings that are either used for the selection efficiency calculation or in order to determine systematic uncertainties are described briefly. The W+jets heavy flavour scale factor and the reweighting of the b-fragmentation function will be discussed in more detail as they are part of this thesis.

6.3.1. Reweighting of the b-fragmentation

The description of the fragmentation of b quarks requires the use of non-perturbative models in the Monte Carlo simulation. The parameters of the models can not be calculated but need to be tuned to data. Several measurements of the b-fragmentation function have been performed in the e^+e^- experiments Aleph [123], Delphi [124], Opal [125] and SLD [126]. All of these measurements favour a modification of the Lund symmetric fragmentation function [111] for the fragmentation of heavy quarks, the so-called Bowler fragmentation function [127]:

$$f(z) \propto \frac{1}{z^{1+r_q b m_q^2}} z^a \left(\frac{1-z}{z}\right)^a \exp\left(-\frac{-b(m_Q^2 + p_\perp^2)}{z}\right). \tag{6.1}$$

m_Q describes the mass of the B hadron, m_q is the constituent mass of the b quark, a, b and r_q describe free parameters of the model and $p_\perp$ is the transverse momentum of the B hadron relative to the b quark flight direction. The variable z is the fraction of $E + p_{\text{long}}$ of the quark, taken by the heavy hadron. The parameter r_q is introduced for each flavour in order to allow a continuous extrapolation between the Lund ($r_q = 0$) and the Bowler ($r_q = 1$) fragmentation function.

The hadronisation and particle decay are simulated with the Monte Carlo generator PYTHIA. The standard DØ Monte Carlo production uses the Bowler function with the PYTHIA default setting $a = 0.3$, $b = 0.58$ and $r_q = 1$ for the fragmentation of heavy quarks. In order to check and tune the parameters in the simulation to the available measurements, the PYTHIA generator has been modified to run in e^+e^- mode with $\sqrt{s} = 91.25$ GeV, but otherwise the same settings as for the standard Monte Carlo production in DØ are kept. By comparing the shape of the fragmentation function between the measurements of Aleph, Delphi, Opal and SLD and the simulation, the fragmentation parameters can be tuned to best match the given data. As currently no measurement of the b-fragmentation in hadron collider data is available, the tune to e^+e^- data gives the best estimate of the fragmentation function.

The fragmentation function is tuned by variation of r_b and a, and keeping the difference $b - a$ fixed to the PYTHIA default value of 0.28. Due to a and b being anti-correlated this choice is made in order to change the fragmentation of the light quarks as least as possible.

A short description of the tuning of the fragmentation function is given here, more details can be found in [128, 129]. As a regeneration of all Monte Carlo samples with the tuned fragmentation parameters is very time consuming, every event is reweighted [130] according to the ratio of the tuned and default Bowler functions, as described in the following.

Tuning of the Bowler fragmentation function to LEP and SLD data The fragmentation model is tuned by adjusting the parameters a and r_q to the measured distribution of the B-hadron energy divided by the beam energy $x_B = 2 \cdot E_B / E_{CM}$. A model-to-data

$$\chi^2 = \sum_{i=0}^{N_{bin}} \frac{(x_B^{\text{i,meas}} - x_B^{\text{i,gen}})^2}{\sigma(x_B^{\text{i,meas}})^2} \tag{6.2}$$

Experiment	r_q	a
ALEPH	0.86 ± 0.02	0.97 ± 0.13
DELPHI	0.94 ± 0.03	1.21 ± 0.24
OPAL	0.90 ± 0.02	1.03 ± 0.15
AOD	0.897 ± 0.013	1.03 ± 0.08
SLD	0.98 ± 0.01	1.30 ± 0.09

Table 6.3.: Fit parameters deduced from the different experimental results for the Bowler fragmentation model. The uncertainties on r_q and a are correlated due to the simultaneous fit of both quantities. *AOD* denotes the combined fit to the results of Aleph, Opal and Delphi.

is calculated for each measured distribution and minimised to determine the optimal r_q and a values. $x_B^{\mathrm{i,meas}}$ denotes the measured x_B per bin i of the distribution, $x_B^{\mathrm{i,gen}}$ the generated x_B value and $\sigma(x_B^{\mathrm{i,meas}})$ the uncertainty on $x_B^{\mathrm{i,meas}}$. The sum runs over all bins of the considered distribution.

Table 6.3 shows the results of r_q and a for the tuning of the fragmentation function. *AOD* denotes the combined fit to the results of Aleph, Opal and Delphi. The parameters resulting from the tuning to the LEP experiments are consistent. Although the parameter set obtained from the SLD data differs, the actual fragmentation functions predicted by PYTHIA agree reasonably. Because of the consistency of the LEP results one parameter set is tuned to the combination of Aleph, Delphi and Opal data, and a separate set is tuned to the SLD data. The difference between both sets can then be used for the estimation of the systematic uncertainty induced by the fragmentation modelling on the physics analysis.

Reweighting of the fragmentation function The standard DØ Monte Carlo generated with PYTHIA is reweighted in order to reach consistency with the tuned fragmentation model. Figure 6.2 shows the Bowler fragmentation function for the tunes to Aleph, Opal and Delphi (AOD) and SLD, compared to the PYTHIA default. The tuned functions show a much harder spectrum than the function with PYTHIA default settings. Each B hadron coming from the hadronisation process gets a weight according to the ratio of the tuned to the default value of the fragmentation function at the corresponding value of z.

The fragmentation influences the b-tagging, as for example the p_T of the B hadron relative to the jet has an influence on the secondary vertex reconstruction. In Fig. 6.3 the dependency of the b-tagging efficiency on the b-fragmentation z is shown. As an example the tight and super-loose working points (see Table 5.1) of the secondary vertex tagger (SVT) with shared track removal, as described in [81], are used. A small dependency of the b-tagging efficiency on the fragmentation z can be seen. For the tight SVT the efficiency increases with increasing z. For the super-loose SVT the effect shows the opposite behaviour. As a larger z leads to a higher momentum of the B hadron w.r.t. the b quark, an increasing efficiency for larger z is expected. The decreasing b-tag efficiency for the super-loose SVT is presumable connected to the additional fake tracks from the jet carried by the secondary vertex.

6.3.2. W+jets heavy flavour scale factor

The W+jets sample is simulated with ALPGEN, interfaced to PYTHIA for the hadronisation, using leading order cross sections. The complete set of W+jets events consists of samples with an additional gluon splitting into light partons (Wlp+jets), c quarks (Wcc+jets) and b quarks (Wbb+jets). In the next-to-leading order (NLO) and higher perturbative calculations, the rel-

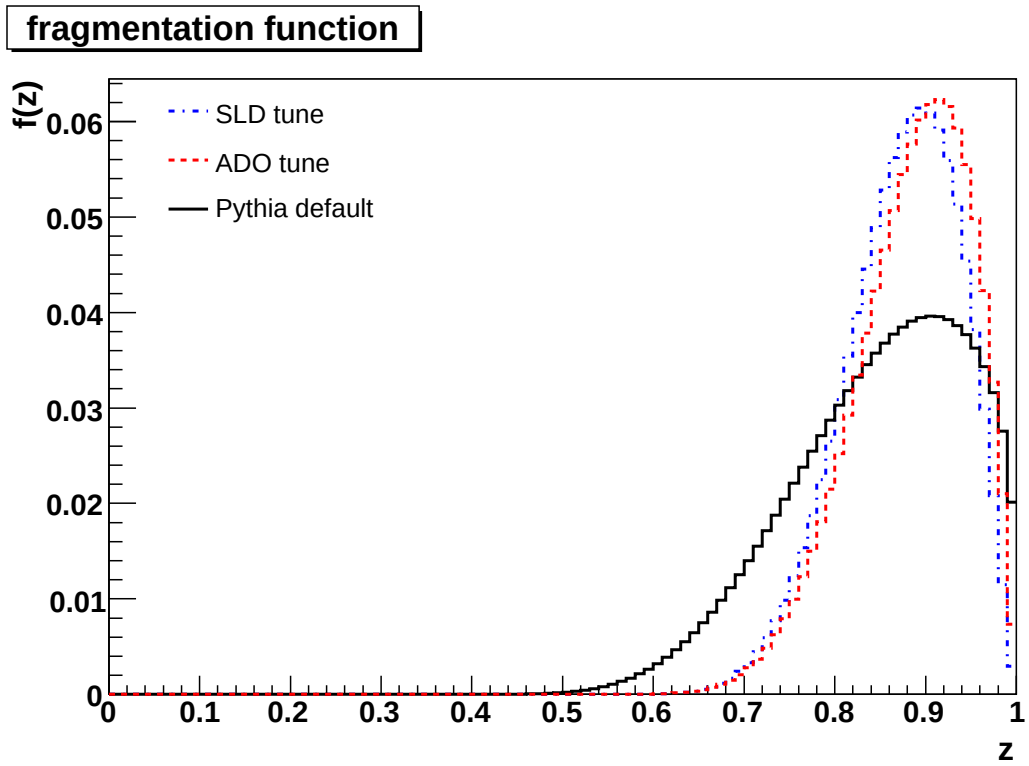

Figure 6.2.: Bowler fragmentation functions as determined by the different tunings and the PYTHIA default.

ative contributions of the three samples are different from leading order calculations. In particular, the Wcc+jets and Wbb+jets contributions are expected to be higher in NLO. As no reliable NLO calculations exist for these samples, the heavy flavour scale factor, defined as the relative fraction of W plus heavy flavour (Wcc+jets and Wbb+jets) to Wlp+jets, has to be measured from data [107].

The lack of heavy flavour contributions to the total background can be seen in a poor agreement of the Monte Carlo prediction to the data. Especially due to the different b-tag probabilities on Wlp+jets, Wcc+jets and Wbb+jets it is possible to measure the W+jets heavy flavour scale factor in W+jets dominated samples after application of b-tagging.

For the study of the W+jets heavy flavour scale factor the same event selection and treatment of signal and background as for the measurement of the $t\bar{t}$ cross section is used. Details about the selection can be found in Section 7.1. For $t\bar{t}$ a top mass of 175 GeV and a cross section of 6.8 pb is assumed. The W+jets ALPGEN samples are produced with DØ release p17.09.06, where ALPGEN version 2.05 is used. The charged Higgs analysis performed later uses updated W+jets samples, produced with p17.09.08 and ALPGEN version 2.11 and a new heavy flavour scale factor needs to be determined, as presented at the end of this section.

Determination of the heavy flavour scale factor In $t\bar{t}$ analyses the total amount of W+jets events is determined by subtracting all Monte Carlo backgrounds, the $t\bar{t}$ signal and the QCD multijet events from the considered data before application of b-tagging. The number of multijet events is determined from data with the Matrix Method described in Section 7.2.1.

The total number of expected W+jets events before b-tagging can be written as

$$N^{data}_{W\text{+jets}} = N_{\text{data}} - N_{\text{signal-like MC}} - N_{\text{Multijet}} \tag{6.3}$$

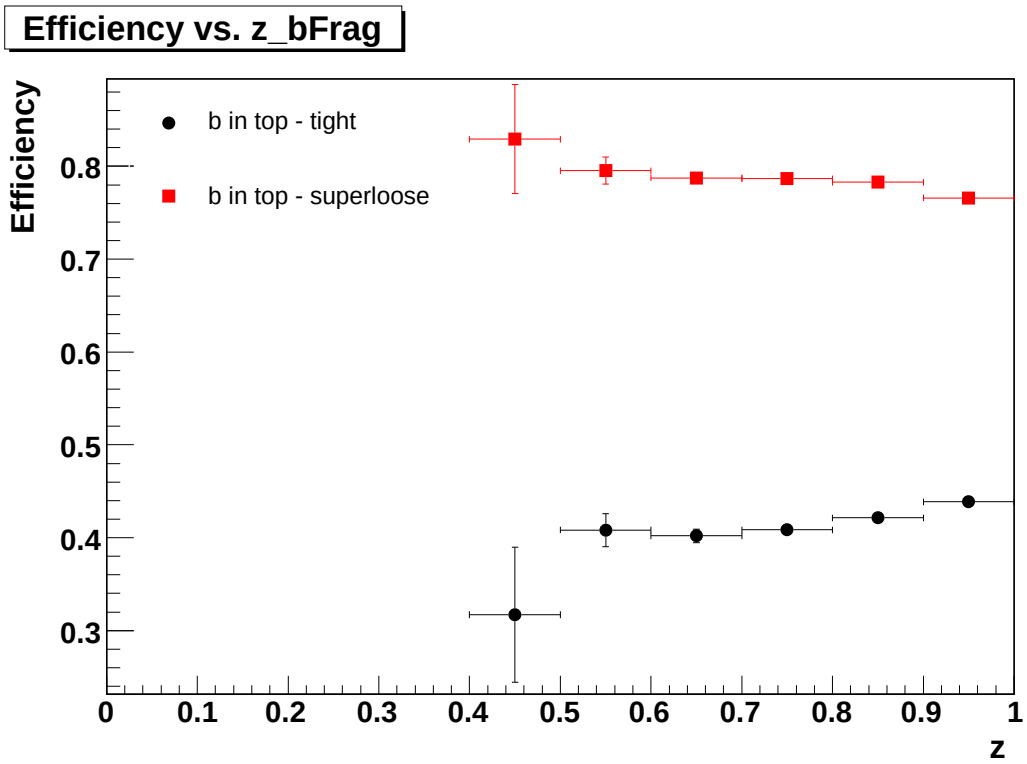

Figure 6.3.: Dependency of the b-tagging efficiency on the z value of the b-fragmentation function.

Signal like Monte Carlo means $t\bar{t}$, Diboson, single top and Z+jets contributions. The W+jets contribution from Monte Carlo itself consists of

$$N^{MC}_{\text{W+jets}} = N_{Wlp\text{+jets}} + k \cdot N_{Wcc\text{+jets}} + k \cdot N_{Wbb\text{+jets}} \tag{6.4}$$

where k is defined as the heavy flavour scale factor and is assumed to be the same for Wcc+jets and Wbb+jets. $N^{MC}_{\text{W+jets}}$ is independent of the data and relies only on Monte Carlo cross sections.

After requiring events with 0, 1 or 2 b-tags the perfect Data/Monte Carlo agreement is achieved if

$$N^{data}_{\text{W+jets}}{}' = N_{\text{data}}{}' - N_{\text{signal like MC}}{}' - N_{\text{Multijet}}{}' \tag{6.5}$$

where N' denotes the number of events in each sample with the considered number of b-tags.

The normalisation of W+jets events to data after b-tagging can be achieved by dividing Eq. 6.3 by Eq. 6.4 and replacing $N^{data}_{\text{W+jets}}{}'$ in Eq. 6.5 by $N^{data}_{\text{W+jets}}/N^{MC}_{\text{W+jets}} \cdot N^{MC}_{\text{W+jets}}{}'$, where $N^{MC}_{\text{W+jets}}{}'$ is given by

$$N^{MC}_{\text{W+jets}}{}' = N_{Wlp\text{+jets}}{}' + k \cdot N_{Wcc\text{+jets}}{}' + k \cdot N_{Wbb\text{+jets}}{}'. \tag{6.6}$$

This changes Eq. 6.5 to

$$\begin{aligned}(N_{\text{data}} - N_{\text{signal like MC}} - N_{\text{Multijet}}) \cdot (N^{MC}_{Wlp\text{+jets}}{}' + k \cdot N^{MC}_{Wcc\text{+jets}}{}' + k \cdot N^{MC}_{Wbb\text{+jets}}{}') \quad = \\ (N_{\text{data}}{}' - N_{\text{signal like MC}}{}' - N_{\text{Multijet}}{}') \cdot (N^{MC}_{Wlp\text{+jets}} + k \cdot N^{MC}_{Wcc\text{+jets}} + k \cdot N^{MC}_{Wbb\text{+jets}}).\end{aligned} \tag{6.7}$$

To simplify the error calculation every sample before b-tagging can be split into two orthogonal samples: the tagged sample (denoted as $'$) and the anti-tagged sample (denoted by $''$).

The final formula for the calculation of the heavy flavour scale factor k is

$$k = \frac{(\text{data}' - \text{X}') \cdot W'' - (\text{data}'' - \text{X}'') \cdot W'}{(\text{data}'' - \text{X}'') \cdot B' - (\text{data}' - \text{X}') \cdot B''} \tag{6.8}$$

where W (B) is the number of events in Wlp+jets (Wbb+jets and Wcc+jets) samples. X denotes the number of events in different MC background samples other than W+jets, i. e. multijet events and the signal-like MC.

Heavy flavour scale factor dependencies The heavy flavour scale factor is studied separately in the e+jets and μ+jets channels. For b-jet identification the Neural Net (NN) b-tagging algorithm (NN tagger) is used [104].

To predict the number of tagged events in simulation the Tag Rate Functions (TRFs) and TaggabilityRFs are applied.

The Matrix Method used to determine the multijet background contribution requires the knowledge of the lepton fake rate ε_{qcd} and the real lepton efficiency ε_{signal}. More details can be found in section 7.2.1.

For every jet multiplicity subsample, b-tag subsample and tag working point the heavy flavour scale factor is calculated according to Eq. 6.8.

As the 3rd and 4th jet multiplicity subsamples are used for top analyses in the l+jets channel, these samples are avoided when determining the heavy flavour scale factor. For every tag working point the heavy flavour scale factor is calculated as a weighted mean of the values measured in the 1st and 2nd jet multiplicity subsamples with 0 b-tags, as these two subsamples give two independent measurements.

The dependency of the heavy flavour scale factor on the output cut of the NN tagger is shown in Fig. 6.4 for the e+jets and μ+jets final states. For the NN cut > 0.6, corresponding to the five tightest working points (being Medium, Tight, VeryTight, UltraTight and MegaTight as listed in Table 5.1 in section 5.7), the behaviour is consistent with a constant. In this region where the scale factor is stable and fits with a constant value, the heavy flavour scale factor is determined. For any other tag working point a different scale factor would be needed. As the calculation in the five tightest tag working points are correlated, the mean value with the average of the statistical uncertainty of each individual measurement is calculated. The red line in Fig. 6.4 shows the fit of a constant to the five tightest working points with the error of the fit. As a pure fit assumes uncorrelated measurements the error band has to be scaled up to the mean error of all five individual measurements. The green band corresponds to a scale factor of 1.5 ± 0.45 that was used before performing the presented study.

The study of the heavy flavour scale factor indicates two features: The heavy flavour scale factor depends on the choice of the tag working point, and the heavy flavour scale factor differs in the e+jets and μ+jets channel. As the scale factor should represent the difference between the ratio of NLO over leading-order calculation for light and heavy flavour Monte Carlo, no dependence on b-tagging or the final state is expected.

Further studies Several studies are carried out to understand the dependency of the heavy flavour scale factor on the tag working point and the difference between the e+jets and μ+jets channels. In particular, the following cases are considered:

- Apply tagging directly to simulated events, to exclude effects due to TRF and taggability parametrisations.

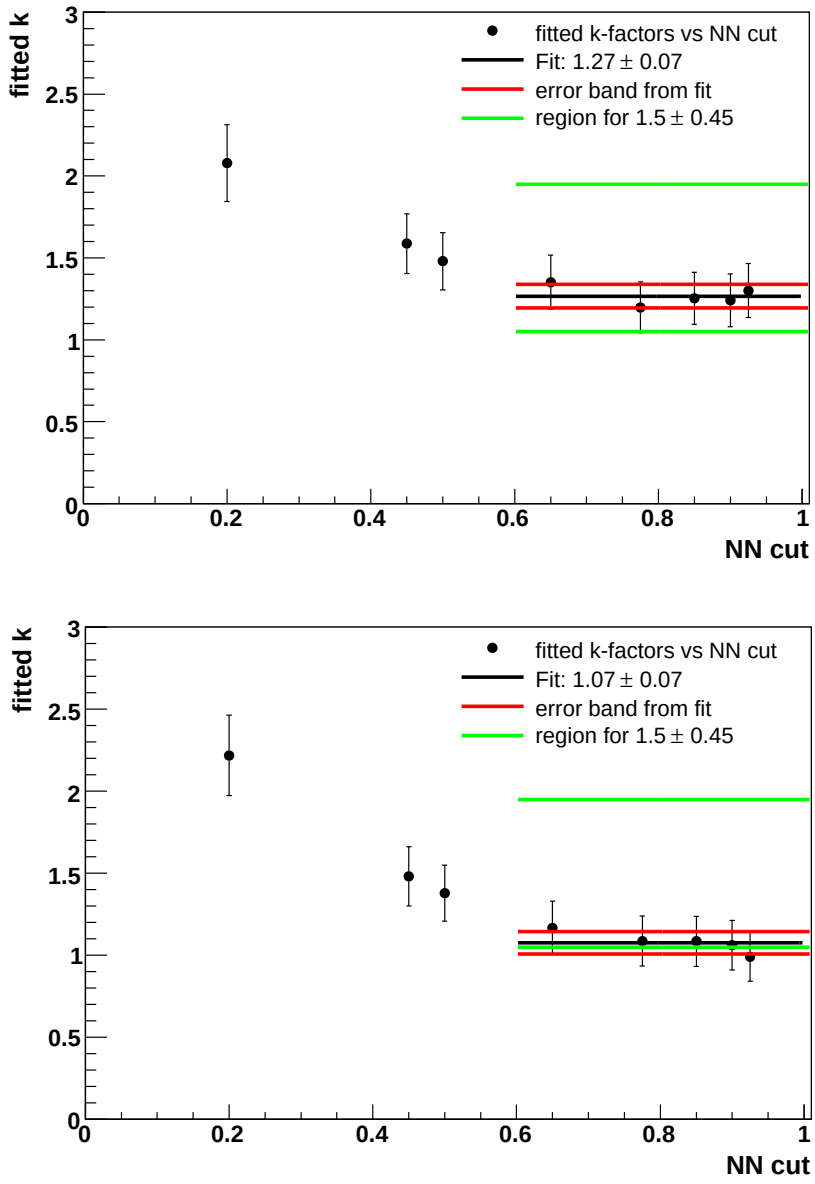

Figure 6.4.: Heavy flavour scale factor versus the Neural Net cut value. Green band: region of 1.5 ± 0.45. Red band: Error from fit. Top (bottom) plot: e+jets (μ+jets).

- Apply taggability directly and use TRFs to exclude effects from the TaggabilityRFs.
- Change the Z+jets flavour composition, to check the influence of the choice of the Z+jets heavy flavour scale factor on the W+jets heavy flavour scale factor.
- Use only W+jets and multijet events for the scale factor calculation.
- Study the effect of multijet background on the scale factor by variation of the lepton fake rate ε_{qcd} after b-tagging.

The detailed descriptions of these studies can be found in [107]. None of the studies revealed the reason for the dependency of the heavy flavour scale factor on b-tag or the final state. Studies to understand this behaviour are still on-going.

study	e+jets	μ+jets
standard approach	1.27 ± 0.07	1.07 ± 0.07
ε_{qcd} after tagging, up	1.13 ± 0.07	1.01 ± 0.06
ε_{qcd} after tagging, down	1.34 ± 0.07	1.08 ± 0.06
Fit in 1 b-tag subsample	1.24 ± 0.07	1.05 ± 0.06
Fit through four tightest NN working points	1.25 ± 0.08	1.05 ± 0.08
Wbb and Wcc TRF and Taggability correction	1.36 ± 0.08	1.16 ± 0.08

Table 6.4.: Heavy flavour scale factors for various studies

Systematic uncertainties and heavy flavour scale factor For the central value of the heavy flavour scale factor only the five tightest working points are taken into account, as they are consistent with a flat factor. For the looser working points the scale factor and probably also the uncertainties have to be increased. The mean of the fitted values for e+jets and μ+jets is taken for the central heavy flavour scale factor. The difference of e+jets and μ+jets is assigned as systematic uncertainty and added linearly instead of quadratically into the combined error.

In Table 6.4 the calculated heavy flavour scale factors for different approaches are shown. The largest deviation of the channel discrepancy and ε_{qcd} variation is taken as systematic error and added in quadrature. The final heavy flavour scale factor k is

$$k = 1.17 \pm 0.11 \text{ (stat)} \pm 0.1 \text{ (syst from channel deviation)}. \tag{6.9}$$

The lepton fake rate ε_{qcd} is varied by $\pm 20\%$ after b-tagging. The variation of ε_{qcd} results in a variation of k by 0.04 up and 0.11 down, where the deviation from the mean of both channels is taken. Additionally, the fit of the heavy flavour scale factor is performed using the subsample with 1 b-tag instead of 0 b-tags, and for only the four tightest working points. Both changes result in a deviation of k by 0.02 down, respectively. The final result for the W+jets heavy flavour scale factor with all systematic uncertainties is

$$k = 1.17 \pm 0.11 \text{ (stat)} \pm 0.14 \text{ (syst)} \tag{6.10}$$

or

$$k = 1.17 \pm 0.18 \text{ (total)}, \tag{6.11}$$

where the error is symmetrised using the largest value for each single source of systematic uncertainty.

Heavy flavour scale factor with p17.09.08 samples The determination of the heavy flavour scale factor for W+jets Monte Carlo generated with p17.09.08 is done in the same way. For the $t\bar{t}$ signal sample ALPGEN is used, with a top mass of 170 GeV and a $t\bar{t}$ cross section of 7.91 pb.

Only the new central value of the heavy flavour scale factor, the statistical uncertainty and the difference between the e+jets and μ+jets final states is recalculated. The relative systematic uncertainty coming from ε_{qcd} and the different fits is taken from Eq. 6.10 and assigned on the scale factor for the p17.09.08 W+jets Monte Carlo. Figure 6.5 shows the dependency of the heavy flavour scale factor on the NN tag working point. The W+jets heavy flavour scale factor for the new samples is

$$k = 1.93 \pm 0.23 \text{ (total)}. \tag{6.12}$$

The large difference with respect to the samples used before in this section purely comes from the different version of ALPGEN for the newly generated Monte Carlo samples.

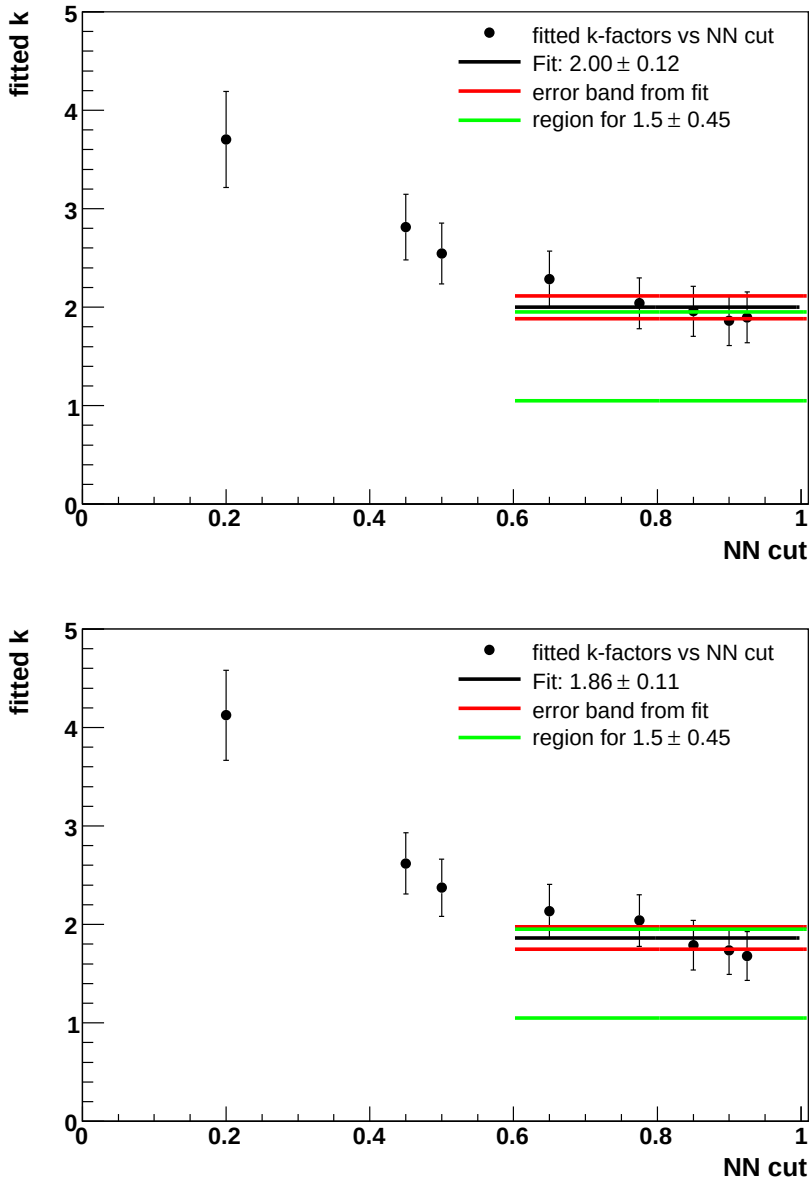

Figure 6.5.: Heavy flavour scale factor versus the Neural Net cut value for new W+jets MC, generated with ALPGEN version 2.11. Green band: region of 1.5 ± 0.45. Red band: Error from fit. Top (bottom) plot: e+jets (μ+jets).

6.3.3. Further scale factors and reweightings

Besides the correction factors derived as part of this thesis, several other important reweighting and scale factors have to be applied on the simulated events. The Jet Energy Scale (JES) correction, jet shifting, smearing and removal (JSSR), corrections on the flavour dependence of taggability and a correction of b-tag TRFs for gluon splitting samples are described in Section 5. Further necessary corrections are electron and muon scale factors, k-factors that refer to differences in next-to-leading-order and leading-order cross section calculations, the correction of the selection efficiency for event-by-event data quality decisions, the reweighting of the luminosity profile and the primary vertex z distribution, the trigger efficiency correction and the Z p_T reweighting. Each of these individual factors will be described briefly in the

following paragraphs.

Electron and muon scale factors Due to the tracker simulation not being sufficiently modelled to describe the data accurately, the efficiency to reconstruct, identify and select leptons is higher in Monte Carlo events than in data. The corresponding efficiencies of the leptons are measured in data [84, 131]. A Monte Carlo to data correction factor is then parametrised as function of η_{det} and ϕ and applied on the leptons in generated events. The correction factors lie between about 92% and 101%.

NLO to LO correction factors Samples that are generated with ALPGEN are usually split into different parton multiplicities. On each event a weight is applied according to the relative cross section that goes into the generation of the separate parton multiplicities. The leading order cross sections are used for the weights. To take into account higher order calculations an overall k-factor that is the fraction of the total NLO cross section over the total LO cross section is applied on the generated events. The size of the factor varies depending on the considered sample.

Data quality calorimeter flag correction As described in section 6.1.1 some calorimeter noise effects only occur in single events, and only these events are declared as bad in data, but are not excluded from the luminosity calculation. Therefore a correction factor on the selection efficiencies in Monte Carlo has to be applied. A correction factor of $(97.14 \pm 0.003)\%$ [108] was determined from data triggered with the zero bias trigger, which is expected to be unbiased by calorimeter noise patterns. A systematic uncertainty of 0.5% is assigned on the correction factor to account for possible differences between the considered data samples.

Luminosity Profile reweighting The minimum bias interactions used by D0SIM and overlaid in the Monte Carlo are real zero bias events collected at a certain instantaneous luminosity. The instantaneous luminosity increased over the years of data taking. The zero bias events overlaid to Monte Carlo events are recorded up to a certain date, and therefore do not contain events with higher instantaneous luminosity recorded later. Therefore, the profile of the instantaneous luminosity in data can differ significantly from the one in Monte Carlo. As the zero bias events are used to reproduce detector and luminosity effects, a good description of the luminosity profiles in Monte Carlo is required. In order to get the luminosity profiles into agreement, the profile in the Monte Carlo is reweighted to the one in data. An event weight is applied, that represents the ratio of the currently considered Monte Carlo sample to the data used in the analysis. Depending on the Monte Carlo sample, the effect of the difference in luminosity profile on the event selection can be of the order of a few per cent.

Primary vertex z reweighting In simulated events the z coordinate of the primary vertex is distributed according to a Gaussian shape, with centre zero and a width of 25 cm. In real data the shape of the luminosity region and the primary vertex are different, and depend, for example, on the instantaneous luminosity. In order to get the z vertex distribution between data and Monte Carlo into agreement an event weight is applied, correcting the z distribution in Monte Carlo to the shape in the data [132]. Although luminosity profile reweighting and the primary vertex z reweighting are correlated, the former alone is not sufficient to describe both effects.

Trigger efficiency correction Due to the missing simulation of the triggers a probability that an event would pass the used trigger conditions is applied on Monte Carlo samples. From

unbiased data, efficiency turn-on curves are measured for each of the leptons or jets to fire a trigger [109]. As the lepton and the jet triggers are independent of each other, the efficiency parametrisations can be applied independently for the different physics objects and the total probability is a product of the individual ones. In the analyses presented in this thesis, the trigger probability per event is of the order of $80 - 90\%$.

Z p_T reweighting In Z+jets dominated data samples a discrepancy between the Z p_T distribution in Monte Carlo and data has been observed. In order to correct the ALPGEN Z+jets Monte Carlo samples for the observed difference, a reweighting procedure was developed [133]. The Z p_T reweighting is derived and applied depending on the jet multiplicity. As the Z+jets contribution in the l+jets channel is small, the effect of Z p_T reweighting does not affect the results. In the dilepton channel, which is dominated by Z+jets background, the reweighting is more important.

7. Lepton+jets event selection and sample composition

In order to enrich the data sample with $t\bar{t}$ events in the lepton+jets (l+jets) final state, an event selection is done that employs the specific properties of this final state. In this chapter the event selection[1)] requirements, and the signal and background samples considered for the analyses are presented.

7.1. Event selection

The analyses consider $t\bar{t} \rightarrow WqWq$ events, where one W boson decays hadronically, resulting in two jets in the final state and the other W boson decays leptonically, providing a high p_T isolated charged lepton (electron in the e+jets or muon in the μ+jets channel) and a neutrino.

The undetected neutrino gives rise to a large missing transverse energy, $\not\!\!E_T$. The signature of the l+jets channel is therefore one isolated high p_T lepton, large $\not\!\!E_T$ from the neutrino, and four or more jets: two from the hadronic W decay and the other two from the decay of the top quarks.

The goal of the event selection is to select events having the same signature as the $t\bar{t}$ final state under study and thus enhance the signal over background ratio. The main background after event selection consists of W+jets events. The e+jets and μ+jets channels have similar event selection requirements. To ensure orthogonality to the dilepton final states events with a second isolated electron or muon are vetoed.

The event selection in the e+jets and μ+jets channel shares the following requirements:

- Good event quality, as described in section 6.1.1.
- Only events with exactly three or at least four jets with $p_T \geq 20$ GeV and $|\eta_{det}| < 2.5$ are considered. Although the l+jets final state results in four quarks, events with three jets are not rejected as mis-reconstruction or merging of jets can origin from a process with more than three quarks.
- The leading jet is required to have $pT > 40$ GeV. This cut suppresses W+jets background with minor loss of signal events.
- At least three tracks have to be attached to the primary vertex. Furthermore, the reconstructed vertex must be within the SMT fiducial region: $|z_{PV}| < 60$ cm.

Additionally, the following cuts are imposed on the event in the e+jets channel:

- One loosely isolated electron with $p_T \geq 20$ GeV and $|\eta_{det}| < 1.1$.
- The electron must come from the primary vertex: $|\Delta z(e, PV)| < 1$ cm.

[1)] In this thesis no difference between preselection and event selection is made in the l+jets channel, as no additional cut after preselection is applied. The b-tag requirements are used to split the events, but not to cut out more events.

- For the tight data sample used for the final analysis the electron is required to fulfil the tight isolation criteria as described in section 5.3.

- In order to ensure orthogonality with the dielectron final state, events with a second tight isolated electron with $p_T \geq 15$ GeV and $|\eta_{det}| < 2.5$ are rejected. Orthogonality with the electron-muon channel is ensured by vetoing events with a tight isolated muon with $p_T > 15$ GeV and $|\eta_{det}| < 2.0$.

- The missing transverse energy must be $\not\!\!E_T > 20$ GeV.

- A so-called triangle cut is imposed on the event, which cuts out a region in the space of missing transverse energy and the polar angle between the lepton and the missing transverse energy: $\Delta\phi(e, \not\!\!E_T) > 0.7 \cdot \pi - 0.045 \cdot \not\!\!E_T$. This cut mainly rejects multijet events where a jet is mis-reconstructed as an isolated lepton, leading to low $\not\!\!E_T$ and a small polar angle.

In the μ+jets channel the requirements are:

- At least one loose isolated muon with $p_T \geq 20$ GeV and $|\eta_{det}| < 2.0$.

- The muon should originate from the primary vertex: $|\Delta z(\mu, PV)| < 1$ cm.

- For the tight data sample used for the final analysis the leading muon is required to fulfil the tight isolation criteria as described in section 5.4.

- In order to reject events from $Z \rightarrow \mu\mu$+jets, the invariant mass $m_{\mu\mu}$ of the leading muon and any other loose muon with $p_T \geq 15$ GeV and $|\eta_{det}| < 2.0$ are constructed. If $m_{\mu\mu}$ is close to the Z peak, i. e. 70 GeV $< m_{\mu\mu} <$ 110 GeV, the event is thrown away.

- Orthogonality with the dimuon channel is ensured by vetoing on events having a second muon with $p_T > 15$ GeV, $n_{seg} = 3$ and medium track quality. The orthogonality with the electron-muon channel is ensured by rejecting events with a tight isolated electron with $p_T \geq 15$ GeV and $|\eta_{det}| < 2.5$.

- The missing transverse energy has to be large: $\not\!\!E_T > 25$ GeV.

- The polar angle between the lepton and the missing transverse energy $\Delta\phi(\mu, \not\!\!E_T)$ is required to fulfil $\Delta\phi(\mu, \not\!\!E_T) > 2.1 - 0.035 \cdot \not\!\!E_T$, to reject multijet events.

In order to not contaminate the signal acceptance calculation with fake leptons, semileptonic (where one W decays to electron, muon or a leptonically decaying tau) or dileptonic (both W bosons must decay in electron, muon or tau) events are chosen on parton level. The total selection efficiency is therefore a product of the acceptance from cuts on reconstructed objects and the branching ratio of the chosen semileptonic or dileptonic decay. Taking the PDG [3] values, the branching ratios for the semileptonic $t\bar{t}$ decay in e+jets ($B = 0.1721$), in μ+jets ($B = 0.17137$) and for the dileptonic $t\bar{t}$ decay ($B = 0.10498$) can be calculated.

On Monte Carlo samples different reweightings and correction factors as presented in section 6.3 have to be applied. As the versions and methods of the reweighting functions and scale factors are a bit different for the analyses presented in this thesis, the specific factors and weights are mentioned in the corresponding sections. In Appendix C.2 the cut flow tables and efficiencies used for the measurement of the ratio of branching fractions R are shown.

7.2. Sample composition

After the event selection the sample consists of signal and different background contributions. The signal contribution are $t\bar{t}$ events, with different decays according to the performed analysis.

The background can be split into two components:

- instrumental background coming from the QCD multijet production where a jet with high electromagnetic fraction mimics an electron in the e+jets channel or a muon from heavy flavour decay within a jet appears isolated in the μ+jets channel;
- physics background originating from processes with a final state similar to the $t\bar{t}$ signal.

The dominating background in the selected sample arises from W+jets. Other physics backgrounds taken into account are single top, diboson, $Z \to \tau\tau$ production and the $Z \to \mu\mu$ ($Z \to ee$) contribution in the μ+jets (e+jets) channel. The details about the different background contributions are described in the following.

7.2.1. Instrumental background and its estimation

The contribution of the QCD multijet background is estimated from data using the Matrix Method. Two samples of events, a loose and a tight set, are needed, where the latter is a subset of the first. The loose set corresponds to the selected sample without the tight isolation requirement on the selected lepton.

Calling the number of events with a true isolated lepton, that is originating from physics backgrounds or $t\bar{t}$ signal, N^{W-like}, and the number of events with a fake isolated lepton N^{QCD}, the number of events in the loose sample, n_ℓ, and the tight sample, n_t, can be written as:

$$\begin{aligned} n_\ell &= N^{W-like} + N^{QCD} \\ n_t &= \varepsilon_{sig} N^{W-like} + \varepsilon_{qcd} N^{QCD} . \end{aligned} \tag{7.1}$$

The values for ε_{qcd} and ε_{sig}, given in Table 7.1, represent the probability for a fake and a real isolated lepton to pass the tight selection criteria, respectively.

Solving the linear system in Eq. 7.1 for N^{QCD} and N^{W-like} yields:

$$N^{W-like} = \frac{n_t - \varepsilon_{qcd} n_\ell}{\varepsilon_{sig} - \varepsilon_{qcd}} \quad \text{and} \quad N^{QCD} = \frac{\varepsilon_{sig} n_\ell - n_t}{\varepsilon_{sig} - \varepsilon_{qcd}} . \tag{7.2}$$

The efficiency ε_{qcd} is determined from data [134]. By selecting events with $\not{E}_T < 10$ GeV, but otherwise the same selection criteria as for the signal sample, the data is enriched in QCD multijet events. In this data sample no real isolated leptons are assumed to be included. The ratio of events with a tight isolated lepton over the number of events in the selected sample with loose isolated leptons yields ε_{qcd}.

The efficiency ε_{sig} for a true isolated lepton to pass the tight isolation criteria is determined from Monte Carlo samples with a true isolated lepton in the final state. The efficiency ε_{sig} is determined in the W+jets and $t\bar{t}$ samples. The final ε_{sig} is the mean of both values. Since the event kinematics of both samples is unlike, the difference of the average and the value determined purely from W+jets or $t\bar{t}$ is assigned as systematic uncertainty.

As shown above, the Matrix Method allows to determine the normalisation of the multijet background. The shape of this background is determined using the sample of events that passes the loose but fails the tight event selection, referred to as the "loose-tight" sample.

	e+jets	μ+jets
ε_{qcd}	0.20 ± 0.02(total)	0.27 ± 0.05(total)
ε_{sig} ($=1$ jet)	0.8362 ± 0.0051(stat) ± 0.0353(sys)	0.9147 ± 0.0056(stat) ± 0.0091(sys)
ε_{sig} ($=2$ jets)	0.8455 ± 0.0025(stat) ± 0.0150(sys)	0.8866 ± 0.0030(stat) ± 0.0068(sys)
ε_{sig} ($=3$ jets)	0.8480 ± 0.0026(stat) ± 0.0012(sys)	0.8732 ± 0.0030(stat) ± 0.0046(sys)
ε_{sig} (≥ 4 jets)	0.8399 ± 0.0035(stat) ± 0.0179(sys)	0.8450 ± 0.0041(stat) ± 0.0218(sys)

Table 7.1.: Efficiency for a fake and real isolated lepton to pass the tight selection criteria.

The performed analyses use b-tagging in order to enrich the data sample with $t\bar{t}$ events, as described in section 7.3. To predict the multijet background contribution after b-tagging, the Matrix Method is applied to the loose and tight samples after b-tagging in the same way as described for the sample without b-tagging requirement. The determination of the statistical uncertainty on the multijet background is discussed in detail in [135].

7.2.2. Physics background

Except for W+jets, the contributions of all physics backgrounds to the selected sample are estimated from Monte Carlo simulation, taking into account the relevant event selection and b-tagging efficiencies.

The following non-W+jets backgrounds are considered:

Diboson background WW, WZ and ZZ samples generated with PYTHIA using CTEQ6L1 PDFs. These processes are normalised to their next-to-leading order (NLO) cross sections, calculated with MCFM [136], of 12.0 pb, 3.68 pb and 1.42 pb, respectively. An uncertainty of 20% on the cross section is assigned, corresponding to half the difference between the LO and NLO prediction.

Single top production The samples for the single top production through the s- and t-channels are generated with the COMPHEP single top Monte Carlo generator [115]. The s-(t-)channel contributions are normalised with the NLO cross sections of 0.88 (1.98) pb. The uncertainty on the cross section is set to 12.5 %. The top quark mass in the single top samples is set to 175 GeV. As the single top background only represents a small contribution to the sample composition, no effects due to top mass dependencies of the single top background are considered in the analyses.

***Z*+jets backgrounds** Z+jets samples with a Z boson decaying to an electron, muon or tau pair are simulated with ALPGEN [114]. The Z boson p_T reweighting, described in section 6.3, is applied in order to achieve agreement of the simulated Z p_T distribution with the data. Additional scale factors are used for the normalisation of the Z+jets background: the Z+light jets cross section is multiplied by a k-factor and the $Z + cc$ and $Z + bb$ cross sections need an additional heavy flavour scale factor.

In the following the background contributions from diboson, single top and Z+jets are referred to as Monte Carlo backgrounds.

For the most important background in the l+jets channel, namely the W+jets background, no reliable NLO calculation exists. Therefore it is necessary to treat it differently.

The W+jets sample consists of events where one W boson is produced via an electroweak interaction, together with additional partons from QCD processes. The W+jets samples are

generated with the ALPGEN event generator, using the CTEQ6L1 parton distribution functions. The parton shower is simulated with PYTHIA.

The complete W+jets sample can be split into three subsamples according to the parton flavours: Wbb+jets, Wcc+jets and Wlp+jets. The relative contribution of these three classes of events can not be evaluated based on the cross sections provided by ALPGEN, as it does not take into account NLO corrections. Especially for Wbb+jets and Wcc+jets the NLO cross section is expected to be different from LO. The fractions of Wbb+jets and Wcc+jets are therefore multiplied by a heavy flavour scale factor of 1.17 ± 0.18 (see section 6.3.2) to achieve good agreement between the data and background model. The overall normalisation of W+jets background before b-tagging is obtained in each jet multiplicity bin by subtracting all Monte Carlo backgrounds and the $t\bar{t}$ signal from the number of signal-like events N^{W-like}, obtained from the Matrix Method. The specific formalism is discussed in Appendix B in the context of the measurement of the ratio of branching fractions R.

7.3. Event b-tag probabilities

In order to enrich the selected samples with $t\bar{t}$ events and to discriminate top decaying into heavy and light flavour quarks, b-tagging is used. The Neural Network tagging algorithm (NN Tagger), described in section 5.7, is applied to split the samples into three classes of events. In particular, into events with zero, one or at least two b-tagged jets. The number of background events with zero, one or at least two b-tags are evaluated using simulated samples. The probabilities to tag a light, c- or b-jet, calibrated to reproduce the corresponding efficiencies in data, is applied on each jet. These probabilities are parametrised in jet p_T and η and are called Tag Rate Functions (TRFs) (details can be found in section 5.7).

To account for differences in the taggability of b-, c- and light jets, a flavour correction is applied. Furthermore the standard TRFs, measured using MC processes with no significant contribution from gluon splitting, are corrected when applied on the Wbb and Wcc samples.

The event b-tagging probabilities are calculated from the per jet b-tagging efficiency $P_{jet(f)}(p_T, \eta)$ for a given flavour f by multiplying the probabilities for all jets in the event. The knowledge that a jet can be either b-tagged or not, and that the sum of the probabilities to tag zero, one and two or more jets is one, is used to calculate the event b-tagging probabilities. The probabilities to have no b-tags, exactly one b-tag and at least two b-tags in the event are determined as:

$$P^{tag}_{event}(n=0) = \prod_{i=1}^{N_{jets}} (1 - P_{jet(f_i)}(p_{T\,i}, \eta_i)) \,, \tag{7.3}$$

$$P^{tag}_{event}(n=1) = \sum_{j=1}^{N_{jets}} P_{jet(f_j)}(p_{T\,j}, \eta_j) \prod_{i=1; i\neq j}^{N_{jets}} (1 - P_{jet(f_i)}(p_{T\,i}, \eta_i)) \,, \tag{7.4}$$

and

$$P^{tag}_{event}(n \geq 2) = 1 - P^{tag}_{event}(n=0) - P^{tag}_{event}(n=1). \tag{7.5}$$

In the simultaneous measurement of the top quark pair production cross section and the ratio of branching fractions R, the event selection efficiency as well as the per event tagging probability of $t\bar{t}$ events are functions of the parameter R. For all backgrounds the event tagging probabilities P^{tag}_{event} and the event selection efficiencies are independent of R. More details can be found in section 8.

8. Simultaneous measurement of the ratio of branching fractions R and the top pair production cross section $\sigma_{t\bar{t}}$

In this chapter a simultaneous measurement of the ratio of branching fractions, $R = B(t \to Wb)/B(t \to Wq)$, with q denoting any down-type quark (d, s, or b), and the top quark pair production cross section $\sigma_{t\bar{t}}$ in the lepton plus jets channel is presented [137, 138]. A total of 0.9 fb^{-1} of $p\bar{p}$ collision data at $\sqrt{s} = 1.96$ TeV, collected with the DØ detector, are used for the measurement.

In the framework of the Standard Model, the ratio $R = B(t \to Wb)/B(t \to Wq)$ can be written as:

$$\begin{aligned} R &= \frac{B(t \to Wb)}{B(t \to Wq)} \\ &= \frac{\mid V_{tb} \mid^2}{\mid V_{tb} \mid^2 + \mid V_{ts} \mid^2 + \mid V_{td} \mid^2} \end{aligned} \tag{8.1}$$

In case of requiring unitarity the equation can be simplified to $R = \mid V_{tb} \mid^2$.

The CKM matrix element $\mid V_{tb} \mid$ is tightly constrained by unitarity constraints, $\mid V_{tb} \mid = 0.9990 - 0.9992$ [3]. This implies a restriction on R to be in the interval 0.9980-0.9984 at 90% C.L. [139]. The branching ratio expectations for the CKM-suppressed decays are $\sim 0.1\%$ for $t \to Ws$ and $\sim 0.01\%$ for $t \to Wd$. However, that severe constraint on $\mid V_{tb} \mid$ is based on two assumptions:

1. there are exactly three generations of quarks,
2. the CKM matrix is unitary.

Without the assumption of three quark generations, $\mid V_{tb} \mid$ is only restricted to be within a very wide window of $\mid V_{tb} \mid = 0.07 - 0.9993$ at 90% C.L. [139]. The measurement of the ratio R provides a model-independent way to cross-check the Standard Model expectation of $R \sim 1$ as well as the assumption of $B(t \to Wb) = 1$, which is made when measuring the $t\bar{t}$ pair production cross section. The simultaneous measurement of R and the $t\bar{t}$ cross section, in contrast to the standard measurements of $\sigma_{t\bar{t}}$, allows to extract the cross section without the assumption of $B(t \to Wb) = 1$, and to achieve a higher precision on R and $\sigma_{t\bar{t}}$ by exploiting their different sensitivity to systematic uncertainties.

The fitted excess of events in the final state $l\nu qJJq$ with respect to non-top standard model processes is interpreted as $t\bar{t}$ production. This excess is denoted here as $N(t\bar{t} \to l\nu qJJq)$ with q being the quark from the top decay and J the jet from W boson decay. With the integrated luminosity $\mathcal{L}$ and the top quark pair production cross section $\sigma(p\bar{p} \to t\bar{t})$, it can be expressed as

$$\begin{aligned} N(t\bar{t} \to l\nu qJJq) &= \\ \mathcal{L} \cdot \sigma(p\bar{p} \to t\bar{t}) &\cdot B^2(t \to Wq) \cdot 2B(W \to l\nu) B(W \to JJ) \cdot \varepsilon(t\bar{t} \to WqWq \to l\nu qJJq). \end{aligned} \tag{8.2}$$

Here $\varepsilon(t\bar{t} \to WqWq \to l\nu qJJq)$ defines the acceptance for $t\bar{t} \to WqWq \to l\nu qJJq$ events. This yields

$$\sigma(p\bar{p} \to t\bar{t}) \cdot B^2(t \to Wq) = \frac{N(t\bar{t} \to l\nu qJJq)}{L \cdot 2B(W \to l\nu)B(W \to JJ) \cdot \varepsilon(t\bar{t} \to WqWq \to l\nu qJJq)}. \tag{8.3}$$

Both quantities, $\sigma(p\bar{p} \to t\bar{t}) \cdot B^2(t \to Wq)$ and R, are fitted simultaneously to the number of $t\bar{t}$ events observed with zero, one or two b-tags in data [138]. In addition to the single and double b-tagged events, the $t\bar{t}$ contribution to the events without b-tags is estimated with a topological discriminant. This information is used as an extra constraint in the final likelihood.

In the following the top quark pair production cross section is called $\sigma(p\bar{p} \to t\bar{t}) \cdot B^2(t \to Wq)$ or $\sigma \cdot B^2$ if it is simultaneously measured with R, i. e. if no constraint on the top quark decay is assumed. In accordance to the $t\bar{t}$ cross section measured with the assumption $B(t \to Wb) = 1$, it is called $\sigma_{t\bar{t}}$ if R is fixed to one.

This chapter starts with a description of the implementation of the maximum likelihood procedure and the template fit. After that the data sample, the variables sensitive to R and the systematic uncertainties are outlined. Finally, the result will be presented and discussed.

8.1. Likelihood maximisation procedure and template fit

The extraction of $\sigma \cdot B^2$ and R is done by performing a maximum likelihood fit of the predicted to the observed number of events in all orthogonal subsamples. The l+jets sample is split into disjoint subsamples according to lepton flavour (e or μ), jet multiplicity (3 or ≥ 4 jets) and number of identified b-jets (0, 1 or ≥ 2), resulting in 12 independent data sets. As the number of observed events in each channel is independent of all other channels, the maximum likelihood can be constructed as the product of Poisson probabilities for each subsample:

$$\mathcal{L}_1 = \prod_i \mathcal{P}(n_i, \mu_i(\sigma \cdot B^2, R)) \tag{8.4}$$

where $\mathcal{P}(n, \mu)$ defines the Poisson probability to observe n events given the predicted number of events μ. In the product, i runs over all possible subsamples.

The predicted number of events per channel is the sum of signal and background contributions. The expected $t\bar{t}$ signal yield depends on the $t\bar{t}$ cross section and on the ratio of branching fractions R. As the W+jets background yield is determined with the Matrix Method before applying the b-tagging, also the number of W+jets events depends on $\sigma \cdot B^2$ and R. Therefore, in every step of the fitting procedure used to extract $\sigma \cdot B^2$ and R, the number of $t\bar{t}$ events is re-determined iteratively, and the number of W+jets background events is re-evaluated.

8.1.1. Handling of the Matrix Method in the maximum likelihood fit

The Matrix Method, described in section 7.2.1, is applied before b-tagging for the determination of the W+jets background normalisation, and after b-tagging for the determination of the multijet background in each b-tagged sample. The amount of W+jets background in the individual b-tag subsamples is then derived by using the calculated amount of W+jets events before b-tagging, multiplied with the b-tag probability in data. In contrast to W+jets, the QCD multijet background is calculated with the Matrix Method after b-tagging. Since the number of events before b-tagging is a sum of the different contributions from 0, 1 and ≥ 2 b-tagged

samples, the results of the Matrix Methods are correlated. These correlation has to be taken into account to guarantee a proper error handling.

By writing down the Matrix Method before and after b-tagging, and solving the resulting system of equations for the observables in the different b-tag subsamples for the tight (μ_t^{1tag}, μ_t^{1tag}, μ_t^{2tag}) and loose-tight ($\mu_{\ell-t}^{0tag}$, $\mu_{\ell-t}^{1tag}$, $\mu_{\ell-t}^{2tag}$) events, the problem of correlations can be resolved. In Appendix B the full derivation of the separate contributions needed in the maximum likelihood function is described. The final formula describe μ_t^{1tag}, μ_t^{1tag} and μ_t^{1tag}, μ_t^{2tag} as function of the signal and Monte Carlo background predictions and the parameters μ_t^{0tag}, $\mu_{\ell-t}^{0tag}$, $\mu_{\ell-t}^{1tag}$, $\mu_{\ell-t}^{2tag}$.

After solving the systems of equations, the final formula for the maximum likelihood can be written as a product of the Poisson constraints for loose minus tight and tight events in the different b-tag subsamples:

$$\begin{aligned}\mathcal{L}_1 \;=\; & \prod_i \mathcal{P}(n_t^{0tag}, \mu_t^{0tag}) \times \mathcal{P}(n_t^{1tag}, \mu_t^{1tag}) \times \mathcal{P}(n_t^{2tag}, \mu_t^{2tag}) \\ & \mathcal{P}(n_{\ell-t}{}^{0tag}, \mu_{\ell-t}^{0tag}) \times \mathcal{P}(n_{\ell-t}{}^{1tag}, \mu_{\ell-t}^{1tag}) \times \mathcal{P}(n_{\ell-t}^{2tag}, \mu_{\ell-t}^{2tag})\end{aligned} \tag{8.5}$$

The index i runs over the electron+3 jets, electron+4 jets, muon+3 jets and muon+4 jets channels. The number of observed events is denoted as n, in contrast to the number of expected events μ.

The maximisation of the likelihood function is done using MINUIT [140] and the errors are determined using the MINOS method [140].

8.1.2. Topological Template fit

In the measurement of R and $\sigma \cdot B^2$, a topological template in the 0 b-tagged subsample is included. A short description of the techniques to perform a stand-alone topological template fit and its inclusion in the maximum likelihood fit is given here. In section 8.4 the construction of the templates and the physics motivation will be outlined.

Considering the 0 b-tagged sample on its own, a likelihood fit to the distribution of a topological discriminant in data can be performed. The topological discriminant can be a likelihood function or a topological variable that shows separation between the considered signal and background samples. For this purpose templates in the discriminant for the $t\bar{t}$ signal and the W-like and QCD multijet backgrounds have to be determined.

In case of the l+jets channel, the relative fractions of W-like and QCD multijet background are already measured as a function of the $t\bar{t}$ cross-section by applying the Matrix Method. This means, that in a fit the number of $t\bar{t}$ ($N_t^{t\bar{t}}$) signal, W-like (N_t^W) and multijet (N_t^{QCD}) background are allowed to vary in the tight sample, but the relative fractions of W-like and multijet are constrained by the Matrix Method.

For the stand-alone fit the likelihood is defined in the following way:

$$\mathcal{L}(N_t^{t\bar{t}}, N_t^W, N_t^{QCD}) = \left[\prod_i \mathcal{P}(n_i, \mu_i)\right] \cdot \mathcal{P}(n_{\ell-t}, \mu_{\ell-t}) \tag{8.6}$$

where $\mathcal{P}(n, \mu)$ denotes the Poisson probability for n observed events given an expectation μ. The index i runs over the bins of the topological discriminant. The number n_i is the observed number of events in bin i, and μ_i is the expected number of events. μ_i is a function of signal

$N_t^{t\bar{t}}$ and backgrounds N_t^W and N_t^{QCD}:

$$\mu_i(N_t^{t\bar{t}}, N_t^W, N_t^{QCD}) = f_i^{t\bar{t}} N_t^{t\bar{t}} + f_i^W N_t^W + f_i^{QCD} N_t^{QCD} \tag{8.7}$$

where $f_i^{t\bar{t}}$, f_i^W, f_i^{QCD} are the fractions in bin i of the $t\bar{t}$, W and multijet discriminant templates. The multijet discriminant template is derived from the "loose-tight" sample. This sample has a contribution from events with real isolated leptons. In order to correct the multijet template for the contamination from $N_t^{t\bar{t}}$ and N_t^W, Eq. 8.7 is modified to [141]:

$$\begin{aligned}\mu_i(N_t^{t\bar{t}}, N_t^W, N_t^{QCD}) = \quad & (f_i^{t\bar{t}} N_t^{t\bar{t}} + f_i^W N_t^W) \cdot \left(1 - \frac{\varepsilon_{qcd}}{1-\varepsilon_{qcd}} \frac{1-\varepsilon_{sig}}{\varepsilon_{sig}}\right) \\ & + f_i^{QCD} \left[N_t^{QCD} + \frac{\varepsilon_{qcd}}{1-\varepsilon_{qcd}} \frac{1-\varepsilon_{sig}}{\varepsilon_{sig}} (N_t^W + N_t^{t\bar{t}}) \right].\end{aligned} \tag{8.8}$$

The equation for the Matrix Method can be written as:

$$\begin{aligned}\mu_\ell &= N_\ell^{t\bar{t}} + N_\ell^W + N_\ell^{QCD} \\ \mu_t &= \varepsilon_{sig} N_\ell^{t\bar{t}} + \varepsilon_{sig} N_\ell^{W+} + \varepsilon_{qcd} N_\ell^{QCD}\end{aligned} \tag{8.9}$$

As the number of loose events μ_ℓ is split into the independent samples $\mu_{\ell-t}$ and μ_t, the equation has to be rewritten in order to get uncorrelated samples. By expressing the number of signal and background events in the tight sample as $N_t^{t\bar{t}} = \varepsilon_{sig} N_\ell^{t\bar{t}}$, $N_t^W = \varepsilon_{sig} N_\ell^W$, and $N_t^{QCD} = \varepsilon_{qcd} N_\ell^{QCD}$, the first equation in Eq. 8.9 becomes:

$$\mu_{\ell-t} = \frac{1-\varepsilon_{sig}}{\varepsilon_{sig}} N_t^{t\bar{t}} + \frac{1-\varepsilon_{sig}}{\varepsilon_{sig}} N_t^W + \frac{1-\varepsilon_{qcd}}{\varepsilon_{qcd}} N_t^{QCD} \tag{8.10}$$

Taking the logarithm of Eq. 8.6 and neglecting constant terms yields:

$$-\log L(N_t^{t\bar{t}}, N_t^W, N_t^{QCD}) = \sum_i -n_i \log \mu_i + \mu_i - n_{\ell-t} \log \mu_{\ell-t} + \mu_{\ell-t} \tag{8.11}$$

where μ_i and $\mu_{\ell-t}$ are functions of $N_t^{t\bar{t}}$, N_t^W and N_t^{QCD} as given by Eq. 8.7 and 8.10, respectively.

The described likelihood function is implemented in the maximum likelihood fit of $\sigma \cdot B^2$ and R. The term $\mathcal{P}(n_t^{0tag}, \mu_t^{0tag})$ in Eq. 8.5 is replaced by the first term in Eq. 8.6, namely

$$\prod_{j=1}^{B} \mathcal{P}(n_j, \mu_j) \tag{8.12}$$

where the index j runs over the bins of the topological discriminant and B is the total number of bins. The predicted number of events per bin μ_j is calculated as given in Eq. 8.9, where $f_j^{t\bar{t}}$ from Eq. 8.19 is inserted.

The final likelihood used for the simultaneous measurement of $\sigma \cdot B^2$ and R can therefore be written as

$$\begin{aligned}\mathcal{L}_1 = \prod_i \Bigg(& \prod_{j=1}^{10} \mathcal{P}(n_j, \mu_j)_i \times \mathcal{P}(n_t^{1tag}, \mu_t^{1tag})_i \times \mathcal{P}(n_t^{2tag}, \mu_t^{2tag})_i \\ & \times \mathcal{P}(n_{\ell-t}{}^{0tag}, \mu_{\ell-t}^{0tag})_i \times \mathcal{P}(n_{\ell-t}{}^{1tag}, \mu_{\ell-t}^{1tag})_i \times \mathcal{P}(n_{\ell-t}{}^{2tag}, \mu_{\ell-t}^{2tag})_i \Bigg)\end{aligned} \tag{8.13}$$

Triggerlist Version	Trigger name	Integrated luminosity [pb^{-1}]
V8.0 - V9.0	EM15_2JT15	4.86
V9.0 - V10.0	EM15_2JT15	24.73
V10.0 - V11.0	EM15_2JT15	9.81
V11.0 - V12.0	EM15_2JT15	62.82
V12.0 - V13.0	E1_SHT15_2J20	227.14
V13.0 - V13.3	E1_SHT15_2J_J25	54.81
V13.3 - V14.0	E1_SHT15_2J_J30	294.27
V14.0 - V15.0	E1_SHT15_2J_J25	234.11
TOTAL		912.55

Table 8.1.: Integrated luminosity collected with the e+jets trigger and the trigger list version. For the Run IIa dataset from August 2002 to December 2005.

8.2. Data sample, Monte Carlo samples and predicted yields

The data sample used for the measurement of R and $\sigma \cdot B^2$ was collected between August 2002 and December 2005, with run numbers 151,817- 213,063. The selection of the data and Monte Carlo samples is done with the package top_cafe [142]. Tables 8.1 and 8.2 list the trigger versions and the integrated luminosity. Details about the triggers are given in section 6.

The simulation of the $t\bar{t}$ signal samples with various decays of the top quark is done with PYTHIA v6.323 [113]. The Parton Distribution Function is set to CTEQ6L1, the factorisation scale is set to $m_t^2 + \sum p_T^2$(jets). The different decays of the $t\bar{t}$ system, namely $t\bar{t} \rightarrow WbW\bar{b}$, $t\bar{t} \rightarrow WbW\bar{q}_l$ and $t\bar{t} \rightarrow Wq_lW\bar{q}_l$, with q_l being a light s- or d-quark, are generated simultaneously. In the simulation, the probability for top quarks to decay to b, s and d quarks is set to equal values of $33.\bar{3}$ %. After the simulation, the events are separated into $t\bar{t} \rightarrow WbW\bar{b}$, $t\bar{t} \rightarrow WbW\bar{q}_l$ and $t\bar{t} \rightarrow Wq_lW\bar{q}_l$ subsamples using the Monte Carlo truth information of the top-decay products. All events are passed through a full DØ detector simulation and overlaid with zero-bias data. Due to the small probability to get $t\bar{t} \rightarrow WbW\bar{b}$ decays when setting all branching fractions to the same value, the standard $t\bar{t}$ sample, where $B(t \rightarrow Wb)$ is set to 100%, is used for this particular decay channel. To evaluate the dependence of the signal acceptance on the top quark mass $t\bar{t}$ samples generated at top quark masses of 165, 170, 175 and 180 GeV are studied.

The various instrumental and physics backgrounds are discussed in detail in section 7.2. The tight data sample and the number of multijet events N_{qcd}, together with the number of W-like events N_{W-like}, calculated from the Matrix Method, are shown in Table 8.3.

The different physics backgrounds and the used cross sections and scale factors are discussed in section 7.2.2. Additionally, for the Z+jets background, the Z+light jets cross section is multiplied by a factor of 1.23 and the Zcc and Zbb cross sections by a factor of 1.66, corresponding to the product of the k-factor of 1.23 and an additional heavy flavour scale factor of 1.35 [143]. A relative uncertainty of 50 % is assigned on the heavy flavour scale factor and 15 % on the light scale factor for the Z+jets background.

The b-tagging is done with the medium NN tagger. A looser b-tag working point is avoided due to the dependence of the W+jets heavy flavour scale factor. The performance of the measurement with tighter working points has been checked on pseudo-experiments without systematic uncertainties included. The statistical uncertainty on the fitted $\sigma \cdot B^2$ and R come out similar for the medium and tight working point. As the medium NN working point shows a smaller uncertainties and has been chosen by other measurements, it is chosen for

Triggerlist Version	Trigger name	Integrated luminosity [pb^{-1}]
V8.0 - V9.0	MU_JT20_L2M0	5.64
V9.0 - V10.0	MU_JT20_L2M0	24.77
V10.0 - V11.0	MU_JT20_L2M0	10.70
V11.0 - V12.0	MU_JT20_L2M0	65.24
V12.0 - V13.0	MU_JT25_L2M0	230.93
V13.0 - V13.2	MUJ2_JT25	31.43
V13.2 - V13.3	MUJ2_JT25_LM3	16.10
V13.3 - V14.0	MUJ2_JT30_LM3	252.17
V14.0 - V14.2	MUJ1_JT25_LM3	0.01
V14.2 - V14.3	MUJ1_JT25_ILM3	20.84
V14.3 - V15.0	MUJ1_JT35_LM3	213.51
TOTAL		871.34

Table 8.2.: Integrated luminosity collected with the μ+jets trigger and the trigger list version. For the Run IIa dataset from August 2002 to December 2005.

jets	Channel	n_ℓ	n_t	N_{qcd}	N_{W-like}
$= 3$	e+jets	2592	1300	277.17 ± 37.52	1022.85 ± 53.20
	μ+jets	1389	1120	41.57 ± 13.35	1078.40 ± 37.75
≥ 4	e+jets	618	320	62.22 ± 9.54	257.78 ± 21.05
	μ+jets	388	306	10.26 ± 5.97	295.74 ± 19.65

Table 8.3.: Numbers of data events in the loose and tight samples and W-like and multijet background contributions in the tight sample before b-tagging obtained from the Matrix Method.

the analysis. In addition, the fit is also performed using the tight working point and compared to the result with medium working point.

Tables 8.4 to 8.11 show the predicted and observed number of events in the e+jets and μ+jets channel. The $t\bar{t}$ cross section is set to 6.8 pb and $R = 1$. The prediction and observation before and after applying the b-tagging are shown for the subsamples with 1, 2, 3 and ≥ 4 jets. The uncertainties for all but the multijet background contribution are statistical only. The uncertainties on the multijet background includes the uncertainties on ε_{sig} and ε_{qcd}. The Z+jets background is split into different contributions according to the Z boson decay ($Z \to ee$, $Z \to \mu\mu$ and $Z \to \tau\tau$) and their jet heavy flavour content. In the tables they are denoted as $Z(ee)bb$, $Z(ee)cc$, $Z(ee)lp$, $Z(\mu\mu)bb$, $Z(\mu\mu)cc$, $Z(\mu\mu)lp$, $Z(\tau\tau)bb$, $Z(\tau\tau)cc$ and $Z(\tau\tau)lp$. The different flavour components of the W+jets background are also shown separately to see the change in the light and heavy flavour contribution before and after b-tagging. The single top s-channel (t-channel) contribution is denoted tb (tqb). The signal component coming from the $t\bar{t}$ semileptonic and dileptonic final states is shown as $ttlj$ and $ttll$, respectively. The sum represents the expected $t\bar{t}$ signal plus background contributions. Due to the normalisation of W+jets to data the sum is equal to the number of observed events before b-tagging.

In Appendix C Monte Carlo to data comparisons as well as the cut flow table for all $t\bar{t}$ signal Monte Carlo samples are shown. The cut flow tables contain the correction factors that need to be applied to correct the Monte Carlo for trigger efficiency, lepton identification and b-fragmentation. Comparing for example Tables C.1, C.2 and C.3 it can be recognised that the $t\bar{t}$ samples with light quarks from top decay pass the cut on the jet p_T with higher efficiency than the $t\bar{t}$ samples with b quarks from top decay, resulting in higher event selection efficiencies

for the $t\bar{t} \to Wq_\ell Wq_\ell$ compared to the $t\bar{t} \to WbWb$ sample.

Contribution	== 1 Jets	== 2 Jets	== 3 Jets	>= 4 Jets
Data	15863.00 ± 125.95	6043.00 ± 77.74	1300.00 ± 36.06	320.00 ± 17.89
Multijet	900.81 ± 230.83	846.18 ± 115.81	277.15 ± 37.52	62.22 ± 9.54
WW	118.89 ± 0.71	160.08 ± 0.84	34.44 ± 0.39	5.96 ± 0.17
WZ	16.89 ± 0.32	27.16 ± 0.41	6.35 ± 0.20	1.26 ± 0.09
Wbb	311.25 ± 3.77	203.40 ± 2.87	51.05 ± 1.11	8.75 ± 0.29
Wcc	951.41 ± 9.74	542.94 ± 6.30	121.84 ± 2.32	16.73 ± 0.60
Wlp	13224.61 ± 65.63	3861.19 ± 26.94	565.15 ± 6.44	73.92 ± 1.61
ZZ	1.40 ± 0.06	1.68 ± 0.06	1.02 ± 0.05	0.26 ± 0.03
$Z(ee)bb$	10.18 ± 0.36	11.75 ± 0.38	5.26 ± 0.28	1.50 ± 0.15
$Z(\tau\tau)bb$	3.13 ± 0.22	2.77 ± 0.15	1.32 ± 0.10	0.46 ± 0.04
$Z(ee)cc$	16.22 ± 0.92	18.09 ± 0.90	8.32 ± 0.55	2.28 ± 0.26
$Z(\tau\tau)cc$	6.26 ± 0.64	6.02 ± 0.57	2.46 ± 0.31	0.80 ± 0.15
$Z(ee)lp$	187.88 ± 3.51	180.39 ± 3.25	51.56 ± 1.20	14.13 ± 0.50
$Z(\tau\tau)lp$	78.18 ± 2.12	47.74 ± 1.32	15.28 ± 0.58	4.87 ± 0.28
tb	5.23 ± 0.08	14.36 ± 0.13	4.21 ± 0.07	0.87 ± 0.03
tbq	12.69 ± 0.14	26.48 ± 0.21	8.98 ± 0.13	2.18 ± 0.07
ttlj	4.89 ± 0.16	48.09 ± 0.52	124.43 ± 0.83	119.12 ± 0.82
ttll	13.17 ± 0.27	44.67 ± 0.50	21.17 ± 0.34	4.71 ± 0.16
sum	15863.08 ± 240.24	6042.98 ± 119.16	1300.00 ± 38.20	320.00 ± 9.76

Table 8.4.: Number of events for e+jets after event selection and with no b-tag requirement. The sum of all predicted events is constraint to be the same as the Data.

Contribution	== 1 Jets	== 2 Jets	== 3 Jets	>= 4 Jets
Data	15452.00 ± 124.31	5631.00 ± 75.04	1095.00 ± 33.09	206.00 ± 14.35
Multijet	870.72 ± 224.49	790.19 ± 108.22	250.92 ± 34.07	54.79 ± 8.39
WW	114.59 ± 0.69	150.00 ± 0.79	31.69 ± 0.36	5.27 ± 0.15
WZ	15.11 ± 0.28	23.08 ± 0.35	5.39 ± 0.17	1.09 ± 0.08
Wbb	214.52 ± 2.72	117.41 ± 1.69	27.08 ± 0.58	4.57 ± 0.16
Wc	0.00 ± 0.00	0.00 ± 0.00	0.00 ± 0.00	0.00 ± 0.00
Wcc	891.14 ± 8.99	484.42 ± 5.48	105.46 ± 1.99	14.02 ± 0.50
Wlp	13038.26 ± 64.73	3781.10 ± 26.45	549.72 ± 6.28	71.33 ± 1.56
ZZ	1.30 ± 0.05	1.42 ± 0.05	0.83 ± 0.04	0.19 ± 0.02
$Z(ee)bb$	8.15 ± 0.30	7.19 ± 0.26	2.81 ± 0.16	0.74 ± 0.08
$Z(\tau\tau)bb$	1.98 ± 0.13	1.60 ± 0.09	0.70 ± 0.06	0.22 ± 0.02
$Z(ee)cc$	15.46 ± 0.87	16.42 ± 0.81	7.25 ± 0.48	1.94 ± 0.22
$Z(\tau\tau)cc$	5.77 ± 0.58	5.22 ± 0.48	2.14 ± 0.28	0.66 ± 0.12
$Z(ee)lp$	186.34 ± 3.48	177.69 ± 3.21	50.45 ± 1.17	13.71 ± 0.49
$Z(\tau\tau)lp$	77.40 ± 2.10	46.97 ± 1.30	14.94 ± 0.56	4.72 ± 0.27
tb	2.70 ± 0.04	4.61 ± 0.05	1.29 ± 0.03	0.26 ± 0.01
tbq	7.62 ± 0.09	13.81 ± 0.12	3.92 ± 0.06	0.81 ± 0.03
ttlj	3.28 ± 0.12	22.34 ± 0.27	44.23 ± 0.34	35.22 ± 0.28
ttll	6.83 ± 0.15	15.14 ± 0.20	6.58 ± 0.13	1.43 ± 0.06
sum	15461.19 ± 233.87	5658.61 ± 111.61	1105.38 ± 34.74	210.95 ± 8.58

Table 8.5.: Number of events for e+jets in the 0 b-tag subsample.

Contribution	== 1 Jets	== 2 Jets	== 3 Jets	>= 4 Jets
Data	411.00 ± 20.27	373.00 ± 19.31	164.00 ± 12.81	88.00 ± 9.38
Multijet	30.09 ± 7.44	54.72 ± 8.62	23.71 ± 4.27	6.62 ± 2.04
WW	4.29 ± 0.05	9.98 ± 0.08	2.67 ± 0.05	0.62 ± 0.03
WZ	1.78 ± 0.08	3.27 ± 0.10	0.79 ± 0.05	0.14 ± 0.02
Wbb	96.72 ± 1.53	74.83 ± 1.27	20.20 ± 0.51	3.44 ± 0.13
Wc	0.00 ± 0.00	0.00 ± 0.00	0.00 ± 0.00	0.00 ± 0.00
Wcc	60.26 ± 1.01	56.70 ± 0.97	15.66 ± 0.38	2.54 ± 0.11
Wlp	186.35 ± 1.97	79.72 ± 0.84	15.29 ± 0.24	2.56 ± 0.07
ZZ	0.10 ± 0.01	0.22 ± 0.02	0.15 ± 0.01	0.05 ± 0.01
$Z(ee)bb$	2.03 ± 0.12	4.19 ± 0.16	2.09 ± 0.12	0.62 ± 0.07
$Z(\tau\tau)bb$	1.14 ± 0.10	1.05 ± 0.07	0.53 ± 0.04	0.20 ± 0.02
$Z(ee)cc$	0.76 ± 0.08	1.64 ± 0.11	1.03 ± 0.09	0.31 ± 0.05
$Z(\tau\tau)cc$	0.48 ± 0.07	0.78 ± 0.09	0.31 ± 0.05	0.13 ± 0.03
$Z(ee)lp$	1.54 ± 0.03	2.68 ± 0.05	1.11 ± 0.03	0.41 ± 0.02
$Z(\tau\tau)lp$	0.79 ± 0.02	0.77 ± 0.02	0.34 ± 0.01	0.15 ± 0.01
tb	2.53 ± 0.04	6.84 ± 0.06	2.00 ± 0.03	0.41 ± 0.02
tbq	5.07 ± 0.07	12.13 ± 0.10	4.15 ± 0.06	1.02 ± 0.03
ttlj	1.62 ± 0.07	21.89 ± 0.25	58.30 ± 0.40	54.98 ± 0.38
ttll	6.34 ± 0.14	21.22 ± 0.24	10.02 ± 0.17	2.21 ± 0.08
sum	401.89 ± 7.92	352.62 ± 8.82	158.35 ± 4.35	76.41 ± 2.09

Table 8.6.: Number of events for e+jets in the 1 b-tag subsample.

Contribution	== 1 Jets	== 2 Jets	== 3 Jets	>= 4 Jets
Data	0.00 ± 0.00	39.00 ± 6.24	41.00 ± 6.40	26.00 ± 5.10
Multijet	0.00 ± 0.00	1.28 ± 0.99	2.53 ± 1.17	0.80 ± 0.81
WW	0.00 ± 0.00	0.10 ± 0.01	0.08 ± 0.01	0.07 ± 0.01
WZ	0.00 ± 0.00	0.81 ± 0.04	0.18 ± 0.02	0.03 ± 0.01
Wbb	0.00 ± 0.00	11.15 ± 0.37	3.77 ± 0.19	0.74 ± 0.05
Wc	0.00 ± 0.00	0.00 ± 0.00	0.00 ± 0.00	0.00 ± 0.00
Wcc	0.00 ± 0.00	1.82 ± 0.06	0.72 ± 0.03	0.17 ± 0.01
Wlp	0.00 ± 0.00	0.37 ± 0.01	0.14 ± 0.00	0.04 ± 0.00
ZZ	0.00 ± 0.00	0.04 ± 0.01	0.04 ± 0.01	0.02 ± 0.00
$Z(ee)bb$	0.00 ± 0.00	0.37 ± 0.03	0.36 ± 0.03	0.15 ± 0.02
$Z(\tau\tau)bb$	-0.00 ± 0.00	0.11 ± 0.02	0.10 ± 0.01	0.05 ± 0.01
$Z(ee)cc$	0.00 ± 0.00	0.03 ± 0.00	0.04 ± 0.01	0.02 ± 0.01
$Z(\tau\tau)cc$	-0.00 ± 0.00	0.02 ± 0.01	0.02 ± 0.00	0.01 ± 0.00
$Z(ee)lp$	-0.00 ± 0.00	0.01 ± 0.00	0.01 ± 0.00	0.01 ± 0.00
$Z(\tau\tau)lp$	0.00 ± 0.00	0.00 ± 0.00	0.00 ± 0.00	0.00 ± 0.00
tb	-0.00 ± 0.00	2.91 ± 0.03	0.92 ± 0.02	0.20 ± 0.01
tbq	0.00 ± 0.00	0.54 ± 0.02	0.91 ± 0.02	0.35 ± 0.01
ttlj	0.00 ± 0.00	3.85 ± 0.07	21.89 ± 0.19	28.92 ± 0.23
ttll	0.00 ± 0.00	8.31 ± 0.11	4.56 ± 0.09	1.07 ± 0.04
sum	0.00 ± 0.00	31.74 ± 1.07	36.27 ± 1.20	32.63 ± 0.84

Table 8.7.: Number of events for e+jets in the ≥ 2 b-tag subsample.

Contribution	== 1 Jets	== 2 Jets	== 3 Jets	>= 4 Jets
Data	13472.00 ± 116.07	5191.00 ± 72.05	1120.00 ± 33.47	306.00 ± 17.49
Multijet	214.78 ± 87.67	131.63 ± 41.65	41.57 ± 13.35	10.26 ± 5.97
WW	88.81 ± 0.58	129.67 ± 0.71	28.36 ± 0.34	5.05 ± 0.14
WZ	14.67 ± 0.28	26.19 ± 0.38	6.26 ± 0.19	1.10 ± 0.08
Wbb	246.75 ± 3.22	192.64 ± 2.82	56.54 ± 1.31	13.16 ± 0.45
Wcc	768.63 ± 8.33	509.29 ± 6.05	137.28 ± 2.67	23.83 ± 0.89
Wlp	11131.49 ± 58.09	3715.22 ± 25.71	625.21 ± 7.14	117.55 ± 2.54
ZZ	2.11 ± 0.07	3.61 ± 0.09	1.13 ± 0.05	0.26 ± 0.02
$Z(\mu\mu)bb$	26.87 ± 0.54	18.05 ± 0.46	5.87 ± 0.27	1.72 ± 0.15
$Z(\tau\tau)bb$	2.00 ± 0.17	1.63 ± 0.11	0.73 ± 0.06	0.28 ± 0.03
$Z(\mu\mu)cc$	58.55 ± 1.73	36.40 ± 1.15	11.36 ± 0.56	3.37 ± 0.30
$Z(\tau\tau)cc$	4.19 ± 0.51	3.66 ± 0.44	1.54 ± 0.23	0.48 ± 0.11
$Z(\mu\mu)lp$	820.32 ± 7.98	287.61 ± 3.35	74.48 ± 1.24	19.59 ± 0.56
$Z(\tau\tau)lp$	68.60 ± 1.97	40.20 ± 1.25	9.79 ± 0.45	3.17 ± 0.22
tb	3.45 ± 0.07	11.16 ± 0.12	3.52 ± 0.07	0.74 ± 0.03
tbq	9.39 ± 0.11	20.63 ± 0.17	6.66 ± 0.10	1.69 ± 0.05
ttlj	2.64 ± 0.12	29.60 ± 0.39	92.45 ± 0.69	99.88 ± 0.72
ttll	8.81 ± 0.21	33.81 ± 0.41	17.27 ± 0.30	3.87 ± 0.14
sum	13472.05 ± 105.89	5191.00 ± 49.55	1120.00 ± 15.52	306.00 ± 6.65

Table 8.8.: Number of events for μ+jets after event selection and with no b-tag requirement. The sum of all predicted events is constraint to be the same as the Data.

Contribution	== 1 Jets	== 2 Jets	== 3 Jets	>= 4 Jets
Data	13148.00 ± 114.66	4865.00 ± 69.75	955.00 ± 30.90	183.00 ± 13.53
Multijet	204.27 ± 69.45	114.93 ± 27.52	36.50 ± 8.86	12.07 ± 4.39
WW	85.40 ± 0.56	121.35 ± 0.66	26.01 ± 0.31	4.50 ± 0.13
WZ	13.11 ± 0.25	22.62 ± 0.33	5.28 ± 0.16	0.90 ± 0.07
Wbb	168.85 ± 2.31	108.25 ± 1.61	29.78 ± 0.69	6.67 ± 0.23
Wc	0.00 ± 0.00	0.00 ± 0.00	0.00 ± 0.00	0.00 ± 0.00
Wcc	720.46 ± 7.70	455.49 ± 5.28	117.66 ± 2.26	19.74 ± 0.74
Wlp	10978.07 ± 57.30	3634.95 ± 25.19	608.01 ± 6.95	113.29 ± 2.45
ZZ	1.88 ± 0.06	3.06 ± 0.08	0.92 ± 0.04	0.20 ± 0.02
$Z(\mu\mu)bb$	17.80 ± 0.40	10.00 ± 0.28	2.92 ± 0.15	0.84 ± 0.08
$Z(\tau\tau)bb$	1.18 ± 0.09	0.92 ± 0.07	0.35 ± 0.03	0.12 ± 0.01
$Z(\mu\mu)cc$	54.29 ± 1.58	32.02 ± 1.00	9.72 ± 0.48	2.75 ± 0.25
$Z(\tau\tau)cc$	3.87 ± 0.46	3.21 ± 0.38	1.29 ± 0.19	0.40 ± 0.09
$Z(\mu\mu)lp$	813.50 ± 7.91	283.56 ± 3.31	72.95 ± 1.22	19.03 ± 0.55
$Z(\tau\tau)lp$	67.88 ± 1.95	39.54 ± 1.22	9.56 ± 0.44	3.07 ± 0.21
tb	1.77 ± 0.04	3.46 ± 0.04	1.06 ± 0.02	0.22 ± 0.01
tbq	5.58 ± 0.07	10.60 ± 0.09	2.83 ± 0.05	0.61 ± 0.02
ttlj	1.77 ± 0.08	13.63 ± 0.20	31.52 ± 0.27	28.47 ± 0.24
ttll	4.42 ± 0.11	11.02 ± 0.16	5.16 ± 0.10	1.12 ± 0.05
sum	13144.11 ± 90.78	4868.58 ± 37.90	961.50 ± 11.60	213.99 ± 5.14

Table 8.9.: Number of events for μ+jets in the 0 b-tag subsample.

Contribution	== 1 Jets	== 2 Jets	== 3 Jets	>= 4 Jets
Data	324.00 ± 18.00	300.00 ± 17.32	130.00 ± 11.40	91.00 ± 9.54
Multijet	10.65 ± 3.71	16.56 ± 4.57	4.35 ± 2.37	0.00 ± 2.03
WW	3.41 ± 0.04	8.25 ± 0.07	2.27 ± 0.04	0.51 ± 0.02
WZ	1.56 ± 0.07	2.91 ± 0.09	0.78 ± 0.04	0.16 ± 0.02
Wbb	77.89 ± 1.35	73.41 ± 1.29	22.25 ± 0.60	5.27 ± 0.20
Wc	0.00 ± 0.00	0.00 ± 0.00	0.00 ± 0.00	0.00 ± 0.00
Wcc	48.16 ± 0.86	52.25 ± 0.91	18.55 ± 0.47	3.80 ± 0.17
Wlp	153.29 ± 1.67	79.78 ± 0.87	17.02 ± 0.26	4.20 ± 0.12
ZZ	0.23 ± 0.02	0.44 ± 0.02	0.17 ± 0.01	0.04 ± 0.01
$Z(\mu\mu)bb$	9.06 ± 0.22	7.10 ± 0.20	2.44 ± 0.12	0.71 ± 0.07
$Z(\tau\tau)bb$	0.82 ± 0.09	0.63 ± 0.06	0.31 ± 0.03	0.12 ± 0.01
$Z(\mu\mu)cc$	4.27 ± 0.19	4.21 ± 0.18	1.55 ± 0.10	0.57 ± 0.06
$Z(\tau\tau)cc$	0.32 ± 0.06	0.43 ± 0.07	0.23 ± 0.04	0.08 ± 0.02
$Z(\mu\mu)lp$	6.82 ± 0.08	4.04 ± 0.05	1.52 ± 0.03	0.55 ± 0.02
$Z(\tau\tau)lp$	0.71 ± 0.02	0.66 ± 0.02	0.22 ± 0.01	0.10 ± 0.01
tb	1.68 ± 0.03	5.33 ± 0.06	1.66 ± 0.03	0.35 ± 0.02
tbq	3.81 ± 0.05	9.61 ± 0.09	3.10 ± 0.05	0.79 ± 0.03
ttlj	0.86 ± 0.05	13.55 ± 0.19	43.45 ± 0.33	46.01 ± 0.34
ttll	4.39 ± 0.11	16.05 ± 0.20	8.17 ± 0.14	1.82 ± 0.07
sum	327.94 ± 4.39	295.21 ± 4.93	128.08 ± 2.53	65.07 ± 2.08

Table 8.10.: Number of events for μ+jets in the 1 b-tag subsample.

Contribution	== 1 Jets	== 2 Jets	== 3 Jets	>= 4 Jets
Data	0.00 ± 0.00	26.00 ± 5.10	35.00 ± 5.92	32.00 ± 5.66
Multijet	0.00 ± 0.00	0.26 ± 0.82	0.75 ± 1.10	0.00 ± 0.92
WW	0.00 ± 0.00	0.07 ± 0.00	0.08 ± 0.01	0.05 ± 0.01
WZ	-0.00 ± 0.00	0.67 ± 0.04	0.20 ± 0.02	0.05 ± 0.01
Wbb	0.00 ± 0.00	10.98 ± 0.38	4.51 ± 0.23	1.22 ± 0.08
Wc	0.00 ± 0.00	0.00 ± 0.00	0.00 ± 0.00	0.00 ± 0.00
Wcc	0.00 ± 0.00	1.54 ± 0.06	1.06 ± 0.06	0.29 ± 0.03
Wlp	0.00 ± 0.00	0.39 ± 0.01	0.15 ± 0.00	0.06 ± 0.00
ZZ	-0.00 ± 0.00	0.11 ± 0.01	0.04 ± 0.01	0.01 ± 0.00
$Z(\mu\mu)bb$	-0.00 ± 0.00	0.96 ± 0.05	0.51 ± 0.04	0.17 ± 0.02
$Z(\tau\tau)bb$	-0.00 ± 0.00	0.07 ± 0.01	0.07 ± 0.01	0.03 ± 0.01
$Z(\mu\mu)cc$	0.00 ± 0.00	0.16 ± 0.02	0.09 ± 0.01	0.05 ± 0.01
$Z(\tau\tau)cc$	-0.00 ± 0.00	0.01 ± 0.00	0.01 ± 0.00	0.01 ± 0.00
$Z(\mu\mu)lp$	0.00 ± 0.00	0.01 ± 0.00	0.01 ± 0.00	0.01 ± 0.00
$Z(\tau\tau)lp$	-0.00 ± 0.00	0.00 ± 0.00	0.00 ± 0.00	0.00 ± 0.00
tb	0.00 ± 0.00	2.38 ± 0.03	0.80 ± 0.02	0.17 ± 0.01
tbq	0.00 ± 0.00	0.42 ± 0.01	0.73 ± 0.02	0.29 ± 0.01
ttlj	0.00 ± 0.00	2.42 ± 0.06	17.48 ± 0.17	25.40 ± 0.21
ttll	-0.00 ± 0.00	6.74 ± 0.10	3.94 ± 0.08	0.93 ± 0.04
sum	0.00 ± 0.00	27.21 ± 0.92	30.42 ± 1.14	28.75 ± 0.95

Table 8.11.: Number of events for μ+jets in the ≥ 2 b-tag subsample.

8.3. Acceptance and b-tag probability as function of R

The total efficiency for a $t\bar{t}$ event to be selected and b-tagged is the product of the selection efficiency and the b-tag probability. Both depend on the top quark decay into b, s or d quarks.

The event selection and event b-tagging probabilities for the three following decays are derived separately:

- $t\bar{t} \rightarrow WbW\bar{b}$ (further will be referred to as $t\bar{t} \rightarrow bb$ or $t\bar{t} \rightarrow WbWb$)
- $t\bar{t} \rightarrow WbW\bar{q}_\ell$ ($t\bar{t} \rightarrow bq_\ell$ or $t\bar{t} \rightarrow WbWq$) and charged conjugate
- $t\bar{t} \rightarrow Wq_\ell W\bar{q}_\ell$ ($t\bar{t} \rightarrow q_\ell q_\ell$ or $t\bar{t} \rightarrow WqWq$) and charged conjugate,

where q_ℓ is a light down-type quark ($\ell = d$ or s). In the analysis no difference is made between d and s quarks.

The total $t\bar{t}$ acceptance $P_p(t\bar{t})$ can be written as

$$P_p(t\bar{t}) = R^2 P_p(t\bar{t} \rightarrow bb) + 2R(1-R)P_p(t\bar{t} \rightarrow bq_\ell) + (1-R)^2 P_p(t\bar{t} \rightarrow q_\ell q_\ell), \tag{8.14}$$

where P_p denotes the event selection efficiency. Due to the different mass of the quark originating from the top quark decay, the $t\bar{t}$ event selection efficiency is expected to show a small dependence on R.

Figures 8.1 and 8.2 show the event selection efficiency as function of R in the individual l+jets channels for the semileptonic final state $t\bar{t} \rightarrow lj$ and the dileptonic contribution $t\bar{t} \rightarrow ll$, respectively. As expected, the selection efficiency is almost independent from R, confirming that the flavour of the quark from top quark decay has only marginal influence on the $t\bar{t}$ event kinematics.

The probability to have 0, 1 or $\geq$ 2 b-tags in a $t\bar{t}$ event depends on the flavour of the jets coming from the top quark decays. A decay of the top quark into d and s quarks results in a significantly smaller event b-tag probability compared to samples with top quarks decaying into b quarks.

Since R is the fraction of top quarks decaying into a b quark and a W-boson, the inclusive $t\bar{t}$ event b-tagging probability can be written in a similar form as the total $t\bar{t}$ acceptance:

$$P_b(t\bar{t}) = R^2 P_b(t\bar{t} \rightarrow b\bar{b}) + 2R(1-R)P_b(t\bar{t} \rightarrow b\bar{q}_\ell) + (1-R)^2 P_b(t\bar{t} \rightarrow q_\ell \bar{q}_\ell), \tag{8.15}$$

where P_b describes the event tagging probability of the considered decay. The determination of P_b for 0, 1 and ≥ 2 tags is described in section 7.3, Eqs. 7.3, 7.4 and 7.5, respectively.

Figures 8.3 and 8.4 show the event b-tagging probabilities as function of R in the e+jets and μ+jets channels with 3 or at least 4 jets for $t\bar{t} \rightarrow lj$ and $t\bar{t} \rightarrow ll$, respectively. The event tagging probabilities for exactly one b-tag, and for two or more b-tags, are given in Tables 8.12 and 8.13, respectively. The distribution of the $t\bar{t}$ events between the 0, 1 and $\geq$ 2 b-tagged samples implies the main sensitivity on the observable R. Figure 8.5 illustrates the change of the predicted yields in the samples with 0, 1 and ≥ 2 b-tagged for various values of R. Larger values of R result in an increase of $t\bar{t}$ events in the 0 b-tagged sample.

To calculate the yield after b-tagging, the total efficiency as a function of R is calculated as a product of the event selection and b-tagging efficiencies:

$$\begin{aligned} P_{total}(t\bar{t}) \;=\; & R^2 P_p(t\bar{t} \rightarrow bb) P_b(t\bar{t} \rightarrow bb) + 2R(1-R)P_p(t\bar{t} \rightarrow bq_\ell) P_b(t\bar{t} \rightarrow bq_\ell) + \\ & + (1-R)^2 P_p(t\bar{t} \rightarrow q_\ell q_\ell) P_b(t\bar{t} \rightarrow q_\ell q_\ell), \end{aligned} \tag{8.16}$$

with P_b describing the tagging probability and P_p the event selection efficiency.

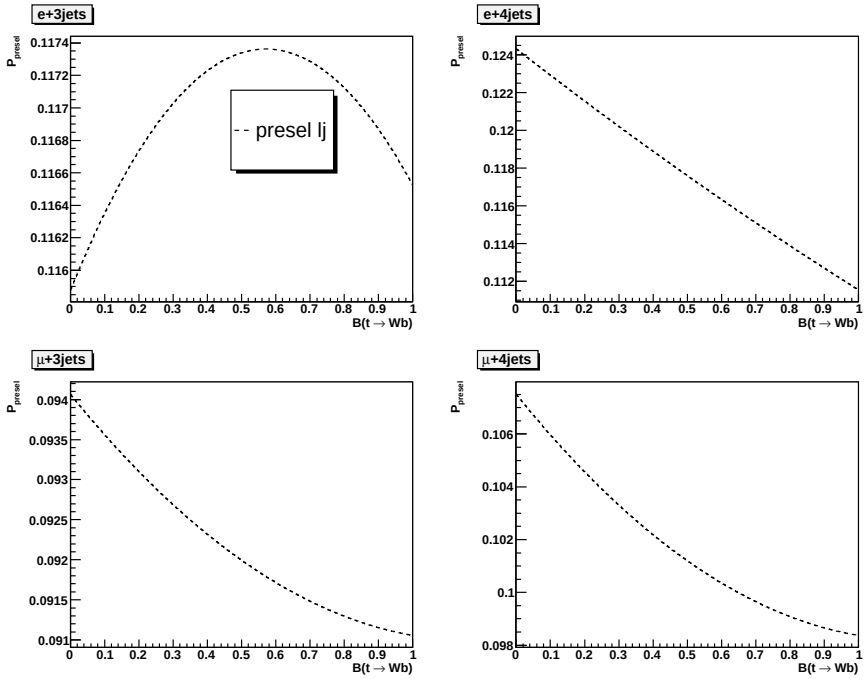

Figure 8.1.: Event selection efficiencies for $t\bar{t} \rightarrow lj$ events in $e+3$ jets, $\mu+3$ jets, $e+4$ jets and $\mu+4$ jets as function of R. The scales are adjusted to see the effect.

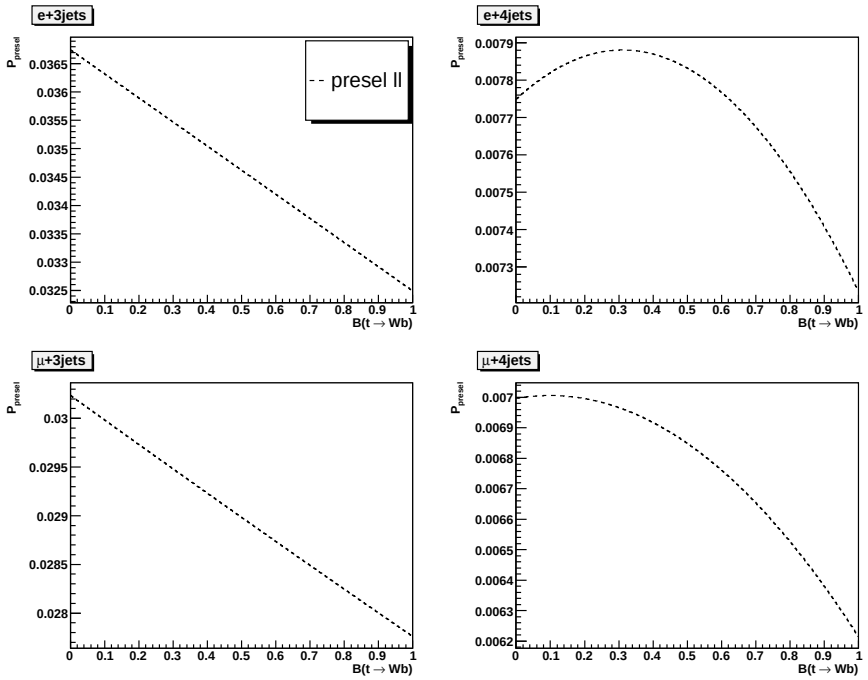

Figure 8.2.: Event selection efficiencies for $t\bar{t} \rightarrow ll$ events in $e+3$ jets, $\mu+3$ jets, $e+4$ jets and $\mu+4$ jets as function of R. The scales are adjusted to see the effect.

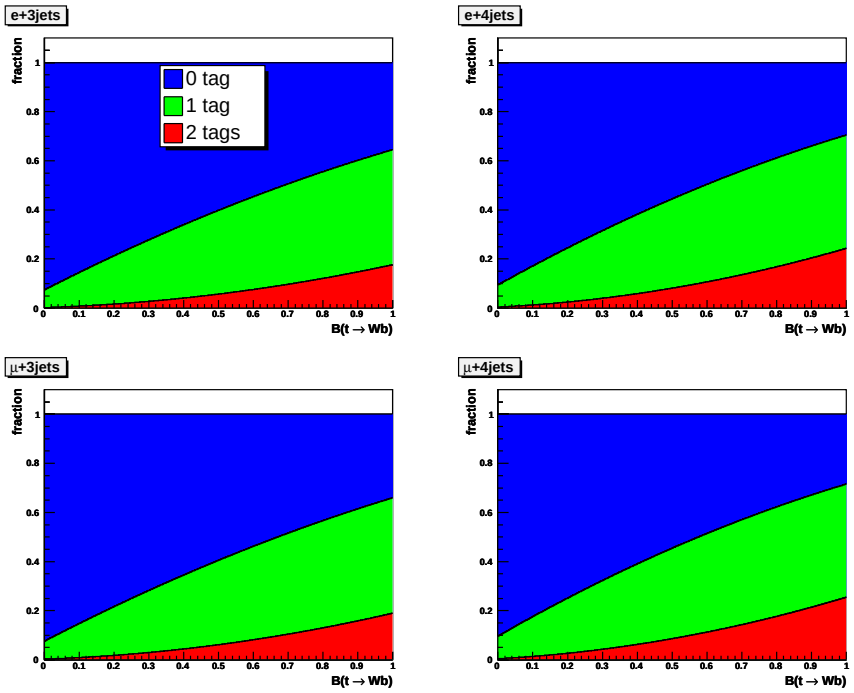

Figure 8.3.: Tagging fractions for $t\bar{t} \rightarrow lj$ events in $e+3$ jets, $\mu+3$ jets, $e+4$ jets and $\mu+4$ jets as function of R.

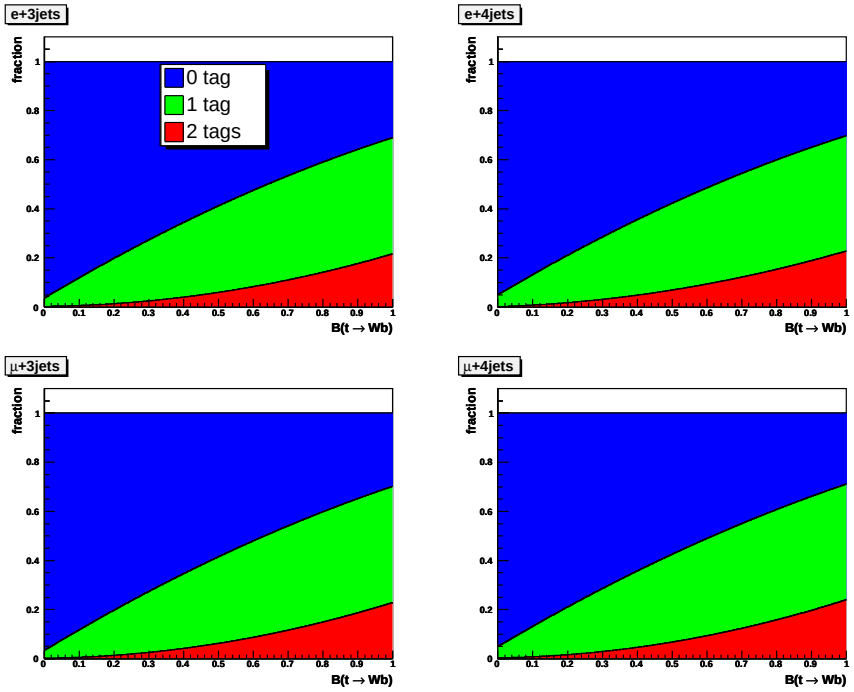

Figure 8.4.: Tagging fractions for $t\bar{t} \rightarrow ll$ events in $e+3$ jets, $\mu+3$ jets, $e+4$ jets and $\mu+4$ jets as function of R.

decay mode	jets	Channel	$t\bar{t} \to bb$	$t\bar{t} \to bq_\ell$	$t\bar{t} \to q_\ell q_\ell$
$t\bar{t} \to lj$	$= 3$	e+jets	0.4686 ± 0.0008	0.4117 ± 0.0031	0.0711 ± 0.0010
		μ+jets	0.4700 ± 0.0009	0.4158 ± 0.0036	0.0721 ± 0.0011
	≥ 4	e+jets	0.4615 ± 0.0007	0.4511 ± 0.0029	0.0896 ± 0.0013
		μ+jets	0.4606 ± 0.0008	0.4606 ± 0.0031	0.0915 ± 0.0013
$t\bar{t} \to ll$	$= 3$	e+jets	0.4734 ± 0.0018	0.4508 ± 0.0068	0.0326 ± 0.0021
		μ+jets	0.4731 ± 0.0018	0.4522 ± 0.0072	0.0308 ± 0.0015
	≥ 4	e+jets	0.4693 ± 0.0037	0.4477 ± 0.0157	0.0479 ± 0.0079
		μ+jets	0.4709 ± 0.0040	0.4561 ± 0.0160	0.0455 ± 0.0056

Table 8.12.: Event tagging probabilities $t\bar{t} \to bb$, $t\bar{t} \to bq_\ell$ and $t\bar{t} \to q_\ell q_\ell$ for exactly one b-tag.

decay mode	jets	Channel	$t\bar{t} \to bb$	$t\bar{t} \to bq_\ell$	$t\bar{t} \to q_\ell q_\ell$
$t\bar{t} \to lj$	$= 3$	e+jets	0.1760 ± 0.0009	0.0243 ± 0.0005	0.0018 ± 0.0002
		μ+jets	0.1891 ± 0.0011	0.0260 ± 0.0006	0.0023 ± 0.0003
	≥ 4	e+jets	0.2428 ± 0.0009	0.0380 ± 0.0006	0.0037 ± 0.0003
		μ+jets	0.2543 ± 0.0010	0.0415 ± 0.0008	0.0039 ± 0.0003
$t\bar{t} \to ll$	$= 3$	e+jets	0.2156 ± 0.0020	0.0093 ± 0.0005	0.0023 ± 0.0011
		μ+jets	0.2279 ± 0.0021	0.0091 ± 0.0004	0.0015 ± 0.0007
	≥ 4	e+jets	0.2276 ± 0.0046	0.0229 ± 0.0036	0.0012 ± 0.0003
		μ+jets	0.2395 ± 0.0048	0.0131 ± 0.0010	0.0030 ± 0.0019

Table 8.13.: Event tagging probabilities $t\bar{t} \to bb$, $t\bar{t} \to bq_\ell$ and $t\bar{t} \to q_\ell q_\ell$ for at least two b-tags.

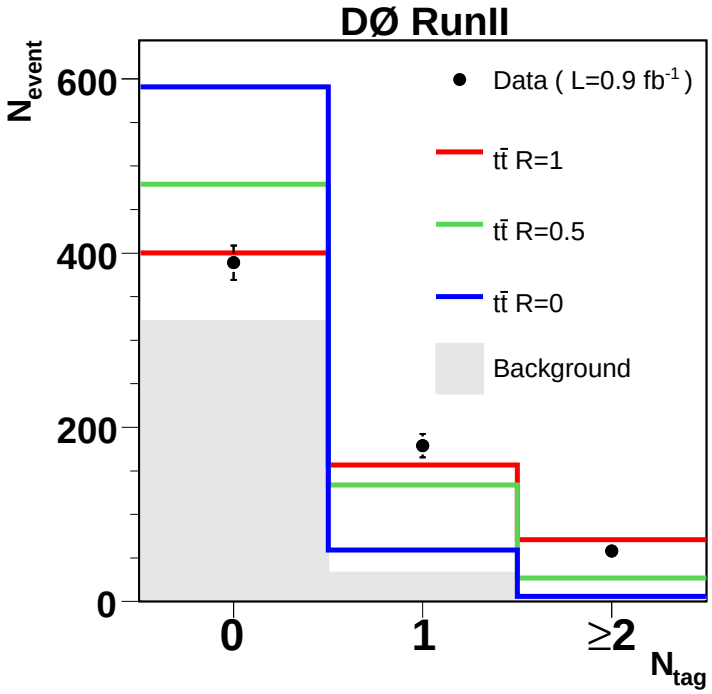

Figure 8.5.: Predicted and observed number of events in the 0, 1 and ≥ 2 tagged samples for various R hypotheses in the $\ell + 4$ jets sample.

8.4. Topological discriminant and zero b-tags

As can be seen from Fig. 8.5, the largest change of the expected number of events as function of R occurs in the 0 b-tagged sample. On the other hand, the sample with 0 b-tags contains the largest background contribution, mainly coming from W+jets events.

In order to improve the sensitivity of the measurement to R, a topological discriminant is constructed, that exploits the differences between the kinematic properties of two classes of events: $t\bar{t}$ signal and W+jets background. The topological discriminant is applied to the subsample with 0 b-tags and ≥ 4 jets. All other backgrounds with real isolated leptons – besides the W+jets background – are small, therefore no additional event class is introduced for these backgrounds. No topological discriminant in events with 3 jets and 0 b-tags is included, since the signal-to-background ratio is about five times smaller, and no significant improvement is expected.

The discriminant is constructed as follows. For signal and background the ratio of the probability density functions $\frac{\mathcal{P}^i_{t\bar{t}}}{\mathcal{P}^i_W}$ are built for each distribution, where $\mathcal{P}^i_{t\bar{t}}$ and $\mathcal{P}^i_W$ denote the probability density functions for the topological variable i to be $t\bar{t}$ signal and W+jets background, respectively. The logarithm of these ratios is fitted with a polynomial. The fit reduces the sensitivity of the discriminant to statistical fluctuation of the Monte Carlo samples. The result of the fits for all input variables is shown in Fig. D.11 for the e+jets channel and in Fig. D.12 for the μ+jets channel in Appendix D.

The discriminant function $\mathcal{D}$ is defined as:

$$\begin{aligned}
\mathcal{D} &= \frac{P_{t\bar{t}}(x_1, x_2, ...)}{P_{t\bar{t}}(x_1, x_2, ...) + P_W(x_1, x_2, ...)} \\
&\approx \frac{\prod_i P^i_{t\bar{t}}}{\prod_i P^i_{t\bar{t}} + \prod_i P^i_W} = \frac{\prod_i P^i_{t\bar{t}}/P^i_W}{\prod_i P^i_{t\bar{t}}/P^i_W + 1} = \frac{\exp\left(\sum_i (\ln \frac{P^i_{t\bar{t}}}{P^i_W})\right)}{\exp\left(\sum_i (\ln \frac{P^i_{t\bar{t}}}{P^i_W})\right) + 1} \\
&\simeq \frac{\exp\left(\sum_i (\ln \frac{P_{t\bar{t}}}{P_W})^i_{fitted}\right)}{\exp\left(\sum_i (\ln \frac{P_{t\bar{t}}}{P_W})^i_{fitted}\right) + 1} .
\end{aligned} \tag{8.17}$$

The first expression is the best discriminator. The second line is the approximation of the best discriminator neglecting correlations among the discriminating variables. Transformations lead to the expression in the last line, where $(\ln \frac{P_{t\bar{t}}}{P_W})^i_{fitted}$ is the fit to $(\ln \frac{\mathcal{P}^i_{t\bar{t}}}{\mathcal{P}^i_W})$ for all topological variables i that are used to build the discriminant.

Before the topological discriminant can be constructed for the final use in the measurement, a set of topological variables which are well described by the background model and show separation of $t\bar{t}$ events from W+jets background has to be chosen. The following input variables to the topological discriminant were studied:

Aplanarity: The normalised momentum tensor $\mathcal{M}$ is defined as:

$$\mathcal{M}_{ij} = \frac{\Sigma_o p^o_i p^o_j}{\Sigma_o |\vec{p^o}|^2}, \tag{8.18}$$

where $\vec{p^o}$ is the momentum vector of a reconstructed object o, and i and j are Cartesian coordinates. In the sum of objects the good jets and the selected lepton are included. The diagonalisation of $\mathcal{M}$ yields three eigenvalues $\lambda_1 \geq \lambda_2 \geq \lambda_3$, with $\lambda_1 + \lambda_2 + \lambda_3 = 1$. Only the four leading jets are used to avoid influence of the modelling of soft radiation

and the underlying event. The Aplanarity $\mathcal{A}$ is defined as $\mathcal{A} = \frac{3}{2}\lambda_3$ and measures the flatness of an event. $\mathcal{A}$ is defined in the range $0 \leq \mathcal{A} \leq 0.5$. Large values of $\mathcal{A}$ correspond to spherical events, small values correspond to more planar events. $t\bar{t}$ events show a more spherical behaviour typical for heavy object decays. W+jets and QCD events show a more planar behaviour.

$\mathcal{C}$: The variable $\mathcal{C}$ is defined here as $\mathcal{C} = 3(\lambda_1\lambda_2 + \lambda_1\lambda_3 + \lambda_2\lambda_3)$ where λ_1, λ_2 and λ_3 are the eigenvalues of the normalised momentum tensor $\mathcal{M}$. $\mathcal{C}$ is in the range $0 \leq \mathcal{C} \leq 1$.

$\mathcal{D}$: The variable $\mathcal{D}$ is defined as $\mathcal{D} = 27\lambda_1\lambda_2\lambda_3$ with λ_1, λ_2 and λ_3 being the eigenvalues of the normalised momentum tensor $\mathcal{M}$. $\mathcal{D}$ is in the range $0 \leq \mathcal{D} \leq 1$. Usually $\mathcal{C}$ and $\mathcal{D}$ are derived from the linear momentum tensor where the sum in the denominator of Eq. 8.18 runs over the absolute value of the momenta instead of the squared momenta. In that case $\mathcal{C}$ and $\mathcal{D}$ measure the the multijet structure and the deviation from planarity of the considered event. The here used modified $\mathcal{C}$ and $\mathcal{D}$ variables are considered as they show good discrimination of signal from background.

Leading jet p_T: The p_T of the jet with the highest p_T in the event. In $t\bar{t}$ events the leading jet is often the b-jet corresponding to the b-quark from top decay, which has higher transverse momentum than the leading jet for W+jets events.

H_T^l: H_T^l is defined as the scalar sum of the p_T of the four leading jets in an event and the p_T of the lepton from W decay. H_T^l tends towards higher values for $t\bar{t}$ events than for W+jets events.

H_T3: H_T3 is defined as the scalar sum of the p_T of the third and fourth jet in an event. As these two jets come mainly from gluon splitting in the W+jets sample but from the W decay in the $t\bar{t}$ sample, H_T3 has higher values for the latter.

JetMt: The variable $JetMt$ is defined as the transverse mass of the vector sum of all four leading jets in the event. For $t\bar{t}$ events this variable includes the two jets from the W boson and the two b quarks and is therefore connected to the invariant mass of the $t\bar{t}$ system. For W+jets events, where two jets are from the W decay and two from gluon splitting, this variable is not expected to show such a behaviour.

M012Mall: $M012Mall$ is defined as the mass of the three leading jets divided by the mass of the event. The mass of the event is defined as the invariant mass of the vector sum of the four leading jets, the lepton from W decay and the reconstructed neutrino. In case the three leading jets are connected to one top quark the numerator defines the top quark mass. Even though the combinatorics smear the effect out this variable still helps for the discrimination of $t\bar{t}$ signal from W+jets background.

ΔRmax: $\Delta Rmax$ is the maximal ΔR between two of the four leading jets in the event. The maximal distance between any pair of jets in $t\bar{t}$ events is smaller than for W+jets events.

All combinations of these variables are then used to construct discriminants $\mathcal{D}$. For each discriminant a set of pseudo-data is generated, in order to estimate the discriminant's performance, using the $t\bar{t}$, W+jets and QCD templates. The width of the fitted signal fraction is taken as a figure of merit. The method to optimise the topological discriminant is the same as used for the measurement of the W helicity, described in [144]. The sample composition for the generation of the pseudo-data is evaluated assuming a $t\bar{t}$ cross section of 6.8 pb and $R = 1$.

Based on the optimisation, the five input variables $\mathcal{C}$, $\mathcal{D}$, Aplanarity, leading jet p_T and $\Delta Rmax$ showed to be the best in the e+jets channel. In the μ+jets channel the discriminant that performs best is build from the six variables $\mathcal{D}$, Aplanarity, H_T3, H_T^l, $JetMt$ and $M012Mall$.

A different choice of optimal variables in the two final states is necessary due to differences in topology and selection. The number of bins is chosen to be 10 in the measurement, to provide good separation power but ensure a small dependence on statistical fluctuations of the topological discriminant templates.

In Appendix D the comparisons of data and Monte Carlo distributions for all selected input variables in the 0 b-tagged data for different jet multiplicity bins are shown in Figs. D.1 to D.8. All variables show good agreement between data and the prediction. To be less sensitive to the statistical fluctuations and be able to fit a polynomial function, some variable are transformed with a logarithm. The normalised distributions of the transformed variables for $t\bar{t}$ signal and W+jets background are shown in Fig. D.9 for e+jets and in Fig. D.10 for μ+jets.

In Figure 8.6 the topological discriminant shapes for $t\bar{t}$, Wlp+jets and multijet events are compared for the e+jets and μ+jets channel, respectively. It can clearly be seen that the discriminant templates for W+jets and multijet events peak at $\mathcal{D}$ of zero, while for $t\bar{t}$ events $\mathcal{D}$ peaks near one.

Figures 8.7 and 8.8 show the data to Monte Carlo comparison for a $t\bar{t}$ cross section of 6.8 pb. Furthermore, a stand-alone topological discriminant fit to the data in the 0 b-tag subsample is shown, as described in section 8.1.2. This fit is not used in the measurement of R and $\sigma \cdot B^2$, but performed to check whether the signal contribution obtained with the stand-alone fit significantly varies from the prediction. No statistically significant difference can be observed between stand-alone fit and the predicted signal contribution.

In order to take into account possible differences in the shape of the topological discriminant due to different top quark decays, the discriminant in each of the three samples $t\bar{t} \rightarrow WbWb$, $t\bar{t} \rightarrow WbWq$ and $t\bar{t} \rightarrow WqWq$ is determined separately. Differences in the p_T of light and heavy flavour jets for example can result in differences of the shape of energy related input variables for the three samples. Figure 8.9 compares the topological discriminant shape of $t\bar{t} \rightarrow WbWb$, $t\bar{t} \rightarrow WbWq$ and $t\bar{t} \rightarrow WqWq$ for the $t\bar{t} \rightarrow l + jets$ final state in the e+jets and μ+jets channel. The Figure shows that the template for $t\bar{t} \rightarrow WqWq$ tends to peak at slightly higher discriminant values than the one for $t\bar{t} \rightarrow WbWb$.

In Appendix D, Figure D.13 and D.14 show the $t\bar{t} \rightarrow WbWb$, $t\bar{t} \rightarrow WbWq$ and $t\bar{t} \rightarrow WqWq$ templates for the discriminant input variables in the e+jets and μ+jets channel, respectively. All energy related variables like H_T^l show a distribution that tends towards higher values for the $t\bar{t} \rightarrow WqWq$ final state than for $t\bar{t} \rightarrow WbWb$.

When including the topological discriminant into a fitting procedure, the fraction of events in each histogram bin i of the discriminant templates have to be calculated. The $t\bar{t}$ fraction $f_i^{t\bar{t}}$ in each histogram bin i can be written as

$$f_i^{t\bar{t}} = n_{frac}^{bb} \cdot f_i^{t\bar{t}\rightarrow b\bar{b}} + n_{frac}^{bq} \cdot f_i^{t\bar{t}\rightarrow b\bar{q}_l} + n_{frac}^{qq} \cdot f_i^{t\bar{t}\rightarrow q_l\bar{q}_l}\,, \tag{8.19}$$

where $f_i^{t\bar{t}\rightarrow b\bar{b}}$ ($f_i^{t\bar{t}\rightarrow b\bar{q}_l}$, $f_i^{t\bar{t}\rightarrow q_l\bar{q}_l}$) is the fraction for the $t\bar{t} \rightarrow bb$ ($t\bar{t} \rightarrow bq_l$, $t\bar{t} \rightarrow q_lq_l$) template in

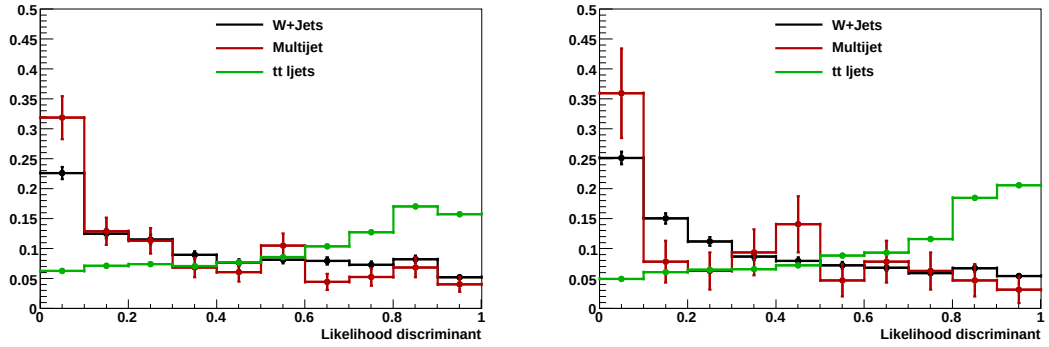

Figure 8.6.: Topological discriminant templates in the e+jets (left) and μ+jets (right) channel for $t\bar{t} \to WbWb$, Wlp+jets and multijet.

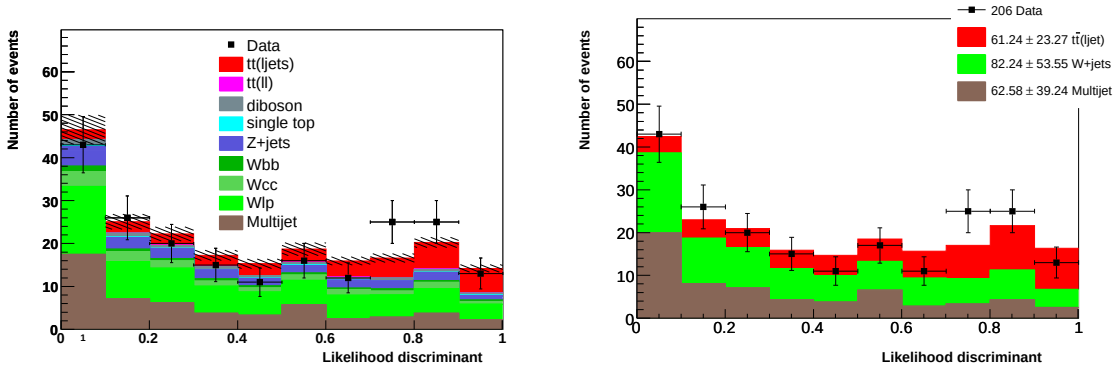

Figure 8.7.: Data-MC comparison for the topological discriminant in the 0 b-tag subsample in the e+jets channel. Left plot: $\sigma \cdot B^2 = 6.8$ pb and $R = 1$ are assumed. Right plot: Fit of $t\bar{t}$, W+jets and multijet templates to the data. For the Medium NN Tagger.

bin i. The fractions n^{bb}_{frac}, n^{bq}_{frac} and n^{qq}_{frac} are defined as:

$$
\begin{aligned}
n^{bb} &= R^2 n_0^{bb} \\
n^{bq} &= 2R(1-R) n_0^{bq} \\
n^{qq} &= (1-R)^2 n_0^{qq} \\
n^{bb}_{frac} &= \frac{n^{bb}}{n^{bb} + n^{bq} + n^{qq}} \\
n^{bq}_{frac} &= \frac{n^{bq}}{n^{bb} + n^{bq} + n^{qq}} \\
n^{qq}_{frac} &= \frac{n^{qq}}{n^{bb} + n^{bq} + n^{qq}}
\end{aligned}
\tag{8.20}
$$

where n_0^{bb} is the expected number of $t\bar{t} \to bb$ events in the 0 b-tag sample. The variables n_0^{bq} and n_0^{qq} define the expected number of $t\bar{t} \to bq$ and $t\bar{t} \to qq$ events, respectively.

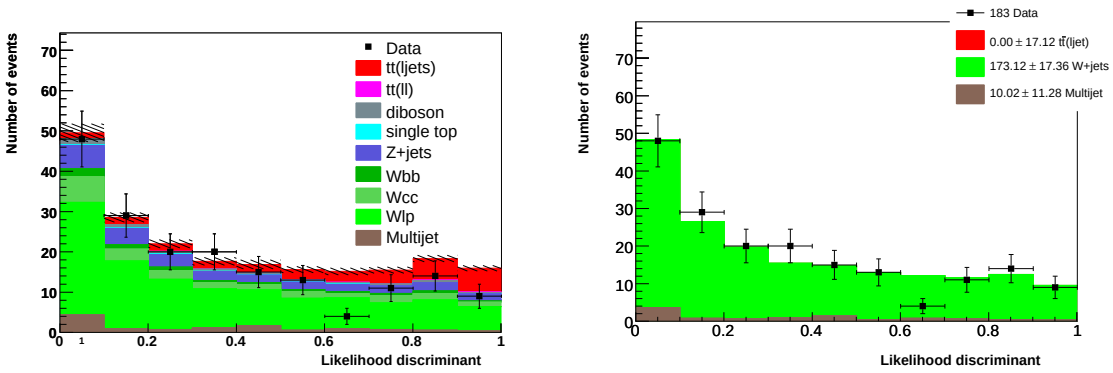

Figure 8.8.: Data-MC comparison for the topological discriminant in the 0 b-tag subsample in the μ+jets channel. Left plot: $\sigma \cdot B^2 = 6.8$ pb and $R = 1$ are assumed. Right plot: Fit of $t\bar{t}$, W+jets and multijet templates to the data. For the Medium NN Tagger.

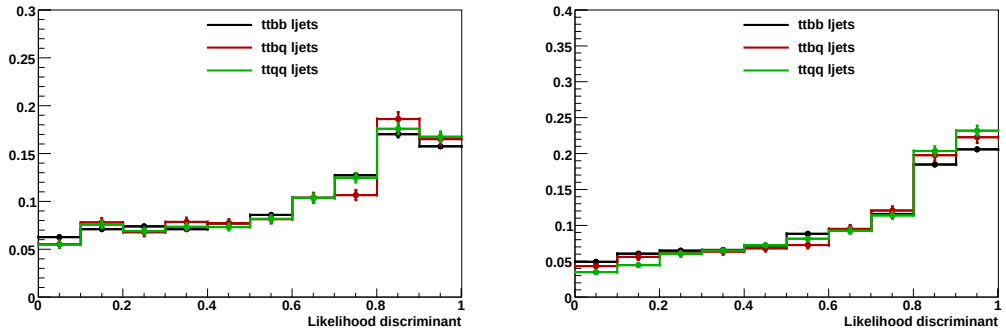

Figure 8.9.: Topological discriminant templates in the e+jets (left) and μ+jets (right) channel for $t\bar{t} \to WbWb$, $t\bar{t} \to WbWq$ and $t\bar{t} \to WqWq$. For the Medium NN Tagger.

8.5. Systematic uncertainties

Beside the statistical uncertainties various systematic uncertainties can affect the measurement of $\sigma \cdot B^2$ and R. As will be shown later, the systematic uncertainty is of the same order as the statistical uncertainty on both observables. Thus correct treatment of the systematic uncertainties and the correlations between various channels is important.

In section 8.5.1 the incorporation and treatment of systematic uncertainties in the maximum likelihood fit is discussed. The treatment of systematic uncertainties influencing the shape of the topological discriminant templates – also referred to as shape changing systematic uncertainties – is discussed in section 8.5.2. The full list of sources of systematic uncertainties studied in the measurement of R and $\sigma \cdot B^2$ is discussed in section 8.5.3

8.5.1. Treatment of systematic uncertainties in the maximum likelihood procedure

Systematic uncertainties is treated in two alternative ways. The usual treatment of systematic uncertainties, referred to as "standard" method, is to vary one source of systematic error by plus and minus one standard deviation at a time, recalculate the expected signal and background, refit the observables, and take the difference between the re-fitted values and the values obtained without any systematic shift as the corresponding uncertainty. The variations for all sources of systematic errors are then summed quadratically in order to obtain the total systematic uncertainty on the observables.

The other way of implementing the systematic uncertainties is via a nuisance parameter method. In the nuisance parameter method, that was first applied to the $t\bar{t}$ cross section measurement described in Ref. [106], a free parameter is introduced for each independent source of systematic uncertainty. Each of these parameters, called nuisance parameters, is allowed to float during the maximum likelihood fit. The probability density function of the nuisance parameter is chosen to be a Gaussian with mean zero and width one. The likelihood $\mathcal{L}_1$ in Eq. 8.13 is multiplied by the product of Gaussian constraints on each nuisance parameter:

$$\mathcal{L}_2 = \prod_{i=1}^{N} \mathcal{G}(\nu_i; 0, 1), \tag{8.21}$$

where ν_i is the nuisance parameter for the independent source of systematic error i, $\mathcal{G}(\nu_i; 0, 1)$ is the probability density function of the nuisance parameter i having the value ν_i, and N is the number of independent sources. The nuisance parameter, multiplied with the one sigma uncertainty of its corresponding systematic error, is then added to the central value of the associated efficiency or cross section. For example, the event b-tagging probability on $t\bar{t}$ events depends on the uncertainty on the Tag Rate Function. If the one standard deviation on the b-tagging probability coming from the b-TRF uncertainty band, is determined to be σ_{b-TRF}, the central value of the b-tagging probability $\hat{p}_{btag}$ can change as

$$p_{btag} = \hat{p}_{btag} + \sigma_{b-TRF} \cdot \nu_{b-TRF}. \tag{8.22}$$

The probability p_{btag} is used for the determination of the expected number of events in the maximum likelihood fit and goes into the likelihood $\mathcal{L}_1$. As can be seen from Eq. 8.22, the b-tag probability is varied by plus or minus one standard deviation if the corresponding nuisance parameter varies by plus or minus one.

With this procedure, each nuisance parameter is allowed to change the selection efficiencies, tagging probabilities, theoretical cross sections or W+jets scale factors during the fitting procedure. At each step of the maximum likelihood fit, all efficiencies, probabilities and scale factors are therefore recalculated as a function of the nuisance parameters. This procedure allows the systematic uncertainties to change the central value of $\sigma \cdot B^2$ and R.

The error extraction from MINOS delivers the total uncertainty on $\sigma \cdot B^2$ and R for the nuisance parameter fit, consisting of all systematic and the statistical uncertainties. The estimate of each individual source of systematic uncertainty on $\sigma \cdot B^2$ and R is carried out by fixing all but the considered nuisance parameter to zero. By comparing the results from the fit with statistical errors only and the result obtained for each systematic uncertainty, the "offset" on the central value, introduced by the considered source of systematic error, can be determined.

8.5.2. Treatment of systematic uncertainties on the topological discriminant

Besides systematic uncertainties that only change the overall normalisation, the shape of the topological discriminant can be affected by various systematic uncertainties. For example, a

higher jet energy scale can lead to a harder spectrum of energy related input variables to the topological discriminant, and therefore to a change of the discriminant shape.

For each systematic uncertainty changing the shape, a template for the one sigma variations of the considered source is generated. The incorporation into the nuisance parameter fit is done using a linear combination of the central template and the templates for plus and minus one standard deviation for each sample. The linear combination can be written as

$$f_i = f_i^0 + \sum_{k=0}^{M} \nu_k (f_i^k - f_i^0)\,, \tag{8.23}$$

where f_i is the fraction of bin i for the discriminant template, as used in the fit, f_i^0 denotes the fraction of bin i for the central discriminant template, ν_k is the nuisance parameter for the source of systematic uncertainty k, and f_i^k is the fraction of bin i for the discriminant template obtained when varying the systematic k by plus or minus one standard deviation. The number M stands for the total number of shape changing systematic uncertainties. The nuisance parameter ν_k can stand for a systematic uncertainty that changes the normalisation and the shape at the same time. Therefore, the correlation between both effects is naturally taken into account in the nuisance parameter method. In order to take into account possible differences between the shapes of plus and minus one sigma, the formula given in Eq. 8.23 can be rewritten as:

$$f_i = f_i^0 + \sum_{k=0}^{M} \begin{cases} if\ (\nu_k > 0) : \nu_k \left(f_i^{k+} - f_i^0\right) \\ if\ (\nu_k < 0) : \nu_k \left(f_i^{k-} - f_i^0\right) \end{cases} \tag{8.24}$$

f_i^{k+} is the fraction of bin i of the plus one sigma template and f_i^{k-} is the fraction of bin i of the minus one sigma template.

8.5.3. Systematic uncertainties for $\sigma \cdot B^2$ and R

Before the presentation of the results in the next section, the different sources of systematic uncertainties considered in the analysis are discussed here. Each of the different sources of systematic uncertainty can affect the event selection efficiencies, the b-tagging probabilities or the shape of the topological discriminant. Uncertainties like jet energy scale have an effect on all efficiencies and the template shape, while other uncertainties, like Monte Carlo cross section uncertainties, only affect the total normalisation.

The uncertainty on the integrated luminosity in DØ is measured to be 6.1 % [57]. This effects signal and background yields in the same way. The uncertainty on the integrated luminosity is assigned as additional systematic uncertainty on the cross section measurement. Since R is a ratio, it is not affected by the luminosity uncertainty.

Uncertainties on the event selection efficiency

Some systematic uncertainties only affect the event selection efficiency.

Uncertainty on the data-MC luminosity profile difference. As will be done in the search for charged Higgs bosons, the luminosity profile in the Monte Carlo has to be reweighted to data. The details of the reweighting are discussed in section 6.3.3. When the simultaneous measurement of R and $\sigma \cdot B^2$ was performed, not all the luminosity profiles in Monte Carlo were available. Therefore the central efficiencies do not include the luminosity profile reweighting. The difference between applying and neglecting the weight

has been estimated in the electron-muon channel [145]. The uncertainty of < 0.5 % is assigned on the $t\bar{t}$ efficiency, 2.2 % on diboson background, and 3.7 % on the Z+jets background. The difference in the uncertainty comes from the different zero bias overlay in the Monte Carlo samples.

Data quality flags uncertainty. The uncertainty on the data quality calorimeter flag correction is estimated to be 0.5 % [108], independent of the sample.

Electron ID scale factor. When the electron identification scale factor was parametrised, the dependence on several variables was ignored. The systematic uncertainty on the electron ID scale factor is estimated by adding in quadrature the difference between using the missing dependencies and the central parametrisation. The contributions to the electron ID scale factor uncertainty are assumed to come from the jet multiplicity dependency (1.2 %) of the H-matrix, track match and likelihood scale factor and from dependencies not taken into account (on p_T and ϕ of the electromagnetic object) (2.2 %). The uncertainty due to the jet multiplicity dependency is calculated as the difference between the efficiency taking the dependence on ΔR between the electron and a jet into account, and neglecting this dependence, which results in 1.2 %. A total systematic uncertainty on the electron ID scale factor of 2.5 % is assigned.

Muon ID and track scale factor. According to the studies summarised in the muon ID certification note [84], the uncertainties on muon identification and tracking are both 0.7 %.

Muon isolation scale factor. The uncertainty on the Monte Carlo to data scale factor of the muon isolation criteria is extracted from [84] to be 2 %.

Z vertex distribution difference between data and MC. An uncertainty of 2.2 % is used on the difference between the primary vertex z distribution in simulated events and the data, as given in [145].

PV scale factor. The event selection efficiency is scaled with a factor of 98.9 %, in order to correct for the difference of the primary vertex selection efficiency between data and Monte Carlo [146]. The relative uncertainty on the scale factor is estimated to be 1.5 %.

Uncertainties on the Monte Carlo cross sections. For the Z+jets sample an uncertainty on the cross section of 15 % [143] is applied. The uncertainty on the diboson cross section is taken to be 20 %, which is half the difference between the leading order and NLO cross section calculations [145]. For the single top cross section an uncertainty on the theoretical NLO calculation of 12.6 % is applied [147].

Z p_T reweighting. The uncertainty of 12 % on the reweighting of the Z p_T distribution in Monte Carlo to match data, as described in section 6.3.3, as estimated in the electron-muon channel [145].

Electron, muon and jet trigger. The systematic uncertainties on the electron, muon and jet trigger parameterisations are taken from the topological cross section measurement [148], which uses the same set of triggers. The uncertainty on the electron trigger parametrisation is $+0.6$ % and -1.18 %, on the muon trigger parametrisation $+2.5$ % and -2.7 % are assigned and ± 0.2 % are assigned on the jet trigger parametrisation.

Uncertainties on the event b-tagging probability

Some sources of systematic uncertainties do not affect the event selection, but only the b-tagging. All of these sources are related to the parametrisations of taggability or tagging.

Uncertainties on the b-,c- and light TRFs. The uncertainties on the b-,c- and light Tag Rate Functions are calculated by varying the corresponding TRF within its assigned one standard deviation error band up and down [104].

Uncertainty on the jet taggability parameterisation. The uncertainty on the Taggability Rate Function parameterisation is calculated by varying the taggability function within its assigned one standard deviation error band up and down.

Uncertainty due to the taggability flavour dependence. To account for the uncertainty on the taggability flavour dependence the parametrisation derived with W+jets events instead of multijet events is used. The difference between the two flavour dependency parametrisations is taken as one standard deviation uncertainty.

Uncertainties on the event selection and b-tagging efficiency

A couple of systematic errors can change the event selection efficiency and the b-tagging probability.

Uncertainty from the limited Monte Carlo statistics. The limited Monte Carlo statistics yields an uncertainty on the event selection efficiency and event b-tagging probability for the signal and each Monte Carlo background sample separately. For the W+jets sample, the uncertainty on the fraction of Wlp, Wbb and Wcc due to limited Monte Carlo statistics is calculated, as not the total normalisation but the flavour composition of W+jets is taken from Monte Carlo samples. The uncertainty on the b-tagging probability takes into account properly the fact that all events before and after tagging have event weights.

b-fragmentation reweighting The systematic uncertainty on the reweighting of the b-fragmentation function from the default in PYTHIA to the value tuned to reproduce e^+e^- collider data is assumed to be the symmetrised difference between the AOD and SLD tunes [130].

Parton distribution function The systematic uncertainty on the parton distribution function (PDF) is estimated by reweighting the $t\bar{t}$ Monte Carlo from CTEQ6L1 to CTEQ6M and its twenty error PDFs. The reweighting of the PDF is done by using the caf_pdfreweight tool [149]. The uncertainty of the relative difference between the 20 error PDFs and the selection and b-tagging efficiencies obtained when reweighting to CTEQ6M is assigned [150]. In the simultaneous measurement of R and $\sigma \cdot B^2$ an independent nuisance parameter is assigned for each of the 20 PDF uncertainties. For the cross section combination and charged Higgs search, presented in section 11, the 20 errors PDFs are added in quadrature and only one nuisance parameter is assigned. The change of the method is done for consistency with the dilepton and τ+lepton channels.

Signal Modelling The uncertainty on the signal modelling is estimated by replacing PYTHIA $t\bar{t}$ Monte Carlo for the standard decay to two b quarks with ALPGEN Monte Carlo. The relative difference on event selection and b-tagging efficiency between both simulations is then assigned to the Monte Carlo samples for $t\bar{t} \to bb$, $t\bar{t} \to bq_\ell$ and $t\bar{t} \to q_\ell q_\ell$.

Uncertainties on the event selection, event b-tagging probability and the discriminant shape

Some uncertainties affect the normalisation and the shape of the discriminant. The following systematic uncertainties are taken to affect both:

Uncertainty on jet energy scale. The uncertainty on the jet energy scale (JES) is determined by varying the JES correction up and down by the sum of the statistical and systematic uncertainties in data and MC, where all individual contributions are added in quadrature.

Uncertainty on jet energy resolution. The uncertainty on the jet energy resolution (JER) is determined by changing the JER correction up and down by one standard deviation.

Uncertainty on jet reconstruction and identification efficiency. The uncertainty on the jet reconstruction and identification (JetID) efficiency is determined by changing the JetID Monte Carlo to data scale factor, which is responsible for removing extra jets from simulation, down by one standard deviation. The uncertainty is symmetrised.

Additionally to these shape changing systematic uncertainties the effect of b-fragmentation reweighting, b TRF, c TRF, light TRF and taggability on the discriminant shape have been checked. None of these sources has a significant effect on the template shape and therefore their effect on the shape is neglected.

Uncertainties on the multijet background yield

The uncertainties on ε_{qcd} and ε_{sig}, as given in Table 7.1 in section 7.2.1, are propagated to the multijet background yield. Additionally, the limited statistics of the "loose-tight" data samples are taken into account, as described in section 8.1.

Uncertainties on the W+jets and Z+jets background flavour composition

On the k-factor and heavy flavour scale factor of the W+jets and Z+jets samples the following uncertainties are assigned:

Uncertainty on Monte Carlo background scale factors. A conservative assumption of 50 % uncertainty on the heavy flavour scale factor in Z+jets is made [143]. As the Z+jets background in the l+jets channel is small, the large uncertainty results only in a negligible contribution to the systematic uncertainty of $\sigma \cdot B^2$ and R.

W+jets heavy flavour scale factor: The uncertainty on the W+jets heavy flavour scale factor is estimated to be 15 %, as described in section 6.3.2.

Table 8.14 summarises the systematic uncertainties that are taken into account. The table is divided into correlated and uncorrelated uncertainties. For the former a 100 % correlation of the same source of systematic error for all considered channels is assumed.

8.6. Measurement and results

The extraction of $\sigma \cdot B^2$ and R can be done with the nuisance parameter method and the standard method of error treatment. Both results are checked for consistency.

Before the fit is performed on the data, the procedure to measure simultaneously the top quark pair production cross section $\sigma \cdot B^2$ and the ratio of branching fractions R, is checked with a variety of ensemble tests. The details about the type of test and the outcome are described in Appendix E. No suspicious behaviour can be observed in the ensemble tests.

In order to get an impression on the improvement due to using the topological discriminant in the zero b-tagged sample, the results are also derived without the discriminant. Additionally, the cross section $\sigma \cdot B$ is extracted with fixed $R = 1$.

Systematic	e+jets	μ+jets
Correlated		
Data quality	X	X
$\Delta z(l, PV)$	X	X
Primary vertex	X	X
Electron ID	X	
Muon ID		X
Muon track		X
Muon isolation		X
Jet ID	X	X
Jet energy scale	X	X
Jet energy resolution	X	X
l+jets trigger	X	X
PDF	X	X
signal modelling	X	X
W+jets heavy flavour scale factor	X	X
Z+jets heavy flavour scale factor	X	X
b-fragmentation	X	X
Luminosity reweighting	X	X
Z p_T reweighting	X	X
b TRF	X	X
c TRF	X	X
light TRF	X	X
Taggability	X	X
Taggability flavour dependence	X	X
Integrated luminosity	X	X
background cross sections	X	X
Uncorrelated		
Monte Carlo statistics	X	X
ε_{qcd} in μ+jets		X
ε_{qcd} in e+jets	X	
ε_{sig} in μ+jets		X
ε_{sig} in e+jets	X	

Table 8.14.: Summary of systematic uncertainties in each channel and the correlations between them. The correlated systematic uncertainties are also correlated within each channel.

8.6.1. Result with the nuisance parameter likelihood

The simultaneous fit of $\sigma \cdot B^2$ and R, using the nuisance parameter method, yields for the combined e+jets and μ+jets channel:

$$\begin{aligned} R &= 0.968^{+0.092}_{-0.083} \text{ (stat+syst)} \\ \sigma \cdot B^2 &= 8.18^{+0.90}_{-0.84} \text{ (stat+syst)} \pm 0.50 \text{ (lumi) pb} \end{aligned}$$

The contribution of the different sources of systematic uncertainties are shown in Table 8.15 (grey rows) for R and $\sigma \cdot B^2$. The uncertainty on R is dominated by the uncertainty on the b-tag TRF. As the main sensitivity on R comes from the distribution of $t\bar{t}$ events between different b-tag subsamples, this behaviour seems reasonable. For the cross section the uncertainty on the event selection, electron identification, W+jets heavy flavour scale factor and the jet energy

scale are dominant. The uncertainty on the event selection includes vertex and data quality requirements, which are fully correlated between the e+jets and μ+jets channels. All of these uncertainties have effects on the total normalisation of the signal and background samples.

Summary of nuisance parameter likelihood (NL) and (S) method for simultaneous fit of R and $\sigma \cdot B^2$

	R (NL)			R (S)		$\sigma \cdot B^2$ [pb] (NL)			$\sigma \cdot B^2$ [pb] (S)	
	result	$+\sigma$	$-\sigma$	$+\sigma$	$-\sigma$	result	$+\sigma$	$-\sigma$	$+\sigma$	$-\sigma$
Statistical only fit	0.968	+0.067	-0.065			8.26	+0.67	-0.64		
Systematics source	Offset	$+\sigma$	$-\sigma$	$+\sigma$	$-\sigma$	Offset	$+\sigma$	$-\sigma$	$+\sigma$	$-\sigma$
Event preselection	-0.000	0.001	0.000	0.000	-0.000	0.00	0.25	-0.22	0.237	-0.228
Muon identification	0.000	0.000	0.000	0.001	-0.001	-0.02	0.09	-0.08	0.091	-0.090
Electron identification	0.000	0.000	0.000	0.001	-0.001	0.02	0.12	-0.10	0.114	-0.112
Lumi reweight	0.000	0.000	-0.000	0.000	-0.000	-0.00	0.04	-0.04	0.041	-0.040
Z pT reweight	0.000	0.000	-0.000	0.000	-0.000	-0.00	0.01	0.00	0.005	-0.005
signal modeling	0.000	0.009	-0.005	0.012	-0.000	-0.01	0.11	-0.25	0.000	-0.333
EM triggers	0.000	0.000	0.000	0.000	-0.000	0.00	0.06	-0.05	0.053	-0.027
Muon triggers	0.000	0.000	0.000	0.001	-0.001	-0.02	0.11	-0.09	0.110	-0.101
Jet triggers	-0.000	0.000	0.000	0.000	-0.000	-0.00	0.02	-0.02	0.017	-0.017
Jet energy scale	-0.001	0.000	0.000	0.000	-0.011	-0.09	0.32	-0.23	0.486	-0.330
Jet energy resolution	-0.000	0.000	0.000	0.000	-0.001	0.00	0.00	0.00	0.014	-0.000
JetID	0.000	0.000	0.000	0.001	-0.000	-0.01	0.13	-0.14	0.143	-0.149
Taggability	0.001	0.015	-0.014	0.015	-0.015	0.01	0.09	-0.08	0.091	-0.088
Flavor dependence of taggability	0.000	0.000	-0.002	0.000	-0.002	-0.00	0.02	0.00	0.000	-0.000
b-tag TRF	**0.004**	**0.059**	**-0.047**	**0.055**	**-0.050**	**0.01**	**0.10**	**-0.09**	**0.098**	**-0.089**
c-tag TRF	0.000	0.000	-0.002	0.002	-0.002	0.00	0.05	-0.05	0.056	-0.055
light tag TRF	-0.000	0.000	-0.001	0.001	-0.001	0.00	0.06	-0.06	0.060	-0.059
b fragmentation	0.000	0.001	-0.001	0.001	-0.001	-0.00	0.10	-0.10	0.099	-0.097
ϵ_{QCD} in e+jet channel	-0.000	0.001	0.000	0.000	-0.002	0.00	0.00	-0.00	0.014	-0.013
ϵ_{sig} in e+jet channel	0.000	0.000	-0.001	0.000	-0.000	-0.00	0.01	0.00	0.000	-0.018
ϵ_{QCD} in μ+jet channel	0.000	0.000	-0.003	0.000	-0.001	-0.00	0.04	0.00	0.022	-0.006
ϵ_{sig} in μ+jet channel	0.000	0.000	-0.002	0.001	-0.000	-0.00	0.04	-0.02	0.000	-0.034
MC background x-section	0.000	0.001	-0.001	0.001	-0.001	-0.00	0.04	-0.04	0.038	-0.038
MC bkg scale factors	0.000	0.001	-0.001	0.001	-0.001	-0.00	0.05	-0.05	0.047	-0.047
MC statistics on W fractions	0.000	0.001	-0.001	0.001	-0.001	-0.00	0.02	-0.02	0.020	-0.020
MC statistics	0.000	0.001	-0.001	0.001	-0.001	-0.00	0.03	-0.02	0.023	-0.023
MC statistics on ttbq , ttqq MC	-0.000	0.002	-0.002	0.002	-0.002	0.00	0.01	-0.00	0.010	-0.010
W+jets heavy flavor scale factor	-0.000	0.005	0.000	0.005	-0.004	0.01	0.21	-0.23	0.242	-0.242
PDF	0.000	0.005	-0.005	0.005	-0.003	-0.00	0.05	-0.04	0.041	-0.043
Statistics for matrix method	-0.003	0.016	-0.016	0.011	-0.010	0.00	0.17	-0.17	0.134	-0.133
Total systematics	+0.003	+0.064	-0.052	0.060	-0.055	-0.09	+0.60	-0.57	0.685	-0.666
	result	$+\sigma$	$-\sigma$			result	$+\sigma$	$-\sigma$		
Nuisance parameter fit	0.968	+0.092	-0.083			8.18	+0.90	-0.84		

Table 8.15.: Systematic uncertainties and result for R and $\sigma \cdot B^2$ in the combined l+jets channel. The Medium NN Tagger is used and the topological discriminant in the 0 b-tag subsample is applied.

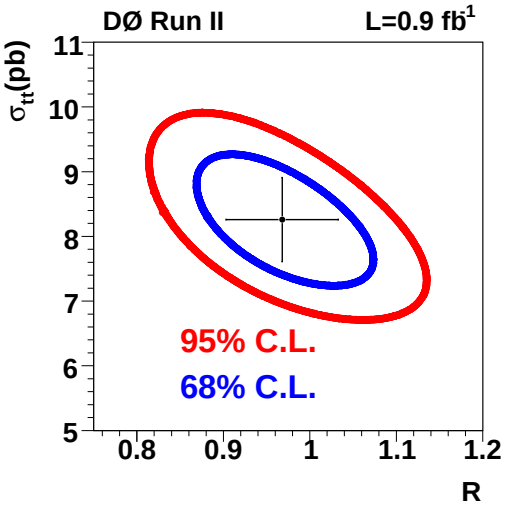

Figure 8.10.: 68% and 95% C.L. in the (R, $\sigma(p\bar{p} \to t\bar{t}) \cdot B(t \to Wq)^2$) plane. The point with error bar is the result fitted without nuisance parameter likelihood. The uncertainties are statistical only. The Medium NN Tagger is used and the topological discriminant in the 0 b-tag subsample is applied.

8.6.2. Result with the standard method

The standard method of handling the systematic uncertainties yields for the combined l+jets channel:

$$\begin{aligned} R &= 0.968^{+0.067}_{-0.065}\,(\text{stat})\,^{+0.060}_{-0.055}\,(\text{syst}) \\ \sigma(p\bar{p} \to t\bar{t}) \cdot B^2(t \to Wq) &= 8.26^{+0.67}_{-0.64}\,(\text{stat})^{+0.69}_{-0.67}\,(\text{syst}) \pm 0.50\,(\text{lumi}). \end{aligned}$$

Within uncertainties, the results are fully consistent with the nuisance parameter fit results. No shift on R with respect to the standard method can be observed when using the nuisance parameter method. On the cross section a shift of 0.1 pb is observed, which mainly arises from the offset due to the jet energy scale uncertainty, as shown in Table 8.15.

The systematic uncertainties obtained with the standard method of error treatment are presented in Table 8.15 (white rows) for R and the cross section. Again it can be seen that the b-tag TRF uncertainty dominates the systematic error on R, while for the cross section jet energy scale, event selection and the W+jets heavy flavour scale factor dominate.

Figure 8.10 shows the 68 % and 95 % C.L. contours for the result of the fit obtained with the standard method, including statistical uncertainties only. The correlation between R and $\sigma \cdot B^2$ is found to be -58 %.

Table 8.16 presents the sample composition for $\sigma \cdot B^2$ of $8.18^{+0.90}_{-0.84}$ (stat+syst) $\pm$ 0.50 (lumi) pb measured with the nuisance parameter method and $R = 1$. The total uncertainty consists of statistical and systematic uncertainties. The line "Other" in the table represents the contributions from diboson, single top and Z+jets backgrounds. All predicted and observed numbers of events in the individual subsamples agree with each other.

Figure 8.11 shows the predicted and observed number of events versus the number of b-tagged jets in the e+jets, μ+jets and combined l+jets channel for the measured $t\bar{t}$ cross section and $R = 1$. In Figs. 8.12, 8.13 and 8.14 the prediction and observation versus the number of jets in the event are shown separately in the 0, 1 and 2 b-tagged samples. All distributions

N_{jets}	sample	0 b tags	1 b tag	≥ 2 b tags
3	W+jets	1394.4 ± 65.1	102.5 ± 9.4	8.3 ± 1.2
	Multijet	287.4 ± 35.9	28.1 ± 3.5	3.3 ± 0.4
	Other	254.0 ± 35.2	29.4 ± 3.5	5.2 ± 0.7
	$t\bar{t}$	109.7 ± 6.6	143.3 ± 5.1	54.3 ± 4.3
	Total	2045.5 ± 82.5	303.3 ± 11.8	71.2 ± 4.5
	Observed	2050	294	76
4	W+jets	188.2 ± 38.0	17.3 ± 3.8	1.8 ± 0.4
	Multijet	66.9 ± 9.9	6.6 ± 1.0	0.8 ± 0.1
	Other	62.2 ± 11.8	8.0 ± 1.4	1.7 ± 0.3
	$t\bar{t}$	83.8 ± 9.4	126.4 ± 11.4	64.2 ± 4.5
	Total	401.1 ± 42.1	158.3 ± 12.1	69.5 ± 4.5
	Observed	389	179	58

Table 8.16.: Sample composition for the measured $\sigma \cdot B^2$ and $R = 1$.

show good agreement between prediction and observation. The samples with 1 and 2 jets also show good data to Monte Carlo agreement, which is important to verify the background model.

Figure 8.15 shows the Monte Carlo to Data comparison of the topological discriminant for the measured $t\bar{t}$ cross section. Within uncertainty, the prediction with the measured $\sigma \cdot B^2$ and R agree with the observed number of events. While in the e+jets channel with ≥ 4 jets, the data tends more to less b-tags, the μ+jets sample shows a trend towards more b-tags, as can be seen in Fig. 8.11. A measurement of $\sigma \cdot B^2$ and R per channel is therefore useful to check whether the individual results agree.

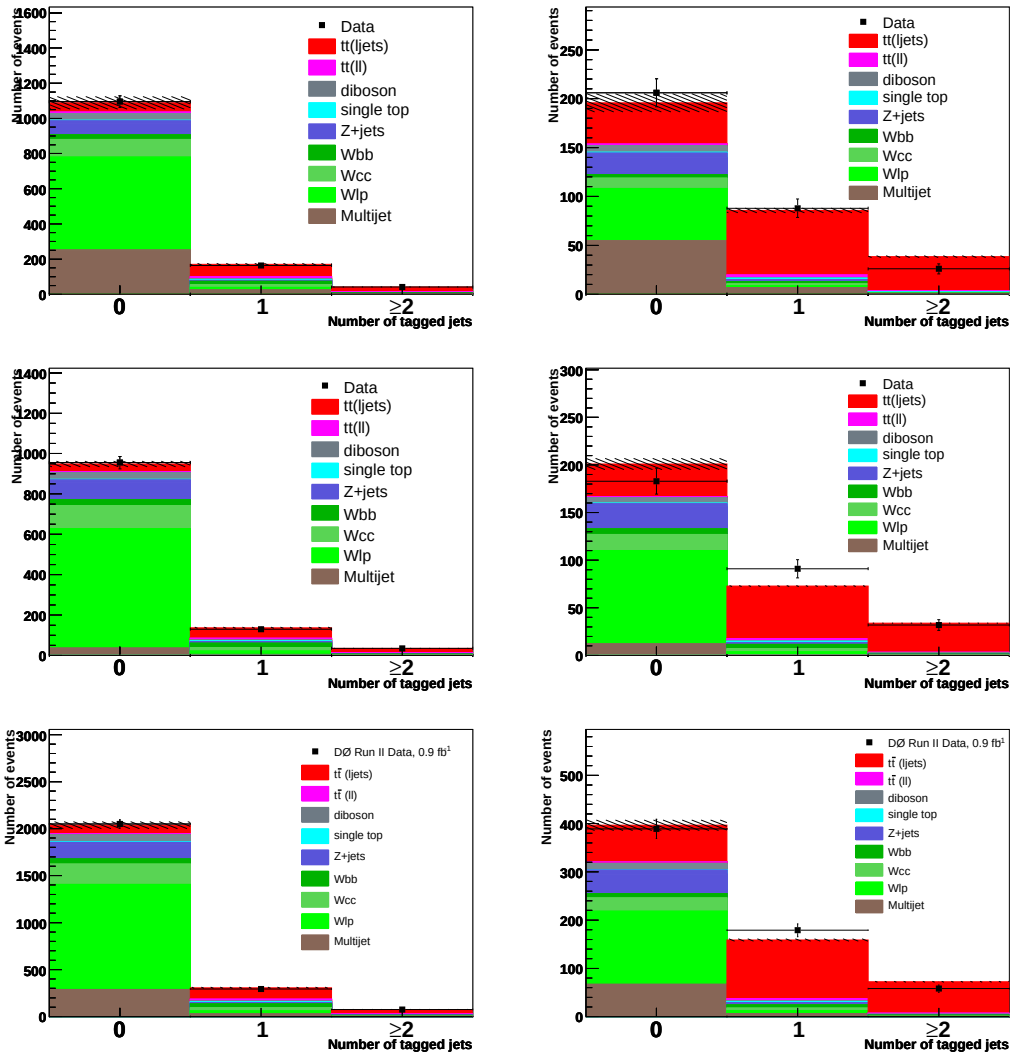

Figure 8.11.: Monte Carlo composition for the 0, 1 and 2 b-tag subsamples. For e+jets (top), μ+jets (middle) and l+jets (bottom). Left plots: exactly three jets. Right plots: at least four jets. For the Medium NN tagger. The $t\bar{t}$ cross section is set to the measured value of 8.18 pb.

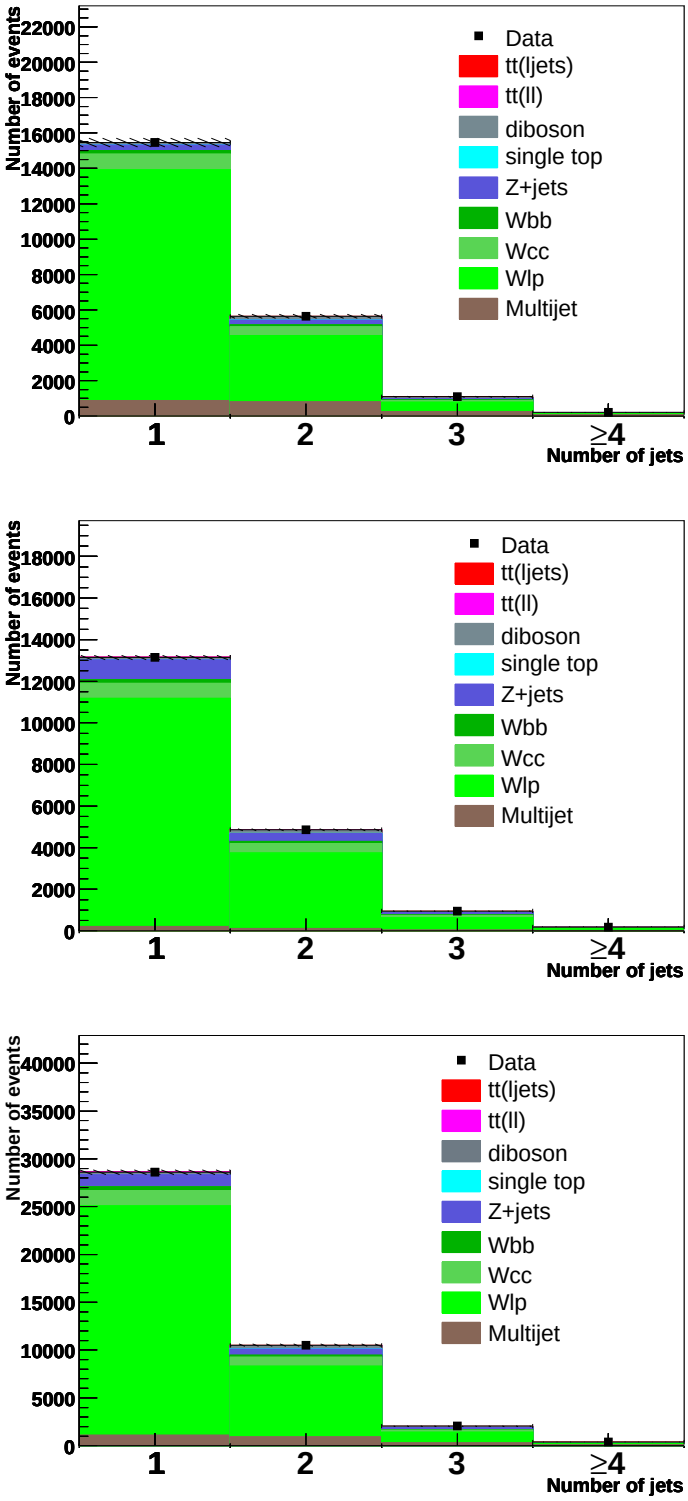

Figure 8.12.: Monte Carlo composition for different jet multiplicity bins in the 0 b-tagged sample. For the Medium NN tagger. For e+jets (top), μ+jets (middle) and l+jets (bottom). The $t\bar{t}$ cross section is set to the measured value of 8.18 pb.

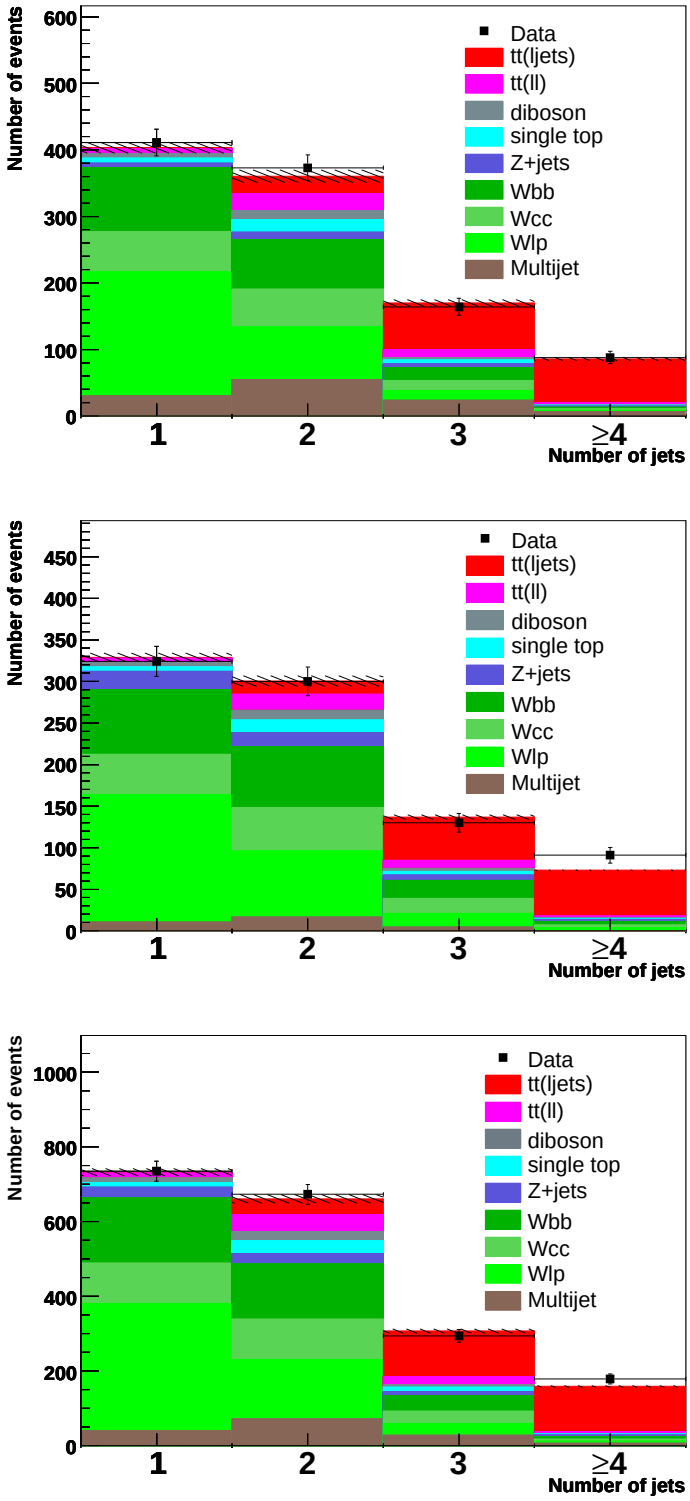

Figure 8.13.: Monte Carlo composition for different jet multiplicity bins in the 1 b-tagged sample. For the Medium NN tagger. For e+jets (top), μ+jets (middle) and l+jets (bottom). The $t\bar{t}$ cross section is set to the measured value of 8.18 pb.

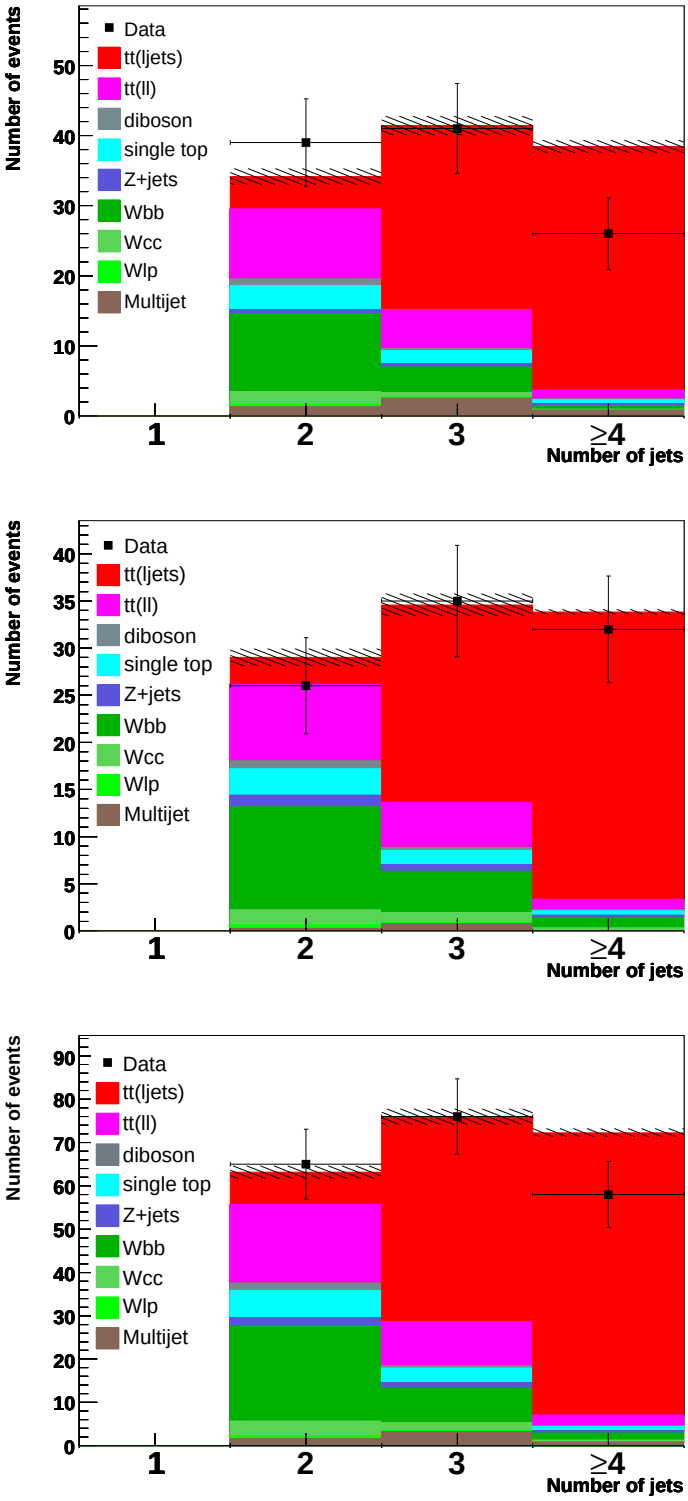

Figure 8.14.: Monte Carlo composition for different jet multiplicity bins in the ≥ 2 b-tagged sample. For the Medium NN tagger. For e+jets (top), μ+jets (middle) and l+jets (bottom). The $t\bar{t}$ cross section is set to the measured value of 8.18 pb.

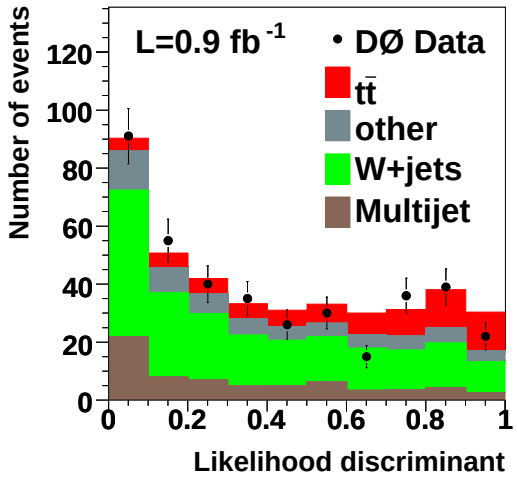

Figure 8.15.: Monte Carlo composition for the topological discriminant in the 0 b-tagged subsample. The Medium NN tagger is used. For the combined l+jets channel. The $t\bar{t}$ cross section is set to the measured value of 8.18 pb.

Tagger	Method	$\sigma(t\bar{t}) \cdot B(t \to Wq)^2$ [pb]	R
Medium	with topological discriminant	$8.18^{+0.90}_{-0.84}$	$0.968^{+0.092}_{-0.083}$
Medium	without topological discriminant	$9.15^{+1.23}_{-1.08}$	$0.876^{+0.102}_{-0.098}$
Tight	with topological discriminant	$7.56^{+0.95}_{-0.87}$	$1.016^{+0.108}_{-0.101}$
Tight	without topological discriminant	$7.91^{+1.16}_{-1.01}$	$0.964^{+0.117}_{-0.115}$
Loose	with topological discriminant	$8.36^{+0.95}_{-0.85}$	$0.982^{+0.083}_{-0.076}$

Table 8.17.: Results on $\sigma \cdot B^2$ and R for different methods and different b-tag working points with the nuisance fit. Statistical and systematic uncertainties are included.

8.6.3. Results for individual channels, for different b-tag working points and methods

In order to check consistency between the e+jets and μ+jets channel and the effect of the topological discriminant in the 0 b-tag subsample, the maximum likelihood fit is repeated for these cases.

In Table 8.17 a comparison between using or not using the topological discriminant is presented. Furthermore, the tight and loose NN b-tag working points are used for the fit. In all cases the nuisance parameter fit is applied. It can be seen from the table that the results are consistent within uncertainties.

Not using the topological discriminant results in higher uncertainties. On R, the relative uncertainty improves from $\sim$ 11 % without the topological discriminant to $\sim$ 9 % when including the discriminant. The effect of the discriminant on $\sigma \cdot B^2$ is an improvement from 13 % to 11 %.

In Table 8.18 the results for the individual e+jets and μ+jets channels are presented for the nuisance parameter fit method. In the μ+jets channel the measured R is higher than in the e+jets channel, which is compatible with the low number of $t\bar{t}$ events when performing a stand-alone fit of the topological discriminant in the zero b-tagged subsample, as shown in Fig. 8.8. Furthermore, the higher value of R is consistent with the observation in Fig. 8.11, where a trend towards more b-tags in data can be seen. The lower result for R in the e+jets final state is also consistent with the observation in Fig. 8.11. Within uncertainties, the individual results from the e+jets and μ+jets channel are consistent with each other.

In Table 8.19 the results of the cross section and R measurement for different top quark masses are listed. The results are shown with the statistical uncertainty only. The relative systematic uncertainty is assumed to be independent as function of the top quark mass. The fitted $\sigma(p\bar{p} \to t\bar{t}) \cdot B(t \to Wq)^2$ and R as function of the top quark mass are shown in Fig. 8.16. The measured cross section as function of the top quark mass are compared to the calculations from Kidonakis [15] and Cacciari [17]. A more detailed study of the dependence of the cross section on the top quark mass is given in section 9.2. While the cross section measurement shows a small dependence on the top quark mass, the measurement of R shows no dependency within the studied range.

Channel	$\sigma(t\bar{t}) \cdot B(t \to Wq)^2$ [pb]	R
l+jets	$8.18^{+0.90}_{-0.84}$	$0.968^{+0.092}_{-0.083}$
e+jets	$8.45^{+1.61}_{-1.13}$	$0.853^{+0.117}_{-0.109}$
μ+jets	$8.25^{+1.16}_{-1.06}$	$1.053^{+0.113}_{-0.100}$

Table 8.18.: Results for the e+jets, μ+jets and combined channels, using the nuisance parameter fit for the Medium Tagger.

Top-Mass	$\sigma(t\bar{t}) \cdot B(t \to Wq)^2$ [pb]	R
165GeV	$9.14^{+0.76}_{-0.72}$	$0.949^{+0.070}_{-0.068}$
170GeV	$8.63^{+0.70}_{-0.67}$	$0.962^{+0.068}_{-0.066}$
175GeV	$8.18^{+0.67}_{-0.64}$	$0.968^{+0.067}_{-0.065}$
180GeV	$7.87^{+0.66}_{-0.62}$	$0.963^{+0.068}_{-0.066}$

Table 8.19.: Results of R and $\sigma_{t\bar{t}}$ for different top masses in the l+jets channel. For the nuisance parameter fit and medium NN b-tagger. Only statistical uncertainties are included.

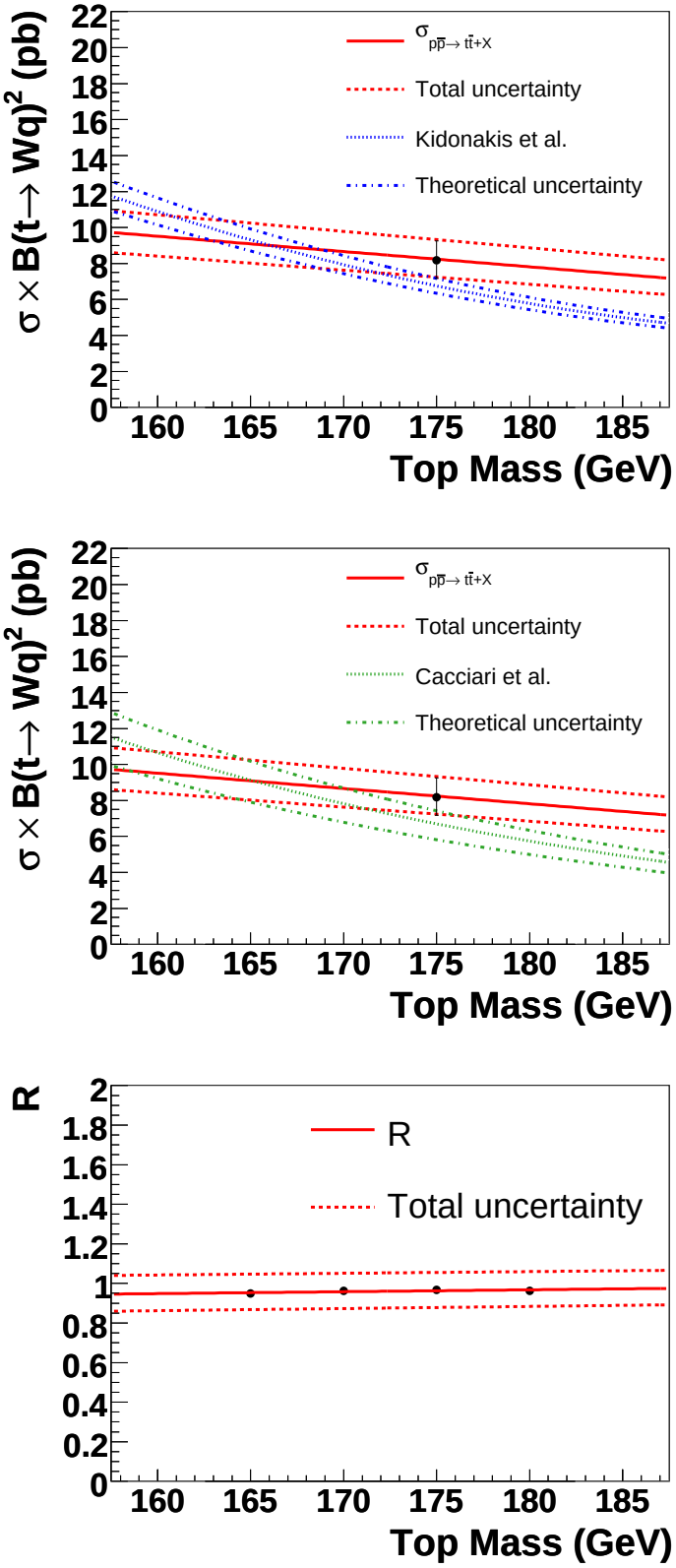

Figure 8.16.: Fitted $\sigma(p\bar{p} \rightarrow t\bar{t}) \cdot B(t \rightarrow Wq)^2$ (top: compared to Kidonakis, middle: compared to Cacciari) and fitted R (bottom) as function of the top quark mass.

8.6.4. Result for $\sigma_{t\bar{t}}$ with $R = 1$

The fitting procedure can be repeated with constraining one of the two observables. Fixing $R = 1$ results in a standard top pair production cross section measurement. In contrast to the standard cross section measurement with b-tags [11], the topological discriminant in the zero b-tagged subsample can give additional sensitivity.

Table 8.20 lists the measured $\sigma_{t\bar{t}}$ for the combined l+jets channel, with and without the topological discriminant in the 0 b-tag sample. As can be seen, the statistical and systematic uncertainties with the topological discriminant are a bit smaller than without. The statistical uncertainty of the measured top quark pair production cross section with R fixed is smaller than for the simultaneous measurement. This behaviour is expected for correlated observables due to the increasing statistical uncertainty when increasing the number of free parameters. The systematic uncertainty, on the other hand, increases for the measurement with R fixed. Comparing the systematic uncertainties for the one dimensional measurement of $\sigma \cdot B^2$ to the result from the simultaneous fit, as shown in Table 8.21, it can be noticed that the systematic uncertainty on the b-tag TRF dominates for the one dimensional measurement. In the simultaneous measurement the b-tag TRF uncertainty is almost completely absorbed by R, reducing the dependency of the cross section on the b-tag probability.

The measurements of R and $\sigma \cdot B^2$ both have the systematic uncertainty of the same order as the statistical one. With few more data both results will be limited by the systematic error. Assuming the same uncertainty on the b-tagging, the simultaneous measurement will result in a smaller uncertainty on $\sigma \cdot B^2$ compared to the one dimensional fit for increasing statistics, due to the b-tag uncertainty being almost completely absorbed in R.

Method	$\sigma_{t\bar{t}}$ standard [pb]
with topological discriminant	$8.08^{+0.53}_{-0.52}$ (stat)$^{+0.744}_{-0.736}$ (syst) $\pm$ 0.49 (lumi)
without topological discriminant	$8.19^{+0.55}_{-0.53}$ (stat)$^{+0.790}_{-0.768}$ (syst) $\pm$ 0.50 (lumi)
with topological discriminant, $\geq$ 4 jets	$8.20^{+0.70}_{-0.67}$ (stat)$^{+0.953}_{-0.966}$ (syst) $\pm$ 0.50 (lumi)
	$\sigma_{t\bar{t}}$ with nuisance parameter fit [pb]
with topological discriminant	$8.10^{+0.87}_{-0.81}$ (stat+syst) $\pm$ 0.49 (lumi)
without topological discriminant	$8.54^{+0.97}_{-0.91}$ (stat+syst) $\pm$ 0.52 (lumi)
with topological discriminant, $\geq$ 4 jets	$8.15^{+1.09}_{-1.03}$ (stat+syst) $\pm$ 0.50 (lumi)

Table 8.20.: Results for $\sigma_{t\bar{t}}$ with $R = 1$ fixed. The result for the Medium NN Tagger with and without using the topological discriminant are shown. For the standard method and the nuisance parameter fit.

8.6.5. Limits on R and V_{tb}

By definition the physically allowed region of R goes from zero to one. As the measurement of R comes out close to the upper boundary, a lower limit on R can be extracted. Furthermore, a lower limit on the CKM matrix element $|V_{tb}|$ can be set.

Summary of systematics on cross section with standard method				
	$\sigma \cdot B^2$ [pb] (2D fit)		$\sigma \cdot B^2$ [pb] ($R = 1$ fixed)	
Systematics source	$+\sigma$	$-\sigma$	$+\sigma$	$-\sigma$
Event preselection	0.237	-0.228	0.233	-0.224
Muon identification	0.091	-0.090	0.084	-0.084
Electron identification	0.114	-0.112	0.117	-0.115
Lumi reweight	0.041	-0.040	0.040	-0.040
Z pT reweight	0.005	-0.005	0.003	-0.003
signal modeling	0.000	-0.333	0.000	-0.259
EM triggers	0.053	-0.027	0.055	-0.028
Muon triggers	0.110	-0.101	0.102	-0.093
Jet triggers	0.017	-0.017	0.017	-0.017
Jet energy scale	0.486	-0.330	0.403	-0.336
Jet energy resolution	0.014	-0.000	0.012	-0.000
JetID	0.143	-0.149	0.143	-0.143
Taggability	0.091	-0.088	0.176	-0.172
Flavor dependence of taggability	0.000	-0.000	0.000	-0.009
b-tag TRF	**0.098**	**-0.089**	**0.408**	**-0.385**
c-tag TRF	0.056	-0.055	0.067	-0.066
light tag TRF	0.060	-0.059	0.054	-0.054
b fragmentation	0.099	-0.097	0.102	-0.099
ϵ_{QCD} in e+jet channel	0.014	-0.013	0.004	-0.013
ϵ_{sig} in e+jet channel	0.000	-0.018	0.000	-0.018
ϵ_{QCD} in μ+jet channel	0.022	-0.006	0.013	-0.009
ϵ_{sig} in μ+jet channel	0.000	-0.034	0.000	-0.028
MC background x-section	0.038	-0.038	0.036	-0.036
MC bkg scale factors	0.047	-0.047	0.044	-0.043
MC statistics on W fractions	0.020	-0.020	0.019	-0.019
MC statistics	0.023	-0.023	0.025	-0.025
W+jets heavy flavour scale factor	0.242	-0.242	0.216	-0.215
PDF	0.041	-0.043	0.023	-0.020
Statistics for matrix method	0.134	-0.133	0.114	-0.111
Total systematic	0.685	-0.666	0.744	-0.736

Table 8.21.: Systematic uncertainties for $\sigma_{t\bar{t}}$ with $R = 1$ fixed (right) compared to the simultaneous fit result (left) in the combined l+jets channel for the standard method. The Medium NN Tagger and the topological discriminant in the 0 b-tag subsample are used. The column for the simultaneous fit result corresponds to Table 8.15.

The limit setting procedure follows the likelihood ratio ordering principle from Feldman and Cousins [37], as described in section 3.2. For twenty-one true values R_{true} between zero and one, in steps of 0.05, 10.000 sets of pseudo-experiments were generated. All yields for signal, Monte Carlo background and multijet backgrounds were varied according to the Poisson distribution around the prediction for the measured $t\bar{t}$ cross section value. The systematic uncertainty is taken into account by varying all nuisance parameters according to a Gaussian distribution with mean zero and standard deviation one.

For each set of ensembles a histogram with the distribution of the measured value R_{meas} is filled, and fitted with an asymmetric Gaussian. In order to interpolate between the R_{true} values, the mean and the two sigmas of the fitted Gaussian are plotted versus R_{true}, shown in Fig. 8.17.

Using in total 1000 interpolated values of R_{true} between zero and one, the 68 %, 95 % and 99%

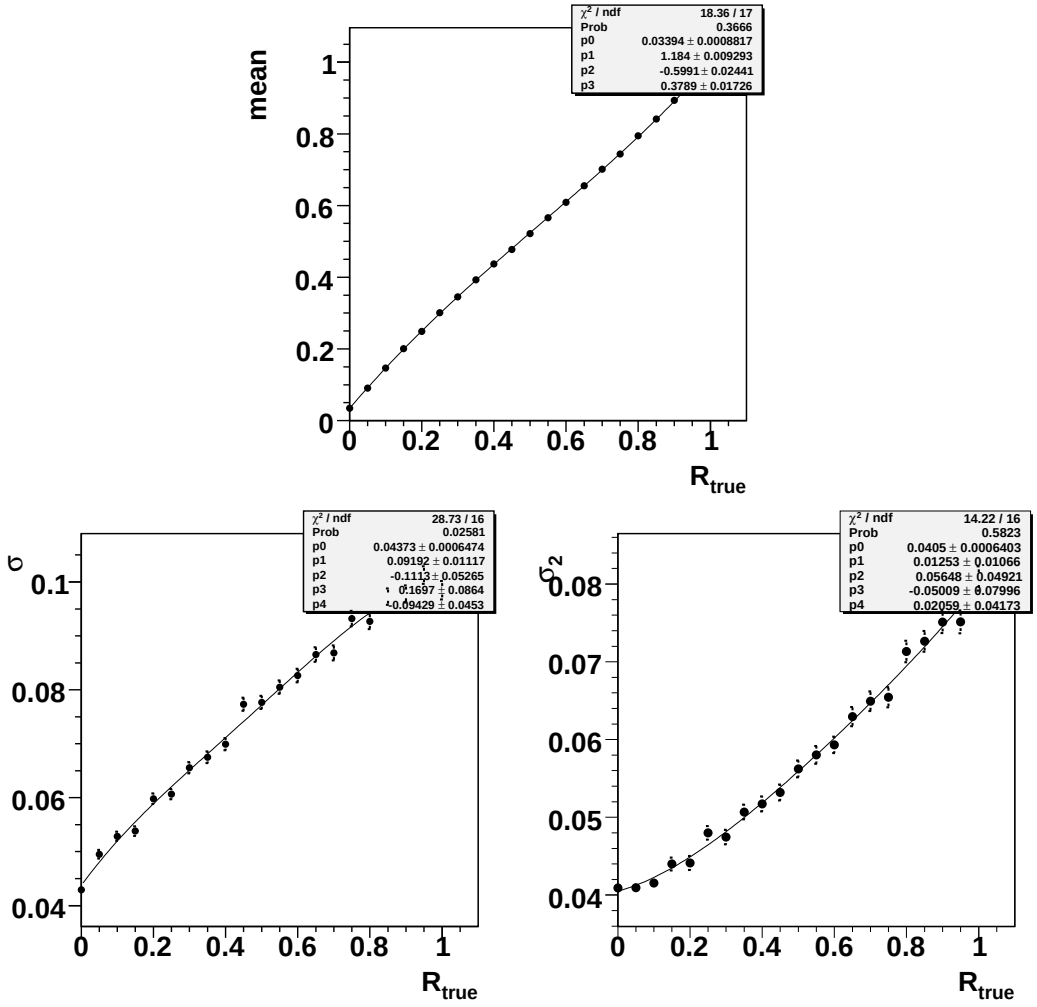

Figure 8.17.: Mean and sigma up and down of the fitted Gaussian for the different R_{true}. Top: Fitted mean. Bottom left: Sigma to upper side of the fitted Gaussian. Bottom right: Sigma to lower side of the fitted Gaussian.

regions of R_{meas} are determined. In Fig. 8.18 the 68%, 95% and 99% Confidence Level bands for R_{true} as a function of R_{meas} are presented. For the measured value of $R = 0.968$ the lower limits are

$$68\ \%\ C.L. : R > 0.879$$
$$95\ \%\ C.L. : R > 0.787$$

The extraction of lower limits on $|V_{tb}|$ is done with two methods. The first method uses the unitary constraint of the CKM matrix and the assumption that only three generations of quarks exist. In that case the denominator in Eq. 8.1 is one, and $|V_{tb}| = \sqrt{R}$. In the second method, these assumptions are dropped. $|V_{tb}|$ can then be extracted by solving Eq. 8.1 for $|V_{tb}|$. The latter results in

$$V_{tb}^2 = \frac{R}{1-R}(V_{ts}^2 + V_{td}^2). \tag{8.25}$$

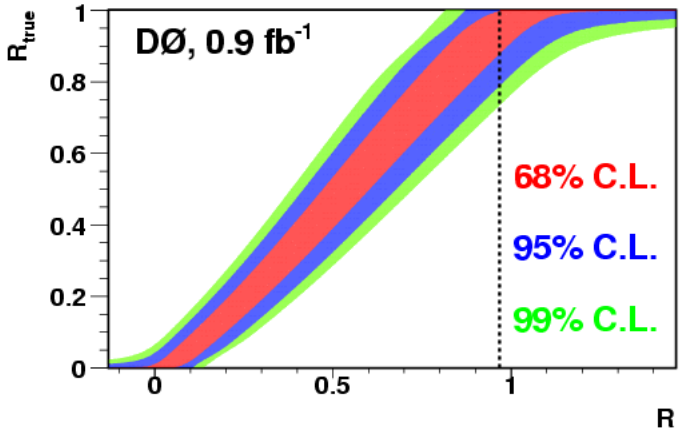

Figure 8.18.: The 68 % (inner band), 95 % (middle band) and 99 % (outer band) Confidence Level bands for R_{true} as a function of R_{meas}. The dashed line corresponds to the measured value.

As the measured values of V_{ts}^2 and V_{td}^2 use the assumption of $V_{tb}^2 = 1$, an upper limit is set on

$$\frac{1-R}{R} = \frac{(V_{ts}^2 + V_{td}^2)}{V_{tb}^2}. \tag{8.26}$$

Assuming three generations of quarks, the lower limit on $|V_{tb}|$ can be set to:

$$68\ \%\ C.L. : |V_{tb}| > 0.935$$
$$95\ \%\ C.L. : |V_{tb}| > 0.884$$

Using Eq. 8.26 the upper limit on $\frac{1-R}{R}$ yields:

$$68\ \%\ C.L. : \frac{(V_{ts}^2 + V_{td}^2)}{V_{tb}^2} < 0.141$$
$$95\ \%\ C.L. : \frac{(V_{ts}^2 + V_{td}^2)}{V_{tb}^2} < 0.266$$

8.7. Conclusion and outlook

The simultaneous measurement of R and $\sigma \cdot B^2$ presented with 900 pb^{-1}, yields

$$\begin{aligned} R &= 0.968^{+0.092}_{-0.083} \text{ (stat+syst)} \\ \sigma(p\bar{p} \to t\bar{t}) \cdot B^2(t \to Wq) &= 8.18^{+0.90}_{-0.84} \text{ (stat+syst)} \pm 0.50 \text{ (lumi) pb.} \end{aligned}$$

Both measured values, R and $\sigma(p\bar{p} \to t\bar{t}) \cdot B^2(t \to Wq)$, are consistent with theoretical calculations within their uncertainty. Using 230 pb^{-1} of data, DØ has measured R to be $1.03^{+0.19}_{-0.17}$ (stat+syst) [151]. The discussed analysis uses the same method to extract R with improved handling of the efficiency and event b-tag probability for the $t\bar{t} \to bq_\ell$ and $t\bar{t} \to q_\ell q_\ell$ samples. More details on the previous measurement can be found in [152]. The CDF collaboration did a measurement of R in 2005, fixing the $t\bar{t}$ cross section to the theoretical calculation [153, 154].

Figure 8.19 compares the current measurement of R to the existing measurements from CDF and DØ. All measurements are in good agreement with the standard model value of $R = 1$ and in agreement with each other. The uncertainty of the presented measurement is by more than a factor of two decreased compared to the last measurement from DØ, and represents the most precise measurement of R until today.

The $t\bar{t}$ cross section measurement was the most precise single measurement when performed in summer 2007. The recently performed combination of the $t\bar{t}$ cross section with b-tagging and topological information in the l+jets channel results in a cross section of 7.42 ± 0.53 (stat) ± 0.46 (syst) ± 0.45 (lumi) pb [11], yielding a smaller relative uncertainty. Both $t\bar{t}$ cross section measurements are fully in agreement with each other.

As the statistical uncertainty decreases with increasing data sets, the simultaneous measurement with R can result in a more precise cross section measurement due to the correlation and absorption of dominating systematic sources. An extension of topological information in different b-tag subsamples might result in further improvement on both quantities, $\sigma \cdot B^2$ and R.

Besides being interesting in itself, the measurement of R can be combined with the measurement of the single top quark production cross section in the s- and t-channels in order to obtain a measurement of the CKM matrix elements $|V_{tq}|$, without assumptions about the unitarity of the CKM matrix and the number of quark families, as discussed in [155].

At the LHC, which produces a much higher number of $t\bar{t}$ events and will deliver a large instantaneous and integrated luminosity, the uncertainty on the measurement of R will be dominated by the systematic errors. An improvement on R relative to the presented result will rely on the precise understanding of the b-tagging at Atlas and CMS. The inclusion of more final states, as for example the dilepton channel, might help to improve the measurement and certainly opens the possibility of combining the measurement with more or other observables than the $t\bar{t}$ cross section.

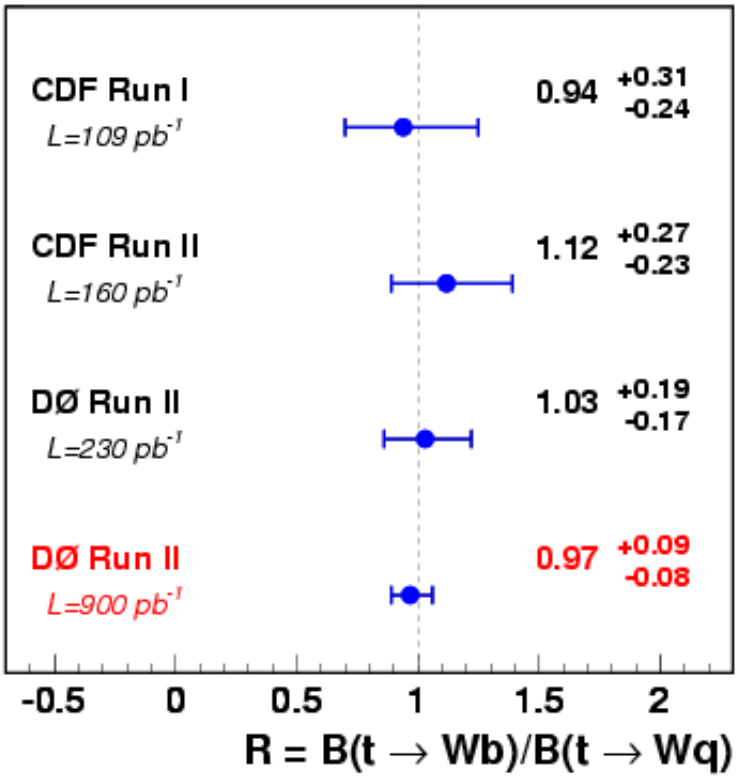

Figure 8.19.: Comparison of R measurements from CDF and DØ.

9. Interpretations of the top quark pair production cross section

In this chapter interpretations of the measured top quark pair production cross section in the l+jets and the dilepton channel are presented. The first interpretation concerns the ratio of the cross section measured in the l+jets over the cross section measured in the dilepton channel. This cross section ratio can be used to set a limit on a simple model involving charged Higgs bosons. A second interpretation is the extraction of the top quark mass from the cross section, by comparing the theoretical prediction of $\sigma_{t\bar{t}}$ to the measured $t\bar{t}$ cross section as function of the top quark mass.

9.1. Measurement of the cross section ratio $R_\sigma = \sigma_{l+\text{jets}}/\sigma_{\text{dilepton}}$

The measurement presented in chapter 8 is based on the assumption that the top quark always decays into a W boson and a b quark: $B(t \to Wb) = 100\%$. From the cross section measured in the l+jets channel and the dilepton channel, the ratio

$$R_\sigma = \frac{\sigma(t\bar{t})_{l+jets}}{\sigma(t\bar{t})_{\text{dilepton}}} \tag{9.1}$$

can be used to study alternative decays beyond the Standard Model [156]. $\sigma(t\bar{t})_{l+jets}$ and $\sigma(t\bar{t})_{\text{dilepton}}$ are the cross sections measured assuming Standard Model branching ratios.

A deviation from the SM prediction $R_\sigma = 1$ would indicate new physics with a non-vanishing branching ratio $B(t \to Xb)$ with X being any particle but the W boson. In particular, X is interpreted as a charged Higgs boson $H^\pm$ in a simple model, where the boson mass is close to the W mass, $B(H^\pm \to cs)$ is 100 % and the event kinematics of the $t \to H^+b$ and $t \to Wb$ decays are similar.

9.1.1. Extraction of the cross section ratio R_σ

For the extraction of the cross section ratio R_σ the measurement of the cross section in the l+jets channel and the dilepton channels are used. In the l+jets channel also dileptonic events contribute. For the ratio it is therefore essential to minimise this contribution. Therefore the l+jets measurement is restricted to the subsample with at least four jets, as the contribution of dilepton events in the l+jets subsample with exactly three jets can not be neglected. Fixing R to one, the cross section in the l+jets channel is measured as

$$\sigma(t\bar{t})_{l+\text{jets}} = 8.27^{+0.96}_{-0.95}\,(\text{stat+syst}) \pm 0.51\,(\text{lumi})\,\text{pb}\,. \tag{9.2}$$

In the $t\bar{t}$ dilepton channel the combination of the channels with two muons ($\mu\mu$), two electrons (ee) or one muon and one electron ($e\mu$) is used [157]:

$$\sigma(p\bar{p} \to t\bar{t})_{\text{dilepton}} = 6.8^{+1.2}_{-1.1}\,(\text{stat})^{+0.9}_{-0.8}\,(\text{syst}) \pm 0.4\,(\text{lumi})\,\text{pb}. \tag{9.3}$$

Pseudo experiments are generated, in order to take the correlation between the systematic uncertainties into account properly. The uncertainties on the lepton identification, primary vertex identification, muon trigger, jet energy calibration, jet identification, jet resolution and the NLO cross section of the diboson background are assumed to be 100% correlated between the l+jets and dilepton channels. All other uncertainties are assumed to be uncorrelated. The uncertainty on the integrated luminosity cancels in the ratio and is excluded.

The generation of ensembles in the l+jets channel is done in the same way as described in section 8.6.5. In the dilepton channel the mean value of the cross section, extracted in each channel, is smeared with a Gaussian distribution in order to take into account the systematic uncertainties. The background yield and the number of observed events then is allowed to fluctuate in each subchannel according to a Poisson distribution.

In order to generate probability densities for measured versus true R_σ, $\sigma(t\bar{t})_{l+\text{jets}}$ is varied from 6 pb to 15 pb in steps of 0.5 pb, and the measured cross section for $\sigma(t\bar{t})_{\text{dilepton}}$ is used as true $\sigma(t\bar{t})_{\text{dilepton}}$. For each R_σ a set of 10.000 ensembles are generated. The set of ensembles for each true R_σ is then fitted with a Gamma distribution

$$f(x) = n\frac{(b(x-s))^{(ab)} \cdot b \cdot e^{-b(x-s)}}{\Gamma(ab+1)} \tag{9.4}$$

where x is the measured value of R_σ, and n, a, b and s are the fit parameters. The Gamma distribution is chosen as it fits best the probability density functions resulting from the ensembles. An interpolation between the different true R_σ can be done in the same way as in section 8.6.5, and continuous confidence intervals are calculated following the Feldman Cousins method.

Figure 9.1 shows the 68 %, 95 % and 99 % Confidence Level bands. The calibrated value of R_σ is extracted by calculating the most probable true R_σ at the point of the measured value of R_σ. The total uncertainty on the calibrated value is given by the 68 % C.L. band.

For the measured value $R_\sigma = 1.22$, obtained by simply dividing the cross sections given in Eq. 9.2 and Eq. 9.3, the final calibrated result comes out as

$$R_\sigma = 1.22^{+0.27}_{-0.26}\ \text{(stat+syst)}$$

The simple division of the cross section in the l+jets by the cross section in the dilepton channel yields $R_\sigma = 1.21 \pm 0.30$, i. e. the uncertainty is only slightly larger than for the result with correct treatment of the systematic uncertainties. This means the correlation between the systematic uncertainties is small.

9.1.2. Extraction of $B(t \to H^+b)$ from the cross section ratio R_σ

A top quark decay into a non-SM particle, which leads to a larger contribution to the l+jets than the dilepton channel, would lead to $R_\sigma > 1$. A simple model is studied, where it is assumed that the top quark can decay into a charged Higgs boson $t \to H^+b$ (and into the charged conjugated state), with $H^+ \to \bar{c}s$ in 100%. The charged Higgs mass is assumed to be 80 GeV and the kinematics is assumed to be the same as for $t \to Wb$.

Such a model with 100 % decay of charged Higgs into jets could be realized in certain Multi-Higgs-Doublet Models (MHDM) [28]. At the Tevatron, such a leptophobic charged Higgs boson with mass about the W mass may be important for $\tan\beta \leq 3.5$ [29]. Another possibility to realise the assumed model are large radiative corrections from SuSy-braking effects, that lead to a suppression of $H^+ \to \tau\nu$ within the MSSM [35]. The measured cross section in the

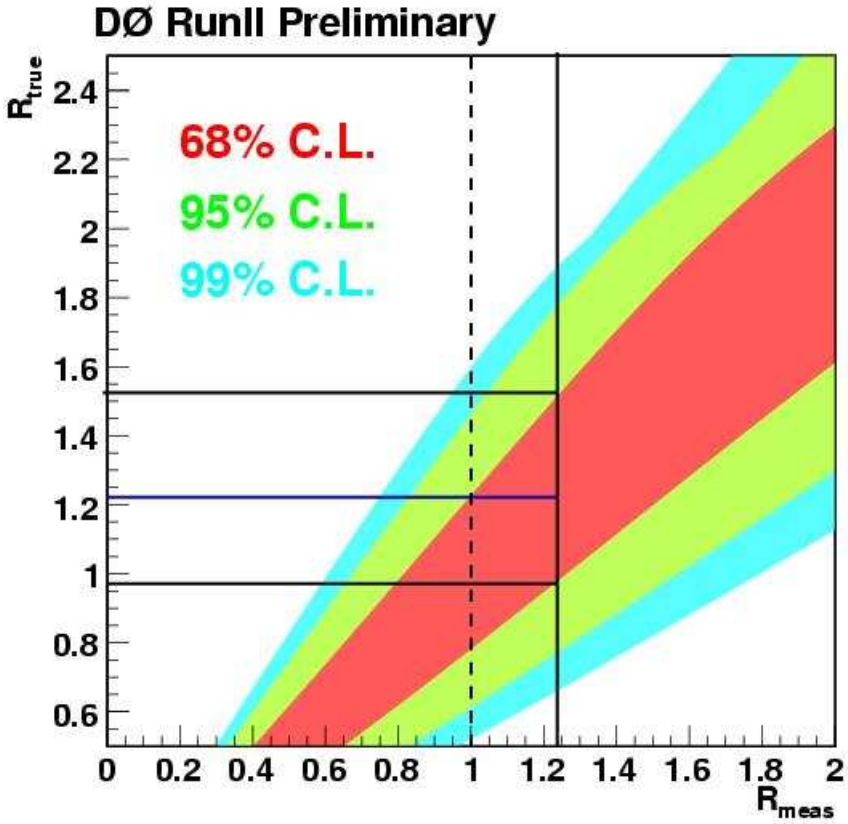

Figure 9.1.: Feldman Cousins confidence level bands for R_σ. R_{true} are the generated values and R_{meas} the measured values of R_σ. The blue line shows the calibrated value, the black lines the one sigma uncertainty. At the vertical black dashed line the expected limit can be extracted.

l+jets channel can be written as

$$\sigma(t\bar{t})_{l+\text{jets}} = \frac{N_{l+\text{jets}}}{\mathcal{L}_{l+\text{jets}}\epsilon^{SM}_{l+\text{jets}}B^{SM}_{l+\text{jets}}} =: \frac{\sigma_{l+\text{jets}}}{B^{SM}_{l+\text{jets}}} \tag{9.5}$$

where $\epsilon^{SM}_{l+\text{jets}}$ is the selection efficiency for $t\bar{t}$ in the l+jets channel, obtained assuming SM production and decay, $B^{SM}_{l+\text{jets}}$ is the branching ratio in the SM decay and $N_{l+\text{jets}}$ are the number of $t\bar{t}$ events in the l+jets final state. $\mathcal{L}_{l+\text{jets}}$ denotes the integrated luminosity used for the cross section measurement in the l+jets channel. $\sigma_{l+\text{jets}}$ is the effective cross section in the l+jets channel.

The measured cross section in the dilepton channel can be written similarly

$$\sigma(t\bar{t})_{\text{dilepton}} = \frac{N_{\text{dilepton}}}{\mathcal{L}_{\text{dilepton}}\epsilon^{SM}_{\text{dilepton}}B^{SM}_{\text{dilepton}}} =: \frac{\sigma_{\text{dilepton}}}{B^{SM}_{\text{dilepton}}} \tag{9.6}$$

In the assumed model the selection efficiency is the same as the one in the SM, therefore

$\epsilon = \epsilon^{SM}_{l+\text{jets}}$. The following definitions, relations and abbreviations are introduced:

$$\begin{aligned} B(W \to l\nu) &= B(W \to e\nu) + B(W \to \mu\nu) + B(W \to \tau\nu \to e\nu\nu) + B(W \to \tau\nu \to \mu\nu\nu) \\ B &:= B(t \to H^+b) = 1 - B(t \to Wb) \\ B^{SM}_{l+\text{jets}} &:= 2 \cdot B(W \to l\nu)B(W \to qq) \\ B^{SM}_{\text{dilepton}} &:= (1 - B(W \to qq))^2 \end{aligned} \tag{9.7}$$

and $\sigma_{t\bar{t}}$ is the $t\bar{t}$ production cross section, independent of the top quark decay.

Due to the dilepton contribution in the l+jets channel one can write

$$\sigma_{l+\text{jets}} = \sigma_{t\bar{t}} \cdot \{2(1-B)B(W \to l\nu) \cdot [(1-B)B(W \to qq) + B] + k \cdot (1-B)^2 [1 - B(W \to qq)]^2\} \tag{9.8}$$

where $k = \frac{\epsilon^{SM}_{\text{dilepton}}(l+\text{jets})}{\epsilon^{SM}_{l+\text{jets}}}$, and $\epsilon^{SM}_{\text{dilepton}}(l+\text{jets})$ is the probability for dileptonic events to pass the l+jets selection.

In the dilepton channel σ_{dilepton} is

$$\sigma_{\text{dilepton}} = \sigma_{t\bar{t}} \cdot B^2(t \to Wb) \cdot B^2(W \to l\nu) \tag{9.9}$$

Inserting Eq. 9.5 and 9.6 into Eq. 9.1 yields

$$R_\sigma = \frac{\sigma_{l+\text{jets}} B^{SM}_{\text{dilepton}}}{\sigma_{\text{dilepton}} B^{SM}_{l+\text{jets}}} = 1 + \frac{B}{1-B} \cdot \frac{1}{B(W \to qq) + 0.5 \cdot k \cdot A} \tag{9.10}$$

with $A = [1 - B(W \to qq)]^2 / B(W \to l\nu)$.

Solving Eq. 9.10 for $B(t \to H^+b)$ results in the final formula

$$B(t \to H^+b) = \frac{(B(W \to qq) + 0.5 \cdot k \cdot A) \cdot (R_\sigma - 1)}{1 + (B(W \to qq) + 0.5 \cdot k \cdot A)(R_\sigma - 1)} \tag{9.11}$$

The factor k is 0.064 for the average over the e+jets and μ+jets final states. This value is calculated by inserting the selection efficiencies $\epsilon^{SM}_{e+\text{jets}} = 0.1116$ and $\epsilon^{SM}_{\mu+\text{jets}} = 0.0984$. The efficiencies $\epsilon^{SM}_{\text{dilepton}}(e+\text{jets}) = 0.0072$ and $\epsilon^{SM}_{\text{dilepton}}(\mu+\text{jets}) = 0.0062$ are taken for the dilepton events, respectively. With $B(W \to qq) = 0.676$ and $B(W \to l\nu) = 0.25$ all parameters except for R_σ are fixed in Eq. 9.10.

In order to extract the calibrated value of B and set limits, the same procedure of generating ensembles as for R_σ is repeated. An asymmetric Gaussian distribution is used for the fit to the distributions for each true B. The measured branching ratio is

$$B(t \to H^+b) = 0.13^{+0.12}_{-0.11} \text{ (stat+syst)} \tag{9.12}$$

As no deviation from the Standard Model value of $B(t \to H^+b) = 0$ can be observed limits on $B(t \to H^+b) = 0$ are set. The limit setting yields an observed limit of

$$B(t \to H^+b) < 0.35 \tag{9.13}$$

at 95 % Confidence Level, and an expected limit for $B = 0$ of

$$B(t \to H^+b) < 0.25 \tag{9.14}$$

at 95 % Confidence Level, assuming $m_{H^+} = m_W$.

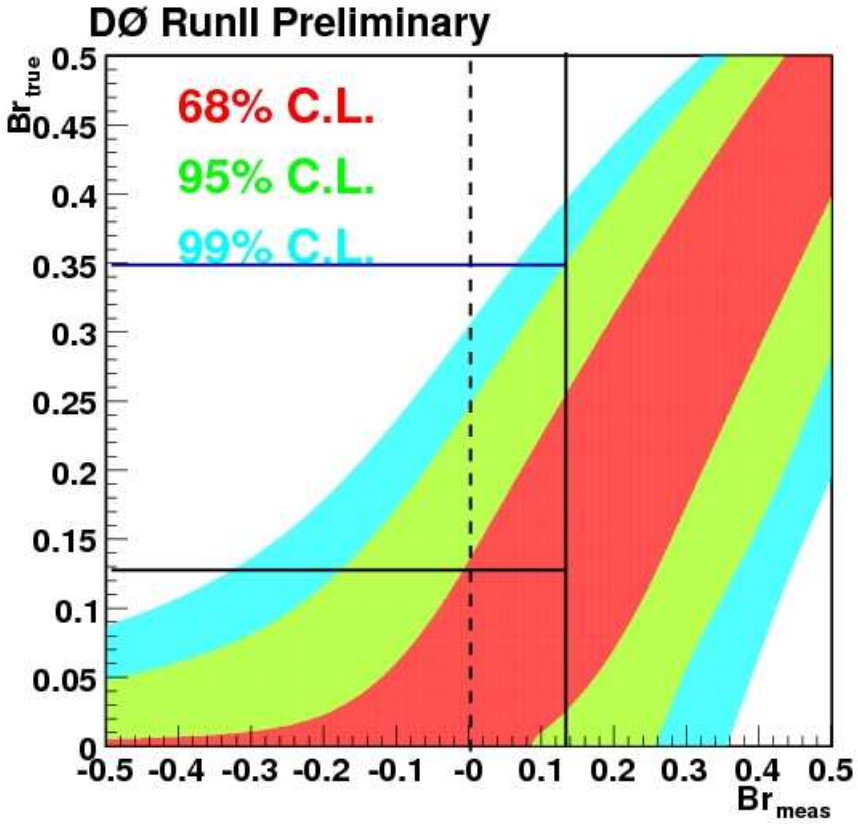

Figure 9.2.: Feldman Cousins confidence level bands for $B = B(t \to H^+b)$. B_{true} are the generated values and B_{meas} the measured values of B. The horizontal lines show the calibrated value and the 95 % Confidence Level limit. At the vertical black dashed line the expected limit can be extracted.

9.1.3. Conclusion

The cross section ratio has been measured by the DØ collaboration in Run I with 125 pb^{-1} [14]. A newer result has been published by CDF, measured with 200 pb^{-1} of data in Run II [158]. At CDF the inverse of the cross section ratio was measured to be $1/R_\sigma = 1.45^{+0.83}_{-0.55}$. Based on the measurement a limit was set on the $t \to Xb$ decay, where hadronically decaying X and equal event kinematics of the standard and non-standard decay are assumed. The reported limit from CDF is $B(t \to Xb) < 0.46$ at 95 % Confidence Level. The analysis presented here shows an almost 30 % improvement compared to the previous limit of CDF.

The limit on the leptophobic charged Higgs model represents an example of how to extract further information using already analysed results. The ratio R_σ is also interesting on its own, as many systematic uncertainties, like the luminosity error, cancel. Deviations from the Standard Model expectation of $R_\sigma = 1$ can be interpreted as a sign for new physics.

9.2. Extraction of the top quark mass from the cross section measurement

The $t\bar{t}$ cross section is extracted for several different top quark masses. Reversely, this dependence can be exploited to measure the top quark mass using the cross section measurement by comparison with the theoretical predictions. As part of this thesis the experimental input to the mass extraction from cross section has been delivered.

The value of the quark masses depends on the renormalisation scheme [159–161]. For the extraction of this parameter, which is for example an important parameter in electroweak fits, it is therefore essential to use a well-defined renormalisation scheme. Direct top quark mass measurements, like for example with template, ideogram, neutrino weighting or matrix element methods, use top mass information from $t\bar{t}$ Monte Carlo. The simulation only uses leading-order matrix elements, followed by parton showers, in which the renormalisation scheme is not well-defined.

An alternative measurement of the top quark mass is the extraction from the $t\bar{t}$ cross section measurements [10, 11]. Besides the simplicity of the cross section measurement in contrast to the complicated and advanced methods used in direct top quark mass measurements, the cross section extraction does not rely on the simulation except for the determination of selection and b-tag efficiencies. Topological and kinematical distributions are not expected to change much with additional NLO corrections. Furthermore, complementary information can be extracted, since the experimental uncertainties in direct top quark mass measurements are different to the experimental uncertainties in cross section measurements.

The top mass extraction from the cross section measurement is done by comparing the measured cross section as function of the top quark mass with two theoretical calculations from Kidonakis [15] and Cacciari [17]. The calculations are fully inclusive calculations in higher-order QCD including soft gluon resummations, representing the most complete calculations available. They are computed using the pole mass definition for the top quark mass. Therefore extracting the top quark mass from the comparison of those calculations with the cross section measurement results in the pole mass. In a very simple extraction, described in detail in [10], the systematic uncertainties from the measured cross section are assumed to be independent from the theoretical cross section uncertainty. The cross section values, measured simultaneously with the ratio of branching fractions R, presented in Table 8.19 in section 8.6, are used for the extraction.

Figure 9.3 (left) shows the measured cross section compared to the calculation from Kidonakis, while Fig. 9.3 (right) shows the comparison to the calculation from Cacciari. The intersection of the parametrisation of the measured cross section and the theory calculation gives the central value of the top quark mass. The intersections of the error bands yield the systematic uncertainty. The top quark mass comes out as

$$M_t = 166.9^{+5.9}_{-5.2}\,\text{(stat+syst)}^{+3.7}_{-3.8}\,\text{(theory) GeV [10]} \tag{9.15}$$

when compared to Kidonakis and

$$M_t = 166.1^{+6.1}_{-5.3}\,\text{(stat+syst)}^{+4.9}_{-6.7}\,\text{(theory) GeV [10]} \tag{9.16}$$

for the comparison to Cacciari.

The same extraction of the top mass from cross section is done for the dilepton channel, resulting in masses fully in agreement with Eq. 9.15 and 9.16. All extracted top masses are in agreement with the world average top quark mass from direct mass measurements of 172.6 ± 1.4 GeV.

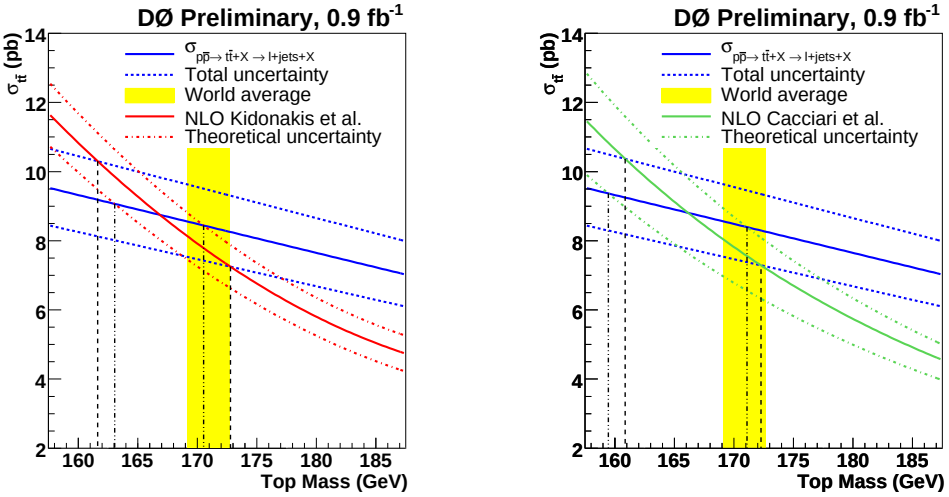

Figure 9.3.: Top mass extraction from $t\bar{t}$ cross section with theory calculation from Kidonakis (left) and Cacciari (right) [10]. The vertical lines show the intersections that are used to determine the uncertainty on the top mass. At the time of the cross section extraction the world average top quark mass was 170.9 ± 1.9 GeV.

The presented measurement represents the first extraction of the top quark mass from a cross section measurement. Based on the combined $t\bar{t}$ cross section in the l+jets channel from a topological and b-tag analysis, a more elaborated analysis has been developed from the simple interpretation [11]. This procedure is repeated on the top pair production cross section combination in the l+jets, dilepton and τ+lepton channel, which will be discussed in section 11.1. The extraction of the top quark mass from that cross section is discussed here briefly [162].

Improved extraction on a more recent dataset

A more elaborate procedure to extract the top quark mass from a cross section measurement [162] is based on the combined measurement of $\sigma_{t\bar{t}}$ in the l+jets, dilepton and τ+lepton channel. The combination of the cross section will be discussed in section 11.1 together with the search for charged Higgs bosons. The cross section values obtained with the nuisance method from Table 11.6 are used. The measurement is compared to a new NLO QCD calculation including soft-gluon resummation in next-to-leading logarithms (NLL) [163] and a calculation that contains all logarithms in NNLL that are relevant for a next-to-next-to-leading order (NNLO) calculation. The latter is therefore called $\text{NNLO}_{\text{approx}}$ [18, 19]. The PDF set is updated to CTEQ6.6 [20].

In contrast to the simple extraction by using the intersections, a method based on a likelihood is used here. Each experimental cross section result is represented as a Gaussian likelihood function centred around the measured value and including all systematic uncertainties.

The uncertainty on the theory calculation is dominated by two sources of systematic errors: The uncertainty on the parton distribution function and on the variation of the factorisation and renormalisation scale. The factorisation and renormalisation scale are set to the top mass. The scale uncertainty is estimated by changing both scales to half and twice the top quark mass. While the PDF uncertainties are modelled by a Gaussian likelihood, the scale uncertainty is represented by a constant within the ranges of the systematic uncertainty and zero

elsewhere. Both functions are convoluted, and the resulting theory likelihood is multiplied with the experimental one.

The influence of the choice of the step function for the scale uncertainty has been checked by using 90 % confidence level for the central region and 10 % for twice the region or including the relation of cross sections and the scale into the function [164]. No effect of the different choices on the resulting top mass uncertainty can be observed.

The final likelihood function depends on the $t\bar{t}$ cross section and top mass. By integration over the cross section space the joint likelihood function only depends on the top quark mass. The minimum of this likelihood yields the central top quark mass and the integration over the top quark mass results in the 68 % confidence region.

The extraction of the top quark mass yields

$$M_t = 167.8 \pm 5.7 \text{ (stat+syst) GeV [162]} \tag{9.17}$$

when compared to NLO+NLL [163], and

$$M_t = 169.6^{+5.4}_{-5.5} \text{ (stat+syst) GeV [162]} \tag{9.18}$$

for the comparison to $\text{NNLO}_{\text{approx}}$ [18]. The theoretical and experimental cross section as function of the top mass together with the joint likelihood function are shown in Fig. 9.4.

All extracted top quark masses are in agreement with the world average value of 172.6 ± 1.4 GeV within the given uncertainties. However, it has to be stressed that the top mass extracted from the cross section measurement is not necessarily the same quantity as the world average. While the first gives the top mass in its pole mass definition, for the latter it is still under discussion to which mass scheme the value corresponds.

The uncertainty on the mass extracted from the cross section measurement has still a large uncertainty. A smaller uncertainty could be achieved by a flatter dependency of the measured cross section from the top mass. This would require a loosening of cuts like the leading jet p_T cut in the l+jets channel, in which the efficiency to pass the cut depends on the phase space of the b-quark from top decay and thus on the top quark mass.

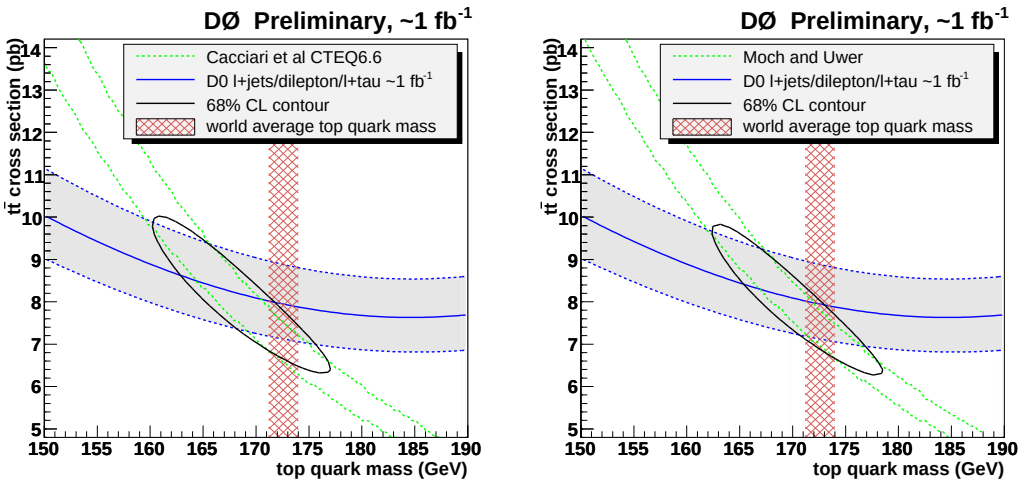

Figure 9.4.: Top mass extraction from combined $t\bar{t}$ cross section with theory calculation from Cacciari (left) and Moch and Uwer (right). The joint likelihoods are shown as well [162].

10. Search for Higgs bosons in the $t\bar{t}H$ channel

The top quark is the heaviest known quark, and has therefore the strongest coupling to the Higgs boson. The associated production of a Higgs boson and a top-antitop quark pair is the only channel where the Yukawa coupling of the top quark and the Higgs boson can be studied directly. Based on the simultaneous measurement of $\sigma \cdot B^2$ and the ratio of branching fractions R, a search for the Higgs boson in the $t\bar{t}H$ channel is derived [165, 166]. The $t\bar{t}$ and $t\bar{t}H$ cross sections are fitted simultaneously, using events with 3, 4 and ≥ 5 jets and 0, 1, 2 and ≥ 3 b-tags. The Higgs boson is assumed to decay into a bottom-antibottom quark pair. This decay dominates for light Higgs, as shown in Fig. 2.5 (right) in section 2.1.3. Limits are set with the Feldman Cousins limit setting procedure.

Based on the idea of the simultaneous measurement an extension is performed, including topological information. The limit setting is done with a modified frequentist approach, as described in [42, 43] and outlined briefly in section 3.3. This limit setting procedure has the advantage that Higgs searches in other channels use it. The common use of one method of limit setting simplifies the combination of the different searches.

10.1. Data, Monte Carlo and predicted yields

For the simultaneous fit of $\sigma_{t\bar{t}}$ and $\sigma_{t\bar{t}H}$, the same data sample and backgrounds are used as for the measurement of the ratio of branching fractions R. For each sample Standard Model couplings are assumed. The $t\bar{t}H$ signal sample is simulated with PYTHIA for various Higgs masses between 105 and 155 GeV. The factorisation scale is set to $((2m_t + m_H)/2)^2 = (m_t + m_H/2)^2$ and the CTEQ6L1 PDF is used.

The event selection criteria are exactly the same as in the measurement of R, described in section 8. Subsamples with ≥ 4 jets and ≥ 2 b-tags are further split into samples with 4 and ≥ 5 jets as well as 2 and ≥ 3 b-tags. Figure 10.1 shows the selection efficiency before b-tagging for the $t\bar{t}H$ sample versus Higgs mass. As can be seen, the selection efficiency increases with increasing Higgs mass for events with ≥ 5 jets, but decreases a bit in the subsample with 4 jets. As the momentum of the two jets from the Higgs increases with increasing Higgs mass, the probability to reconstruct five jets with $p_T \geq 20$ GeV increases. In Fig. 10.2 the 1, 2 and ≥ 3 b-tag probability versus Higgs mass are plotted. The probability is constant with the Higgs mass, as expected because of constant Tag Rate Functions for jet p_T of $\simeq 30$ GeV and larger (see section 5.7 for details).

Table 10.1 shows the number of expected and observed events in different jet and b-tag multiplicity subsamples. The assumed $t\bar{t}$ cross section is 7.3 pb, i. e. the theory prediction at a top quark mass of 172.6 GeV. The $t\bar{t}H$ cross sections is set to the Standard Model prediction as shown in Fig. 2.5 (left) in section 2.1.3.

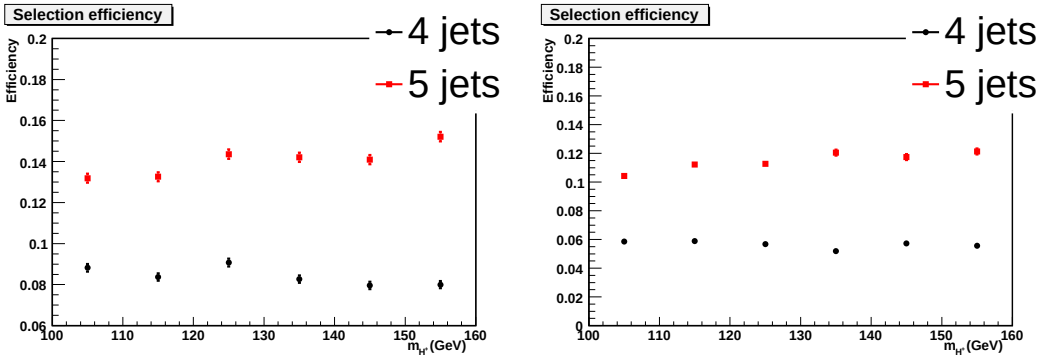

Figure 10.1.: Selection efficiency of $t\bar{t}H$ versus Higgs mass in the 4 and $\geq$ 5 jet multiplicity sample. Left: e+jets; Right: μ+jets.

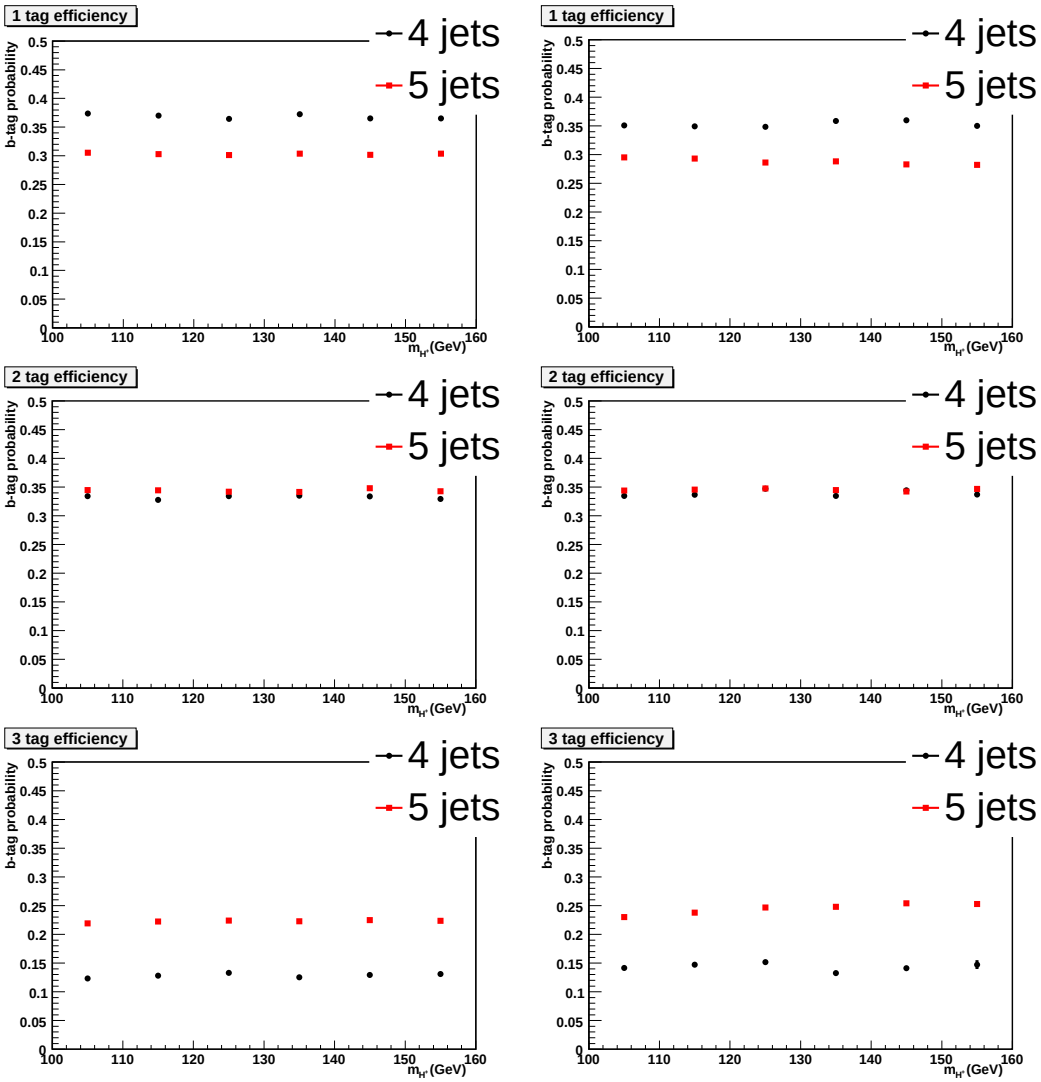

Figure 10.2.: b-tag probability of $t\bar{t}H$ versus Higgs mass in the 4 and $\geq$ 5 jet multiplicity sample. Left: e+jets; Right: μ+jets. Top: 1 b-tag; Middle: 2 b-tags; Bottom: $\geq$ 3 b-tags.

	e+jets					
	4j1t	4j2t	4j3t	5j1t	5j2t	5j3t
$t\bar{t}H$ Signal	0.029	0.026	0.01	0.036	0.040	0.026
$t\bar{t}$ & bkg	65.483	25.923	1.649	14.371	6.808	0.560
Observed	66	19	2	22	5	

	μ+jets					
	4j1t	4j2t	4j3t	5j1t	5j2t	5j3t
$t\bar{t}H$ Signal	0.017	0.016	0.007	0.026	0.030	0.020
$t\bar{t}$ & bkg	55.997	23.224	1.425	12.081	5.428	0.460
Observed	71	24	1	20	6	1

Table 10.1.: Number of $t\bar{t}H$ signal and background events in the 4 jet 1 b-tag sample (4j1t) to the ≥ 5 jet ≥ 3 b-tag sample (5j3t). The Higgs mass is set to 105 GeV.

10.2. Simultaneous fit of the $t\bar{t}$ and $t\bar{t}H$ cross section

The simultaneous fit of $\sigma_{t\bar{t}}$ and $\sigma_{t\bar{t}H}$ is based on the procedure of the simultaneous fit of $\sigma \cdot B^2$ and R, as described in section 8. The method considers subsamples with ≥ 3 b-tags and ≥ 5 jets separately. No topological discriminant in the zero b-tag sample is used. The likelihood function in the maximum likelihood procedure, described in section 8.1, can here be written as

$$\mathcal{L}_1 \;=\; \prod_i \mathcal{P}(n_i, \mu_i(\sigma_{t\bar{t}}, \sigma_{t\bar{t}H}))\,. \tag{10.1}$$

i is the product runs over 24 independent data sets: e+jets and μ+jets with 3, 4 and ≥ 5 jets in the subsamples with 0, 1, 2 or ≥ 3 b-tagged jets.

The sources of systematic uncertainties are the same as for the simultaneous measurement of R and $\sigma \cdot B^2$. The main background to $t\bar{t}H$ in the high jet multiplicity bins arises from $t\bar{t}$ events, with additional production, e. g. due to additional gluon radiation with the gluon decaying into $b\bar{b}$ ($t\bar{t}b\bar{b}$). As this specific background contribution is not taken into account separately, the total amount of $t\bar{t}b\bar{b}$ events is estimated from an inclusive $t\bar{t}$ sample. In PYTHIA, the $t\bar{t}b\bar{b}$ contribution has been estimated to be 2% of the $t\bar{t}$ sample in the ≥ 5 jet ≥ 3 b-tag multiplicity subsample. Conservatively, an uncertainty of 100% is assigned on the 2% contribution in the ≥ 3 b-tag subsample. Table 10.2 shows a breakdown of the systematic uncertainties of $\sigma_{t\bar{t}}$ and $\sigma_{t\bar{t}H}$, respectively. The table represents the measurement for a Higgs mass of 105 GeV. Although upper limits on the mass of Standard Model Higgs bosons of 114.4 GeV are measured by LEP [167], lower Higgs masses can be interesting in models beyond the Standard Model. The source of systematic error due to the $t\bar{t}b\bar{b}$ contribution shows to be small in the simultaneous fit of $\sigma_{t\bar{t}}$ and $\sigma_{t\bar{t}H}$. The main uncertainty on $\sigma_{t\bar{t}H}$ is the statistical uncertainty. The largest systematic uncertainty comes from the uncertainty on the b-tag TRFs. The nuisance parameter fit for the signal modelling, i. e. the difference between ALPGEN and PYTHIA, results in a large change (offset) of the measured $\sigma_{t\bar{t}H}$ with respect to the cross section measured using the statistical error only. ALPGEN and PYTHIA differ especially for high jet multiplicities, where the highest sensitivity to $\sigma_{t\bar{t}H}$ lies.

For each Higgs mass between 105 GeV and 155 GeV, varied in steps of 10 GeV, $\sigma_{t\bar{t}}$ and $\sigma_{t\bar{t}H}$ are fitted. Table 10.3 shows the results of the nuisance parameter fit. The $t\bar{t}$ cross section stays constant when changing the Higgs mass. All fitted $t\bar{t}H$ cross sections are negative, but

consistent with zero within the assigned uncertainty. As the total uncertainty on $t\bar{t}H$ gets smaller for higher Higgs mass, the sensitivity increases.

	$\sigma_{t\bar{t}}$ [pb]			$\sigma_{t\bar{t}H}$ [pb]		
	result	$+\sigma$	$-\sigma$	result	$+\sigma$	$-\sigma$
Statistical only fit	8.20	+0.58	-0.58	0.017	+0.172	-0.109
Systematics source	Offset	$+\sigma$	$-\sigma$	Offset	$+\sigma$	$-\sigma$
Event preselection	0.00	0.25	-0.21	0.000	0.000	-0.009
Muon identification	-0.02	0.09	-0.08	0.000	0.000	0.000
Electron identification	0.04	0.13	-0.11	0.000	0.017	-0.011
Lumi reweight	0.00	0.04	-0.04	0.000	0.000	-0.001
Z pT reweight	-0.00	0.01	0.00	0.000	0.000	-0.001
signal modeling	-0.10	0.06	0.00	-0.055	0.000	0.000
EM triggers	0.01	0.06	-0.05	0.000	0.007	-0.007
Muon triggers	-0.03	0.09	-0.09	0.000	0.000	0.000
Jet triggers	0.00	0.00	-0.02	0.000	0.000	-0.003
Jet energy scale	-0.17	0.21	-0.16	-0.036	0.000	0.000
Jet energy resolution	-0.00	0.00	0.00	0.000	0.000	0.000
JetID	-0.02	0.13	-0.11	-0.002	0.000	0.000
Taggability	0.07	0.19	-0.17	0.002	0.027	-0.019
Flavor dependence of taggability	-0.00	0.00	0.00	0.000	0.000	-0.002
b-tag TRF	0.31	0.39	-0.34	0.016	0.081	-0.057
c-tag TRF	0.01	0.06	-0.06	0.000	0.000	-0.003
light tag TRF	0.00	0.05	-0.05	-0.000	0.000	0.000
$t\bar{t}b\bar{b}$ correction	-0.00	0.03	0.00	0.000	0.000	-0.009
b fragmentation	0.00	0.11	-0.10	0.000	0.002	-0.002
ϵ_{QCD} in e+jet channel	-0.00	0.04	0.00	-0.001	0.014	0.000
ϵ_{sig} in e+jet channel	0.00	0.00	-0.00	-0.000	0.000	0.000
ϵ_{QCD} in μ+jet channel	-0.00	0.03	0.00	0.000	0.000	-0.001
ϵ_{sig} in μ+jet channel	-0.00	0.04	0.00	-0.000	0.009	0.000
MC background x-section	0.00	0.04	-0.04	0.000	0.000	-0.008
MC bkg scale factors	-0.00	0.05	-0.05	0.000	0.000	-0.009
MC statistics on W fractions	0.00	0.02	-0.02	0.000	0.000	-0.008
MC statistics	0.00	0.03	-0.02	-0.000	0.000	-0.009
MC statistics on $t\bar{t}H$	0.00	0.00	-0.01	0.000	0.000	-0.005
W+jets heavy flavor scale factor	0.04	0.21	-0.22	-0.003	0.000	0.000
PDF	0.00	0.00	-0.01	0.000	0.000	-0.002
Statistics for matrix method	-0.02	0.00	0.00	-0.005	0.000	0.000
Luminosity uncertainty	-0.00	0.55	-0.46	0.000	0.000	0.000
Total systematics	+0.11	+0.85	-0.73	-0.081	+0.089	-0.065
	result	$+\sigma$	$-\sigma$	result	$+\sigma$	$-\sigma$
Nuisance parameter fit	8.36	+1.08	-0.98	-0.032	+0.174	-0.100

Table 10.2.: Result for $\sigma_{t\bar{t}}$ and $\sigma_{t\bar{t}H}$ from the simultaneous fit. The Higgs mass is chosen as 105 GeV. The first line shows the result with no systematic errors included, the last line with all systematic uncertainties included.

As no sign for $t\bar{t}H$ can be observed, limits on $\sigma_{t\bar{t}H} \times B(H \to b\bar{b})$ are calculated with the frequentist approach of Feldman and Cousins. The procedure is the same as described in section 8.6.5. For each generated Higgs mass, the limit setting procedure is repeated.

The observed and expected 95 % Confidence Level limits and the 68 % error band around the expected limit are shown in Fig. 10.3. The observed limit is slightly better, but close to the expectation.

m_H [GeV]	$\sigma_{t\bar{t}}$ [pb]	$\sigma_{t\bar{t}H} \times B(H \to b\bar{b})$ [pb]
105	$8.36^{+1.08}_{-0.98}$	$-0.032^{+0.174}_{-0.100}$
115	$8.36^{+1.08}_{-0.98}$	$-0.019^{+0.168}_{-0.099}$
125	$8.36^{+1.08}_{-0.97}$	$-0.024^{+0.154}_{-0.091}$
135	$8.35^{+1.08}_{-0.97}$	$-0.013^{+0.155}_{-0.090}$
145	$8.35^{+1.08}_{-0.97}$	$-0.014^{+0.155}_{-0.090}$
155	$8.35^{+1.08}_{-0.97}$	$-0.016^{+0.147}_{-0.086}$

Table 10.3.: Fitted $\sigma_{t\bar{t}}$ and $\sigma_{t\bar{t}H} \times B(H \to b\bar{b})$ for different Higgs masses. For the nuisance parameter fit. The luminosity uncertainty is included.

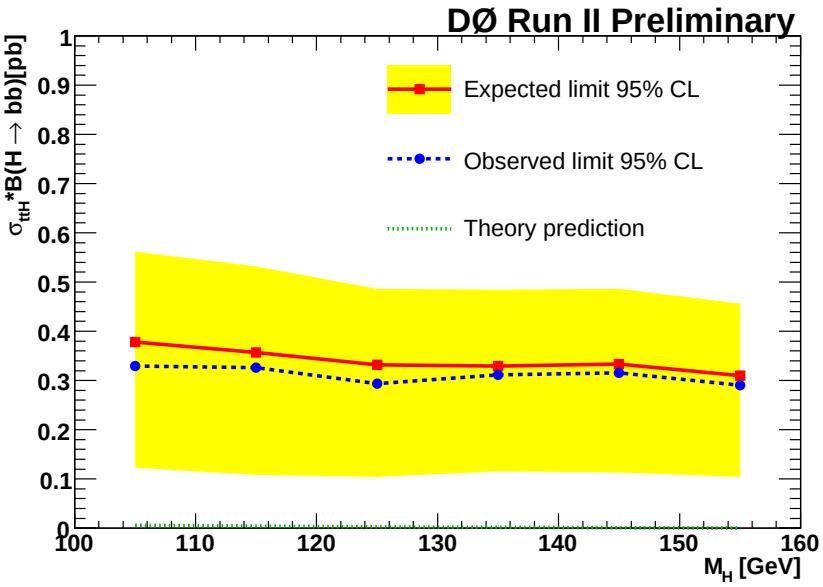

Figure 10.3.: The 95 % CL upper expected (red) and observed (blue) limit on $\sigma_{t\bar{t}H} \times B(H \to b\bar{b})$. The theory prediction (green) is a NLO SM calculation.

Figure 10.4 shows the limits divided by the NLO $\sigma_{t\bar{t}H} \times B(H \to b\bar{b})$ prediction. Due to the steeply falling theoretical cross section as function of Higgs mass this ratio is about 70 for a 105 GeV Higgs, and grows to more than 1000 for a Higgs mass of 155 GeV.

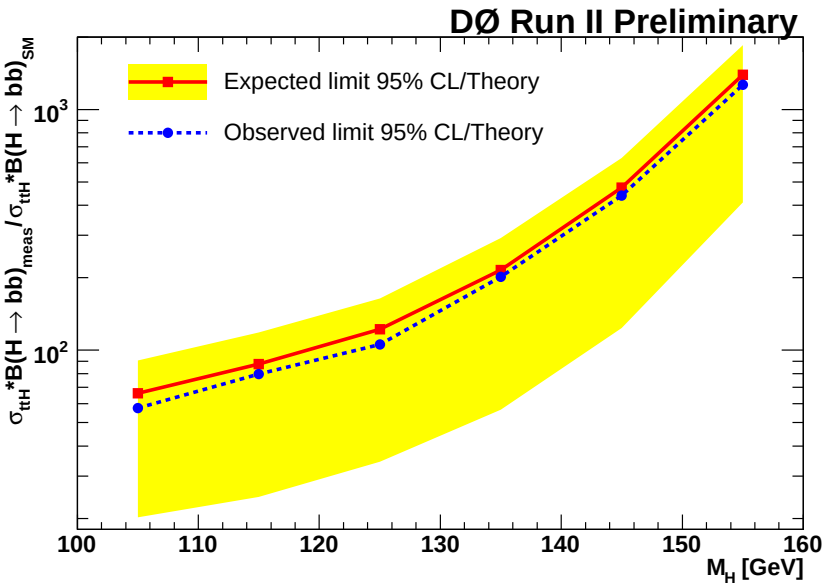

Figure 10.4.: The 95 % CL upper expected (red) and observed (blue) limit on $\sigma_{t\bar{t}H} \times B(H \to b\bar{b})$ as a function of the Higgs mass over the NLO SM calculation.

	e+jets					
	4j1t	4j2t	4j3t	5j1t	5j2t	5j3t
Signal	0.0675	0.0684	0.0318	0.0765	0.0882	0.0669
$t\bar{t}$	110 ± 0.6	60.5 ± 0.4	5.98 ± 0.12	25.2 ± 0.3	15.0 ± 0.2	1.97 ± 0.07
non-$t\bar{t}$ Bkg	62 ± 2.7	8.0 ± 0.6	0.25 ± 0.15	12.5 ± 1.4	2.2 ± 0.7	0.08 ± 0.23
Observed	179	57	10	42	22	3

	μ+jets					
	4j1t	4j2t	4j3t	5j1t	5j2t	5j3t
Signal	0.0433	0.0462	0.0237	0.0555	0.0684	0.0504
$t\bar{t}$	91 ± 0.5	51.5 ± 0.4	5.04 ± 0.11	20.5 ± 0.2	12.1 ± 0.2	1.47 ± 0.05
non-$t\bar{t}$ Bkg	56 ± 2.5	7.4 ± 1.1	0.60 ± 0.44	12.5 ± 1.4	1.6 ± 0.4	0.14 ± 0.11
Observed	170	68	9	44	20	2

Table 10.4.: Summary of expected and observed yields for different final states from the 4 jet 1 b-tag sample (4j1t) to the ≥ 5 jet ≥ 3 b-tag sample (5j3t) [165]. The expectations are shown for a Higgs mass of 105 GeV. The uncertainties are statistical only. The uncertainties on the signal are of the order $\pm 0.001 - 0.002$

10.3. Topological analysis

The method presented in section 10.2 relies only on event counting, no topological information is used. Furthermore, the analysis and limit setting method is different from the one used for other Higgs bosons search channels, which would lead to complications for the combination with those channels.

The search for the Higgs boson in $t\bar{t}H$ is extended by including topological information, using the CL_s limit setting procedure and a two times larger data set of 2.1 fb^{-1}. The analysis is briefly discussed here and has been published as a conference note in [166]. As part of this thesis the selection efficiencies, b-tag probabilities, H_T distributions and systematic uncertainties for the data set of 0.9 fb^{-1} were contributed to this analysis. The calculations from the additional 1.2 fb^{-1} data set and the limit setting were done by other collaborators [165].

The study of topological variables to discriminate $t\bar{t}H$ from $t\bar{t}$ and other backgrounds show that H_T, the scalar sum of jet p_T's of the five leading jets, is a good candidate.

In Fig. 10.5 the H_T distributions for all channels with 4 or ≥ 5 jets and 1, 2 or ≥ 3 b-tags in the full data set of 2.1 fb^{-1} are shown. A $t\bar{t}$ cross section of 7.3 pb is assumed. The contribution of the $t\bar{t}H$ signal for a Higgs boson mass of 105 GeV is multiplied by a factor of 100 and overlaid (solid black histogram). The H_T distributions peak at larger values for $t\bar{t}H$ events than for $t\bar{t}$.

In Table 10.4 the predicted and observed number of events in the different final states are listed. The $t\bar{t}H$ yields are shown for a SM Higgs boson mass of 105 GeV. The $t\bar{t}$ contribution is calculated for a theoretical $t\bar{t}$ cross section of $\sigma_{t\bar{t}} = 7.3$ pb at a top quark mass of 172.6 GeV. The lower number of expected events in the subsamples indicates that the data prefers a higher $t\bar{t}$ cross section, which is consistent with the measurements of $\sigma_{t\bar{t}}$ in this thesis. An uncertainty of 10 % is assigned on the theoretical $t\bar{t}$ cross section. Within the statistical and systematic uncertainties, the expected and observed $t\bar{t}$ and non-$t\bar{t}$ backgrounds are consistent with the number of observed events in all subsamples. In all subsamples of the μ+jets channel the number of observed events is larger than the number of predicted events. This reflects again the lower assumed $\sigma_{t\bar{t}}$ then measured in the data, which is more significant for μ+jets than for e+jets in the full data sample.

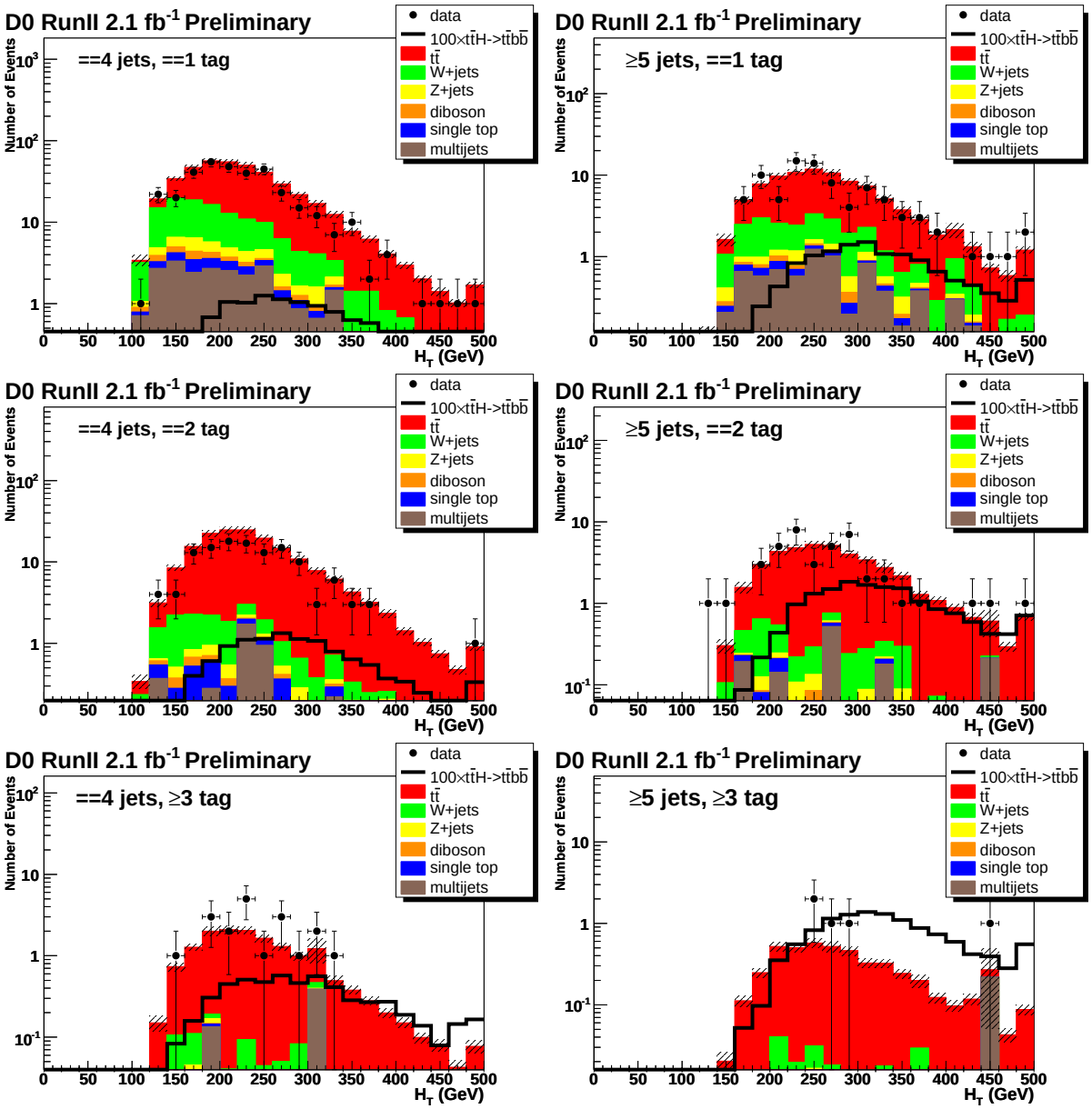

Figure 10.5.: H_T distributions corresponding to a data set of 2.1 fb^{-1} [166]. Top: 1 b-tag; Middle: 2 b-tags; Bottom: $\geq$ 3 b-tags. Left: 4 jets; Right: $\geq$ 5 jets. The e+jets and μ+jets final states are combined. The $t\bar{t}H$ signal is plotted for a Higgs mass of 105 GeV and $\sigma(t\bar{t}H) \times B(H \rightarrow b\bar{b})$ to 5.5 fb. The signal is enhanced by a factor of 100.

As no evidence for SM $t\bar{t}H$ production can be seen, limits are set on $\sigma_{t\bar{t}H} \times B(H \rightarrow b\bar{b})$. The H_T distributions for 12 different channels, namely the subsamples with 1, 2 and $\geq$ 3 b-tags, 4 and $\geq$ 5jets in e+jets and μ+jets final states are used as inputs to the limit calculation. The limit is determined with a modified frequentist approach as presented in section 3.3 and described in detail in [38]. The method uses pseudo-experiments including systematic errors, similar to the Feldman Cousins method presented in section 8. Similar to the nuisance parameter method, the limit program allows the fit of systematic uncertainties to the data. Letting the $t\bar{t}$ cross section float within its uncertainty in the background-only hypothesis, a $0.7\sigma = 7\%$ higher cross section than the input is measured, i. e. the top pair production cross section is

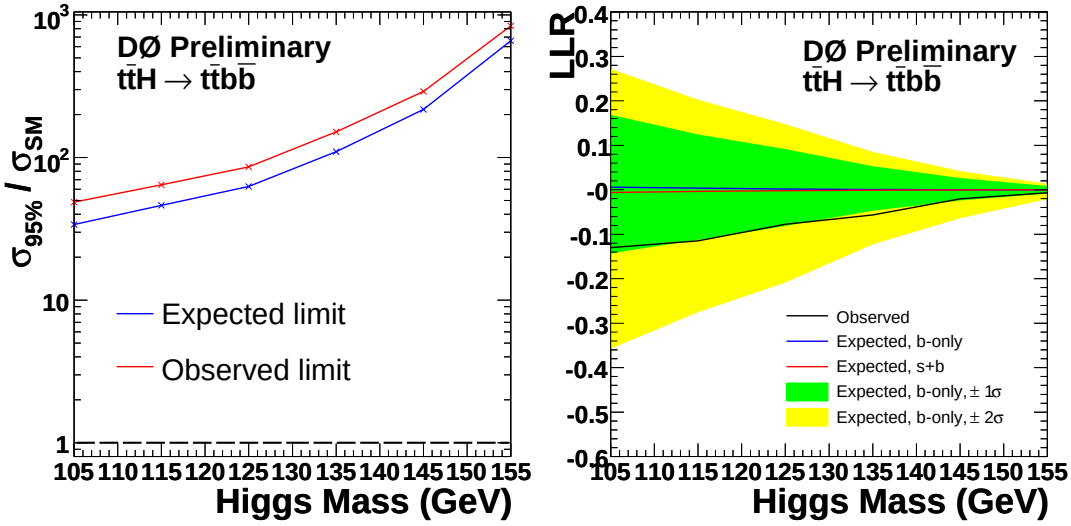

Figure 10.6.: The 95% CL upper expected (red) and observed (blue) limit on $\sigma_{t\bar{t}H} \times B(H \to b\bar{b})$ as a function of the Higgs mass over the NLO SM calculation (left) and observed and predicted LLR as a function of the Higgs mass (right) [166].

fitted to 7.8 pb. The increase in cross section is not surprising, as the dedicated cross section measurement with half of the data (see table 8.1 and 8.2 in section 8) show a much higher result than 7.3 pb.

As systematic uncertainties that can change the shape of the H_T templates, the jet energy scale and the error on the b-tag TRFs are taken into account. All other uncertainties are not considered as shape changing and are only assigned on the total yields.

In Figure 10.6 the ratio of $\sigma(t\bar{t}H) \times B(H \to b\bar{b})$ over the Standard Model NLO calculation is shown. Furthermore the Log-Likelihood-Ratio (LLR), as given in Eq. 3.10 in section 3.3, is plotted. The observed and expected limits agree with each other.

For a 105 GeV Higgs mass, the observed and expected limits on the $t\bar{t}H$ cross section times branching fraction $H \to b\bar{b}$ are 34 and 49 times larger than the SM value, respectively.

10.4. Comments and outlook

The search for Higgs bosons on the $t\bar{t}H$ channel results in limits that are by more than a factor of 30 over the SM expectation. The presented analysis is the first attempt at DØ to extract limits on the $t\bar{t}H$ cross section, and a couple of improvements can be done.

The inclusion of topological information is a good candidate for further improvements. The gain of using the H_T distribution to discriminate signal and background in section 10.3 has been checked by repeating the same method of limit setting with counting only. The latter yields about 10 % weaker expected limits. Although the H_T distribution does not show large discrimination power when considering Fig. 10.5, this is already a large gain compared to counting only. It can thus be expected that including more variables and the usage of a multivariate technique results in better discrimination of $t\bar{t}H$ from $t\bar{t}$ and therefore higher sensitivity.

Furthermore, the measurement of the $t\bar{t}H$ cross section is still statistically limited. With larger data sets the limit can therefore be expected to improve almost proportional to the square of the ratio of integrated luminosities of the higher data set over to the currently used one.

Another possibility would be to not restrict the search to Higgs bosons decaying into a $b\bar{b}$ pair, but use the inclusive Higgs decay. Especially for high mass Higgs, where the branching ratio into a $b\bar{b}$ decay becomes small, but the decays into WW and ZZ increase, the consideration of inclusive Higgs decays is expected to lead to higher sensitivity. But also at low mass Higgs, where the decay into $\tau\bar{\tau}$ is considerable, an improvement can be expected. For the presented search for Higgs bosons on the $t\bar{t}H$ channel, the same event selection as for $t\bar{t}$ events is adopted. An optimisation of the selection efficiency for a higher $t\bar{t}H$ signal over background ratio can result in further improvements of the sensitivity.

In conclusion, the presented search for Higgs bosons in the $t\bar{t}H$ channel with 2.1 fb^{-1} results in a limit on $\sigma_{t\bar{t}H} \times B(H \to b\bar{b})$ that is by a factor of 34 above the SM expectation for a Higgs mass of 105 GeV. The analysis is the first search for Higgs in the $t\bar{t}H$ channel at DØ, which still has much room for optimisations.

However, in models beyond the Standard Model the $t\bar{t}H$ channel might play a more important role, which could result in a better factor of the extracted limits over the theory prediction. Furthermore, in such models Higgs masses below 114 GeV are not yet excluded, making the full range of considered Higgs masses interesting. One such example is given in [168].

At the LHC, the $t\bar{t}H$ production is an important channel. Studies at the Atlas collaboration, for example, show that the $t\bar{t}H$ channel is one of the three channels that can contribute to the Higgs discovery in the low mass region of up to 130 GeV [169,170].

11. Combination of the top quark pair production cross section and global search for charged Higgs bosons

In order to check the consistency between all individual top quark pair production cross section measurements and to the theoretical prediction, the measurement is performed in all possible final states. Exotic decays of the top quark, as for example $t \rightarrow H^+b$, can lead to deviations of the measured $\sigma_{t\bar{t}}$ from the Standard Model expectation in a certain final state.

In this chapter the combination of the $t\bar{t}$ cross section in the l+jets channel, the dilepton channels with two electrons (ee) [171], two muons ($\mu\mu$) [172] or one electron and one muon ($e\mu$) [173] and the τ+lepton channels [174] with one isolated electron ($e + \tau$) or muon ($\mu + \tau$) are described. The calculation of the selection efficiencies from the dilepton and τ+lepton final states is not subject of this thesis and is therefore only described briefly in the following.

Based on the combination, a global fit is performed to search for charged Higgs bosons $H^{+1)}$. For the search two methods are discussed: One where the SM top quark pair production cross section is assumed, and one analysis where the $t\bar{t}$ cross section is fitted simultaneously with the branching ratio of top to charged Higgs $B(t \rightarrow H^+b)$ [175, 176]. The latter represents the first search for charged Higgs bosons in the $t\bar{t}$ decay, independent of the $t\bar{t}$ production mechanism.

11.1. Combination of $\sigma_{t\bar{t}}$ in various channels

Different final states require the consideration of different background samples, different physical objects and the optimisation of the selection cuts in each channel separately. In the end, the measurement of the top quark pair production cross section in each of the individual channels is performed separately. The combination of various final states into one combined cross section measurement requires not only the statistical independence of all considered channels, but also the correct implementation of various methods to calculate the background contributions and the correct treatment of correlations between different sources of systematic uncertainties.

The $t\bar{t}$ cross sections in the dilepton, τ+lepton and l+jets channels are combined. The combined measurement is more precise than the individual cross sections and, in combination with the SM branching ratios, can be compared to theoretical predictions.

11.1.1. Data samples, Monte Carlo samples and predicted yields

For each of the individual final states a separate data sample, background composition and selection criteria is chosen. A short description is given in this section. Further details of the dilepton and τ+lepton channel are given in [177].

[1)] no difference is made between H^+ and H^-. H^+ also refers to its charged conjugate state.

Data sample

The full Run IIa data set, collected between August 2002 and April 2006, is used for the cross section combination. For the l+jets channel the triggers and integrated luminosities as listed in Tables 6.1 for the e+jets and in Table 6.2 for the μ+jets channel are used. Details about triggers, data quality and the data samples are given in section 6. The final Jet Energy Scale calibration, described in section 5.5, is applied.

The same data sample is used for the τ+lepton final state. In case of the dileptonic channels, data samples are collected using the OR of the single electron and muon triggers [171–173, 177]. The analysed datasets correspond to an integrated luminosity of about 1 fb^{-1}, as shown in Table 11.1.

Monte Carlo samples

In contrast to the measurement of R, the matrix elements of the Standard Model $t\bar{t}$ signal Monte Carlo are generated with ALPGEN, followed by PYTHIA for parton shower and hadronisation. The PDF is set to CTEQ6L1 and the factorisation scale to $m_t^2 + \sum p_T^2(\text{jets})$. The ALPGEN Monte Carlo generates more events with high jet multiplicities than PYTHIA. The top quark mass for the central cross section result is changed from 175 GeV to 170 GeV, which is closer to the 2007 world average top quark mass of 170.9 GeV [178].

The considered background in the l+jets channel is the same as for the measurement of R. For the Monte Carlo samples of the W+jets background a more recent ALPGEN version is used, which made it necessary to re-determine its heavy flavour scale factor. Also the k-factor, heavy flavour scale factor and Z p_T reweighting for Z+jets are changed according to more recent calculations and studies [171].

The main background in the dilepton channels consists of Z+jets, simulated with ALPGEN. For the τ+lepton channel W+jets and Z+jets events form the dominant background. Only a short overview of the selection and sample composition of the non-l+jets channels is given in the following. In [177] details about the selection and sample composition of all non-l+jets final states can be found.

All used Monte Carlo samples are reweighted with b-fragmentation, luminosity profile and primary vertex z reweighting.

Event selection

The event selection for the l+jets final state is the same as described in section 7.1. Additional cuts are applied to ensure independence of all final states, as described below.

To select the dilepton and τ+lepton events one isolated lepton (e or μ) for the τ+lepton channel or two isolated leptons with opposite electric charge for the ee, $\mu\mu$ and $e\mu$ channels are required. The electric charge of the τ and the electron or muon are required to be opposite in the τ+lepton channel. The output value of a dedicated τ identification neural network [179] is required to be above 0.8 for the τ candidates. Events with at least two jets within $|\eta| < 2.5$, one of which has to have $p_T > 30$ GeV and the others $p_T > 20$ GeV, are accepted. In the $e\mu$ channel also events with one jet are used. In the τ+lepton channels, all jets matched within $\Delta R < 0.5$ to the selected tau candidate are removed. Leptons are required to have $p_T > 15$ GeV in the ee, $\mu\mu$ and $e\mu$ channels while an electron (muon) with $p_T > 20$ GeV is required in the $e + \tau$ ($\mu + \tau$) channels. Muons are accepted in the region $|\eta| < 2.0$. Electrons must be within $|\eta| < 1.1$ in the $e\tau$ channel and within $|\eta| < 1.1$ or $1.5 < |\eta| < 2.5$ in both the ee and $e\mu$ final states. In the τ+lepton channel at least one b-tagged jet with a Neural Net working point of Medium is required.

Statistical independence of the dilepton channels is achieved by vetoing events that contain an isolated electron in the $\mu\mu$ and a second electron in the $e\mu$ channel. In the e+jets channel a muon and a second electron are vetoed. Events that pass the $\mu\mu$ selection or contain an isolated electron are rejected in the μ+jets channel. All events that pass the full τ+lepton selection are rejected in the l+jets channels. The independence of the dilepton and τ+lepton channels is ensured by requiring no second isolated electron and no muon in the $e + \tau$ final state as well as no second muon or an isolated electron in the $\mu + \tau$ final state. Furthermore events that pass the $\mu\mu$ selection are rejected.

The efficiency ε_{QCD} for a fake isolated lepton to pass the tight isolation criteria, is updated to the full data set, resulting in $\varepsilon_{QCD} = 0.194 \pm 0.016$ in the e+jets channel, and $\varepsilon_{QCD} = 0.279 \pm 0.048$ in the μ+jets channel [134].

Predicted yields

In Table 11.1 the expected and observed number of events for the l+jets, dilepton and τ+lepton channels are shown. For the expected number of $t\bar{t}$ events the cross section is set to $\sigma_{t\bar{t}} = 7.91$ pb [15, 17], at a top quark mass of 170 GeV. In order to calculate the expectation from the selection efficiencies, the efficiency has to be multiplied with the branching ratio that matches the requirement on parton level. The used branching ratios for each channel are listed in Table 11.2.

Channel	Luminosity [pb^{-1}]	$t\bar{t}$	$t\bar{t}$+background	observed
e+jets 3 jets 1 tag	1038	79.04 ± 0.32	180.73 ± 4.71	183
e+jets $\geq$ 4 jets 1 tag		78.94 ± 0.31	100.95 ± 2.23	113
e+jets 3 jets 2 tag		29.71 ± 0.15	40.40 ± 1.16	40
e+jets $\geq$ 4 jets 2 tag		40.35 ± 0.18	43.59 ± 0.89	30
μ+jets 3 jets 1 tag	996	57.03 ± 0.27	140.81 ± 3.78	133
μ+jets $\geq$ 4 jets 1 tag		63.69 ± 0.27	82.11 ± 2.34	99
μ+jets 3 jets 2 tag		23.05 ± 0.13	32.61 ± 1.19	31
μ+jets $\geq$ 4 jets 2 tag		34.44 ± 0.16	36.99 ± 1.00	34
ee	1074	11.22 ± 0.14	14.59 ± 0.4	17
$e\mu$ 1 jet	1069	8.58 ± 0.11	18.08 ± 0.66	21
$e\mu$ 2 jets		35.19 ± 0.17	44.55 ± 0.69	39
$\mu\mu$	1009	8.79 ± 0.10	15.15 ± 0.57	12
$e + \tau$	1038	10.31 ± 0.18	14.66 ± 1.75	16
$\mu + \tau$	996	12.15 ± 0.17	22.31 ± 2.85	20

Table 11.1.: Luminosity and number of expected and observed events in the l+jets, dilepton and τ+lepton channels for $\sigma_{t\bar{t}} = 7.91$ pb. The uncertainties are statistical only.

11.1.2. Maximum Likelihood fit

The combined measurement of the $t\bar{t}$ cross section from the various channels is done with a maximum likelihood fit, as described in section 8.1. The binned likelihood function is the

$t\bar{t}$ decay	e+jets/$e+\tau$ lj	e+jets ll	μ+jets/$\mu+\tau$ ljc	μ+jets ll
$t\bar{t} \to W^+bW^-b$	0.17137	0.06627	0.1721	0.06607

$t\bar{t}$ decay	ee	$e\mu$	$\mu\mu$	τ+lepton ll
$t\bar{t} \to W^+bW^-b$	0.016197	0.03226	0.01607	0.104976

Table 11.2.: Branching ratios for the different final states. The selection of final states depends on the considered channel.

product of Poisson probabilities for each independent channel, as given in Eq. 8.4. The function describes 14 bins: l+jets with electron or muon, 3 or ≥ 4 jets and 1 or ≥ 2 b-tags, dilepton with ee, $\mu\mu$ and $e\mu$ ≥ 2 jets, $e\mu$ with one jet, and τ+lepton with electron or muon, at least one b-tag and ≥ 2 jets. In addition, 12 Poisson terms to account for the statistical fluctuation of the multijet background in the l+jets channels for 0, 1 and ≥ 2 b-tags as well as two Poisson terms accounting for the multijet background fluctuations in the τ+lepton channels are multiplied to the likelihood function. As described in section 8.5.1, the systematic uncertainties are included as nuisance parameters, where each independent source of systematic error is represented by a Gaussian term.

In case of the l+jets channel the full correlation between the different 0, 1 and ≥ 2 b-tagged subsamples is taken into account, as derived in section 8.1.

11.1.3. Systematic uncertainties

The systematic uncertainties affecting preselection efficiencies or b-tag probabilities for each of the considered channels have to be taken into account with the proper correlation.

A large set of systematic uncertainties is similar to the sources discussed in section 8.5.3. In this section only the ones that changed with respect to the measurement of R or that are additionally considered will be discussed.

In contrast to the simultaneous measurement of R and $\sigma \cdot B^2$, discussed in chapter 8, the treatment of the luminosity uncertainty changed. While so far the 6.1% luminosity error was extracted on the measured cross section, it is now assigned as additional nuisance parameter to the selection efficiency. This enables one to take into account that the luminosity uncertainty is symmetric on the selection efficiency, resulting in an asymmetric uncertainty on the cross section. Furthermore, it allows one to easily include the luminosity uncertainty in the limits of the charged Higgs search.

Uncertainties on the selection efficiency

Uncertainties only affecting the selection efficiency are:

Uncertainty on the data-MC luminosity profile difference. The reweighting of the luminosity profiles of Monte Carlo to Data is applied on the central result. The uncertainty on the luminosity reweighting in the l+jets channels and the τ+lepton channel is taken from the $e\mu$ channel [173], resulting in 3 % uncertainty on all samples except for $t\bar{t}$ and W+jets. On the latter samples -0.2 % relative uncertainty are assigned. In each of the dilepton samples the uncertainty of the luminosity profile reweighting is derived by changing the maximum allowed weight from the default of 3 to a larger value of 5 and determine the relative difference.

PV scale factor. The preselection efficiency is not corrected for the difference of the primary vertex selection efficiency between data and Monte Carlo [171] in the l+jets and τ+lepton channels, i. e. a scale factor of 1 is used. The relative uncertainty on this scale factor is estimated to be 1.0 % .

Uncertainties on Monte Carlo cross sections. For the Z+jets sample a cross section of $256.6^{+5.1}_{-12.0}$ pb is used. For the diboson samples the NLO cross section is applied, where the uncertainty is taken to be 20 %, which is half of the difference between the leading order and NLO cross sections.

Z p_T reweighting factor. The uncertainty due to reweighting of the Z p_T in Monte Carlo to match data is taken from the studies of the $e\mu$ channel [173], where an alternative parametrisation of the Z p_T with respect to the central value is used. On all Z+jets samples a constant value of 5.2 % relative uncertainty is assigned in the l+jets and τ+lepton channel, while in the dilepton channels the change between central parametrisation and the error parametrisation is determined for each Z+jets contribution separately.

Uncertainty on the branching fraction. The uncertainties on the branching fractions $B(W \to XX)$ are taken from the PDG [3] and propagated in the semileptonic and dileptonic decays. This results in 0.8 % and 1.7 % relative uncertainty on semileptonic and dileptonic $t\bar{t}$ decays, respectively.

Dilepton trigger. In the dilepton channels single lepton triggers are used. The statistical fluctuations on the bins for the binned efficiencies are taken as uncertainty.

W+jets normalisation. In the τ+lepton channel the W+jets background is normalised to data before application of the tight τ+lepton selection criteria and the b-tagging. The selection criteria of the sample where the W+jets normalisation is determined are the same as in the l+jets channel. The Matrix Method is used to calculate the amount of W+jets. The factors are found to be 1.33 ± 0.1 in the $e + \tau$ channel and 1.52 ± 0.1 in the $\mu + \tau$ channel.

Tau correction. In order to correct the Monte Carlo for differences of the rate of jets faking τ's, a correction factor of 1.07 ± 0.12 is applied on W+jets and semileptonic $t\bar{t}$ events in the τ+lepton final state.

MET modelling. In the dilepton channels an uncertainty on the modelling of the missing transverse energy $\not{E}_T$ is applied, as the modelling of $\not{E}_T$ is most important in these final states. By comparing the $\not{E}_T$ distribution in data to Monte Carlo and rescaling the Monte Carlo samples to match data, the uncertainty is calculated.

Uncertainties on the b-tagging event probability

The treatment of b-tagging is the same in the τ+lepton as in the l+jets channel. The assigned sources of uncertainties are identical to the simultaneous fit of $\sigma \cdot B^2$ and R.

Uncertainties on the selection and b-tagging efficiency

Some uncertainties influence the selection and b-tagging efficiency. Those uncertainties are:

Signal Modelling The uncertainty on the signal modelling is estimated by replacing ALPGEN $t\bar{t}$ Monte Carlo with PYTHIA Monte Carlo. The relative difference on preselection and b-tagging efficiency between both simulations is then symmetrised and assigned to the central efficiencies determined with ALPGEN.

Uncertainty due to shifting. The JSSR shifting (see section 5.5) is not used for the central cross section result in the l+jets and τ+lepton channels, but in the dilepton final states. In order to estimate the uncertainty due to shifting, the shifting is switched on or off for $t\bar{t}$ signal, and the relative difference on preselection and b-tagging efficiency is assigned as systematic uncertainty.

Uncertainty on b-jet energy scale. As the jet energy scale is not expected to be the same for heavy flavour as for light flavour jets, but the central JES being derived independently from the jet flavour, an additional uncertainty for b-jets is applied. The central calibration is not changed for b-jets. To estimate the uncertainty, all b-jets are re-calibrated by multiplication of a factor 0.9823 or $1/0.9823$ on their JES correction.

Jet trigger in τ sample. Tight τ's are reconstructed as narrow jets, therefore the jet-trigger parametrisations are also used on τ's. In order to estimate the effect on the selection and b-tag efficiencies in the τ+lepton final states, jets that are matched to a selected τ candidate are removed before calculating the trigger probability. The difference is assigned as systematic uncertainty.

Tau energy scale. Similar to the jet energy scale an energy scale correction on τ candidates has to be applied. This correction is neglected in the τ+lepton channel. The uncertainty on neglecting it is derived by calculating the difference on selection and b-tag probabilities between applying and not applying the tau energy scale. The resulting relative difference is symmetrised and assigned as systematic uncertainty.

Uncertainties on the W+jets and Z+jets background flavour composition

Due to the change in W+jets Monte Carlo and the recalculation of Z+jets k-factors and heavy flavour scale factors, different uncertainties than for the R measurement are used.

Uncertainty on Monte Carlo background scale factors. An uncertainty of 20 % on the heavy flavour scale factor in Z+jets is assigned.

W+jets fractions matching and higher order effects: The uncertainty on the W+jets heavy flavour scale factor is estimated to be 11.0 % (see section 6.3.2).

Uncertainties on the multijet background yield

In the l+jets channel the same method to estimate the multijet background as for the simultaneous measurement of R and $\sigma \cdot B^2$ is used.

In the τ+lepton channel the multijet background is estimated with events, where τ and electron (or muon) have the same sign of the electric charge. By assuming that those events are fake multijet background and subtracting the contribution of same sign events measured in the signal and non-multijet background samples from the number of observed events in data, the multijet background is estimated. The statistical uncertainty on the number of same sign events dominates the uncertainty on the multijet background estimate.

In the dilepton channel the fake background is determined by estimating the number of events with jets faking a lepton in data. In the ee final state, for example, templates for real and fake electrons are fitted to the electron likelihood distribution in data. The fit errors are taken as systematic uncertainties.

Combined systematic uncertainties

In Table 11.3 the systematic uncertainties affecting each considered channel and their correlations are presented.

Systematic	ee	$e\mu$	$\mu\mu$	e+jets	μ+jets	$e+\tau$	$\mu+\tau$
Correlated							
Data quality	X	X	X	X	X	X	X
$\Delta z(l, PV)$	X	X	X	X	X	X	X
Primary vertex	X	X	X	X	X	X	X
Electron ID	X	X		X		X	
Muon ID		X	X		X		X
Muon track		X	X		X		X
Muon isolation		X	X		X		X
Jet ID	X	X	X	X	X	X	X
Jet energy scale	X	X	X	X	X	X	X
JSSR Shifting on/off	X	X	X	X	X	X	X
Jet energy resolution	X	X	X	X	X	X	X
l+jets trigger				X	X	X	X
dilepton trigger	X	X	X				
PDF	X	X	X	X	X	X	X
signal modelling	X	X	X	X	X	X	X
W+jets heavy flavour scale factor				X	X	X	X
Z+jets heavy flavour scale factor	X	X	X	X	X	X	X
b-fragmentation	X	X	X	X	X	X	X
$b-$ Jet energy scale	X	X	X	X	X	X	X
Luminosity reweighting	X	X	X	X	X	X	X
Z p_T reweighting	X	X	X	X	X	X	X
b TRF				X	X	X	X
c TRF				X	X	X	X
light TRF				X	X	X	X
Taggability				X	X	X	X
Taggability flavour dependence				X	X	X	X
Integrated luminosity	X	X	X	X	X	X	X
MET modelling	X	X	X				
background cross sections	X	X	X	X	X	X	X
branching fractions	X	X	X	X	X	X	X
Tau correction						X	X
Tau identification						X	X
W+jets normalisation						X	X
Uncorrelated							
Monte Carlo statistics	X	X	X	X	X	X	X
Statistics in loose–tight				X	X		
ε_{qcd} in μ+jets					X		
ε_{qcd} in e+jets				X			
ε_{signal} in μ+jets					X		
ε_{signal} in e+jets				X			
fake EM statistical	X	X					
fake MU statistical		X	X				
fake EM fit systematics		X					
fake MU fit systematics		X					
Statistics in same sign data						X	X

Table 11.3.: Summary of systematic uncertainties in each channel and the correlations between the systematic errors.

11.1.4. Results

The central result is extracted with the nuisance parameter method, while the "standard method" of treating systematic uncertainties is only used as a cross check. The difference between the two methods is described in detail in section 8.5.1. The central results are given for a top quark mass of 170 GeV.

The central result on $\sigma_{t\bar{t}}$ for the combined l+jets, dilepton and τ+lepton channels with the nuisance parameter method yields

$$\sigma_{t\bar{t}} \;=\; 8.16^{+0.95}_{-0.84}\,\text{(stat+syst) pb}\,.$$

In Table 11.4 the individual systematic uncertainties are shown for the nuisance and standard method. The main uncertainties arise from the luminosity, b-tagging, event preselection, lepton identification and Jet Energy Scale.

Using the standard method of systematic uncertainty treatment, the cross section combination yields

$$\sigma_{t\bar{t}} \;=\; 7.88^{+0.47}_{-0.46}\,\text{(stat)}\,^{+0.80}_{-0.73}\,\text{(syst)}\;\text{pb}\;\;[= 7.88^{+0.93}_{-0.86}\,\text{(stat+syst) pb}]\,.$$

In Table 11.4 (right) the breakdown of systematic uncertainties on $\sigma_{t\bar{t}}$ for the standard method is shown. It can be observed that the result obtained with the nuisance parameter method is by almost 0.3 pb larger than the result wit the standard method. Considering the offset per individual source of systematic error, it turns out that the result changes for the b-tag TRF. The shift corresponds to a nuisance parameter value of -0.8, i. e. in the data lower b-tag probabilities seem to be preferred. When performing the simultaneous measurement of R and $\sigma \cdot B^2$ the effect is similar in case of fixing R to one and not using a topological discriminant in the zero b-tag bin. The latter decreases the effect significantly. In the simultaneous fit of R and $\sigma \cdot B^2$ the effect of lower b-tag probability is fully absorbed into R, resulting in no significant offset of the cross section and a lower value of R.

The $t\bar{t}$ cross section results for the individual channels at a top quark mass of 170 GeV can be found in Table 11.5 and are plotted in Fig. 11.1 for the nuisance parameter fit method. As expected, the l+jets channel dominates the combination due to its high statistics. The dilepton channels with their four subchannels – ee, $\mu\mu$ with at least two jets and $e\mu$ with one and at least two jets – show a larger statistics than the two τ+lepton channels and therefore dominate the combination of dilepton with the τ+lepton final state. All individual results are consistent within their uncertainties and consistent with the NLO theory calculation of 7.91 ± 0.7 pb at a top quark mass of 170 GeV.

Mass dependence of the $t\bar{t}$ cross section in the combined l+jets, dilepton and τ+lepton channel In order to check the top mass dependence of the measured cross section, ALPGEN $t\bar{t}$ Monte Carlo with input masses of 160, 165, 175 and 180 is generated and the $\sigma_{t\bar{t}}$ fit is redone. The same relative uncertainties on the central efficiency and b-tag probability as for the top mass of 170 GeV are assigned.

The results for the different top quark masses with the standard method and the nuisance fit are shown in Table 11.6. In Fig. 11.2 the cross section versus mass is plotted, together with recently performed theory calculations from Moch and Uwer [18, 19] at next-to-leading order (NLO) containing all next-to-next-to-leading-logarithmic (NNLL) corrections, and from Cacciari at NLO including next-to-leading-logarithmic corrections [163]. The dependence of the measured cross section on the top quark mass m_t is fitted with a cubic function. The central result is [164]

$$\sigma(m_t) = [44.27 - 1.858\,10^{-1} m_t - 1.219\,10^{-3} m_t^2 + 6.181\,10^{-6} m_t^3]\;\text{pb} \qquad (11.1)$$

	$\sigma_{t\bar{t}}$ [pb] (nuisance)			$\sigma_{t\bar{t}}$ (standard) [pb]	
Systematics source	result	$+\sigma$	$-\sigma$	$+\sigma$	$-\sigma$
Statistical only fit	7.88	+0.47	-0.46		
Systematics source	Offset	$+\sigma$	$-\sigma$	$+\sigma$	$-\sigma$
Event preselection	-0.00	0.11	-0.10	0.102	-0.100
Muon identification	0.01	0.10	-0.10	0.104	-0.102
Electron identification and smearing	0.02	0.11	-0.10	0.107	-0.105
Luminosity reweighting	0.00	0.02	0.00	0.016	-0.004
Z pT reweighting	0.00	0.01	-0.01	0.012	-0.012
signal modeling	-0.01	0.06	-0.06	0.125	-0.068
EM triggers	0.00	0.00	0.00	0.047	-0.027
Muon triggers	-0.01	0.08	-0.07	0.076	-0.075
Dilepton trigger	0.00	0.06	0.00	0.032	-0.010
Opposite charge requirement	0.00	0.02	-0.02	0.021	-0.021
Jet triggers	-0.00	0.01	-0.01	0.014	-0.014
Jet energy scale	-0.05	0.16	-0.14	0.172	-0.161
Jet shifting	-0.06	0.09	-0.09	0.110	-0.112
b-Jet energy scale	-0.00	0.03	-0.03	0.034	-0.034
Jet energy resolution	-0.00	0.00	0.00	0.006	-0.011
JetID	-0.03	0.11	-0.11	0.113	-0.111
Jet Trigger in tau-sample	0.00	0.01	0.00	0.009	-0.000
Tau energy scale	0.00	0.02	-0.02	0.020	-0.020
MET modelling error	0.00	0.00	-0.01	0.007	-0.007
Taggability	0.06	0.17	-0.16	0.171	-0.165
Flavor dependence of taggability	0.00	0.00	0.00	0.000	-0.010
b-tag TRF	0.31	0.31	-0.29	0.386	-0.358
c-tag TRF	0.01	0.05	-0.06	0.058	-0.057
light tag TRF	0.00	0.04	-0.05	0.046	-0.046
b fragmentation	0.02	0.13	-0.12	0.129	-0.126
ϵ_{QCD} and ϵ_{sig}	-0.00	0.03	-0.03	0.034	-0.033
MC background x-section	-0.00	0.03	-0.03	0.035	-0.032
MC signal & bkg branching ratio	0.00	0.09	-0.08	0.082	-0.080
MC bkg scale factors	0.00	0.04	-0.04	0.038	-0.037
MC statistics	-0.00	0.06	-0.06	0.057	-0.056
W+jets heavy flavor scale factor	0.01	0.13	-0.13	0.141	-0.140
W normalization factor	0.00	0.00	-0.01	0.001	-0.001
Tau correction	0.00	0.02	-0.02	0.020	-0.020
Tau reconstruction	0.00	0.01	-0.01	0.007	-0.007
Instrumental background	-0.00	0.02	-0.01	0.015	-0.015
PDF	-0.00	0.09	-0.08	0.084	-0.085
Luminosity	0.00	0.52	-0.44	0.512	-0.453
Statistics for matrix method	-0.02	0.12	-0.12	0.118	-0.110
Total systematics	+0.24	+0.76	-0.67	0.796	-0.729
	result	$+\sigma$	$-\sigma$		
Nuisance parameter fit	8.16	+0.95	-0.84		

Table 11.4.: Systematic uncertainties and result for $\sigma_{t\bar{t}}$ in the combined l+jets, dilepton and τ+lepton channel for the nuisance parameter likelihood (left) and the standard method (right) of error treatment.

and the upper and lower 68 % confidence level error bands are

$$\sigma(m_t) + \Delta\sigma^+(m_t) = [48.30 - 2.019\,10^{-1} m_t - 1.310\,10^{-3} m_t^2 + 6.700\,10^{-6} m_t^3] \text{ pb} \quad (11.2)$$

$$\sigma(m_t) - \Delta\sigma^-(m_t) = [39.63 - 1.664\,10^{-1} m_t - 1.072\,10^{-3} m_t^2 + 5.472\,10^{-6} m_t^3] \text{ pb}. \quad (11.3)$$

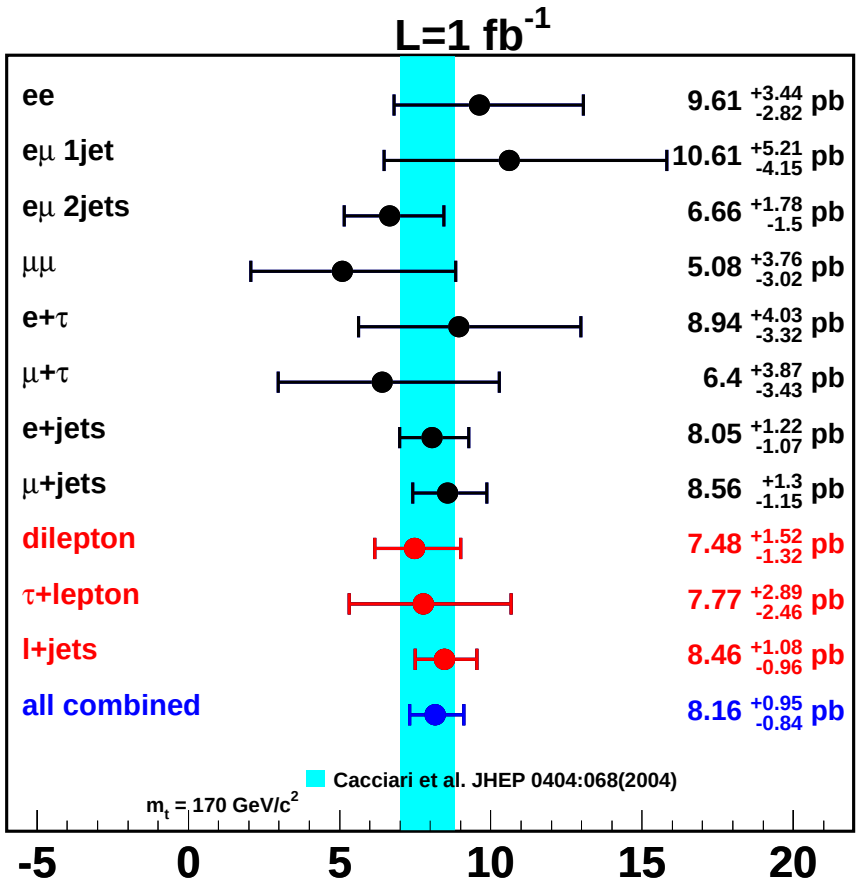

Figure 11.1.: Measured $t\bar{t}$ production cross section for individual channels with the nuisance parameter method.

channel	$\sigma_{t\bar{t}}$ [pb]
ee	$9.61^{+3.44}_{-2.82}$ (stat+syst)
$e\mu$ 1 jet	$10.61^{+5.21}_{-4.15}$ (stat+syst)
$e\mu$ 2 jet	$6.66^{+1.78}_{-1.50}$ (stat+syst)
$e\mu$ combined	$7.22^{+1.71}_{-1.50}$ (stat+syst)
$\mu\mu$	$5.08^{+3.76}_{-3.02}$ (stat+syst)
dilepton combined	$7.48^{+1.52}_{-1.32}$ (stat+syst)
$e + \tau$	$8.94^{+4.03}_{-3.32}$ (stat+syst)
$\mu + \tau$	$6.40^{+3.87}_{-3.43}$ (stat+syst)
τ+lepton combined	$7.77^{+2.89}_{-2.46}$ (stat+syst)
dilepton and τ+lepton combined	$7.56^{+1.41}_{-1.22}$ (stat+syst)
e+jets	$8.05^{+1.22}_{-1.07}$ (stat+syst)
μ+jets	$8.56^{+1.30}_{-1.15}$ (stat+syst)
l+jets combined	$8.46^{+1.08}_{-0.96}$ (stat+syst)

Table 11.5.: Measured $t\bar{t}$ production cross section for individual channels with nuisance parameter method.

top mass	$\sigma_{t\bar{t}}$ [pb] (standard method)	$\sigma_{t\bar{t}}$ [pb] (nuisance method)
160	$8.64^{+0.52}_{-0.50}$ (stat)	$8.93^{+1.02}_{-0.91}$ (stat+syst)
165	$8.07^{+0.49}_{-0.47}$ (stat)	$8.35^{+0.97}_{-0.86}$ (stat+syst)
170	$7.88^{+0.47}_{-0.46}$ (stat)	$8.16^{+0.95}_{-0.84}$ (stat+syst)
175	$7.58^{+0.46}_{-0.45}$ (stat)	$7.83^{+0.93}_{-0.82}$ (stat+syst)
180	$7.39^{+0.45}_{-0.43}$ (stat)	$7.67^{+0.91}_{-0.81}$ (stat+syst)

Table 11.6.: Measured $t\bar{t}$ production cross section for different top quark masses in the l+jets, dilepton and τ+lepton channels.

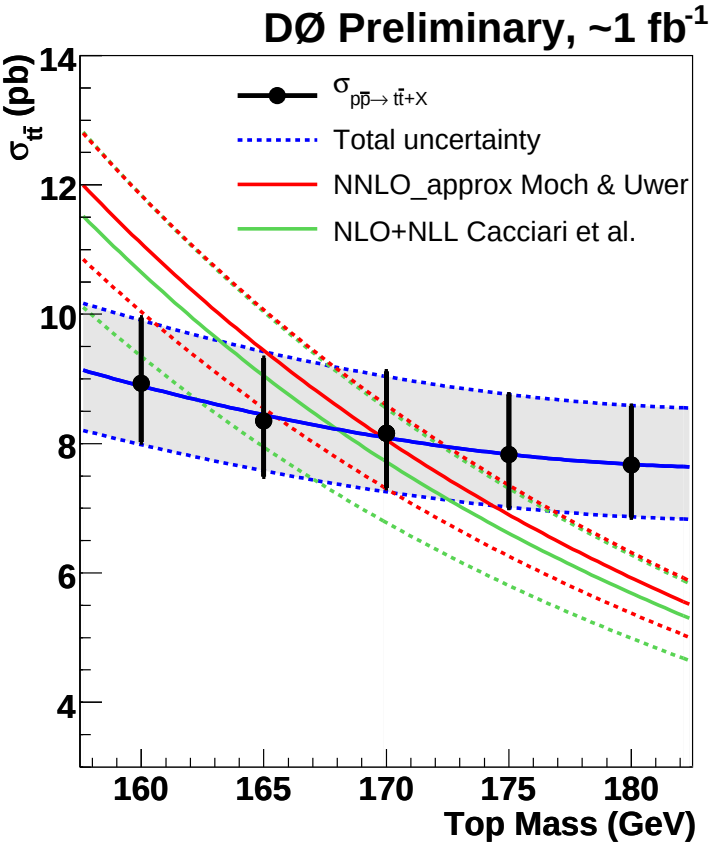

Figure 11.2.: Measured $\sigma_{t\bar{t}}$ as function of the top quark mass [176]. The theoretical curves are the NLO+NNLL calculation from Moch and Uwer [18, 19] and the NLO+NLL calculation from Cacciari [163] and the PDF set CTEQ6.6.

11.2. Search for charged Higgs bosons in the top quark decay

In various extensions of the Standard Model, as for example in Supersymmetry, the existence of an additional Higgs doublet is predicted. Besides three neutral physical Higgs particles, two charged Higgs bosons $H^{\pm}$ are expected in these models. In case of the charged Higgs boson being lighter than the top quark, it can originate from top quark decays. For a fixed $t\bar{t}$ production cross section, the presence of the charged Higgs can significantly modify the expected number of events in the different $t\bar{t}$ final states, as will be shown in this section.

The search for charged Higgs bosons in top quark decays is based on the cross section combination presented in section 11.1. The branching fraction of the charged Higgs boson depends on the ratio of the vacuum expectation values of the two Higgs doublets, $\tan\beta$. For small values of $\tan\beta$ it is dominated by the decay into jets, while for large $\tan\beta$ it is dominated by the decay into τ and τ-neutrino. The difference in the decay of the charged Higgs boson from the W boson decay changes the ratio of the various $t\bar{t}$ final states. In case of the tauonic Higgs decay for example, the number of events in the τ+lepton channel increases with decreasing event numbers in the l+jets and dilepton final states.

Two models for charged Higgs boson decays are considered: One where the charged Higgs boson decays purely into $\tau\nu$, and one where it decays only into $c\bar{s}$.

The tauonic model is valid in the MSSM for large $\tan\beta$. For $\tan\beta \geq 15$ the charged Higgs decays into τ's to almost 100%. As discussed in section 9.1, the purely leptophobic decay of charged Higgs into a charm and a strange quark can occur in general Multi-Higgs-Doublet Models (MHDM) or due to radiative corrections from SUSY-breaking effects in the MSSM [28, 29, 35].

In case of the tauonic model two methods are used for the measurement of $B(t \to H^+b)$. In the first method the $t\bar{t}$ cross section is fixed to the theoretical NLO calculation. The second method is a simultaneous extraction of the $t\bar{t}$ cross section and $B(t \to H^+b)$. For the purely leptophobic model the simultaneous fit can not be performed properly, as will be discussed in section 11.2.4.

11.2.1. Acceptance and event b-tag probability as function of $B(t \to H^+b)$

The event selection and b-tag probabilities are derived for the following three cases:

- $t\bar{t} \to W^{\pm}\bar{b}W^{\mp}b$ (referred to as $t\bar{t} \to WW$)
- $t\bar{t} \to W^{\pm}\bar{b}H^{\mp}b$ (referred to as $t\bar{t} \to WH$)
- $t\bar{t} \to H^{\pm}\bar{b}H^{\mp}b$ (referred to as $t\bar{t} \to HH$)

Since the momentum of the quark originating from the top quark decay can be different due to the difference in the mass of the decay boson (W or H^+) the efficiency to select a $t\bar{t}$ event can depend on the top quark decay. The $t\bar{t}$ selection efficiency as function of the top quark decay and the branching ratio $X := B(t \to H^+b)$ can be computed as:

$$P_p(t\bar{t}) = (1-X)^2 P_p(t\bar{t} \to WW) + 2X(1-X)P_p(t\bar{t} \to WH^+) + X^2 P_p(t\bar{t} \to H^+H^-),$$

where P_p denotes the selection efficiency for the different scenarios. Additionally, b-jet identification is used in the l+jets and τ+lepton channels. The per event b-tagging probability for $t\bar{t}$ events can be calculated as:

$$P_b(t\bar{t}) = (1-X)^2 P_b(t\bar{t} \to WW) + 2X(1-X)P_b(t\bar{t} \to WH^+) + X^2 P_b(t\bar{t} \to H^+H^-),$$

where P_b is the event tagging probability for a particular decay channel.

The total $t\bar{t}$ selection and b-tag efficiency is a product of the selection and b-tagging efficiencies:

$$\begin{aligned} P_{total}(t\bar{t}) &= (1-X)^2 P_p(t\bar{t}\to WW)P_b(t\bar{t}\to WW) + 2X(1-X)P_p(t\bar{t}\to WH)P_b(t\bar{t}\to WH) \\ &+ X^2 P_p(t\bar{t}\to HH)P_b(t\bar{t}\to HH), \end{aligned} \tag{11.4}$$

Equation 11.4 has the same form as Eq. 8.16 for the dependency of the $t\bar{t}$ selection efficiency on the ratio of branching fractions R. The only difference is that R is now replaced by $(1-X)$ and instead of different quark types from the top decay (b and light quarks) different boson types ($W^\pm$ and $H^\pm$) are considered.

In case of the measurement of the ratio of branching fractions R, the dependency of the b-tag probability is dominating the dependency of $P_{total}(t\bar{t})$ on R. For the charged Higgs, the dependency of $P_{total}(t\bar{t})$ on X can be dominated either by the event selection or b-tagging probability, depending on the final state and the charged Higgs decay. For the tauonic charged Higgs, for example, the difference between the $t\bar{t}\to WW$, $t\bar{t}\to WH^+$ and $t\bar{t}\to H^+H^-$ occurs due to differences in the selection efficiency. For charged Higgs decays to a virtual top and a b quark, the change of b-tagging efficiency plays a more important role than the acceptance variation, as the heavy flavour content differs between Standard Model $t\bar{t}$ events and $t\bar{t}$ events with H^+ decay.

Figure 11.3 shows the selection efficiency as function of $B(t\to H^+b)$ for a charged Higgs mass of 80 GeV and 150 GeV in the tauonic and leptophobic charged Higgs model. For the tauonic model, it can be seen that for all channels but the τ+lepton channel the selection efficiency decreases with increasing $B(t\to H^+b)$, as long as the charged Higgs mass is low. For high charged Higgs masses also the τ+lepton channel shows a decreasing behaviour. This comes from the lower momentum of the b-jet, resulting in lower acceptance of events with at least two jets with $p_T \geq 20$ GeV. In the leptophobic model all channels show decreasing behaviour. For $B(t\to H^+b)=1$ the acceptance in all final states is zero, as at least one lepton is required, but the decay $t\bar{t}\to H^+bH^-\bar{b}\to c\bar{s}b\bar{c}s\bar{b}$ only contains jets.

11.2.2. Predicted yields for the presence of a charged Higgs boson

The Standard Model $t\bar{t}$ signal and background samples are the same as for the cross section combination. Additionally, $t\bar{t}$ Monte Carlo with at least one top quark decaying into a charged Higgs boson and a b quark is generated with PYTHIA for charged Higgs masses of 80, 100, 120, 140, 150 and 155 GeV. The samples with the decay of the charged Higgs boson to $\tau\bar{\nu}$ and $c\bar{s}$ are generated separately. The top quark mass is set to 170 GeV. The mixture of $t\bar{t}\to WW$, $t\bar{t}\to WH$ and $t\bar{t}\to HH$ is then calculated using Eq. 11.4.

Tables 11.7 and 11.8 list the predicted yields for the e+jets and μ+jets channel with $\sigma_{t\bar{t}} = 7.3$ pb, $B(t\to H^+b)=0.0$ and $B(t\to H^+b)=0.2$ for the tauonic model and a charged Higgs mass of 80 GeV. The cross section is chosen in order to match the theory prediction from Cacciari at the current world average top quark mass of 172.6 GeV. In the Standard Model $t\bar{t}$ cross section measurement for the l+jets final states, the normalisation of the W+jets background depends on the number of $t\bar{t}$ events. If a charged Higgs boson is present, the number of $t\bar{t}$ events depends on $B(t\to H^+b)$, therefore the W+jets background is re-calculated for each charged Higgs branching ratio.

Table 11.9 shows the change of the expected number of events for the $e\mu$ channel, and Table 11.10 for the $e+\tau$ and $\mu+\tau$ channels. The $t\bar{t}$ cross section is also set to 7.3 pb, and the tauonic decaying charged Higgs with mass of 80 GeV is chosen as an example. It can clearly be seen that the expected number of events decreases from $B(t\to H^+b)=0.0$ over

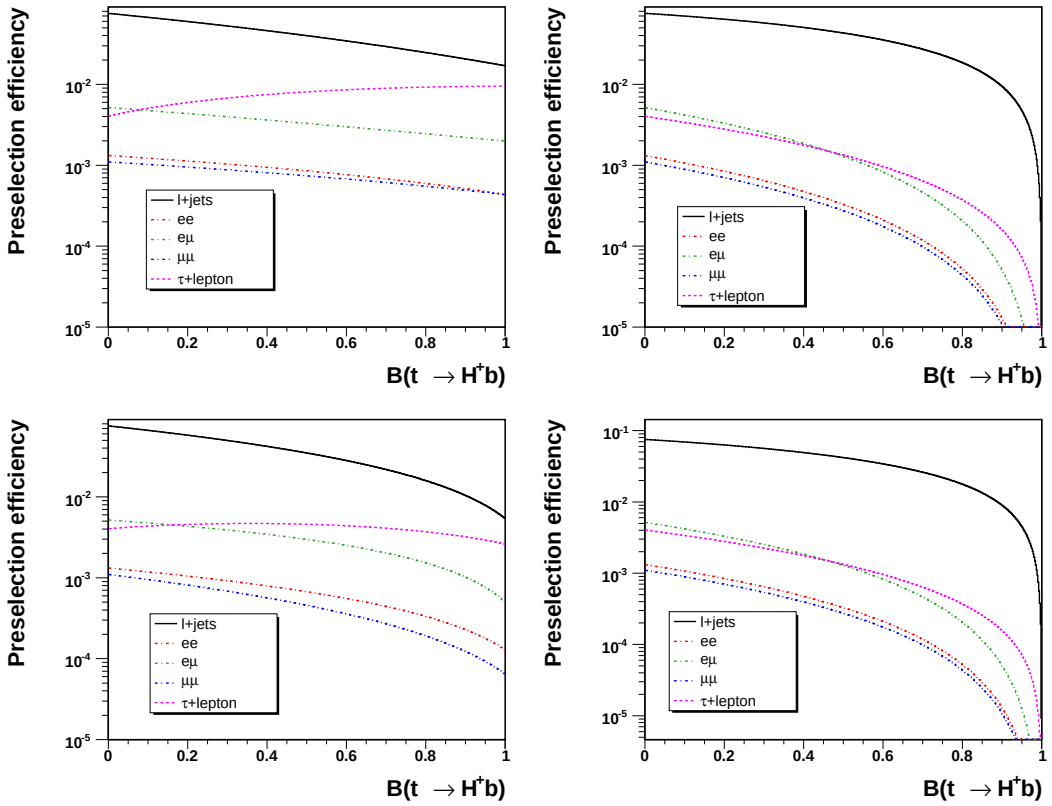

Figure 11.3.: Preselection efficiency as function of $B(t \rightarrow H^+b)$. Top: For a charged Higgs mass of 80 GeV. Bottom: For a charged Higgs mass of 150 GeV. Left: tauonic model. Right: Leptophobic model.

$B(t \rightarrow H^+b) = 0.2$ to $B(t \rightarrow H^+b) = 0.4$ in the $e\mu$ channel, but increases in the τ+lepton final states.

In Figure 11.4 the observed number of events in all considered channels is compared with predictions for $\sigma_{t\bar{t}} = 7.3$ pb and three different sets of $B(t \rightarrow H^+b)$ in the tauonic and leptophobic model, respectively, for a charged Higgs mass of 80 GeV. For the tauonic model the number of predicted events increases with increasing $B(t \rightarrow H^+b)$ only in the τ+lepton channel, and decreases everywhere else. In case of the leptophobic model the number of events decreases in all channels with increasing top to charged Higgs branching ratio.

Yield table				
Contribution	3 Jet 1 tag	$\geq$4 Jet 1 tag	3 Jet $\geq$2 tag	$\geq$4 Jet $\geq$2 tag
Multijets	31.49	7.94	2.72	1.08
tb	2.33	0.54	1.05	0.26
tbq	4.78	1.39	1.04	0.48
WW	3.22	0.81	0.09	0.08
WZ	0.91	0.20	0.21	0.04
ZZ	0.14	0.07	0.04	0.02
$Z(\tau\tau)bb$	0.58	0.18	0.14	0.04
$Z(\tau\tau)cc$	0.37	0.15	0.02	0.01
$Z(\tau\tau)lp$	0.43	0.19	0.003	0.002
$Z(ee)bb$	2.09	0.75	0.38	0.15
$Z(ee)cc$	1.20	0.42	0.05	0.03
$Z(ee)lp$	1.30	0.52	0.01	0.006
$B(t \to H^+b) = 0.0$				
W+jets	54.64	10.19	5.10	1.20
ttlj	62.38	69.61	22.78	35.69
ttll	10.57	3.24	4.64	1.55
Total predicted	176.42	96.21	38.27	40.64
$B(t \to H^+b) = 0.2$				
W+jets	56.16	13.60	5.24	1.60
ttlj	45.28	50.65	16.33	25.84
ttll	16.34	4.28	7.12	1.98
Total predicted	166.61	81.70	34.45	31.63
Observed	183	113	40	30

Table 11.7.: Predicted and observed number of events for e+jets with different $B(t \to H^+b)$ in the subsamples with 3 or at least 4 jets and 1 or at least 2 b-tags. For 80 GeV charged Higgs and assuming $B(t \to \tau\nu) = 100\%$.

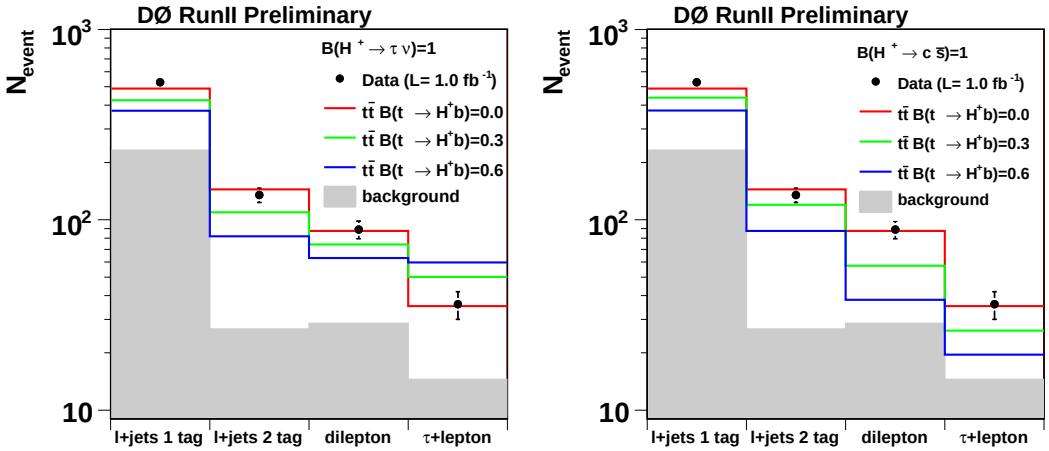

Figure 11.4.: Predicted and observed number of events for different $B(t \to H^+b)$ in the tauonic (left) and leptophobic (right) model for a charged Higgs mass of 80 GeV.

Contribution	3 Jet 1 tag	$\geq$4 Jet 1 tag	3 Jet $\geq$2 tag	$\geq$4 Jet $\geq$2 tag
Multijets	9.71	0.00	1.02	0.00
tb	1.97	0.42	0.93	0.20
tbq	3.73	0.98	0.84	0.36
WW	2.70	0.68	0.09	0.06
WZ	0.88	0.23	0.24	0.07
ZZ	0.20	0.05	0.05	0.01
$Z(\tau\tau)bb$	0.28	0.11	0.06	0.04
$Z(\tau\tau)cc$	0.22	0.10	0.01	0.006
$Z(\tau\tau)lp$	0.25	0.10	0.002	0.001
$Z(\mu\mu)bb$	2.53	0.76	0.56	0.23
$Z(\mu\mu)cc$	1.58	0.72	0.10	0.04
$Z(\mu\mu)lp$	1.67	0.68	0.01	0.008
$B(t \to H^+b) = 0.0$				
W+jets	60.06	14.96	5.85	1.67
ttlj	45.00	56.32	17.73	30.58
ttll	7.64	2.45	3.54	1.21
Total predicted	138.41	78.56	31.03	34.50
$B(t \to H^+b) = 0.2$				
W+jets	61.28	17.89	5.97	2.00
ttlj	32.24	40.03	12.59	21.74
ttll	11.49	3.42	5.32	1.64
Total predicted	130.74	66.16	27.78	26.42
Observed	133	99	31	34

Table 11.8.: Predicted and observed number of events for μ+jets with different $B(t \to H^+b)$ in the subsamples with 3 or at least 4 jets and 1 or at least 2 b-tags. For 80 GeV charged Higgs and assuming $B(t \to \tau\nu) = 100\%$.

Contribution	1 Jet $e\mu$	$\geq$ 2 Jets $e\mu$
WW	2.79	1.22
WZ	0.37	0.17
$Z(\tau\tau)$	5.48	5.36
fake_EM	0.22	0.74
fake_MU	0.64	1.86
$B(t \to H^+b) = 0.0$		
ttemu	7.91	32.48
Total predicted	17.42	41.84
$B(t \to H^+b) = 0.2$		
ttll	6.88	27.12
Total predicted	16.38	36.48
$B(t \to H^+b) = 0.4$		
ttll	5.92	22.40
Total predicted	15.42	31.76
Observed	21	39

Table 11.9.: Predicted and observed number of events for $e\mu$ with different $B(t \to H^+b)$ in the subsamples with one or at least two jets. For 80 GeV charged Higgs and assuming $B(H^+ \to \tau\nu) = 100\%$.

Contribution	$e+\tau$	$\mu+\tau$
W+jets	0.57	0.80
tb	-0.010	-0.00
tbq	0.08	0.054
WW	0.13	0.11
WZ	0.01	0.03
ZZ	0.02	0.02
$Z(\tau\tau)bb$	0.15	0.24
$Z(\tau\tau)cc$	0.10	0.14
$Z(\tau\tau)lp$	0.07	0.16
$Z(ee)bb$ or $Z(\mu\mu)bb$	0.09	0.31
$Z(ee)cc$ or $Z(\mu\mu)cc$	0.06	0.16
$Z(ee)lp$ or $Z(\mu\mu)lp$	0.07	0.15
$B(t \to H^+b) = 0.0$		
ttll	4.78	6.87
ttlj	4.73	4.34
Total predicted	13.87	21.38
$B(t \to H^+b) = 0.2$		
ttll	10.88	14.24
ttlj	3.08	2.98
Total predicted	18.32	27.39
$B(t \to H^+b) = 0.4$		
ttll	15.97	19.69
ttlj	1.78	1.87
Total predicted	22.10	31.73
Same sign Data	3	8
Observed	16	20

Table 11.10.: Predicted and observed number of events for $e+\tau$ and $\mu+\tau$ with different $B(t \to H^+b)$. For 80 GeV charged Higgs and assuming $B(t \to \tau\nu) = 100\%$.

11.2.3. Fit of $B(t \to H^+b)$ for fixed $\sigma_{t\bar{t}}$

Fixing the $t\bar{t}$ cross section to its theoretical value, a global fit of $B(t \to H^+b)$ in the l+jets, dilepton and τ+lepton channels is performed. The extraction of the branching ratio of a top quark decaying into charged Higgs and b-quark is done with the maximum likelihood fit defined in Eq. 8.4. The product runs over all 14 channels that are used to extract the cross section, discussed in section 11.1. In each channel the predicted number of events is calculated as function of $B(t \to H^+b)$, with the $t\bar{t}$ cross section fixed to 7.3 ± 0.7 pb. The uncertainty on the cross section is assumed to be fully correlated between all channels. The nuisance parameter method is used for the extraction of the branching ratio.

Table 11.11 shows the statistical and systematic uncertainty for the fitted $B(t \to H^+b)$, for a charged Higgs mass of 80 GeV and the tauonic charged Higgs model. Different sources of systematic uncertainties are merged into classes. The fake background includes the uncertainty on the same sign data of the τ+lepton channel. The relative uncertainty on the $t\bar{t}$ cross section of 10 % and the luminosity uncertainty of 6.1 % are the dominant uncertainties on the branching ratio. Furthermore, the b-tag uncertainty is large. The total systematic error even exceeds the statistical uncertainty. In Table 11.12 the statistical and systematic uncertainties in the leptophobic model for the example of 80 GeV charged Higgs are listed. The uncertainties on luminosity and $t\bar{t}$ cross section are larger than for the tauonic model, as the behaviour of the change of the branching ratio is more similar between the different channels compared to the tauonic model, making the measurement more sensitive to a change in $t\bar{t}$ cross section or luminosity.

Source	$+\sigma$	$-\sigma$
Statistical uncertainty	0.047	-0.046
Lepton identification	0.010	-0.010
Tau identification	0.007	-0.006
Jet identification	0.010	-0.010
Jet corrections	0.020	-0.019
Jet Trigger in tau-sample	0.002	-0.000
Tau energy scale	0.004	-0.004
Trigger	0.007	-0.006
b-jet identification	0.030	-0.030
signal modelling	0.010	-0.010
background estimation	0.010	-0.010
fake background	0.019	-0.016
other	0.010	-0.010
Matrix method ε_{QCD} and ε_{sig}	0.003	-0.003
$t\bar{t}$ cross section error	0.051	-0.052
Luminosity	0.032	-0.027
Total systematic	0.077	-0.075

Table 11.11.: Statistical and systematic uncertainties on $B(t \to H^+b)$ for a charged Higgs mass of 80 GeV in the tauonic model. For this example the central value with standard method of error treatment is found to be $B(t \to H^+b) = -0.053$.

As no sensitivity to charged Higgs can be observed, limits are set using the Feldman Cousins procedure. Pseudo-experiments, as described in section 8.6.5, are generated for 21 values of $B(t \to H^+b)$.

Source	$+\sigma$	$-\sigma$
Statistical uncertainty	+0.058	-0.059
Lepton identification	0.017	-0.017
Tau identification	0.004	-0.004
Jet identification	0.009	-0.009
Jet corrections	0.016	-0.019
Jet Trigger in tau-sample	0.000	-0.002
Tau energy scale	0.004	-0.004
Trigger	0.007	-0.011
b-jet identification	0.031	-0.030
signal modelling	0.024	-0.025
background estimation	0.013	-0.014
fake background	0.013	-0.015
other	0.017	-0.017
Matrix method ε_{QCD} and ε_{sig}	0.003	-0.003
$t\bar{t}$ cross section error	0.076	-0.085
Luminosity	0.049	-0.053
Total systematic	0.105	-0.115

Table 11.12.: Statistical and systematic uncertainties on $B(t \to H^+b)$ for a charged Higgs mass of 80 GeV in the leptophobic model. For this example the central value with standard method of error treatment is found to be $B(t \to H^+b) = -0.059$.

Table 11.13 and 11.14 show the resulting expected and observed upper limits on $B(t \to H^+b)$ for each generated charged Higgs mass in the tauonic and leptophobic model, respectively.

H^+ mass [GeV]	expected	observed
80	0.19	0.15
100	0.18	0.14
120	0.20	0.16
140	0.21	0.18
150	0.21	0.19
155	0.21	0.18

Table 11.13.: Upper limits on the branching ratio $B(t \to H^+b)$ for each generated H^+ mass point in the tauonic model.

In Fig. 11.5 the expected and observed upper limit on $B(t \to H^+b \to \tau^+\nu b)$ versus charged Higgs mass is shown for the combined l+jets, dilepton and τ+lepton channel. The limits are compared to tree level calculations of $B(t \to H^+b)$ in the MSSM [180], shown as blue curves for various values of $\tan\beta$.

Figure 11.6 shows the upper limits on $B(t \to H^+b \to c\bar{s}b)$ versus charged Higgs mass. The limits are again compared to tree level MSSM calculations, here for large and small values of $\tan\beta$. The leptophobic model can be realised for large $\tan\beta$ in the MHDM (see section 2.2.2) and for low $\tan\beta$, where the leptophobic decay can get dominant for radiative corrections from SUSY-breaking effects. In case of the MHDM $\tan\beta$ has to be replaced by coupling constants.

Comparing the upper limits on the branching ratio to the tree level calculations from the

H^+ mass [GeV]	expected	observed
80	0.25	0.21
100	0.25	0.22
120	0.25	0.22
140	0.24	0.21
150	0.22	0.19
155	0.22	0.19

Table 11.14.: Upper limits on the branching ratio $B(t \to H^+b)$ for each generated H^+ mass point in the leptophobic model.

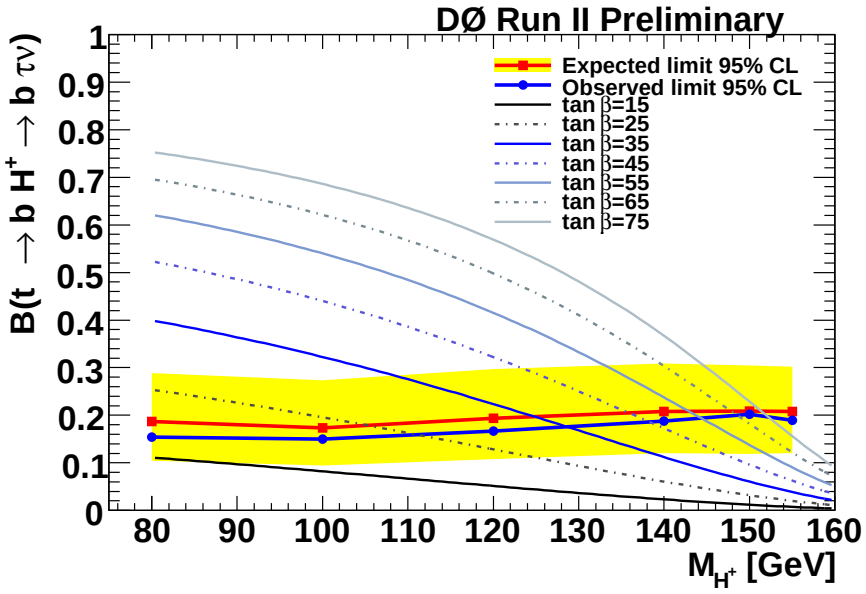

Figure 11.5.: Observed (blue) and expected (red) limit with one standard deviation band (yellow) for the tauonic charged Higgs model versus charged Higgs mass for the combined l+jets, τ+lepton and dilepton channels. The limits are compared to the calculation of $B(t \to H^+b)$ at tree level MSSM using Eq. (12) from [180] (blue spectra).

MSSM yields lower limits on the charged Higgs mass versus $\tan\beta$. In Table 11.15 the lower limits on the charged Higgs mass for large $\tan\beta$ in the tauonic model, and for small and large $\tan\beta$ in the leptophobic model, are shown. These limits can be translated in the $\tan\beta$ versus m_{H^+} parameter space of the MSSM, as will be discussed in section 11.2.5.

In Appendix F limits on $B(t \to H^+b)$ with part of the here used final states – l+jets and dilepton for example – are briefly discussed. The result of the limits on $B(t \to H^+b)$ using a Bayesian limit setting method are discussed in Appendix G.

The upper limits on $B(t \to H^+b)$ are better in the tauonic than the leptophobic model, especially for low m_{H^+}. Comparing the limits obtained with the l+jets and dilepton channel from appendix F to the full combination shows that the τ+lepton channel improves the limits in the tauonic model for low masses. In the leptophobic model the τ+lepton final state represents a disappearance channel with very low statistics, whereas in the tauonic model sensitivity due to τ+lepton being an appearance channel can be gained.

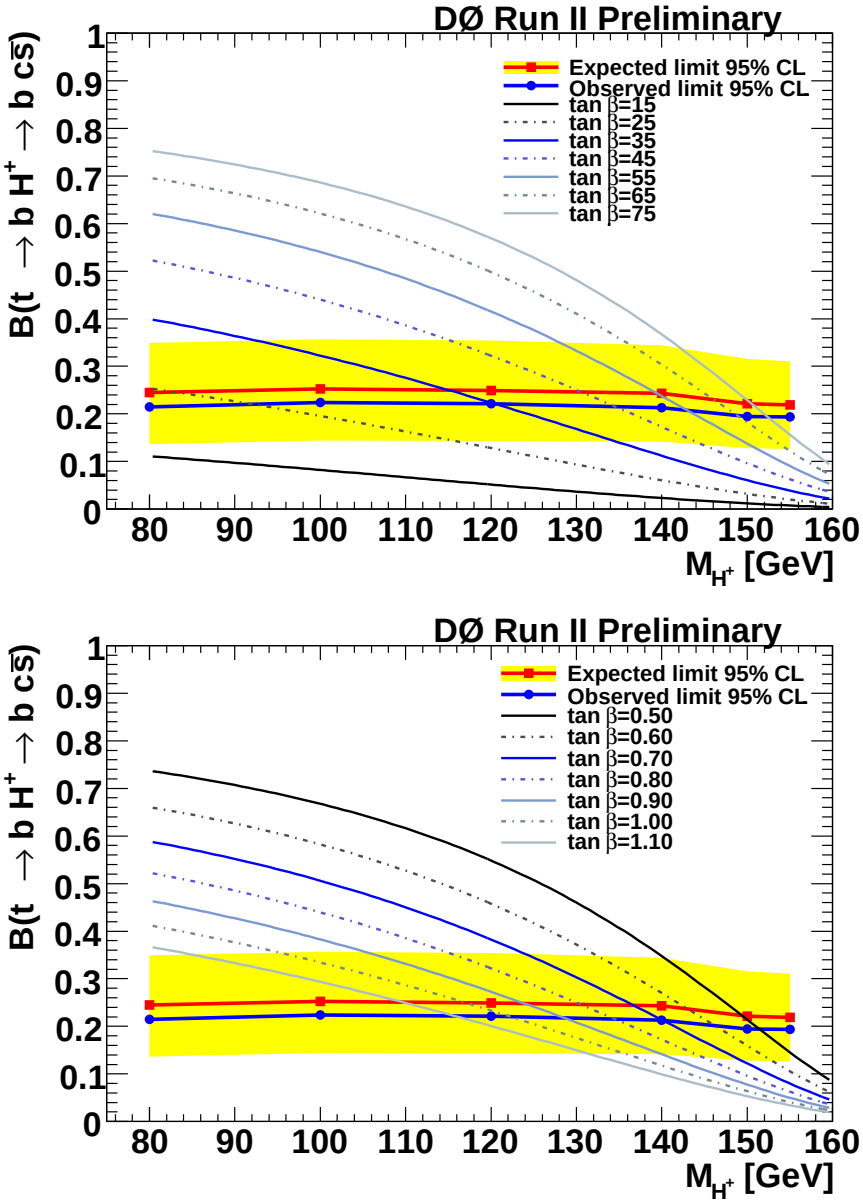

Figure 11.6.: Observed (blue) and expected (red) limit with one standard deviation band (yellow) in the leptophobic model versus H^+ mass for the combined l+jets, τ+lepton and dilepton channels. The limits are compared to the calculation of $B(t \to H^+b)$ at tree level for different values of large tan β using Eq. (12) from [180] (blue spectra). Top: comparison to tree level MSSM calculations for large tan β. Bottom: comparison to tree level MSSM calculations for small tan β.

$\tan\beta$	$H^{\pm}$ mass limit [GeV] (tauonic)	$H^{\pm}$ mass limit [GeV] (leptophobic)
0.50		151
0.60		146
0.70		140
0.80		134
0.90		129
1.0		122
1.1		115
15	none	none
25	113	92
35	130	120
45	139	134
55	145	143
65	149	149
75	153	152

Table 11.15.: Lower mass limits on $H^{\pm}$ in the tauonic and leptophobic model for different values of $\tan\beta$. The calculations are at tree level.

11.2.4. Simultaneous fit of $B(t \to H^+b)$ and $\sigma_{t\bar{t}}$

As the uncertainty on the measurement of $B(t \to H^+b)$ is dominated by the uncertainty on the $t\bar{t}$ cross section, it is obvious that the one dimensional fit of $B(t \to H^+b)$ is highly model dependent. A measurement of the branching ratio of the top quark to charged Higgs decay, independent of any assumption about the theoretical $t\bar{t}$ cross section, is performed by a simultaneous fit of $B(t \to H^+b)$ and $\sigma_{t\bar{t}}$. The two dimensional fit in case of the tauonic charged Higgs model is presented in this section.

The fitting procedure is the same as for the one dimensional fit of the cross section or $B(t \to H^+b)$. Again the nuisance parameter method and the standard method of error treatment are used. For the final limits the results from the nuisance parameter method are taken. The fit on both quantities is performed for each generated charged Higgs mass. In Table 11.16 and 11.17 the statistical and systematic uncertainties on $\sigma_{t\bar{t}}$ and $B(t \to H^+b)$ are shown, respectively, for an example of 80 GeV charged Higgs. Comparing Table 11.16 to Table 11.4, where the cross section only is fitted, it becomes obvious that the statistical uncertainty increases for the two dimensional fit, as expected. The systematic uncertainties related to the τ+lepton channel increase for the simultaneous measurement compared to the one dimensional measurement of $B(t \to H^+b)$. Comparing Table 11.17 to the corresponding Table 11.11 for the determination of $B(t \to H^+b)$, the same effect of increasing systematic uncertainties related to the τ+lepton channel can be observed. For example, the uncertainty on the fake background, which is dominantly the same sign event statistics in τ+lepton, increases by a factor of two when switching from the one dimensional to the simultaneous fitting method. The same factor of two can be observed for the τ energy scale and τ identification. This indicates that the τ+lepton final state is important for the two dimensional fit of $\sigma_{t\bar{t}}$ and $B(t \to H^+b)$. As this is the only channel where the number of events increases for increasing charged Higgs content, the observed behaviour makes sense. Comparing the tables for the systematic errors on $B(t \to H^+b)$ further, it can be seen that the statistical uncertainty increases for the two dimensional method, but the large uncertainties from the $t\bar{t}$ cross section and the luminosity drop out. Uncertainties, like for example on the b-jet identification, also decrease for the two dimensional fit, showing that the b-tagging gives only little information on the charged Higgs branching ratio in the tauonic model, as expected. The large uncertainty on the fake background is in principle also statistical, as it contains the statistical uncertainty of same sign data in the τ+lepton channel and on the loose–tight events in the l+jets channel.

Tables 11.18 and 11.19 show the fitted results of $B(t \to H^+b)$ and $\sigma_{t\bar{t}}$ for the standard method of error treatment and the nuisance method, respectively, for the generated charged Higgs masses. Additionally, the correlation coefficients between $B(t \to H^+b)$ and $\sigma_{t\bar{t}}$ are listed. For high charged Higgs masses the correlation between the two observables gets large, resulting in an increasing statistical uncertainty on both quantities. For these high masses the gain from loosing the two main systematic uncertainties is balanced by the larger statistical uncertainty, resulting in worse limits than for the one dimensional fit. Figure 11.8 shows the nuisance parameter fit result of the $t\bar{t}$ cross section measured simultaneously with the charged Higgs branching ratio, as function of the charged Higgs mass. Within uncertainties, the cross section is constant as function of charged Higgs mass.

In Figure 11.7 the 68 % and 95 % Confidence Level contours in the ($B(t \to H^+b)$, $\sigma_{t\bar{t}}$) plane are shown for different charged Higgs masses. Only statistical uncertainties are included, and the area of the contour is calculated assuming error ellipses. For a too high correlation, as it occurs for large charged Higgs masses, the calculation of the area neglecting the correlation coefficient is not appropriate anymore and results in the statistical uncertainty of the measured value (black lines) to be in disagreement with the 68 % Confidence Level contour (blue). However, the ellipses give an impression on the high correlation for large charged Higgs masses.

Source	$+\sigma$ [GeV]	$-\sigma$ [GeV]
Statistical uncertainty	0.68	-0.64
Lepton identification	0.151	-0.149
Tau identification	0.120	-0.121
Jet identification	0.073	-0.074
Jet corrections	0.140	-0.122
Jet Trigger in tau-sample	0.045	-0.000
Tau energy scale	0.097	-0.091
Trigger	0.109	-0.082
b-jet identification	0.399	-0.373
signal modelling	0.279	-0.237
background estimation	0.153	-0.150
fake background	0.328	-0.288
other	0.159	-0.163
Matrix method ε_{QCD} and ε_{sig}	0.023	-0.024
Luminosity	0.522	-0.463
Total systematic	0.867	-0.784

Table 11.16.: Statistical and systematic uncertainties on $\sigma_{t\bar{t}}$ for the simultaneous fit with $B(t \to H^+b)$ for a charged Higgs mass of 80 GeV in the tauonic model. In this example the central value with standard method of error treatment is found to be $\sigma_{t\bar{t}} = 7.73$ pb.

Source	$+\sigma$	$-\sigma$
Statistical uncertainty	0.067	-0.066
Lepton identification	0.001	-0.001
Tau identification	0.014	-0.014
Jet identification	0.005	-0.005
Jet corrections	0.014	-0.014
Jet Trigger in tau-sample	0.005	-0.000
Tau energy scale	0.011	-0.010
Trigger	0.008	-0.000
b-jet identification	0.003	-0.003
signal modelling	0.014	-0.016
background estimation	0.003	-0.003
fake background	0.036	-0.033
other	0.006	-0.006
Matrix method ε_{QCD} and ε_{sig}	0.002	-0.002
Luminosity	0.002	-0.003
Total systematic	0.047	-0.044

Table 11.17.: Statistical and systematic uncertainties on $B(t \to H^+b)$ for the simultaneous fit with $\sigma_{t\bar{t}}$ for a charged Higgs mass of 80 GeV in the tauonic model. In this example the central value with standard method of error treatment is found to be $B(t \to H^+b) = -0.022$.

As no indication for a charged Higgs is found, upper limits on the charged Higgs branching ratio are calculated with the Feldman Cousins method. For the generation of pseudo-experiments the cross section is set to the measured value. In the fit to the pseudo-data, $\sigma_{t\bar{t}}$

m_{H^+} [GeV]	$B(t \to H^+b)$	$\sigma_{t\bar{t}}$ [pb]
80	$-0.022^{+0.067}_{-0.066}(\text{stat})^{+0.047}_{-0.044}(\text{syst})$	$7.73^{+0.68}_{-0.64}(\text{stat})^{+0.87}_{-0.78}(\text{syst})$
100	$-0.015^{+0.061}_{-0.058}(\text{stat})^{+0.041}_{-0.038}(\text{syst})$	$7.78^{+0.64}_{-0.59}(\text{stat})^{+0.85}_{-0.77}(\text{syst})$
120	$-0.018^{+0.070}_{-0.069}(\text{stat})^{+0.049}_{-0.046}(\text{syst})$	$7.75^{+0.72}_{-0.66}(\text{stat})^{+0.87}_{-0.78}(\text{syst})$
140	$-0.003^{+0.084}_{-0.083}(\text{stat})^{+0.052}_{-0.049}(\text{syst})$	$7.85^{+0.93}_{-0.82}(\text{stat})^{+0.91}_{-0.81}(\text{syst})$
150	$0.029^{+0.093}_{-0.095}(\text{stat})^{+0.051}_{-0.047}(\text{syst})$	$8.18^{+1.19}_{-1.02}(\text{stat})^{+0.90}_{-0.80}(\text{syst})$
155	$0.017^{+0.098}_{-0.102}(\text{stat})^{+0.056}_{-0.050}(\text{syst})$	$8.06^{+1.29}_{-1.10}(\text{stat})^{+0.91}_{-0.81}(\text{syst})$

Table 11.18.: Fit results for $B(t \to H^+b)$ and $\sigma_{t\bar{t}}$ with the standard method.

m_{H^+} [GeV]	$B(t \to H^+b)$	$\sigma_{t\bar{t}}$ [pb]	correlation coefficient
80	$-0.014^{+0.078}_{-0.083}$	$8.05^{+1.12}_{-1.02}$	0.72
100	$-0.008^{+0.070}_{-0.073}$	$8.10^{+1.08}_{-0.98}$	0.66
120	$-0.007^{+0.080}_{-0.086}$	$8.10^{+1.15}_{-1.04}$	0.75
140	$0.009^{+0.092}_{-0.097}$	$8.24^{+1.32}_{-1.17}$	0.85
150	$0.041^{+0.101}_{-0.103}$	$8.58^{+1.55}_{-1.32}$	0.90
155	$0.027^{+0.108}_{-0.113}$	$8.45^{+1.65}_{-1.40}$	0.91

Table 11.19.: Fit results for $B(t \to H^+b)$ and $\sigma_{t\bar{t}}$ with the nuisance parameter method and correlation coefficients between $B(t \to H^+b)$ and $\sigma_{t\bar{t}}$. The uncertainties contain the combined statistical, systematic and luminosity uncertainty. The correlation coefficients are measured for the statistical only fit.

and $B(t \to H^+b)$ are allowed to float, resulting in the full inclusion of the higher statistical and the different systematic uncertainties due to the two dimensional fit in the limit on $B(t \to H^+b)$.

Figure 11.9 shows the resulting limits on $B(t \to H^+b)$ versus the charged Higgs mass. In Table 11.20 the upper limits on $B(t \to H^+b)$ for various charged Higgs masses are listed. In comparison to the limits obtained with the one dimensional method, as given in Table 11.13, the improvement for low charged Higgs masses is about 30 %. At large charged Higgs masses the expected limits are about the same. In Table 11.21 the lower limits on the charged Higgs mass for given $\tan\beta$ are shown, as resulting from the comparison of the limits on the branching ratio to tree-level MSSM calculations.

The simultaneous fit does not work properly in case of leptophobic decaying charged Higgs. The fit relies on the different behaviour in the various channels with increasing charged

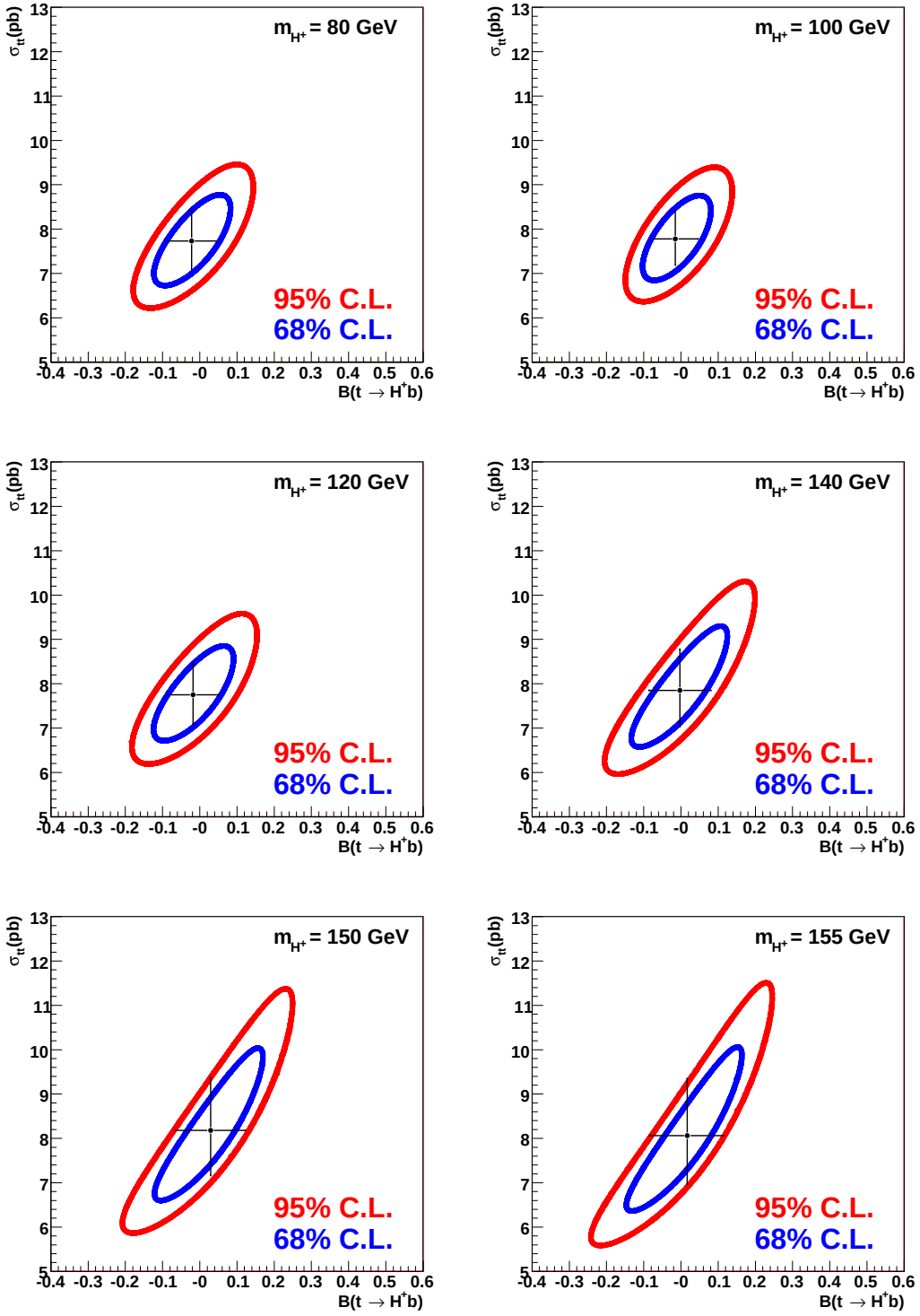

Figure 11.7.: Contour plots for the simultaneous fit of $B(t \to H^+b)$ and $\sigma_{t\bar{t}}$ in the tauonic charged Higgs model. Only the statistical uncertainty is included.

Higgs component. For the tauonic decaying charged Higgs, the l+jets and dilepton channels represent disappearance channels, where the number of $t\bar{t}$ events decreases with increasing $B(t \to H^+b)$. The τ+lepton channel on the other hand is an appearance channel, as the number of expected $t\bar{t}$ events increases with increasing $B(t \to H^+b)$. The information on the

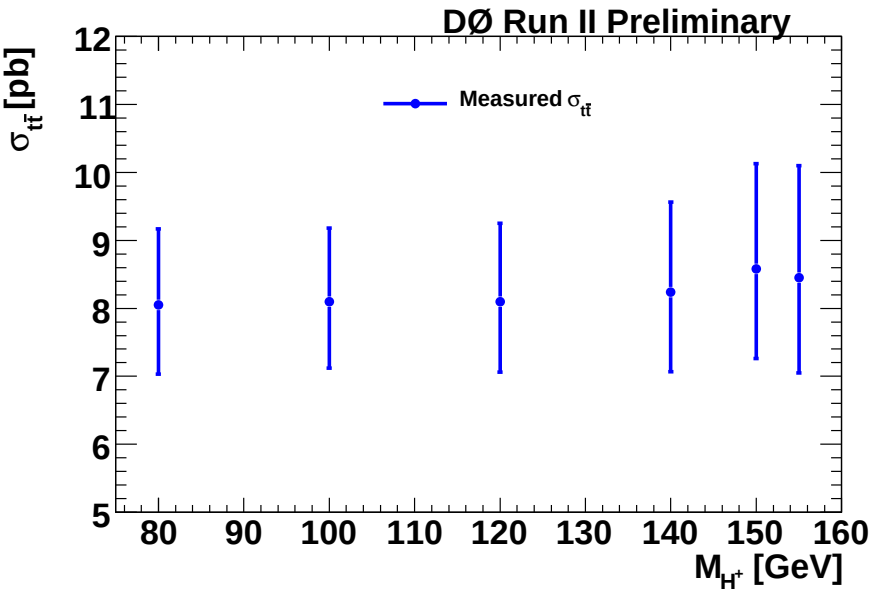

Figure 11.8.: Fitted $t\bar{t}$ cross section versus charged Higgs mass in the tauonic charged Higgs model.

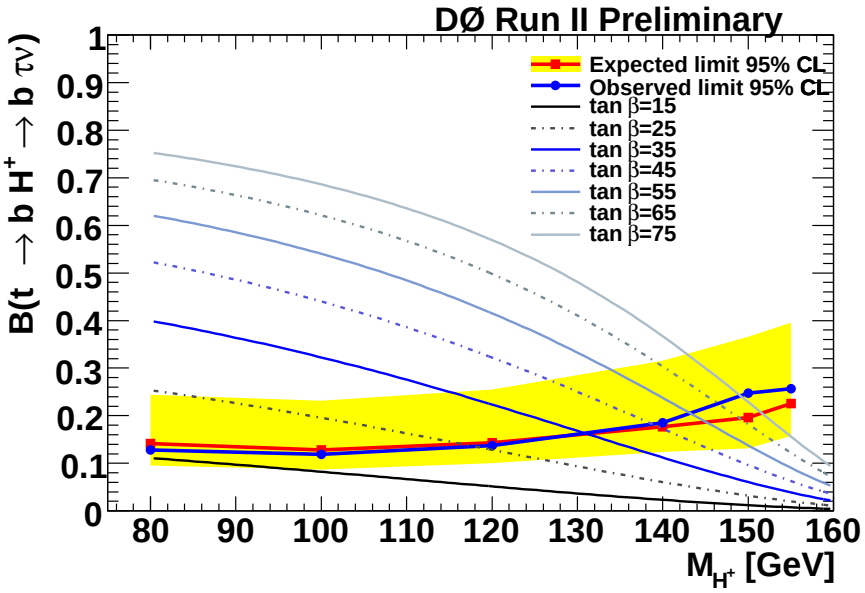

Figure 11.9.: Limit on $B(t \rightarrow H^+b)$ versus charged Higgs mass. $B(t \rightarrow H^+b)$ and $\sigma_{t\bar{t}}$ are fitted simultaneously.

distribution of $t\bar{t}$ events between all channels therefore delivers information on the charged Higgs contribution and results in a reasonable correlation of $\sigma_{t\bar{t}}$ and $B(t \rightarrow H^+b)$ during the fitting procedure. At high charged Higgs masses the τ+lepton channel behaves like a disappearance channel, resulting in lower sensitivity and therefore in higher correlation. As the decrease in the $t\bar{t}$ yield for τ+lepton with increasing $B(t \rightarrow H^+b)$ is slower than for the l+jets and dilepton channel, the simultaneous fit still delivers useful information, but no improvement of the limits on $B(t \rightarrow H^+b)$ for the simultaneous over the one dimensional fit can be

H^+ mass [GeV]	expected	observed
80	0.14	0.14
100	0.12	0.12
120	0.14	0.15
140	0.17	0.20
150	0.19	0.26
155	0.22	0.27

Table 11.20.: Upper limits on the branching ratio $B(t \to H^+b)$ for each H^+ mass point for the simultaneous fit with $\sigma_{t\bar{t}}$.

$\tan\beta$	$H^\pm$ mass limit [GeV] (tauonic)
15	none
25	118
35	131
45	139
55	143
65	146
75	149

Table 11.21.: Lower mass limits on $H^\pm$ in the tauonic model for for the simultaneous fit with $\sigma_{t\bar{t}}$ and for different values of $\tan\beta$. The calculations are at tree level.

seen.

In case of leptophobic decaying charged Higgs, all considered final states represent disappearance channels. This means, the effect of decreasing $t\bar{t}$ cross section and increasing $B(t \to H^+b)$ are almost 100% correlated. With this high correlation a simultaneous fit results in large uncertainties on both fitted quantities, yielding worse measurements on $B(t \to H^+b)$ than with a fixed $t\bar{t}$ cross section.

The inclusion of an appearance channel for leptophobic charged Higgs, i. e. the alljets final state, would solve this problem and enable better sensitivity for a one dimensional and a simultaneous fit. Besides an appearance channel, the expansion of the counting experiment to the use of topological information would be another possibility to improve the sensitivity. Examples for possible extensions of the search for charged Higgs bosons in future analyses are discussed in section 11.2.6.

11.2.5. Translation of the limits into the $\tan\beta$ versus charged Higgs mass plane

The intersections of the tree-level MSSM calculations for a given $\tan\beta$ with the limits on $B(t \to H^+b)$ versus charged Higgs mass can be interpreted as exclusion regions in the m_{H^+} versus $\tan\beta$ parameter space. Assuming the MSSM in the large $\tan\beta$ region and the leptophobic model in the small $\tan\beta$ region, charged Higgs masses up to 150 GeV can be excluded for each model, depending on $\tan\beta$.

Figure 11.10 shows the resulting exclusion region in m_{H^+} versus $\tan\beta$. The limits in the large $\tan\beta$ region are obtained by using the results from the simultaneous fit of $B(t \to H^+b)$ in the tauonic model with the $t\bar{t}$ cross section, as presented in section 11.2.4. For the small $\tan\beta$ region the leptophobic model is assumed.

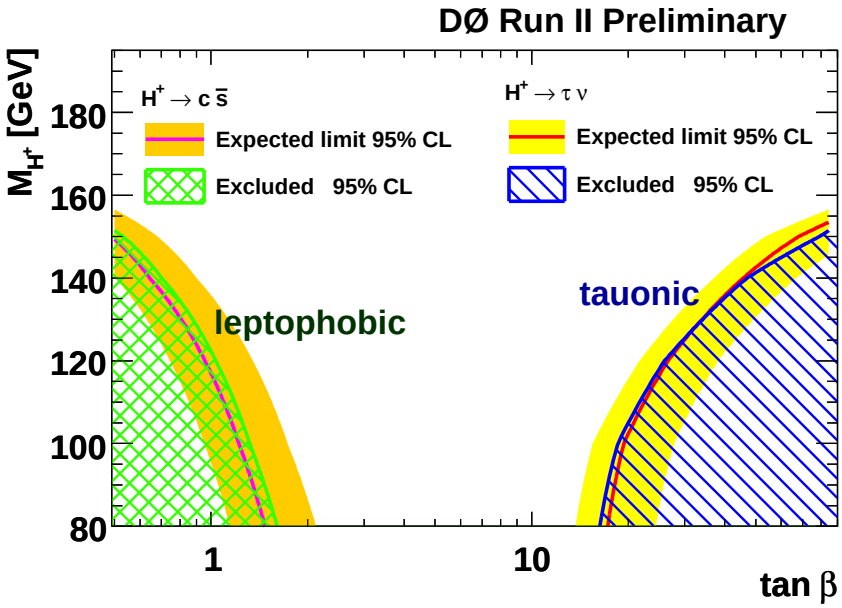

Figure 11.10.: Observed and expected limit with one standard deviation band on the charged Higgs mass as a function of $\tan\beta$. The large $\tan\beta$ region represents the MSSM. The limits are derived with the two-dimensional fit. The small $\tan\beta$ region assumes the leptophobic model.

11.2.6. Possible extensions: Topological studies

The presented search for charged Higgs bosons gives the most stringent limits until today on $B(t \to H^+b)$ for the tauonic model. Especially the performance of the simultaneous fit with the $t\bar{t}$ production cross section results in about 30% improvement for low charged Higgs masses. With the inclusion of more appearance channels the result is expected to improve further, also at high charged Higgs masses.

For leptophobic decaying charged Higgs bosons the performed analysis does not show as high a sensitivity as for the tauonic model. This can be understood by the miss of appearance channels. Similar to the tauonic model, a large improvement can be expected if a simultaneous fit with the $t\bar{t}$ cross section would be possible.

Besides a proper balance and the use of both appearance and disappearance channels, improvement can also be expected by including topological information that distinguishes Standard Model $t\bar{t}$ decays from charged Higgs decays. A recently performed search for leptophobic decaying charged Higgs bosons from CDF [181] with 2.2 fb^{-1}, that uses dijet mass templates in the l+jets channel, results in much better limits for high mass charged Higgs than the here performed analysis. As the here presented analysis is systematically limited, the better limits in the CDF analysis can be expected to be a result of including the topological information and not purely due to a larger data set.

In this section a brief study of possible topological informations in the l+jets channel for the leptophobic model is presented. Especially the dijet mass is considered. In the tauonic model the reconstruction of the tauonic decaying charged Higgs is more difficult than the decay into quarks. A possibility in the tauonic model is to use the fact that events with an electron or a muon from a tauonic decay look different from events with an electron or a muon from a direct W decay.

Topology in the tauonic model The $t\bar{t}$ final states in the l+jets channel are separated into events with either both bosons decaying into electron, muon or tauon (dilepton final state), or events with one boson decaying directly into quarks (semileptonic final state). In the Standard Model $t\bar{t}$ sample, events with semileptonic and dileptonic final state have different topologies due to softer leptons and softer jets from τ decay compared to direct decay from the W boson. For high jet multiplicities, the dileptonic contribution to the total SM $t\bar{t}$ yields is much smaller than the semileptonic, as demonstrated for example in Fig. 8.14 of section 8.

As in case of tauonic decaying charged Higgs the final state of the event contains at least one τ decaying into hadrons or leptons, the kinematics become more and more similar to the dileptonic final state with increasing $B(t \to H^+b)$. This difference can be used to gain some discrimination power between $t\bar{t} \to WW$, $t\bar{t} \to WH$ and $t\bar{t} \to HH$.

By comparing $t\bar{t} \to WW$ and $t\bar{t} \to WH$ in the semileptonic and $t\bar{t} \to WW$ to $t\bar{t} \to HH$ in the dileptonic final state, the discrimination power of simple variables like lepton p_T and jet p_T can be checked.

Figure 11.11 and 11.12 show the lepton p_T distribution and the scalar sum of jet p_T (H_T) for $t\bar{t} \to WW$ and $t\bar{t} \to WH$ in the semileptonic final state with charged Higgs masses of 80, 120 and 150 GeV. The distributions are shown before application of b-tagging. The lepton p_T is much softer for $t\bar{t} \to WH$ events, as expected. For higher charged Higgs masses the lepton p_T gets harder, as the momentum of the tauon and thus the momentum of the isolated electron or muon increases. The H_T distribution gets softer for higher m_{H^+}, as the b quark from the top decaying into charged Higgs gets less momentum. Comparing $t\bar{t} \to WW$ and $t\bar{t} \to HH$ in the dileptonic final state shows the same trend, as demonstrated in Fig. 11.13 and 11.14.

These studies show that in the tauonic model simple variables can help in the l+jets channel to improve the sensitivity to charged Higgs decay. A multivariate technique, combining several of such variables, would result in an even better discrimination than each of the individual distributions.

Topology in the leptophobic model In the leptophobic model the charged Higgs decays into a charm and strange quark. In the l+jets channel with four jets in the final state, $t\bar{t}$ events contain two b-jets and two light flavour jets, the latter from the W or H^+ boson. As the mass of the W boson is fixed around 80 GeV, the invariant mass of the two light jets represents a good possibility to distinguish SM $t\bar{t}$ events from events containing charged Higgs with masses higher than the W boson. This variable has already been proposed in [29] for the search of leptophobic decaying charged Higgs bosons.

The reconstruction of the dijet mass from the two light flavour jets is done by considering only events with at least four jets and at least two b-tagged jets. In the Monte Carlo, the b-tagged jets are determined by throwing a random number between zero and one for each jet. If the probability given by the TRF is larger than the random number, the jet is considered to be b-tagged. In each event, the procedure to chose b-tagged jets is iterated until at least two jets are b-tagged. The event b-tag probability to have at least two b-tagged jets is multiplied to the total weight of the event. This ensures a lower weight for events where two jets are chosen as b-tagged with the random procedure, although all jets have low probability to get b-tagged in the event. If at least two non-tagged jets are in the event, the invariant mass of the two jets with highest p_T is calculated. If less than two non-tagged jets are found, the invariant mass is set to minus one.

As in events with exactly four jets and two b-tags it is more likely to find the two jets from the W or H^+ boson decay, events with five or more jets are considered separately. Figure 11.15 shows the dijet mass distribution for semileptonic $t\bar{t} \to WW$ and $t\bar{t} \to WH$ events, the latter with charged Higgs masses of 80, 120 and 150 GeV. As expected, the distribution for 80 GeV

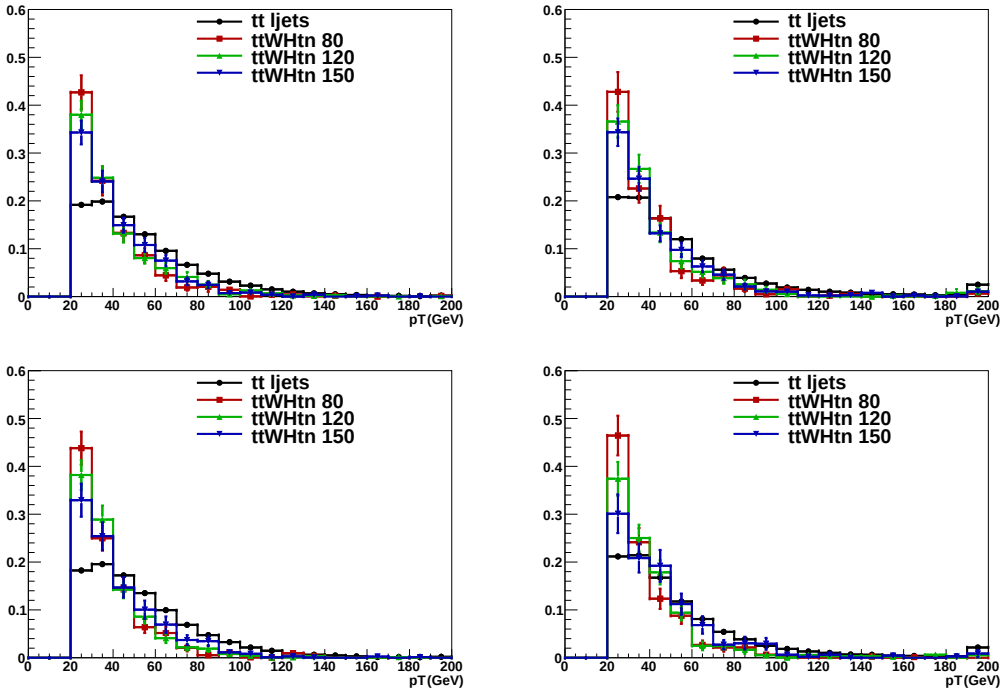

Figure 11.11.: Comparison of lepton p_T distribution of $t\bar{t} \to WW$ and $t\bar{t} \to WH$ events in the semileptonic final state. For charged Higgs masses with 80, 120 and 150 GeV. All distributions are normalised to one. Top: 3 jet multiplicity; Bottom: ≥ 4 jet multiplicity; Left: e+jets; Right: μ+jets.

charged Higgs looks similar to SM $t\bar{t}$ events. For higher charged Higgs masses, the distribution of $t\bar{t} \to WH$ shows a good separation from $t\bar{t} \to WW$ in the four jet multiplicity sample. For very high m_{H^+} of 150 GeV, the distribution gets flat. As the b-jet from the top decaying into H^+ has smaller momentum at these high charged Higgs masses, the probability to be b-tagged gets smaller for this jet. Therefore the probability that the wrong two jets are considered as light flavour jets increases, resulting in a smeared, flat distribution. For at least five jets in the event, the distributions do not show a clear peak at the boson mass, also showing that either energy is missing due to the fifth jet being from final state radiation, or the wrong pair of jets being used for the dijet mass calculation.

The dijet mass distributions show already good discrimination power. Adding to the function for the maximum likelihood fit the topological information for the subsample with at least four jets and $\geq$ 2 b-tags, would improve the limits for high charged Higgs masses in the leptophobic model. The dijet templates could be improved by using a kinematic fit to the top quark pair, yielding a higher probability to correctly choose the two jets from the boson decay, as was done in the CDF analysis with dijet templates.

Besides the dijet mass, some other possible variables are studied on parton level: The angular distribution between the top quark and the b-quark, the latter boosted into the top quark rest-frame. And the angular distribution between the boson decaying into quarks and the highest p_T quark from its decay, the latter boosted into the boson's rest-frame. Figure 11.16 shows both distributions for the e+jets and μ+jets channels with exactly four jets in the final state. Each event is multiplied with the probability to have at least two b-tags. Some small differences can be seen between $t\bar{t} \to WW$ and $t\bar{t} \to WH$ for high charged Higgs masses. Reconstructing those variables after detector simulation will smear the distributions, i. e. the

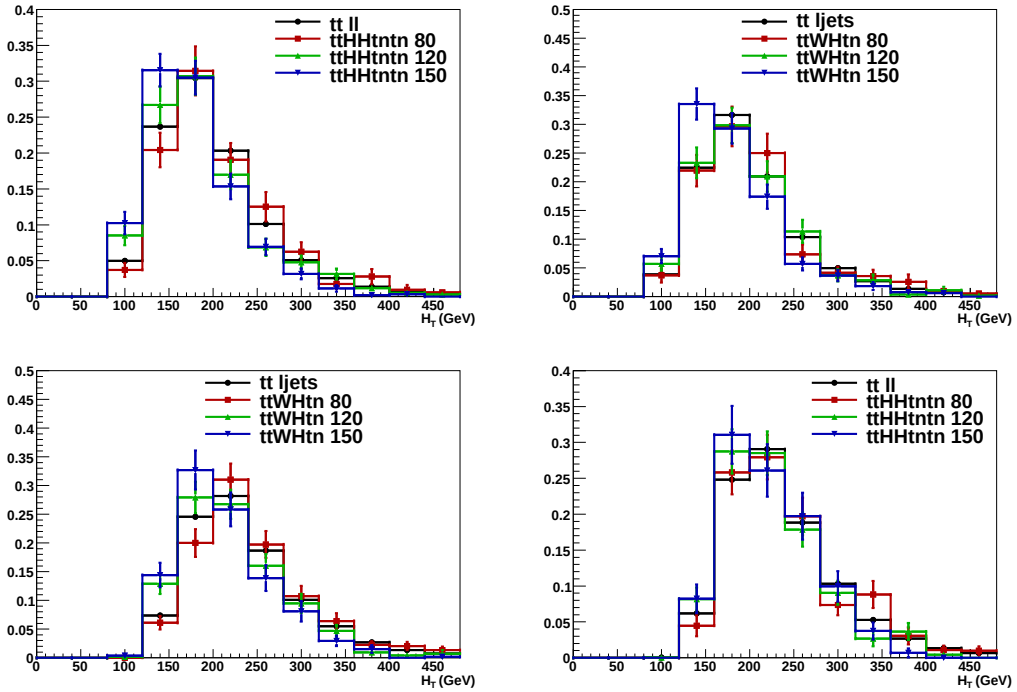

Figure 11.12.: Comparison of H_T distribution of $t\bar{t} \rightarrow WW$ and $t\bar{t} \rightarrow WH$ events in the semileptonic final state. For charged Higgs masses with 80, 120 and 150 GeV. All distributions are normalised to one. Top: 3 jet multiplicity; Bottom: ≥ 4 jet multiplicity; Left: e+jets; Right: μ+jets.

angles are not a good variable to discriminate $t\bar{t} \rightarrow WH$ from $t\bar{t} \rightarrow WW$.

11.2.7. Conclusion and outlook

The presented search for charged Higgs bosons in top quark decays yields upper limits on $B(t \rightarrow H^+b)$ of the order of 0.2, depending on the considered model and the charged Higgs mass. The first simultaneous fit of the top quark pair production cross section and the branching ratio of top quarks to charged Higgs has been performed, showing about 30% improvement over the result with fixed $\sigma_{t\bar{t}}$.

From DØ two older results on the search for charged Higgs bosons in Run I exist [182, 183]. The limits on the tauonic model can be compared to a previously performed search form CDF, with a data set of about 200 pb^{-1} [184]. CDF excludes $B(t \rightarrow H^+b) > 0.4$ for tauonic decaying charged Higgs bosons at 95% C.L. Additionally, CDF performed scans of the MSSM $\tan\beta$ versus m_{H^+} parameter space for various benchmark models, including several decay modes of the charged Higgs boson. A recent result from CDF on leptophobic decaying charged Higgs with 2.2 fb^{-1} results in the exclusion of $B(t \rightarrow H^+b) > 0.1$ to $B(t \rightarrow H^+b) > 0.3$ for charged Higgs masses above 90 GeV [181]. The analysis uses a template method where the dijet mass of the charged Higgs is reconstructed and used as template to distinguish charged Higgs and background events. For high mass charged Higgs the limits are thus stronger than the here presented limits on the leptophobic model.

Including topological information into the performed analysis is expected to improve the sensitivity to charged Higgs, but goes beyond the scope of this thesis. Additional final states would also improve the limits and enable the simultaneous fit not only for the tauonic

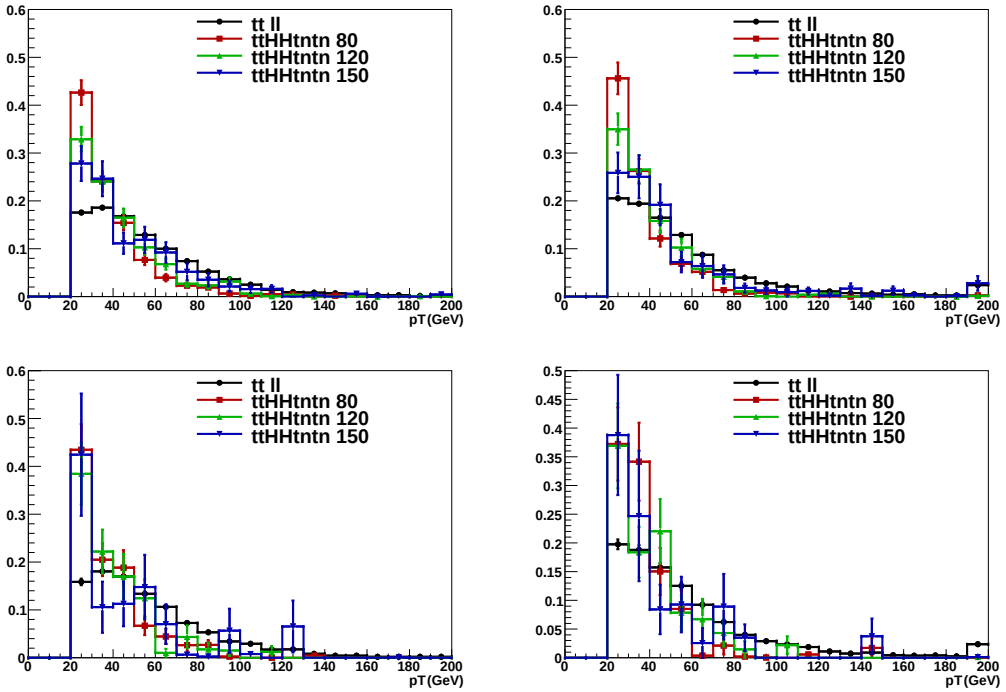

Figure 11.13.: Comparison of the lepton p_T distribution of $t\bar{t} \rightarrow WW$ and $t\bar{t} \rightarrow HH$ events in the dileptonic final state. For charged Higgs masses with 80, 120 and 150 GeV. All distributions are normalised to one. Top: 3 jet multiplicity; Bottom: ≥ 4 jet multiplicity; Left: e+jets; Right: μ+jets.

model. The inclusion of the alljets channel, for example, would provide an appearance channel that decouples the sensitivity to the $t\bar{t}$ cross section from the charged Higgs branching ratio $B(t \rightarrow H^+b)$. This would then enable the simultaneous fit to be performed for leptophobic decaying charged Higgs bosons. Another extension, that was planned to be done, is the inclusion of different charged Higgs decays in order to perform a full scan over the MSSM parameter space. Due to momentarily missing Monte Carlo samples for three body decays of the charged Higgs boson the scan could not yet be performed.

The presented studies on the search for charged Higgs bosons clearly show that a counting method where the $t\bar{t}$ cross section has to be fixed, is not statistically limited, but limited by the uncertainty on the cross section. Especially for searches at the LHC, where much larger statistics are expected, topological information or the mixture of disappearance and appearance channels are essential. A simultaneous fit, as presented here, might yield valuable information and seems also be desirable for methods using topological information, as the absorption of certain systematic uncertainties by one observable results in the more precise measurement of the other. This concept has already been shown for the simultaneous measurement of R and $\sigma \cdot B^2$.

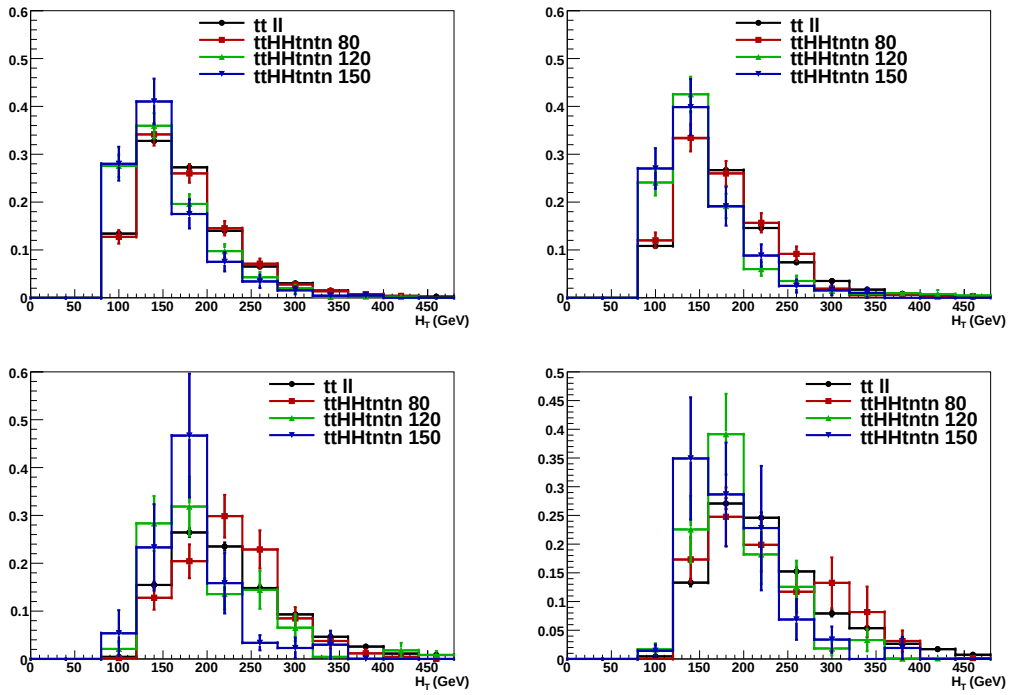

Figure 11.14.: Comparison of the H_T distribution of $t\bar{t} \rightarrow WW$ and $t\bar{t} \rightarrow HH$ events in the dileptonic final state. For charged Higgs masses with 80, 120 and 150 GeV. All distributions are normalised to one. Top: 3 jet multiplicity; Bottom: ≥ 4 jet multiplicity; Left: e+jets; Right: μ+jets.

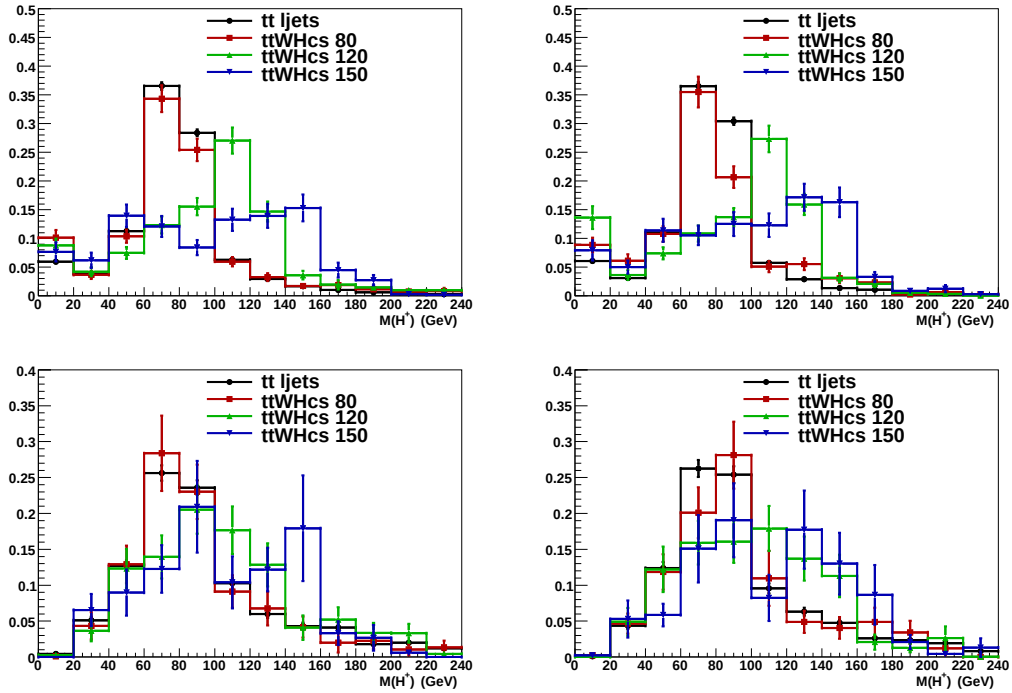

Figure 11.15.: Comparison of the dijet mass distribution of $t\bar{t} \rightarrow WW$ and $t\bar{t} \rightarrow WH$ events. For charged Higgs masses with 80, 120 and 150 GeV. All distributions are normalised to one. Top left: e+jets, 4 jets; Top right: μ+jets, 4 jets; Bottom left: e+jets $\geq$ 5 jets; Bottom right: μ+jets, $\geq$ 5 jets.

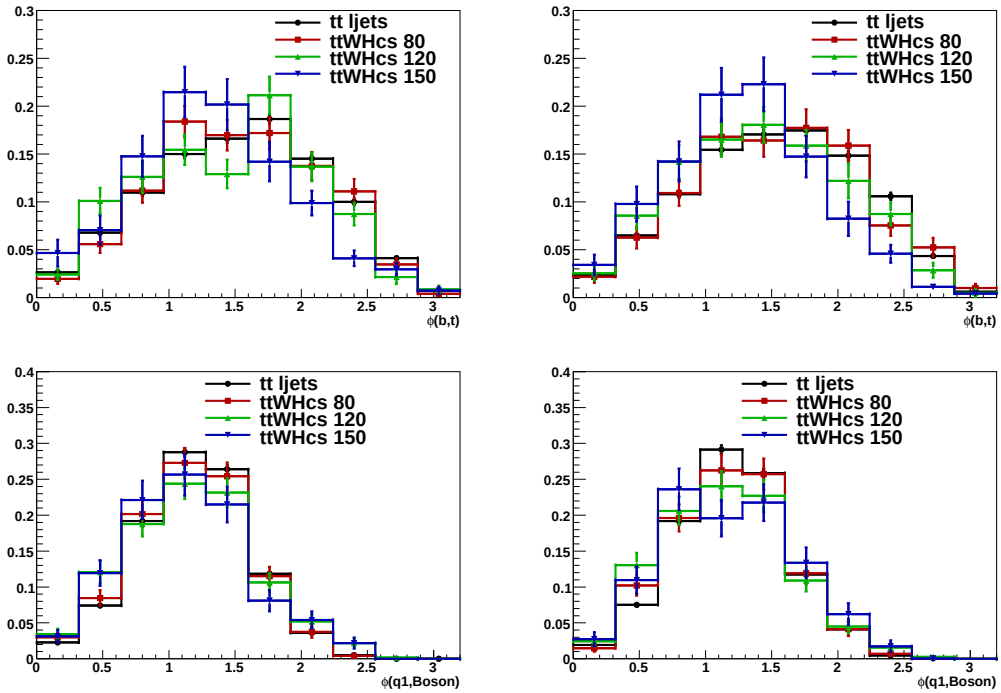

Figure 11.16.: Comparison of the angular distribution of $t\bar{t} \rightarrow WW$ and $t\bar{t} \rightarrow WH$ events. For charged Higgs masses with 80, 120 and 150 GeV. All distributions are normalised to one. Top: angular distribution between the top quark and the b-quark, the latter boosted into the top quark rest-frame; Bottom: angular distribution between the boson decaying into quarks and the highest p_T quark from its decay, the latter boosted into the boson's rest-frame; Left: e+jets, 4 jets; Right: μ+jets, 4 jets.

12. Summary and Outlook

In this thesis measurements and searches in the top quark sector have been presented.

With about 0.9 fb^{-1} of data collected by the DØ detector, the precise measurement of the top quark pair production cross section and the ratio of branching fractions R has been performed in the lepton plus jets final state. The measurement of R represents the most precise measurement to date. Its uncertainty is by more than a factor of two better than the previous measurement, allowing to put the best direct constraints on the CKM matrix element $|V_{tb}|$ to date. The result is in agreement with all previous measurements and with the Standard Model prediction. Simultaneously with R the top quark pair production cross section $\sigma(p\bar{p} \rightarrow t\bar{t}) \cdot B^2(t \rightarrow Wq)$ has been extracted, which was the most precise single $t\bar{t}$ cross section result in summer 2007. In spring 2008 the analysis was published in the Physics Review Letters as the first simultaneous measurement of the top quark pair production cross section and the ratio of branching fractions, with

$$\begin{aligned} R &= 0.968^{+0.092}_{-0.083}\ \text{(stat+syst)} \\ \sigma(p\bar{p} \rightarrow t\bar{t}) \cdot B^2(t \rightarrow Wq) &= 8.18^{+0.90}_{-0.84}\ \text{(stat+syst)} \pm 0.50\ \text{(lumi) pb} \end{aligned}$$

for a top quark mass of 175 GeV. A limit on $|V_{tb}|$ of

$$95\ \%\ C.L. : |V_{tb}| > 0.884$$

was extracted, where unitarity of the CKM matrix was assumed, as well as a limit on

$$95\ \%\ C.L. : \frac{(V_{ts}^2 + V_{td}^2)}{V_{tb}^2} < 0.266\,,$$

where no assumption about three quark generations or unitarity of the CKM matrix is made.

Furthermore, the top quark pair production cross section in the lepton plus jets, dilepton and tau plus lepton final states have been combined for a dataset of about 1 fb^{-1}, resulting in

$$\sigma_{t\bar{t}} = 7.83^{+0.93}_{-0.82}\ \text{(total) pb}$$

for a top quark mass of 175 GeV. The result is fully compatible with other cross section measurements and the theory prediction.

Based on the cross section combination a global search for the charged Higgs boson in top quark decays in various $t\bar{t}$ final states has been performed. Since the charged Higgs decays differ from the W boson decays, a high branching ratio of top quarks to charged Higgs bosons $B(t \rightarrow H^+b)$ can result in a deviation compared to the number of $t\bar{t}$ events predicted by the Standard Model. Limits on a purely tauonic and a leptophobic charged Higgs model have been set, resulting in $B(t \rightarrow H^+b) < 0.2$ in the tauonic model and $B(t \rightarrow H^+b) < 0.26$ in the leptophobic model. The former represents the most stringent limit on tauonic decaying charged Higgs bosons until today, and both are the first limits from DØ on the low mass charged Higgs in Run II. In case of the tauonic model, the first two dimensional fit of $\sigma_{t\bar{t}}$ and $B(t \rightarrow H^+b)$ has been performed, resulting in a 30 % improvement of the sensitivity for low charged Higgs masses compared to the fit of $B(t \rightarrow H^+b)$. The cross section combination and

the search for charged Higgs have been presented for the first time at the summer conferences 2008.

Besides these two main results of this thesis, interpretations of the same data sets or measurements in a slightly different way have been presented. The cross section ratio in the lepton plus jets over the dilepton channel has been extracted, which can be used to set a limit on the decay of top quarks into b-quark and any other boson but the W. Furthermore, the top quark mass can be extracted from the cross section measurement.

Last but not least, the simultaneous measurement of R and $\sigma_{t\bar{t}}$ was changed into a simultaneous measurement of $\sigma_{t\bar{t}}$ and the associated production of a Higgs boson and a top quark pair $\sigma_{t\bar{t}H} \cdot B(H \rightarrow b\bar{b})$. The latter yields the first measurement of $\sigma_{t\bar{t}H} \cdot B(H \rightarrow b\bar{b})$ at DØ and the currently best limits on $\sigma_{t\bar{t}H} \cdot B(H \rightarrow b\bar{b})$ from the Tevatron.

With the start of the LHC at CERN statistics will no longer be a a limiting factor for analyses based on $t\bar{t}$ events. Even at the Tevatron, the statistics will increase by more than a factor of six until the end of Run II, compared to the data used for the shown analyses. Many of the here presented analyses already have a systematic uncertainty that is larger than or comparable to the statistical uncertainty. For example, the search for charged Higgs bosons is highly depending on the uncertainty of the theoretical $t\bar{t}$ cross section. In order to improve the results, an improvement of the methods is therefore essential. In case of the charged Higgs boson this can be achieved with the inclusion of topological information and the extension to more final states, as discussed in this thesis.

A. Trigger requirements in the e+jets and μ+jets channel

In this section the individual trigger lists that are used for the e+jets and μ+jets trigger are described briefly.

Electron plus jets channel In the e+jets channel, the triggers EM15_2JT15, E1_SHT15_2J20, E1_SHT15_2J_J25 or E1_SHT15_2J_J30 are required. The following requirements on Level 1, Level 2 and Level 3 are used per trigger:

EM15_2JT15 Requires one calorimeter EM trigger tower with $E_T > 10$ GeV and two jet towers with $E_T > 5$ GeV on Level 1. On Level 2 there must be one EM candidate with electromagnetic fraction $f_{em} > 0.85$ and two jet candidates with $E_T > 10$ GeV. On Level 3 one electron with $E_T > 15$ GeV and two jet candidates with $E_T > 15$ GeV must be present in the event.

E1_SHT15_2J20 Requires one calorimeter EM trigger tower with $E_T > 11$ GeV on Level 1 and one tight electron candidate with $E_T > 15$ GeV and two jet candidates with $E_T > 20$ GeV on Level 3. No Level 2 requirement is imposed.

E1_SHT15_2J_J25 On Level 1 at least one EM object with $E_T > 19$ GeV and $|\eta| < 3.2$ must be found. One EM candidate with $E_T > 15$ GeV is required on Level 2. On Level 3 two jets with $E_T > 20$ GeV, one jet with $E_T > 25$ GeV and an electron with $E_T > 15$ GeV and a tight shower shape are required.

E1_SHT15_2J_J30 There must be one EM object with $E_T > 11$ GeV at Level 1 and one calorimeter electron object with $E_T > 15$ GeV on Level 2. On Level 3 two jets with $E_T > 20$ GeV, where one of the jets must have $E_T > 30$ GeV, and an electron with $E_T > 15$ GeV and a tight shower shape are required.

Muon plus jets channel In the μ+jets channel the triggers MU_JT20_L2M0, MU_JT25_L2M0, MUJ2_JT25, MUJ2_JT25_LM3, MUJ2_JT30_LM3, MUJ1_JT25_ILM3 and MUJ1_JT35_LM3 are used. The following requirements on Level 1, Level 2 and Level 3 apply for the muon plus jets trigger:

MU_JT20_L2M0 On Level 1 a muon scintillator trigger and one calorimeter jet trigger tower with $E_T > 3$ GeV or $E_T > 5$ GeV – depending on the trigger list – are required. One muon candidate with medium quality must be found on Level 2. Depending on the trigger list an additional jet with $E_T > 10$ GeV must be in the event. At Level 3 at least one jet with $E_T > 20$ GeV is required.

MU_JT25_L2M0 On Level 1 a muon scintillator trigger and one calorimeter jet trigger tower with $E_T > 3$ GeV are required. One muon candidate with medium quality and one jet with $E_T > 10$ GeV must be found on Level 2. At Level 3 at least one jet with $E_T > 25$ GeV is required.

MUJ2_JT25 One muon scintillator trigger and one calorimeter jet trigger tower with $E_T >$ 5 GeV at Level 1, one muon candidate with medium quality on Level 2 and at least one jet with $E_T > 25$ GeV and $|\eta| < 3.6$ on Level 3 are required.

MUJ2_JT25_LM3 Requires one single muon trigger based on muon scintillator and loose wires and one calorimeter jet trigger tower with $E_T > 5$ GeV at Level 1, at least one muon with medium quality and at least one jet with $E_T > 8$ GeV on Level 2 and at least one jet with $E_T > 25$ GeV and $|\eta| < 3.6$ as well as one loose muon with $p_T > 3$ GeV on Level 3.

MUJ2_JT30_LM3 Requires one single muon trigger based on muon scintillator and loose wires and one calorimeter jet trigger tower with $E_T > 3$ GeV at Level 1, at least one muon with medium quality and at least one jet with $E_T > 8$ GeV on Level 2 and at least one jet with $E_T > 30$ GeV and $|\eta| < 3.6$ as well as one loose muon with $p_T > 3$ GeV on Level 3.

MUJ1_JT25_LM3 On Level 1 one single muon trigger based on muon scintillator and loose wires and one calorimeter jet trigger tower with $E_T > 5$ GeV is required. At least one muon with medium quality and at least one jet with $E_T > 8$ GeV must be found in the event on Level 2, and at least one jet with $E_T > 25$ GeV and $|\eta| < 3.6$ as well as one loose muon with $p_T > 3$ GeV are required on Level 3.

MUJ1_JT25_ILM3 On Level 1 one single muon trigger based on muon scintillator and loose wires and one calorimeter jet trigger tower with $E_T > 5$ GeV is required. At least one muon with medium quality and at least one jet with $E_T > 8$ GeV must be found in the event on Level 2. At Level 3 at least one jet with $E_T > 25$ GeV and $|\eta| < 3.6$ as well as one loose muon with $p_T > 3$ GeV and one loose isolated muon with $p_T > 3$ GeV are required.

MUJ1_JT35_LM3On Level 1 one single muon trigger based on muon scintillator and loose wires and one calorimeter jet trigger tower with $E_T > 5$ GeV is required. At least one muon with medium quality and at least one jet with $E_T > 8$ GeV must be found in the event on Level 2, and at least one jet with $E_T > 35$ GeV and $|\eta| < 3.6$ as well as one loose muon with $p_T > 3$ GeV are required on Level 3.

B. Handling of the Matrix Method in the maximum likelihood fit for R and $\sigma \cdot B^2$

The extraction of the $t\bar{t}$ cross section and R, but also the branching ratio of top quarks to charged Higgs bosons, is performed with a maximum likelihood fit. In the l+jets channel, the normalisation of the W+jets background is treated differently from other Monte Carlo background, as for example single top or diboson production. In contrast to the latter, the total W+jets contribution is determined with the Matrix Method before application of the b-tagging. In the following the correlations due to the W+jets normalisation between different b-tag subsamples are resolved and the final equations that are used in the maximum likelihood function are derived.

The Matrix Method is applied three times: before b-tagging, in samples with one b-tag and in samples with two b-tags. The loose and tight samples that are used are therefore μ_ℓ and μ_t (before tagging), μ_ℓ^{1tag} and μ_t^{1tag}, μ_ℓ^{2tag} and μ_t^{2tag}. The number of events in the 0 b-tagged sample can be written as $\mu - \mu^{1tag} - \mu^{2tag}$ for the loose and the tight sample. Each of the number of events in the different b-tagged samples, as well as the number of events in the subsample with zero b-tags, are considered as free, independent parameters in the analysis, constraint to the number of observed events. The number of observed events is denoted in the following as n, in contrast to the number of expected events μ or N for individual samples. The equations of the Matrix Method before b-tagging can be written as

$$\begin{aligned} N_{\text{real\_lepton}} &= \varepsilon_{sig}\frac{n_t - \varepsilon_{qcd} n_\ell}{\varepsilon_{sig} - \varepsilon_{qcd}} \\ N_{QCD} &= \varepsilon_{qcd}\frac{\varepsilon_{sig} n_\ell - n_t}{\varepsilon_{sig} - \varepsilon_{qcd}} \end{aligned} \tag{B.1}$$

with $N_{\text{real\_lepton}}$ and N_{QCD} being the number of events with a true or fake isolated lepton in the tight sample.

The true number of μ_ℓ and μ_t is not known, therefore they can vary freely, but within the constraint to their corresponding number of observed events n_ℓ and n_t. The number of tight events μ_t is a subset of μ_ℓ, therefore μ_t and μ_ℓ are not independent of each other. Rewriting Eq. B.1 in terms of the loose minus tight sample $\mu_{\ell-t}$ and the tight sample μ_t and purely in terms of the number of expected events, gives

$$\begin{aligned} N_{\text{real\_lepton}} &= \varepsilon_{sig}\frac{\mu_t - \varepsilon_{qcd}(\mu_t + \mu_{\ell-t})}{\varepsilon_{sig} - \varepsilon_{qcd}} \\ N_{QCD} &= \varepsilon_{qcd}\frac{\varepsilon_{sig}(\mu_{\ell-t} + \mu_t) - \mu_t}{\varepsilon_{sig} - \varepsilon_{qcd}} \,. \end{aligned} \tag{B.2}$$

In order to construct a maximum likelihood, the predicted number of events with true and fake isolated leptons (μ_t and $\mu_{\ell-t}$) in the different b-tag subsamples have to be expressed in terms of the predicted number of signal and background events, where background events are all but the W+jets background. The prediction on the latter is implicitly included in the Matrix Method before b-tagging. Once μ_t and $\mu_{\ell-t}$ are constructed in this way, the predictions in the

loose minus tight and tight samples can then be constraint to the corresponding observed number of events. The number of loose minus tight events is a freely floating number, that is constraint to the corresponding number of observed events as

$$\mathcal{P}(n_{\ell-t}^{1tag}, \mu_{\ell-t}^{1tag}) \times \mathcal{P}(n_{\ell-t}^{2tag}, \mu_{\ell-t}^{2tag}). \tag{B.3}$$

Taking into account the Matrix Method in the one and two b-tagged subsamples, the number of multijet events can be written as

$$\begin{aligned} N_{QCD}^{1tag} &= \varepsilon_{qcd} \frac{\varepsilon_{sig}(\mu_{\ell-t}^{1tag} + \mu_t^{1tag}) - \mu_t^{1tag}}{\varepsilon_{sig} - \varepsilon_{qcd}} \\ N_{QCD}^{2tag} &= \varepsilon_{qcd} \frac{\varepsilon_{sig}(\mu_{\ell-t}^{2tag} + \mu_t^{2tag}) - \mu_t^{2tag}}{\varepsilon_{sig} - \varepsilon_{qcd}} \end{aligned} \tag{B.4}$$

where the number of events in the loose sample after b-tagging is already split up into the independent loose minus tight and tight samples $\mu_{\ell-t}$ and μ_t, respectively. As the number of events in the loose minus tight and the tight samples before b-tagging already include the number of events in the subsamples with 1 and ≥ 2 b-tags, the pre-tagged samples are spilt into the sample with zero, one and at least two b-tags. In that way the pre-tagged sample is expressed in terms of independent subsamples:

$$\begin{aligned} \mu_t &= \mu_t^{0tag} + \mu_t^{1tag} + \mu_t^{2tag} \\ \mu_{\ell-t} &= \mu_{\ell-t}^{0tag} + \mu_{\ell-t}^{1tag} + \mu_{\ell-t}^{2tag} \end{aligned} \tag{B.5}$$

Using Eq. B.5, the Matrix Method before b-tagging given in Eq. B.2, can be rewritten as

$$\begin{aligned} N_{\text{real\_lepton}} &= \varepsilon_{sig} \frac{(1-\varepsilon_{qcd})(\mu_t^{0tag} + \mu_t^{1tag} + \mu_t^{2tag}) - \varepsilon_{qcd}(\mu_{\ell-t}^{0tag} + \mu_{\ell-t}^{1tag} + \mu_{\ell-t}^{2tag})}{\varepsilon_{sig} - \varepsilon_{qcd}} \\ N_{QCD} &= \varepsilon_{qcd} \frac{\varepsilon_{sig}(\mu_{\ell-t}^{0tag} + \mu_{\ell-t}^{1tag} + \mu_{\ell-t}^{2tag}) + (\varepsilon_{sig}-1)(\mu_t^{0tag} + \mu_t^{1tag} + \mu_t^{2tag})}{\varepsilon_{sig} - \varepsilon_{qcd}}. \end{aligned} \tag{B.6}$$

Similar to Eq. B.3, the number of tight events in the zero b-tagged sample is constraint to the observed number of events:

$$\mathcal{P}(n_t^{0tag}, \mu_t^{0tag}) \times \mathcal{P}(n_{\ell-t}^{0tag}, \mu_{\ell-t}^{0tag}) \tag{B.7}$$

This equation has to be modified when a topological discriminant in the zero b-tagged sample is introduced. The modification is explained in section 8.1.2.

The number of tight events in the one and two b-tag subsamples are also constraint within Poisson statistics to their number of observed events:

$$\mathcal{P}(n_t^{1tag}, \mu_t^{1tag}) \times \mathcal{P}(n_t^{2tag}, \mu_t^{2tag}) \tag{B.8}$$

At this point, the only missing part for the full implementation of the Matrix Method into the maximum likelihood is to express μ_t^{1tag} and μ_t^{2tag} in terms of the predicted signal and background events, that depend on the $t\bar{t}$ cross section and R.

The number of predicted events in the tight b-tagged samples can be expressed as

$$\begin{aligned} \mu_t^{1tag} &= P_{\text{signal}}^{1tag} N_{\text{signal}} + N_{QCD}^{1tag} + P_{W+\text{jets}}^{1tag} N_{W+\text{jets}} + P_{\text{bkg}}^{1tag} N_{\text{bkg}} \\ \mu_t^{2tag} &= P_{\text{signal}}^{2tag} N_{\text{signal}} + N_{QCD}^{2tag} + P_{W+\text{jets}}^{2tag} N_{W+\text{jets}} + P_{\text{bkg}}^{2tag} N_{\text{bkg}} \end{aligned} \tag{B.9}$$

where P^{tag} means the b-tag efficiency for the signal and background samples.

Using the relation

$$N_{W+\text{jets}} = N_{\text{real\_lepton}} - N_{\text{signal}} - N_{\text{bkg}}, \tag{B.10}$$

expressing that the number of W+jets events is extracted from the Matrix Method before b-tagging, it is possible to write the number of W+jets events after b-tagging in Eq. B.9 in terms of the number of events with real isolated leptons ($N_{\text{real\_lepton}}$), the number of signal events (N_{signal}) and Monte Carlo background (N_{bkg}) before b-tagging. Inserting Eq. B.10 into Eq. B.9 results in

$$\begin{aligned} \mu_t^{1tag} &= P_{\text{signal}}^{1tag} N_{\text{signal}} + N_{QCD}^{1tag} + P_{W+\text{jets}}^{1tag} N_{\text{real\_lepton}} \\ &\quad - P_{W+\text{jets}}^{1tag} N_{\text{signal}} - P_{W+\text{jets}}^{1tag} N_{\text{bkg}} + P_{\text{bkg}}^{1tag} N_{\text{bkg}} \\ \mu_t^{2tag} &= P_{\text{signal}}^{2tag} N_{\text{signal}} + N_{QCD}^{2tag} + P_{W+\text{jets}}^{2tag} N_{\text{real\_lepton}} \\ &\quad - P_{W+\text{jets}}^{2tag} N_{\text{signal}} - P_{W+\text{jets}}^{2tag} N_{\text{bkg}} + P_{\text{bkg}}^{2tag} N_{\text{bkg}} \end{aligned} \tag{B.11}$$

where $N_{\text{real\_lepton}}$ and N_{QCD} depend on μ_t^{1tag} and μ_t^{2tag}. Equation B.11 can be considered as a system of two equations with two unknowns μ_t^{1tag} and μ_t^{2tag}. Solving this system for μ_t^{1tag} and μ_t^{2tag} results in an expression of the number of events in the tight samples with a certain number of b-tags as a function of the b-tag efficiencies, ε_{sig}, ε_{qcd}, μ_t^{0tag}, $\mu_{\ell-t}^{0tag}$, $\mu_{\ell-t}^{1tag}$, $\mu_{\ell-t}^{2tag}$ and the number of predicted signal and Monte Carlo background (single top, Z+jets, diboson) events in the different b-tag subsamples. Expressing the number of multijet events N_{QCD}^{1tag} and N_{QCD}^{2tag} in terms of Eq. B.4 and $N_{\text{real\_lepton}}$ in terms of Eq. B.2, the number of tight events in the one and two b-tagged subsample can be written as

$$\begin{aligned} \mu_t^{1tag} &= k_1 + a_1\mu_t^{0tag} + b_1\mu_t^{1tag} + c_1\mu_t^{2tag} + d_1\mu_{\ell-t}^{0tag} + e_1\mu_{\ell-t}^{1tag} + f_1\mu_{\ell-t}^{2tag} \\ \mu_t^{2tag} &= k_2 + a_2\mu_t^{0tag} + b_2\mu_t^{1tag} + c_2\mu_t^{2tag} + d_2\mu_{\ell-t}^{0tag} + e_2\mu_{\ell-t}^{1tag} + f_2\mu_{\ell-t}^{2tag}. \end{aligned} \tag{B.12}$$

The factors k_1 and k_2 are given by:

$$\begin{aligned} k_1 &= P_{\text{signal}}^{1tag} N_{\text{signal}} - P_{W+\text{jets}}^{1tag} N_{\text{bkg}} - P_{W+\text{jets}}^{1tag} N_{\text{signal}} + P_{\text{bkg}}^{1tag} N_{\text{bkg}} \\ k_2 &= P_{\text{signal}}^{2tag} N_{\text{signal}} - P_{W+\text{jets}}^{2tag} N_{\text{bkg}} - P_{W+\text{jets}}^{2tag} N_{\text{signal}} + P_{\text{bkg}}^{2tag} N_{\text{bkg}}. \end{aligned} \tag{B.13}$$

The factors a_1, b_1, c_1, d_1, e_1 and f_1 are defined by:

$$\begin{aligned} a_1 = c_1 &= \frac{P^{1tag}_{\text{W+jets}}\varepsilon_{sig}(1-\varepsilon_{qcd})}{\varepsilon_{sig}-\varepsilon_{qcd}} \\ b_1 &= \frac{\varepsilon_{sig}\varepsilon_{qcd}-\varepsilon_{qcd}+P^{1tag}_{\text{W+jets}}\varepsilon_{sig}-P^{1tag}_{\text{W+jets}}\varepsilon_{sig}\varepsilon_{qcd}}{\varepsilon_{sig}-\varepsilon_{qcd}} \\ d_1 = f_1 &= \frac{-P^{1tag}_{\text{W+jets}}\varepsilon_{sig}\varepsilon_{qcd})}{\varepsilon_{sig}-\varepsilon_{qcd}} \\ e_1 &= \frac{\varepsilon_{sig}\varepsilon_{qcd}-P^{1tag}_{\text{W+jets}}\varepsilon_{sig}\varepsilon_{qcd}}{\varepsilon_{sig}-\varepsilon_{qcd}} \end{aligned} \tag{B.14}$$

The factors a_2, b_2, c_2, d_2, e_2 and f_2 are defined similar to Eq. B.14 as:

$$\begin{aligned} a_2 = b_2 &= \frac{P^{2tag}_{\text{W+jets}}\varepsilon_{sig}(1-\varepsilon_{qcd})}{\varepsilon_{sig}-\varepsilon_{qcd}} \\ c_2 &= \frac{\varepsilon_{sig}\varepsilon_{qcd}-\varepsilon_{qcd}+P^{2tag}_{\text{W+jets}}\varepsilon_{sig}-P^{2tag}_{\text{W+jets}}\varepsilon_{sig}\varepsilon_{qcd}}{\varepsilon_{sig}-\varepsilon_{qcd}} \\ d_2 = e_2 &= \frac{-P^{2tag}_{\text{W+jets}}\varepsilon_{sig}\varepsilon_{qcd})}{\varepsilon_{sig}-\varepsilon_{qcd}} \\ f_2 &= \frac{\varepsilon_{sig}\varepsilon_{qcd}-P^{2tag}_{\text{W+jets}}\varepsilon_{sig}\varepsilon_{qcd}}{\varepsilon_{sig}-\varepsilon_{qcd}} \end{aligned} \tag{B.15}$$

From Eq. B.12 the final expression for μ_t^{1tag} can then be extracted as

$$\begin{aligned} \mu_t^{1tag} = \frac{1}{(c_2-1)(b_1-1)-c_1b_2} \times \Big(& k_2c_1 - k_1c_2 + k_1 \\ & + \mu_t^{0tag}(c_1a_2-(c_2-1)a_1) \\ & + \mu_{\ell-t}^{0tag}(c_1d_2-(c_2-1)d_1) \\ & + \mu_{\ell-t}^{1tag}(c_1e_2-(c_2-1)e_1) \\ & + \mu_{\ell-t}^{2tag}(c_1f_2-(c_2-1)f_1)\Big) \end{aligned} \tag{B.16}$$

and for μ_t^{2tag} as

$$\begin{aligned} \mu_t^{2tag} = \frac{1}{(c_2-1)(b_1-1)-c_1b_2} \times \Big(& k_1b_2 - k_2c_1 + k_2 \\ & + \mu_t^{0tag}(b_2a_1-(b_1-1)a_2) \\ & + \mu_{\ell-t}^{0tag}(b_2d_1-(b_1-1)d_2) \\ & + \mu_{\ell-t}^{1tag}(b_2e_1-(b_1-1)e_2) \\ & + \mu_{\ell-t}^{2tag}(b_2f_1-(c_2-1)f_2)\Big) \end{aligned} \tag{B.17}$$

The number of expected events μ_t^{1tag} and μ_t^{2tag} are functions of the signal and Monte Carlo background predictions and the parameters μ_t^{0tag}, $\mu_{\ell-t}^{0tag}$, $\mu_{\ell-t}^{1tag}$, $\mu_{\ell-t}^{2tag}$.
The final product of the maximum likelihood is given in Eq 8.5 in section 8.

C. Validation plots and cut flow tables for the simultaneous measurement of R and $\sigma \cdot B^2$

In this section Monte Carlo to data comparison plots, as well as cut flow tables belonging to the measurement of R and $\sigma \cdot B^2$, discussed in chapter 8, are shown.

C.1. Data to Monte Carlo comparison plots

Several data to Monte Carlo comparison plots for different variables and for the e+jets and μ+jets channel are shown. Various variables in the 0, 1 and ≥ 2 b-tag subsample for the 3 and ≥ 4 jet multiplicities are considered. A selection of lepton p_T and η, jet p_T and missing transverse energy is shown in Fig. C.2 to C.13. All plots are for the medium NN b-tagger, a $t\bar{t}$ cross section of 6.8 pb and $R = 1$. All distributions show reasonable agreement between data and Monte Carlo prediction. The red area is the $t\bar{t}$ signal, the green areas are for the different W+jets contributions (Wlp+jets, Wcc+jets and Wbb+jets). The brown represents the multijet contribution. The rest are the small single top, Z+jets and diboson backgrounds. A detailed legend used for all Data to Monte Carlo comparison plots can be found in Fig. C.1.

In each plot the Kolmogorov-Smirnov (KS) probability is given, which is a measure of the quality of the agreement between the prediction and the data. The method provides an unbiased probability estimate for un-binned data. Therefore the number of bins for the calculation of the KS probability is increased by a factor of 200 compared to the shown binning.

Figure C.1.: Legend to be used for the Data to Monte Carlo comparisons plots in the e+jets channel. For the μ+jets channel $ZMuMU$ has the same colors as ZEE in the e+jets channel. The number of observed and expected events are given for the e+jets subsample with at least four jets and no b-tagged jets.

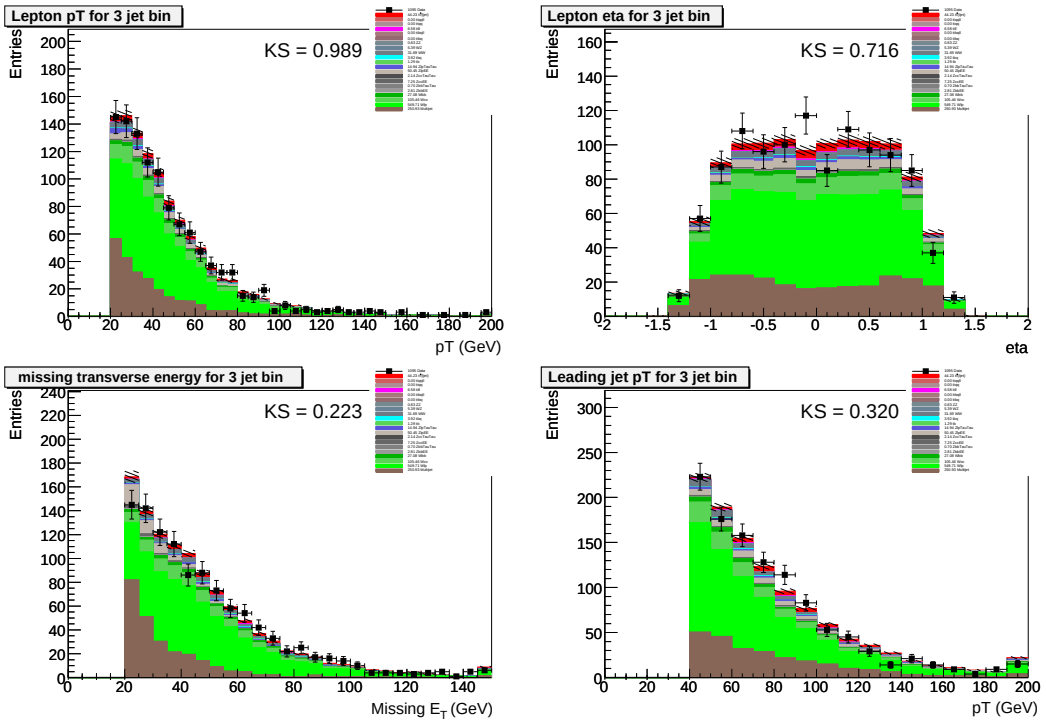

Figure C.2.: Data to Monte Carlo comparisons in the e+jets channel for 3 jets with 0 b-tags. Top left: lepton p_T; Top right: lepton η; Bottom left: $\not\!\!E_T$; Bottom right: leading jet p_T.

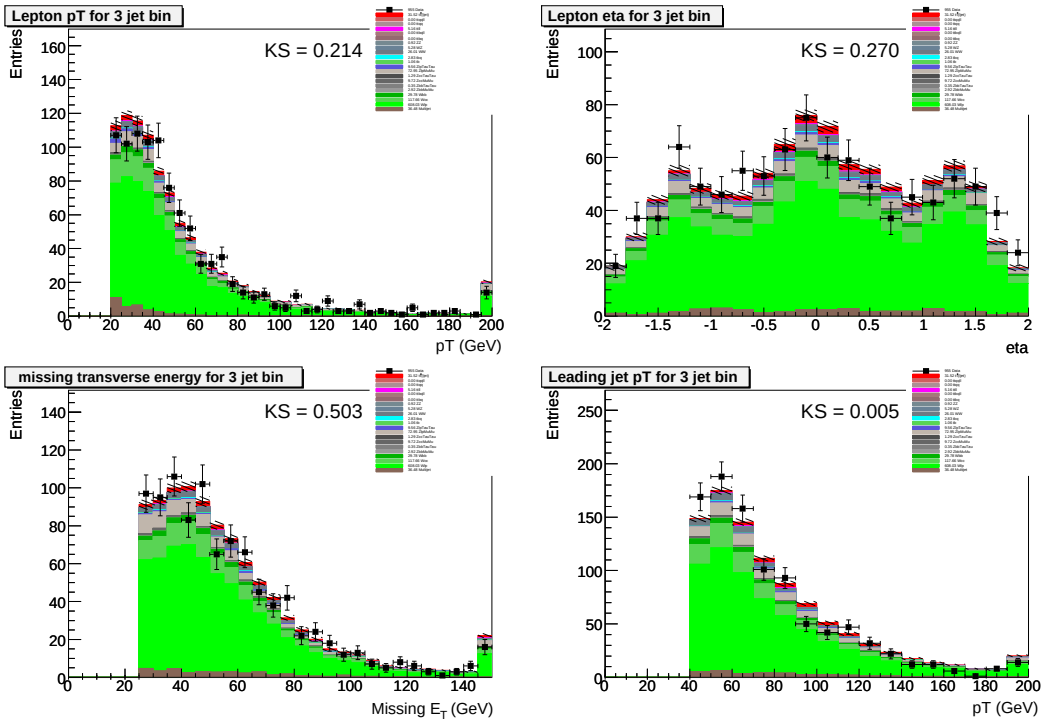

Figure C.3.: Data to Monte Carlo comparisons in the μ+jets channel for 3 jets with 0 b-tags. Top left: lepton p_T; Top right: lepton η; Bottom left: $\not{E}_T$; Bottom right: leading jet p_T.

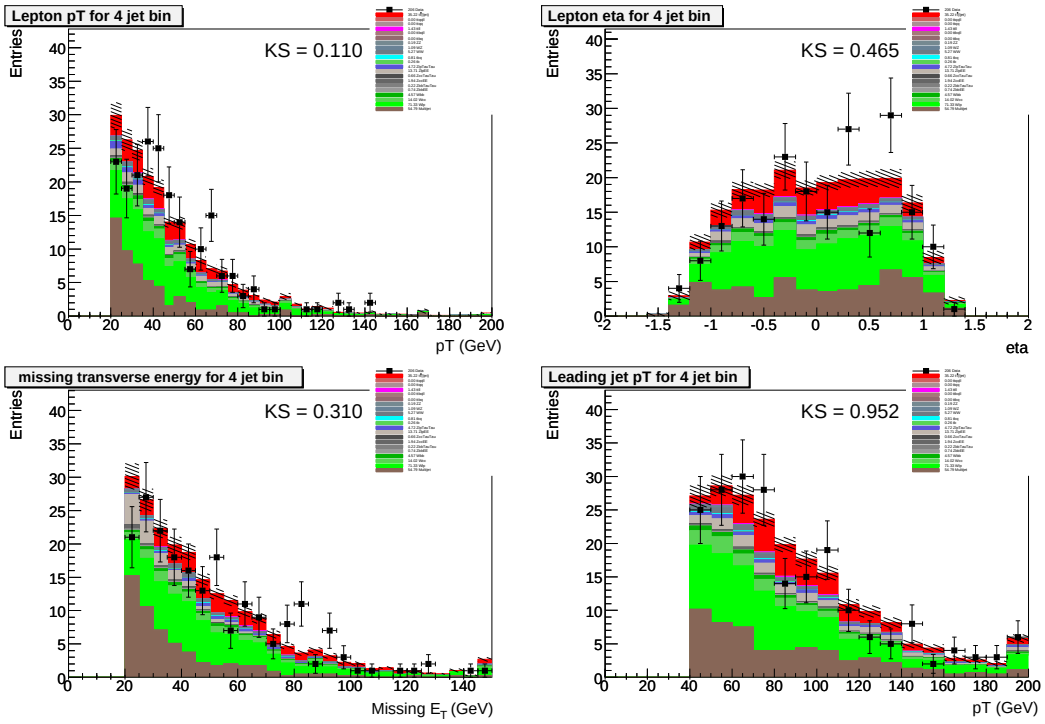

Figure C.4.: Data to Monte Carlo comparisons in the e+jets channel for $\geq$ 4 jets with 0 b-tags. Top left: lepton p_T; Top right: lepton η; Bottom left: $\not{E}_T$; Bottom right: leading jet p_T.

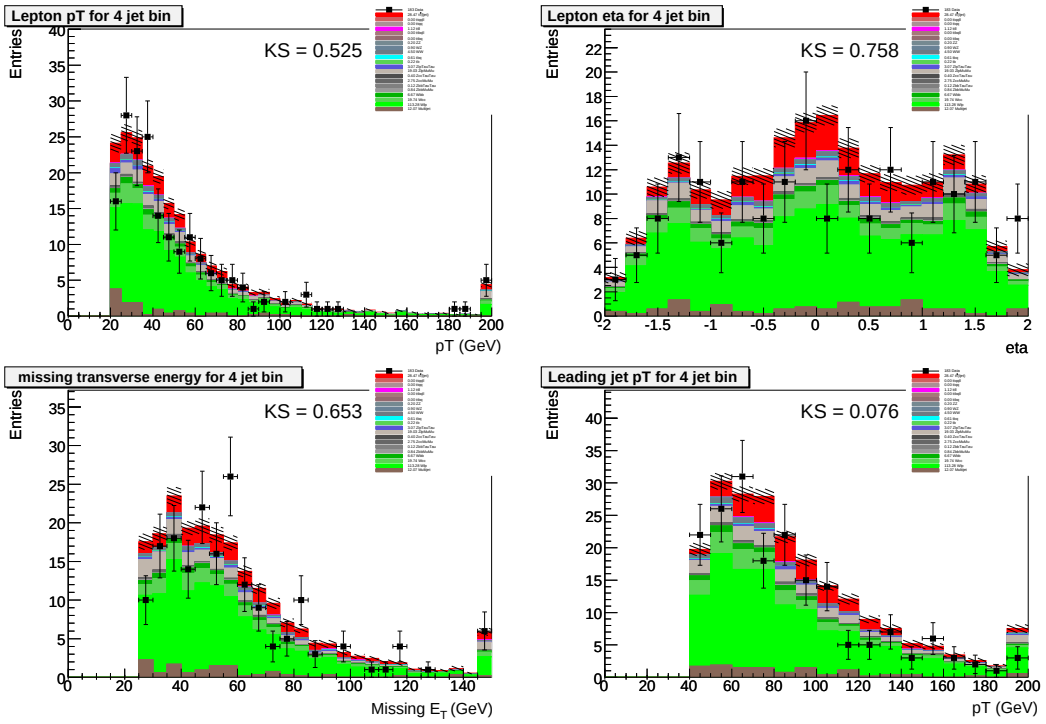

Figure C.5.: Data to Monte Carlo comparisons in the μ+jets channel for ≥ 4 jets with 0 b-tags. Top left: lepton p_T; Top right: lepton η; Bottom left: $\not\!\!E_T$; Bottom right: leading jet p_T.

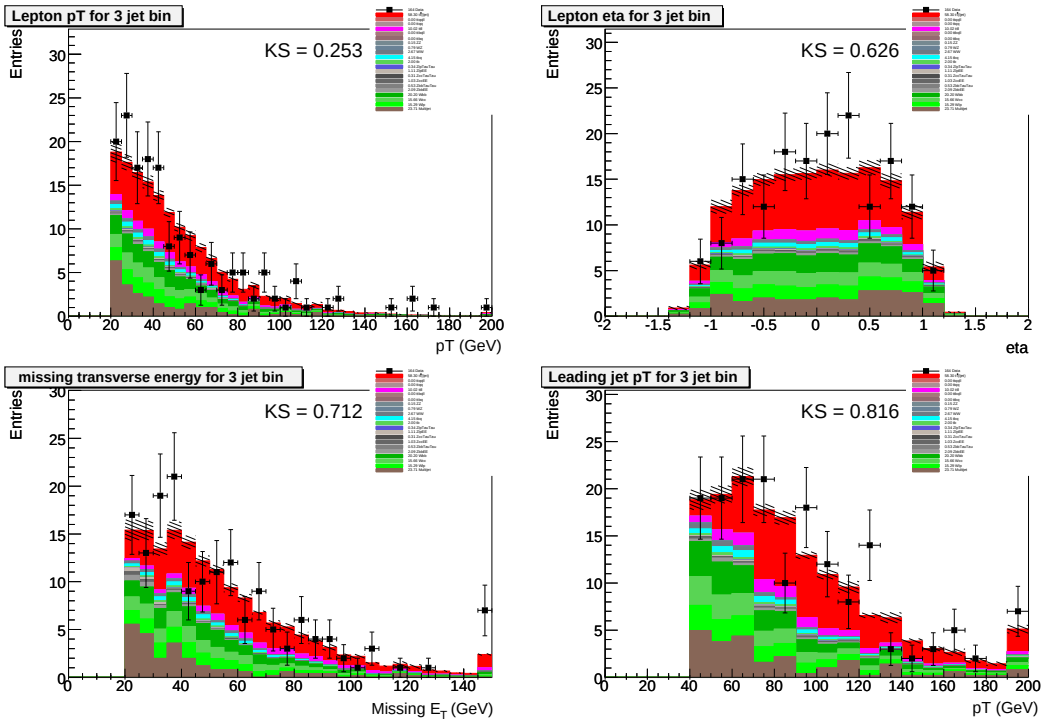

Figure C.6.: Data to Monte Carlo comparisons in the e+jets channel for 3 jets with 1 b-tag. Top left: lepton p_T; Top right: lepton η; Bottom left: $\not\!\!E_T$; Bottom right: leading jet p_T.

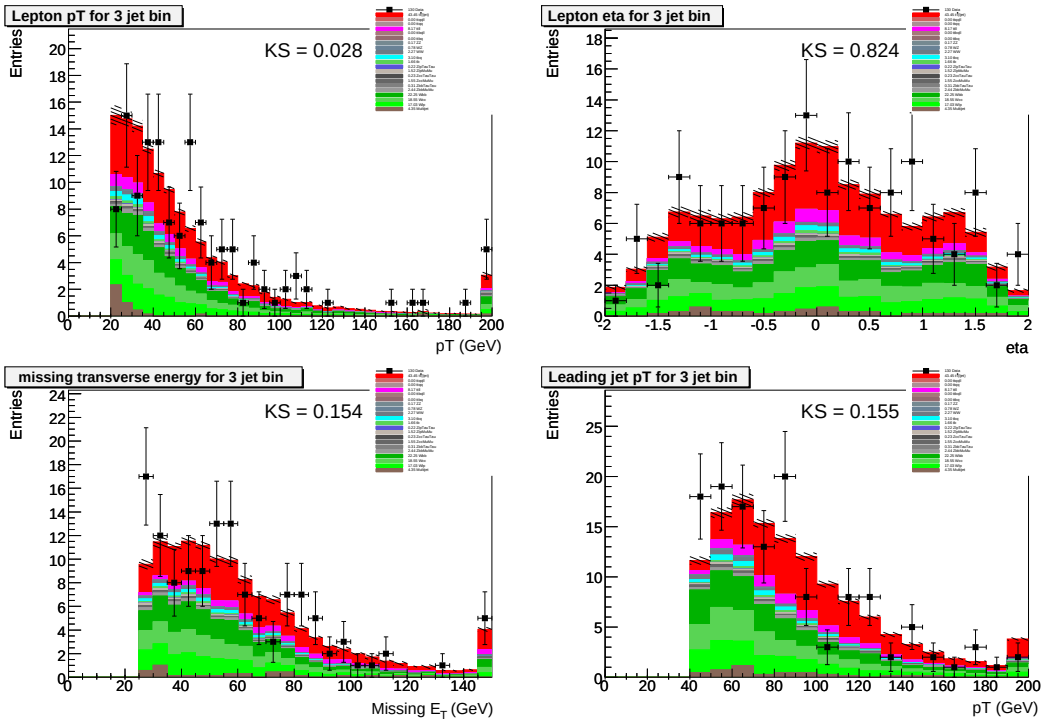

Figure C.7.: Data to Monte Carlo comparisons in the μ+jets channel for 3 jets with 1 b-tag. Top left: lepton p_T; Top right: lepton η; Bottom left: $\not\!\!E_T$; Bottom right: leading jet p_T.

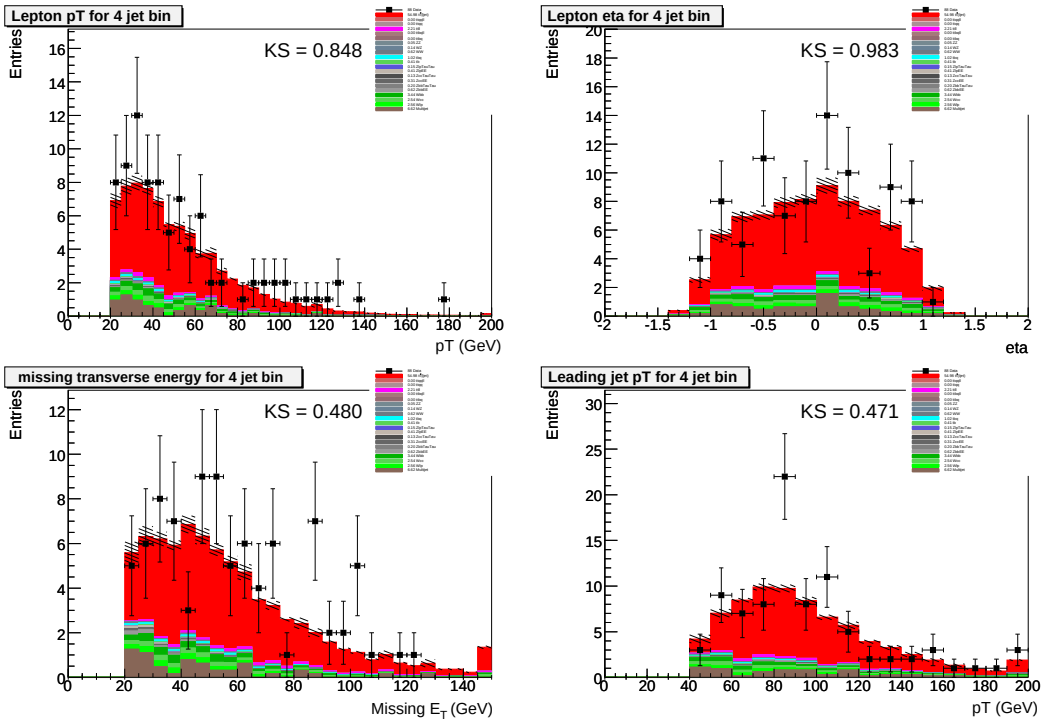

Figure C.8.: Data to Monte Carlo comparisons in the e+jets channel for $\geq$ 4 jets with 1 b-tag. Top left: lepton p_T; Top right: lepton η; Bottom left: $\not\!\!E_T$; Bottom right: leading jet p_T.

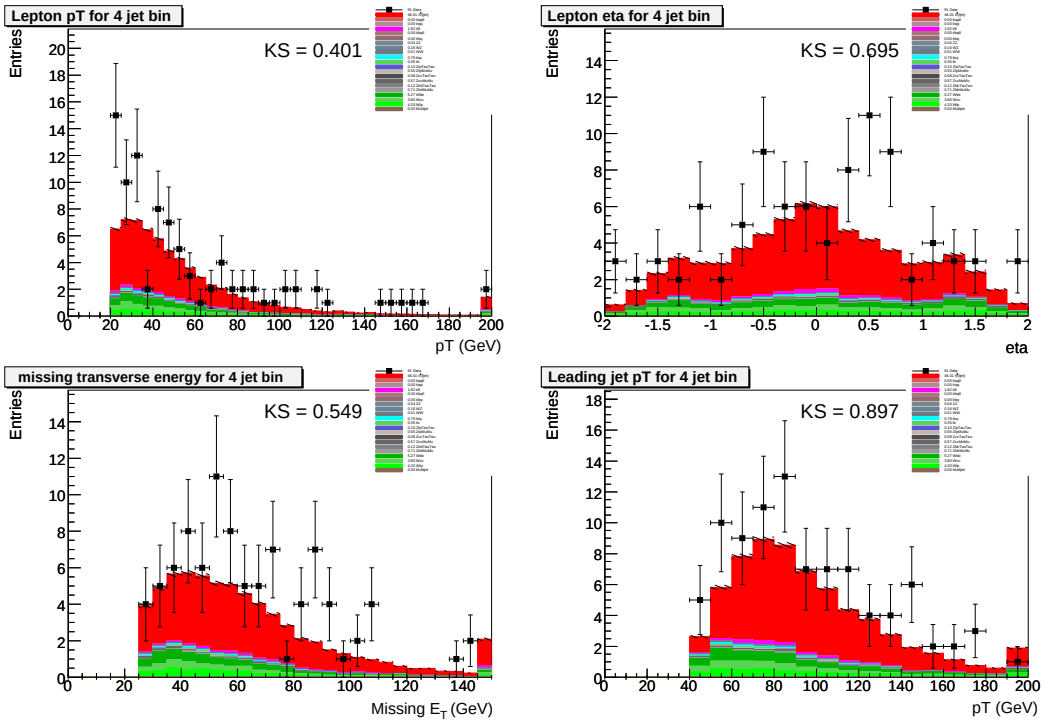

Figure C.9.: Data to Monte Carlo comparisons in the μ+jets channel for $\geq$ 4 jets with 1 b-tag. Top left: lepton p_T; Top right: lepton η; Bottom left: $\not\!\!E_T$; Bottom right: leading jet p_T.

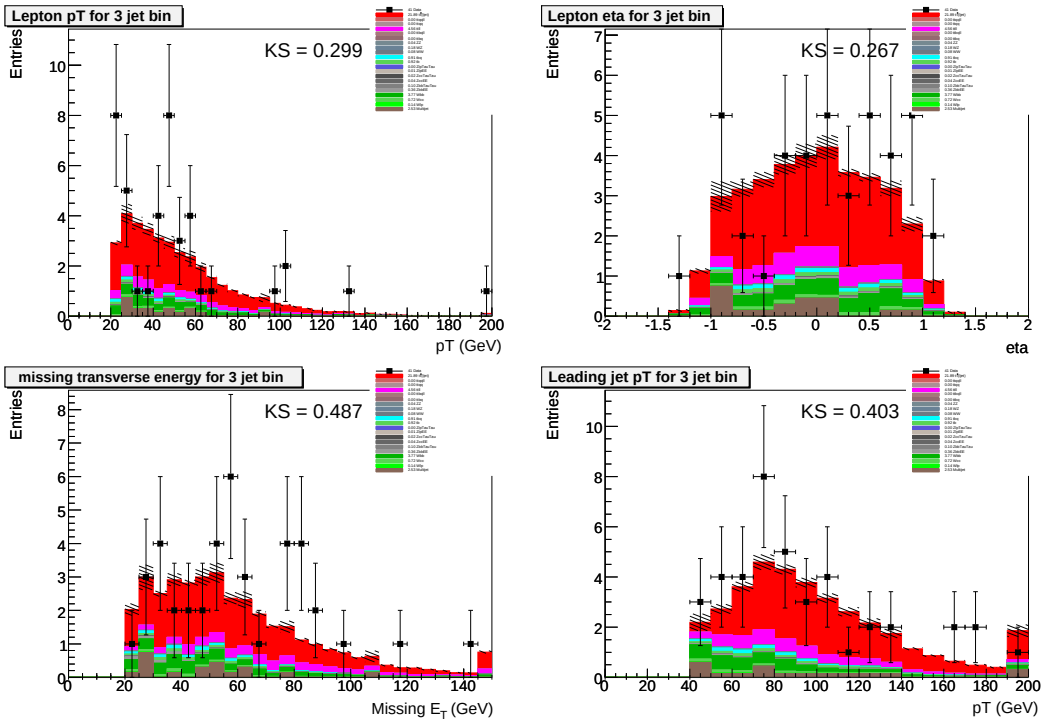

Figure C.10.: Data to Monte Carlo comparisons in the e+jets channel for 3 jets with ≥ 2 b-tags. Top left: lepton p_T; Top right: lepton η; Bottom left: $\not{E}_T$; Bottom right: leading jet p_T.

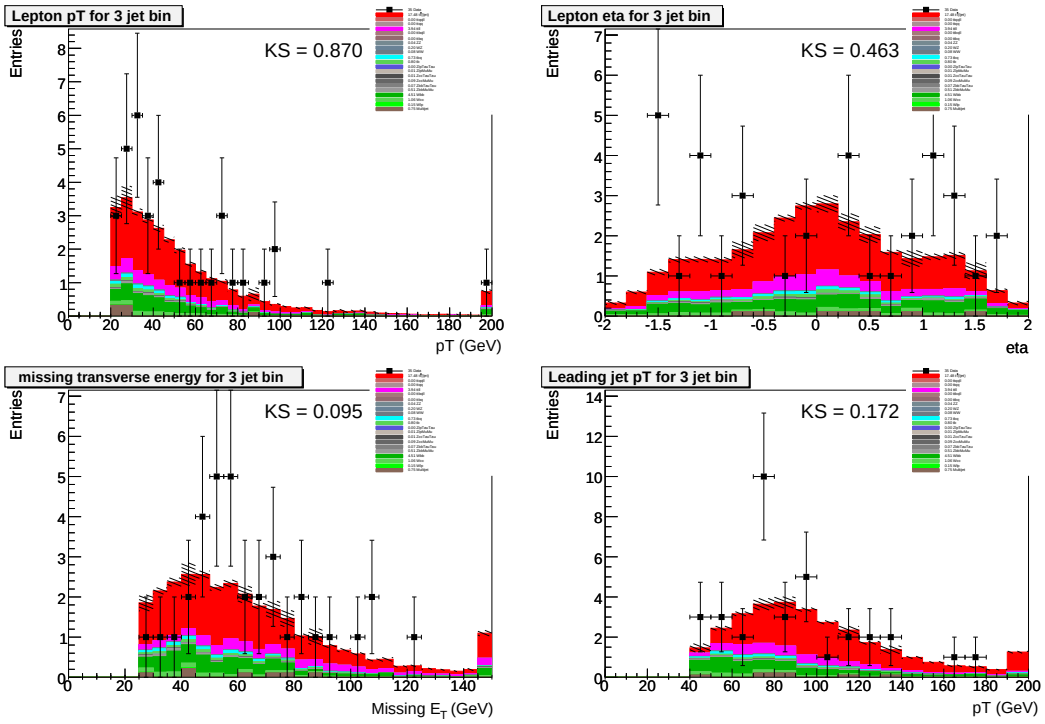

Figure C.11.: Data to Monte Carlo comparisons in the μ+jets channel for 3 jets with ≥ 2 b-tags. Top left: lepton p_T; Top right: lepton η; Bottom left: $\not{E}_T$; Bottom right: leading jet p_T.

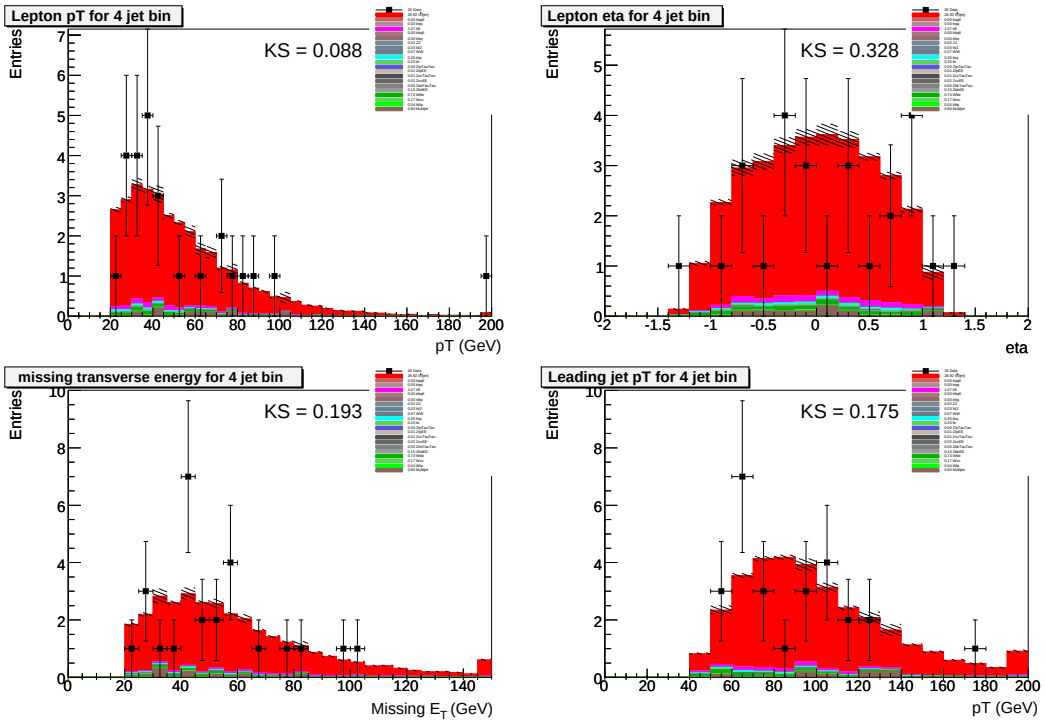

Figure C.12.: Data to Monte Carlo comparisons in the e+jets channel for ≥ 4 jets with ≥ 2 b-tags. Top left: lepton p_T; Top right: lepton η; Bottom left: $\not\!\!E_T$; Bottom right: leading jet p_T.

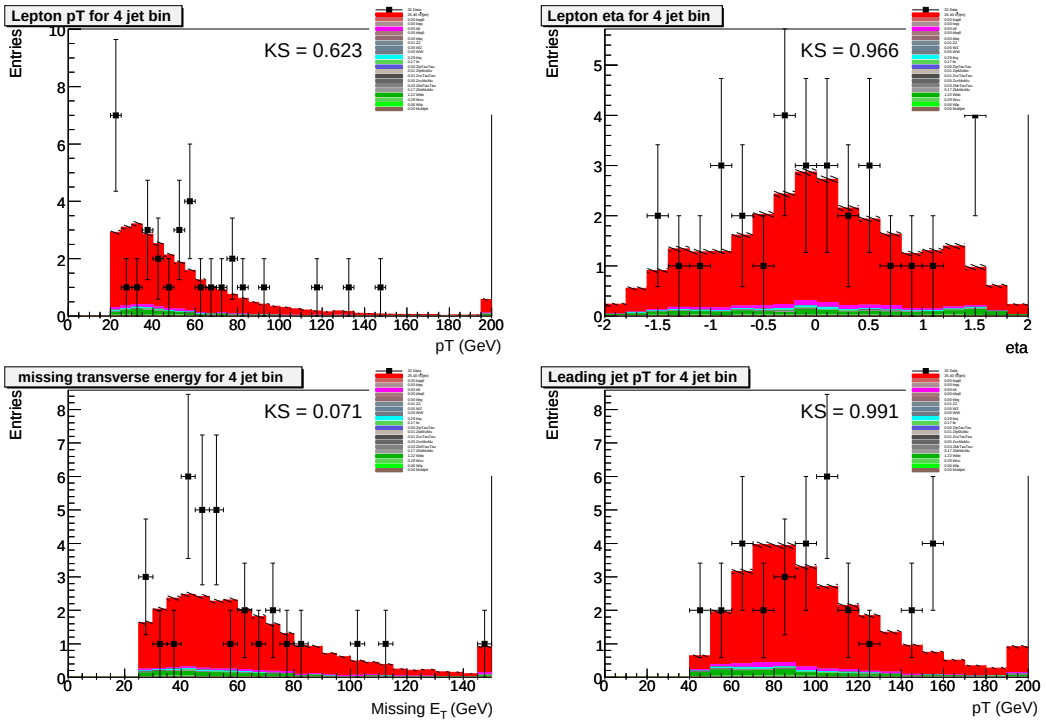

Figure C.13.: Data to Monte Carlo comparisons in the μ+jets channel for ≥ 4 jets with ≥ 2 b-tags. Top left: lepton p_T; Top right: lepton η; Bottom left: $\not\!\!E_T$; Bottom right: leading jet p_T.

C.2. Cut flow tables

For each $t\bar{t}$ signal Monte Carlo $t\bar{t} \rightarrow WbWb$, $t\bar{t} \rightarrow WbWq_\ell$ and $t\bar{t} \rightarrow Wq_\ell Wq_\ell$ Tables with the exclusive and cumulative preselection efficiencies in the exclusive 3 and inclusive 4 jet multiplicity bin are shown. Additionally the κ factors (scale and average reweighting factors), the data quality scale factor and primary vertex selection scale factors are listed.

All selection efficiencies are with respect to the parton level filter, where the semileptonic final state is chosen based on Monte Carlo truth information. Therefore the respective branching ratios of 0.17137 in the e+jets and 0.1721 in the μ+jets channel must be multiplied on the selection efficiency in the tables, in order to get the full event selection efficiency for the considered sample.

Cut flow for $t\bar{t} \rightarrow WbWb$ in $e + jets$			
Selection or κ	Events left	Exclusive selection efficiency[%]	Cumulative selection efficiency[%]
	242365		
$\geq$ 4good jets	112530	46.430 ± 0.101	46.430 ± 0.101
leading jet cut	111892	99.433 ± 0.022	46.167 ± 0.101
loose electron	46104	41.204 ± 0.147	19.023 ± 0.080
muon veto	46098	99.987 ± 0.005	19.020 ± 0.080
2nd electron veto	46090	99.983 ± 0.006	19.017 ± 0.080
vertex selection	45395	98.492 ± 0.057	18.730 ± 0.079
$\not\!\!E_T$	40587	89.409 ± 0.144	16.746 ± 0.076
triangle selection	38093	93.855 ± 0.119	15.717 ± 0.074
tight electron	34148	89.644 ± 0.156	14.089 ± 0.071
Trigger probability		96.832 ± 0.01	13.643 ± 0.068
$\kappa_{electron\ reco,ID}$		98.530 ± 0.005	13.443 ± 0.067
$\kappa_{electron\ likelihood}$		89.111 ± 0.025	11.982 ± 0.060
$\kappa_{b-fragmentation}$		97.772 ± 1.055	11.706 ± 0.076
Data Quality		97.14 ± 0.5	11.365 ± 0.064
Prmary vertex selection SF		98.88 ± 1.5	11.237 ± 0.064
ϵ_{total}			11.237 ± 0.064

Table C.1.: Preselection efficiencies for $t\bar{t} \rightarrow WbWb$ in the e+jets channel for four or more jets.

Cut flow for $t\bar{t} \to WbWq$ in $e + jets$			
Selection or κ	Events left	Exclusive selection efficiency[%]	Cumulative selection efficiency[%]
	35693		
≥ 4 good jets	16823	47.132 ± 0.264	47.132 ± 0.264
leading jet cut	16741	99.513 ± 0.054	46.903 ± 0.264
loose electron	6963	41.592 ± 0.381	19.508 ± 0.210
muon veto	6962	99.986 ± 0.014	19.505 ± 0.210
2nd electron veto	6960	99.971 ± 0.020	19.500 ± 0.210
vertex selection	6854	98.477 ± 0.147	19.203 ± 0.208
$\not{E}_T$	6191	90.327 ± 0.357	17.345 ± 0.200
triangle selection	5813	93.894 ± 0.304	16.286 ± 0.195
tight electron	5206	89.558 ± 0.401	14.585 ± 0.187
Trigger probability		96.870 ± 0.024	14.129 ± 0.181
$\kappa_{electron\ reco,ID}$		98.538 ± 0.014	13.922 ± 0.178
$\kappa_{electron\ likelihood}$		89.138 ± 0.065	12.412 ± 0.159
$\kappa_{b-fragmentation}$		98.966 ± 0.703	12.292 ± 0.180
Data Quality		97.14 ± 0.5	11.940 ± 0.172
Prmary vertex selection SF		98.88 ± 1.5	11.806 ± 0.170
ϵ_{total}			11.806 ± 0.170

Table C.2.: Preselection efficiencies for $t\bar{t} \to WbWq$ in the e+jets channel for four or more jets.

Cut flow for $t\bar{t} \to WqWq$ in $e + jets$			
Selection or κ	Events left	Exclusive selection efficiency[%]	Cumulative selection efficiency[%]
	35795		
≥ 4 good jets	17507	48.909 ± 0.264	48.909 ± 0.264
leading jet cut	17432	99.572 ± 0.049	48.700 ± 0.264
loose electron	7401	42.456 ± 0.374	20.676 ± 0.214
muon veto	7401	100.000 ± 0.000	20.676 ± 0.214
2nd electron veto	7399	99.973 ± 0.019	20.670 ± 0.214
vertex selection	7297	98.621 ± 0.136	20.386 ± 0.213
$\not{E}_T$	6491	88.954 ± 0.367	18.134 ± 0.204
triangle selection	6136	94.531 ± 0.282	17.142 ± 0.199
tight electron	5506	89.733 ± 0.387	15.382 ± 0.191
Trigger probability		96.854 ± 0.024	14.898 ± 0.184
$\kappa_{electron\ reco,ID}$		98.528 ± 0.013	14.678 ± 0.182
$\kappa_{electron\ likelihood}$		89.061 ± 0.063	13.076 ± 0.162
$\kappa_{b-fragmentation}$		99.974 ± 0.149	13.074 ± 0.163
Data Quality		97.14 ± 0.5	12.696 ± 0.176
Prmary vertex selection SF		98.88 ± 1.5	12.553 ± 0.175
ϵ_{total}			12.553 ± 0.175

Table C.3.: Preselection efficiencies for $t\bar{t} \to WqWq$ in the e+jets channel for four or more jets.

Cut flow for $t\bar{t} \to WbWb$ in $mu + jets$			
Selection or κ	Events left	Exclusive selection efficiency[%]	Cumulative selection efficiency[%]
	240928		
≥ 4 good jets	113943	47.293 ± 0.102	47.293 ± 0.102
leading jet cut	113353	99.482 ± 0.021	47.048 ± 0.102
Z muon veto	46655	41.159 ± 0.146	19.365 ± 0.081
loose muon	46648	99.985 ± 0.006	19.362 ± 0.081
2nd muon veto	46647	99.998 ± 0.002	19.361 ± 0.081
electron veto	46612	99.925 ± 0.013	19.347 ± 0.080
vertex selection	45982	98.648 ± 0.053	19.085 ± 0.080
$\not\!\!E_T$	39643	86.214 ± 0.161	16.454 ± 0.076
triangle selection	36880	93.030 ± 0.128	15.307 ± 0.073
tight muon	31901	86.499 ± 0.178	13.241 ± 0.069
Trigger probability		87.585 ± 0.057	11.596 ± 0.060
$\kappa_{muon\ ID\ x\ acc\ x\ cosmic\ veto}$		97.500 ± 0.056	11.324 ± 0.060
$\kappa_{muon\ track}$		92.221 ± 0.029	10.452 ± 0.055
$\kappa_{Rat11<0.08\ and\ Rattrk<0.06}$		100.195 ± 0.005	10.475 ± 0.055
$\kappa_{b-fragmentation}$		99.008 ± 1.257	10.370 ± 0.070
Data Quality		97.14 ± 0.5	10.073 ± 0.061
Prmary vertex selection SF		98.88 ± 1.5	9.960 ± 0.061
ϵ_{total}			9.960 ± 0.061

Table C.4.: Preselection efficiencies for $t\bar{t} \to WbWb$ in the μ+jets channel for four or more jets.

Cut flow for $t\bar{t} \to WbWq$ in $mu + jets$			
Selection or κ	Events left	Exclusive selection efficiency[%]	Cumulative selection efficiency[%]
	35280		
≥ 4 good jets	17103	48.478 ± 0.266	48.478 ± 0.266
leading jet cut	17022	99.526 ± 0.052	48.248 ± 0.266
Z muon veto	7016	41.217 ± 0.377	19.887 ± 0.213
loose muon	7014	99.971 ± 0.020	19.881 ± 0.212
2nd muon veto	7014	100.000 ± 0.000	19.881 ± 0.212
electron veto	7009	99.929 ± 0.032	19.867 ± 0.212
vertex selection	6912	98.616 ± 0.140	19.592 ± 0.211
$\not\!\!E_T$	5974	86.429 ± 0.412	16.933 ± 0.200
triangle selection	5513	92.283 ± 0.345	15.626 ± 0.193
tight muon	4769	86.505 ± 0.460	13.518 ± 0.182
Trigger probability		87.936 ± 0.142	11.886 ± 0.161
$\kappa_{muon\ ID\ x\ acc\ x\ cosmic\ veto}$		97.542 ± 0.145	11.612 ± 0.158
$\kappa_{muon\ track}$		92.242 ± 0.075	10.719 ± 0.146
$\kappa_{Rat11<0.08\ and\ Rattrk<0.06}$		100.220 ± 0.012	10.745 ± 0.147
$\kappa_{b-fragmentation}$		97.576 ± 0.741	10.490 ± 0.165
Data Quality		97.14 ± 0.5	10.189 ± 0.161
Prmary vertex selection SF		98.88 ± 1.5	10.075 ± 0.160
ϵ_{total}			10.075 ± 0.160

Table C.5.: Preselection efficiencies for $t\bar{t} \to WbWq$ in the μ+jets channel for four or more jets.

Cut flow for $t\bar{t} \to WqWq$ in $mu + jets$			
Selection or κ	Events left	Exclusive selection efficiency[%]	Cumulative selection efficiency[%]
	35135		
≥ 4 good jets	17480	49.751 ± 0.267	49.751 ± 0.267
leading jet cut	17416	99.634 ± 0.046	49.569 ± 0.267
Z muon veto	7180	41.226 ± 0.373	20.435 ± 0.215
loose muon	7179	99.986 ± 0.014	20.433 ± 0.215
2nd muon veto	7179	100.000 ± 0.000	20.433 ± 0.215
electron veto	7174	99.930 ± 0.031	20.418 ± 0.215
vertex selection	7074	98.606 ± 0.138	20.134 ± 0.214
$\not\!\!E_T$	6153	86.980 ± 0.400	17.512 ± 0.203
triangle selection	5740	93.288 ± 0.319	16.337 ± 0.197
tight muon	4970	86.585 ± 0.450	14.145 ± 0.186
Trigger probability		87.887 ± 0.142	12.431 ± 0.164
$\kappa_{muon\ ID\ x\ acc\ x\ cosmic\ veto}$		97.647 ± 0.142	12.159 ± 0.162
$\kappa_{muon\ track}$		92.175 ± 0.075	11.215 ± 0.150
$\kappa_{Rat11<0.08\ and\ Rattrk<0.06}$		100.206 ± 0.012	11.242 ± 0.150
$\kappa_{b-fragmentation}$		99.817 ± 0.129	11.223 ± 0.151
Data Quality		97.14 ± 0.5	10.902 ± 0.166
Prmary vertex selection SF		98.88 ± 1.5	10.779 ± 0.165
ϵ_{total}			10.779 ± 0.165

Table C.6.: Preselection efficiencies for $t\bar{t} \to WqWq$ in the μ+jets channel for four or more jets.

Cut flow for $t\bar{t} \to WbWb$ in $e + jets$			
Selection or κ	Events left	Exclusive selection efficiency[%]	Cumulative selection efficiency[%]
	242365		
$= 3$ good jets	92618	38.214 ± 0.099	38.214 ± 0.099
leading jet cut	91674	98.981 ± 0.033	37.825 ± 0.099
loose electron	48487	52.891 ± 0.165	20.006 ± 0.081
muon veto	48477	99.979 ± 0.007	20.002 ± 0.081
2nd electron veto	48467	99.979 ± 0.007	19.998 ± 0.081
vertex selection	47755	98.531 ± 0.055	19.704 ± 0.081
$\not\!\!E_T$	42731	89.480 ± 0.140	17.631 ± 0.077
triangle selection	40146	93.951 ± 0.115	16.564 ± 0.076
tight electron	35512	88.457 ± 0.159	14.652 ± 0.072
Trigger probability		96.694 ± 0.012	14.167 ± 0.069
$\kappa_{electron\ reco,ID}$		98.535 ± 0.005	13.960 ± 0.068
$\kappa_{electron\ likelihood}$		89.149 ± 0.025	12.448 ± 0.061
$\kappa_{b-fragmentation}$		98.399 ± 0.395	12.250 ± 0.077
Data Quality		97.14 ± 0.5	11.899 ± 0.066
Prmary vertex selection SF		98.88 ± 1.5	11.766 ± 0.065
ϵ_{total}			11.766 ± 0.065

Table C.7.: Preselection efficiencies for $t\bar{t} \to WbWb$ in the e+jets channel for exactly three jets.

Cut flow for $t\bar{t} \to WbWq$ in $e + jets$			
Selection or κ	Events left	Exclusive selection efficiency[%]	Cumulative selection efficiency[%]
	35693		
= 3 good jets	13687	38.346 ± 0.257	38.346 ± 0.257
leading jet cut	13563	99.094 ± 0.081	37.999 ± 0.257
loose electron	7257	53.506 ± 0.428	20.332 ± 0.213
muon veto	7254	99.959 ± 0.024	20.323 ± 0.213
2nd electron veto	7251	99.959 ± 0.024	20.315 ± 0.213
vertex selection	7125	98.262 ± 0.153	19.962 ± 0.212
$\not{E}_T$	6399	89.811 ± 0.358	17.928 ± 0.203
triangle selection	6021	94.093 ± 0.295	16.869 ± 0.198
tight electron	5330	88.524 ± 0.411	14.933 ± 0.189
Trigger probability		96.747 ± 0.028	14.447 ± 0.182
$\kappa_{electron\ reco,ID}$		98.529 ± 0.014	14.234 ± 0.179
$\kappa_{electron\ likelihood}$		89.199 ± 0.064	12.700 ± 0.160
$\kappa_{b-fragmentation}$		98.625 ± 0.684	12.528 ± 0.181
Data Quality		97.14 ± 0.5	12.169 ± 0.173
Prmary vertex selection SF		98.88 ± 1.5	12.033 ± 0.172
ϵ_{total}			12.033 ± 0.172

Table C.8.: Preselection efficiencies for $t\bar{t} \to WbWq$ in the e+jets channel for exactly three jets.

Cut flow for $t\bar{t} \to WqWq$ in $e + jets$			
Selection or κ	Events left	Exclusive selection efficiency[%]	Cumulative selection efficiency[%]
	35795		
= 3 good jets	13374	37.363 ± 0.256	37.363 ± 0.256
leading jet cut	13277	99.275 ± 0.073	37.092 ± 0.255
loose electron	7072	53.265 ± 0.433	19.757 ± 0.210
muon veto	7071	99.986 ± 0.014	19.754 ± 0.210
2nd electron veto	7067	99.943 ± 0.028	19.743 ± 0.210
vertex selection	6949	98.330 ± 0.152	19.413 ± 0.209
$\not{E}_T$	6265	90.157 ± 0.357	17.502 ± 0.201
triangle selection	5851	93.392 ± 0.314	16.346 ± 0.195
tight electron	5162	88.224 ± 0.421	14.421 ± 0.186
Trigger probability		96.733 ± 0.030	13.949 ± 0.179
$\kappa_{electron\ reco,ID}$		98.542 ± 0.014	13.746 ± 0.177
$\kappa_{electron\ likelihood}$		89.062 ± 0.065	12.245 ± 0.158
$\kappa_{b-fragmentation}$		100.013 ± 0.097	12.248 ± 0.158
Data Quality		97.14 ± 0.5	11.897 ± 0.171
Prmary vertex selection SF		98.88 ± 1.5	11.764 ± 0.170
ϵ_{total}			11.764 ± 0.170

Table C.9.: Preselection efficiencies for $t\bar{t} \to WqWq$ in the e+jets channel for exactly three jets.

Cut flow for $t\bar{t} \to WbWb$ in $mu + jets$			
Selection or κ	Events left	Exclusive selection efficiency[%]	Cumulative selection efficiency[%]
	240928		
= 3 good jets	94789	39.343 ± 0.100	39.343 ± 0.100
leading jet cut	93922	99.085 ± 0.031	38.983 ± 0.099
Z muon veto	42645	45.405 ± 0.162	17.700 ± 0.078
loose muon	42608	99.913 ± 0.014	17.685 ± 0.078
2nd muon veto	42603	99.988 ± 0.005	17.683 ± 0.078
electron veto	42558	99.894 ± 0.016	17.664 ± 0.078
vertex selection	41908	98.473 ± 0.059	17.394 ± 0.077
$\not{E}_T$	36408	86.876 ± 0.165	15.112 ± 0.073
triangle selection	33973	93.312 ± 0.131	14.101 ± 0.071
tight muon	29821	87.779 ± 0.178	12.378 ± 0.067
Trigger probability		87.444 ± 0.060	10.823 ± 0.059
$\kappa_{muon\ ID\ x\ acc\ x\ cosmic\ veto}$		97.460 ± 0.059	10.562 ± 0.058
$\kappa_{muon\ track}$		92.255 ± 0.031	9.752 ± 0.053
$\kappa_{Rat11<0.08\ and\ Rattrk<0.06}$		100.198 ± 0.005	9.774 ± 0.053
$\kappa_{b-fragmentation}$		98.018 ± 0.431	9.585 ± 0.068
Data Quality		97.14 ± 0.5	9.310 ± 0.051
Prmary vertex selection SF		98.88 ± 1.5	9.206 ± 0.055
ϵ_{total}			9.206 ± 0.055

Table C.10.: Preselection efficiencies for $t\bar{t} \to WbWb$ in the μ+jets channel for exactly three jets.

Cut flow for $t\bar{t} \to WbWq$ in $mu + jets$			
Selection or κ	Events left	Exclusive selection efficiency[%]	Cumulative selection efficiency[%]
	35280		
= 3 good jets	13701	38.835 ± 0.259	38.835 ± 0.259
leading jet cut	13577	99.095 ± 0.081	38.484 ± 0.259
Z muon veto	6218	45.798 ± 0.428	17.625 ± 0.203
loose muon	6215	99.952 ± 0.028	17.616 ± 0.203
2nd muon veto	6215	100.000 ± 0.000	17.616 ± 0.203
electron veto	6209	99.903 ± 0.039	17.599 ± 0.203
vertex selection	6099	98.228 ± 0.167	17.287 ± 0.201
$\not{E}_T$	5330	87.391 ± 0.425	15.108 ± 0.191
triangle selection	4914	92.195 ± 0.367	13.929 ± 0.184
tight muon	4297	87.444 ± 0.473	12.180 ± 0.174
Trigger probability		87.626 ± 0.153	10.672 ± 0.153
$\kappa_{muon\ ID\ x\ acc\ x\ cosmic\ veto}$		97.515 ± 0.155	10.420 ± 0.151
$\kappa_{muon\ track}$		92.186 ± 0.083	9.616 ± 0.139
$\kappa_{Rat11<0.08\ and\ Rattrk<0.06}$		100.209 ± 0.013	9.638 ± 0.140
$\kappa_{b-fragmentation}$		99.525 ± 0.770	9.616 ± 0.159
Data Quality		97.14 ± 0.5	9.340 ± 0.155
Prmary vertex selection SF		98.88 ± 1.5	9.236 ± 0.154
ϵ_{total}			9.236 ± 0.154

Table C.11.: Preselection efficiencies for $t\bar{t} \to WbWq$ in the μ+jets channel for exactly three jets.

Cut flow for $t\bar{t} \to WqWq$ in $mu + jets$			
Selection or κ	Events left	Exclusive selection efficiency[%]	Cumulative selection efficiency[%]
	35135		
= 3 good jets	13532	38.514 ± 0.260	38.514 ± 0.260
leading jet cut	13436	99.291 ± 0.072	38.241 ± 0.259
Z muon veto	6201	46.152 ± 0.430	17.649 ± 0.203
loose muon	6193	99.871 ± 0.046	17.626 ± 0.203
2nd muon veto	6193	100.000 ± 0.000	17.626 ± 0.203
electron veto	6189	99.935 ± 0.032	17.615 ± 0.203
vertex selection	6098	98.530 ± 0.153	17.356 ± 0.202
$\not{E}_T$	5358	87.865 ± 0.418	15.250 ± 0.192
triangle selection	4996	93.244 ± 0.343	14.219 ± 0.186
tight muon	4387	87.810 ± 0.463	12.486 ± 0.176
Trigger probability		87.836 ± 0.154	10.967 ± 0.156
$\kappa_{muon\ ID\ x\ acc\ x\ cosmic\ veto}$		97.617 ± 0.154	10.722 ± 0.153
$\kappa_{muon\ track}$		92.276 ± 0.081	9.901 ± 0.142
$\kappa_{Rat11<0.08\ and\ Rattrk<0.06}$		100.209 ± 0.013	9.925 ± 0.142
$\kappa_{b-fragmentation}$		100.079 ± 0.119	9.931 ± 0.143
Data Quality		97.14 ± 0.5	9.647 ± 0.157
Prmary vertex selection SF		98.88 ± 1.5	9.538 ± 0.156
ϵ_{total}			9.538 ± 0.156

Table C.12.: Preselection efficiencies for $t\bar{t} \to WqWq$ in the μ+jets channel for exactly three jets.

D. Control plots for the topological discriminant used in the measurement of R

In this section different control and validation plots for the construction of the topological discriminant used for the measurement of the ratio of branching fractions R are shown. The construction and optimisation of the discriminant are discussed in section 8.4.

Figures D.1 to D.8 show the data to Monte Carlo comparison plots for all input variables to the topological discriminant. The comparison is done for the samples with 1, 2, 3 and at least 4 jets. As the discriminant is used in the ≥ 4 jet sample, the background model validation for each input variable is done in the samples with less than four jets. All variables show good agreement between data and the prediction from the background model.

The red area is the $t\bar{t}$ signal, the green areas are for the different W+jets contributions (Wlp+jets, Wcc+jets and Wbb+jets). The brown represents the multijet background. The rest are the small single top, Z+jets and diboson contributions. A detailed legend used for all Data to Monte Carlo comparison plots can be found in Fig. C.1 in Appendix C.

Figures D.9 and D.10 show the normalised distributions of the transformed input variables for $t\bar{t}$ signal and W+jets background in the e+jets and μ+jets channel, respectively.

In Figs. D.13 and D.14 the $t\bar{t} \rightarrow WbWb$, $t\bar{t} \rightarrow WbWq$ and $t\bar{t} \rightarrow WqWq$ templates for the discriminant input variables are displayed in the e+jets and μ+jets channel, respectively.

The variables in the e+jets channel are the $\mathcal{C}$ variable (top left), $\mathcal{C}$ (top right), aplanarity $\mathcal{A}$ (middle left), the leading jet p_T (middle right) and the maximum ΔR between all jet combinations (bottom). For the plots in the μ+jets channel the aplanarity $\mathcal{A}$ (top left), H_T3 – the scalar sum of the p_T for the third leading jet and lower – (top right), H_T^l (middle left), $\mathcal{D}$ (middle right), JetMt (bottom left) and the variable M01Mall (bottom right) are shown.

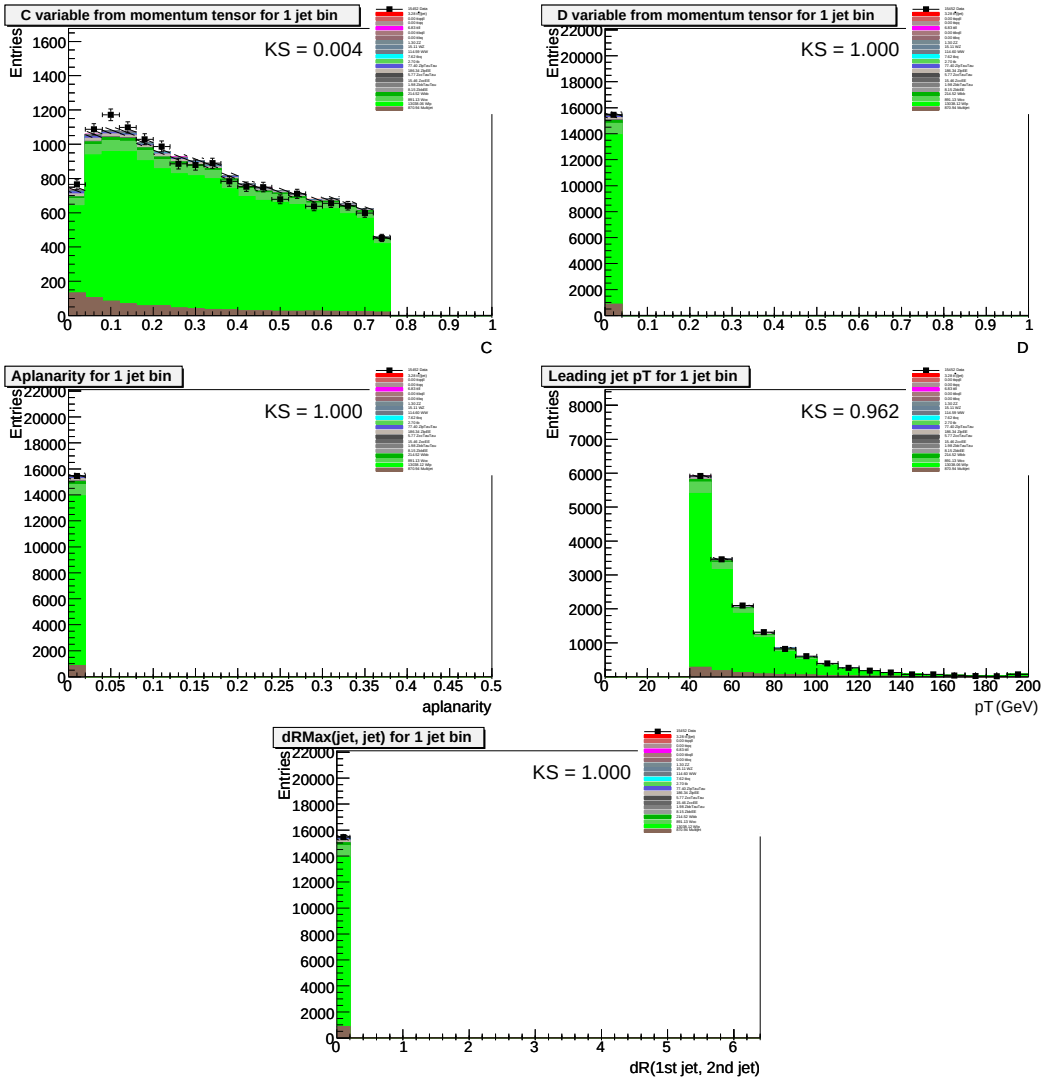

Figure D.1.: Data to Monte Carlo comparisons for the input variables to the topological discriminant function in the 0 b-tagged sample. For the e+jets channel and $= 1$ jet.

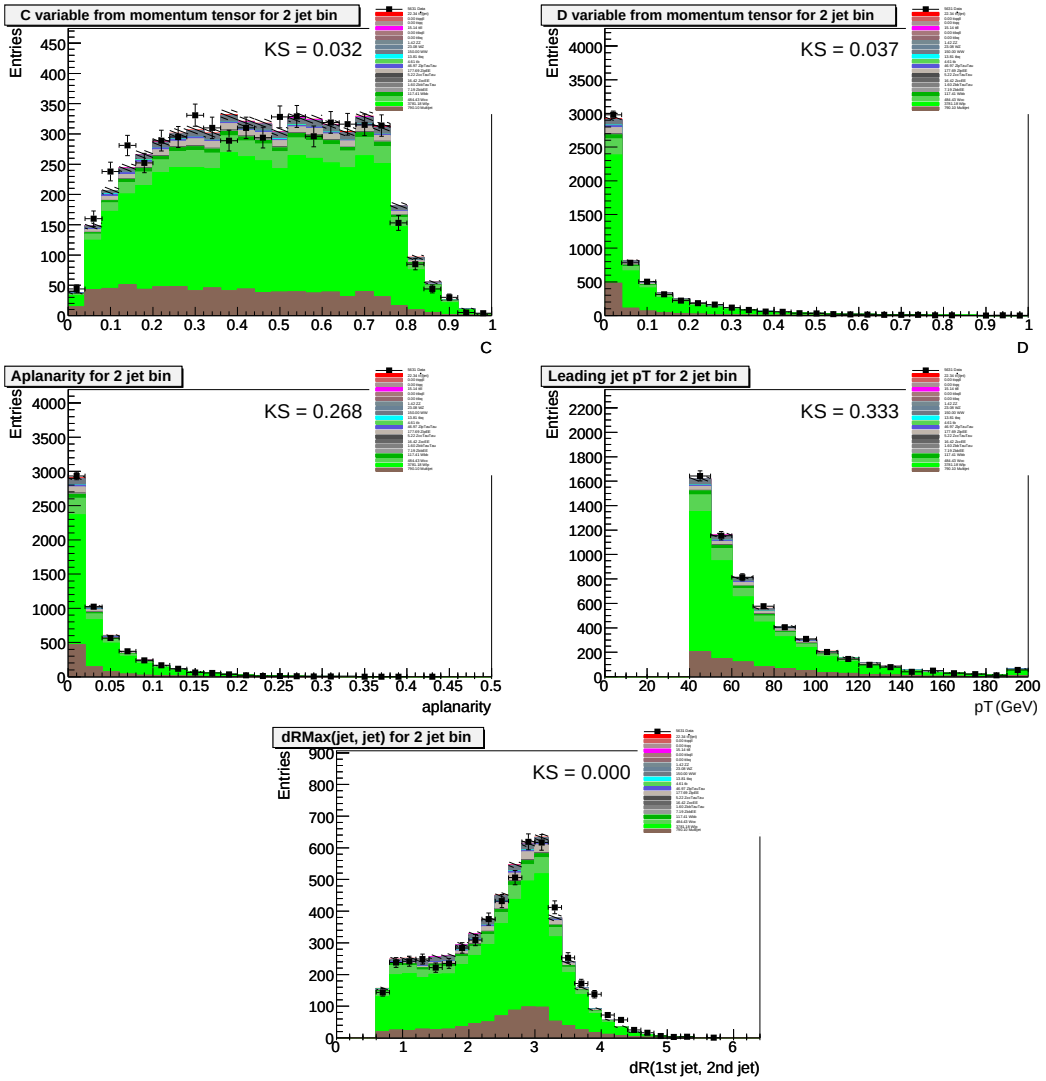

Figure D.2.: Data to Monte Carlo comparisons for the input variables to the topological discriminant function in the 0 b-tagged sample. For the e+jets channel and $=$ 2 jets.

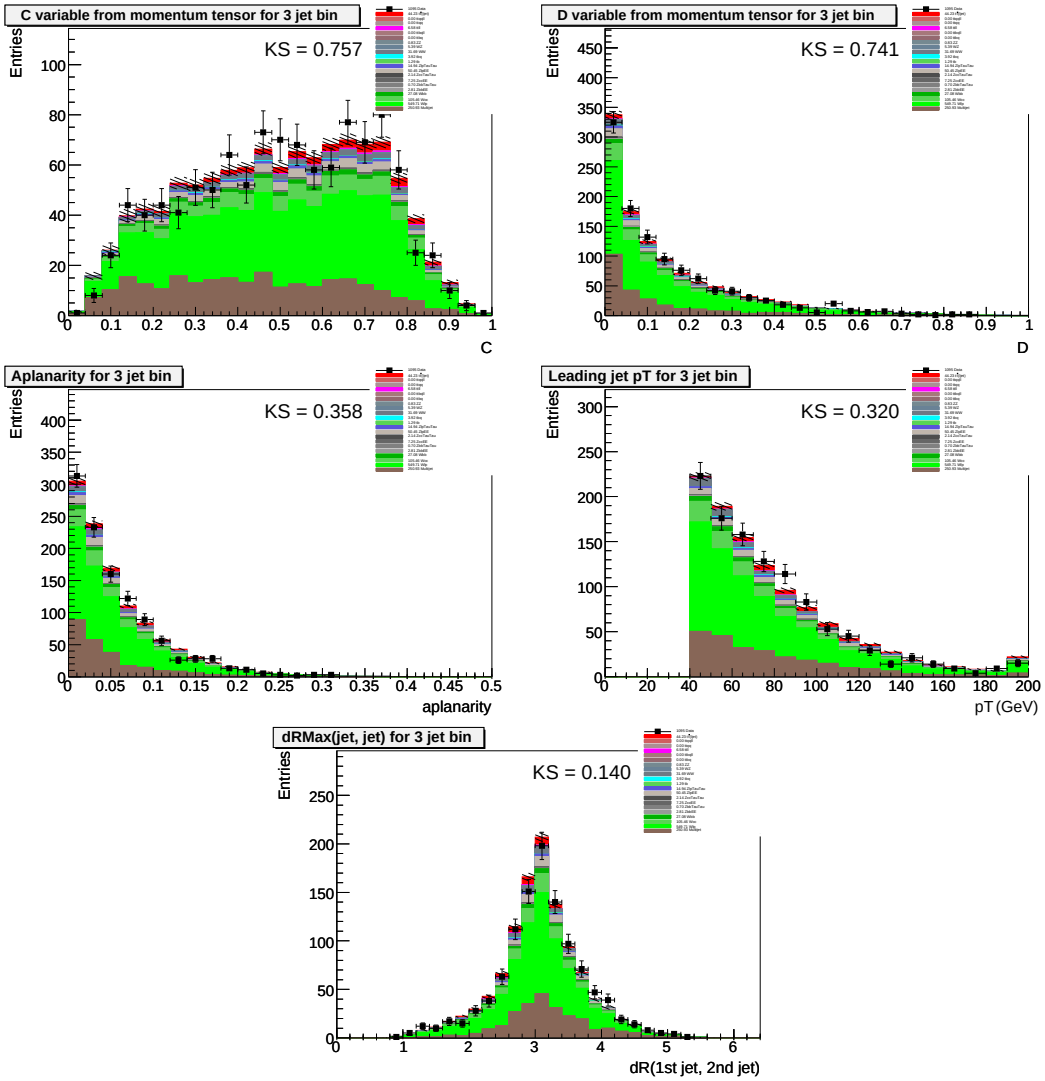

Figure D.3.: Data to Monte Carlo comparisons for the input variables to the topological discriminant function in the 0 b-tagged sample. For the e+jets channel and $= 3$ jets.

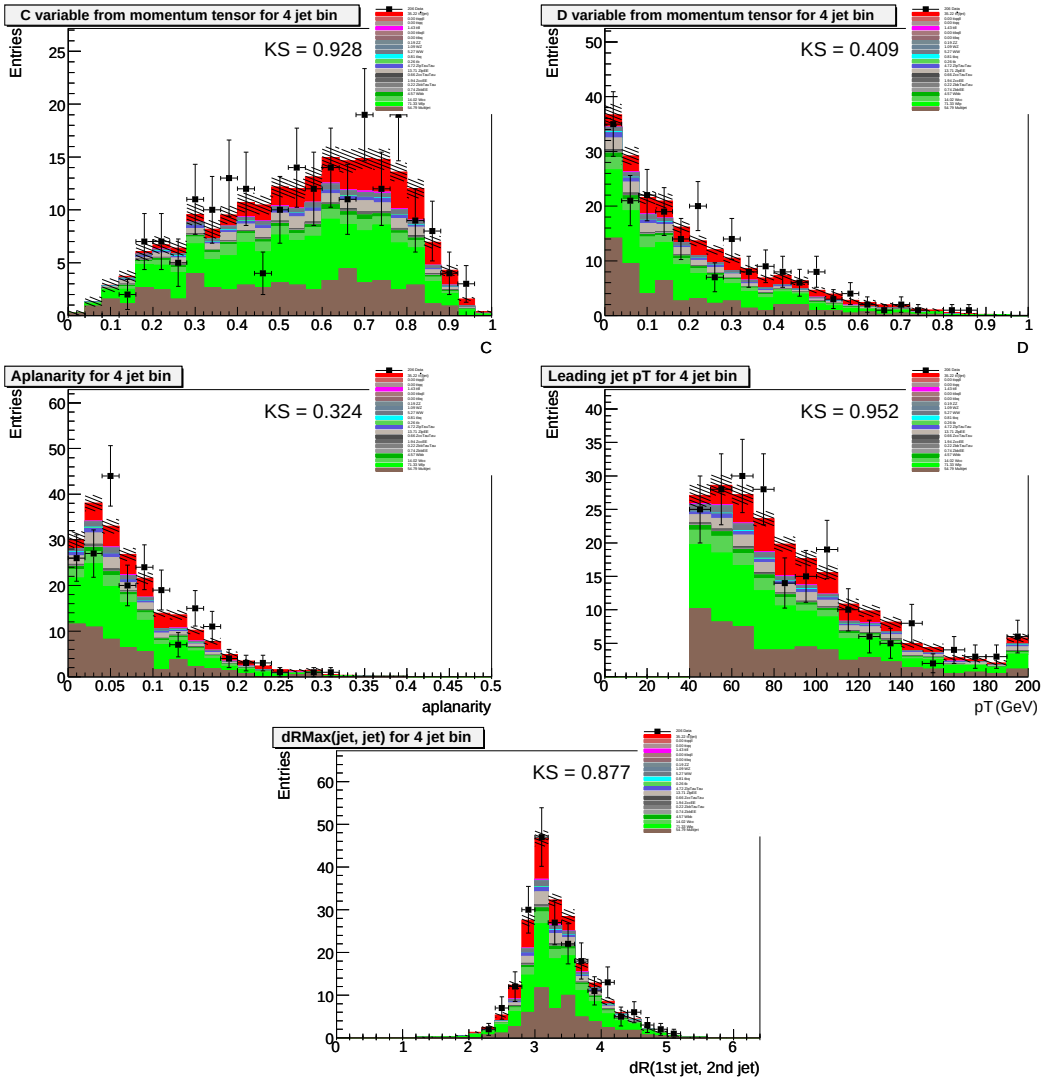

Figure D.4.: Data to Monte Carlo comparisons for the input variables to the topological discriminant function in the 0 b-tagged sample. For the e+jets channel and $\geq$ 4 jets.

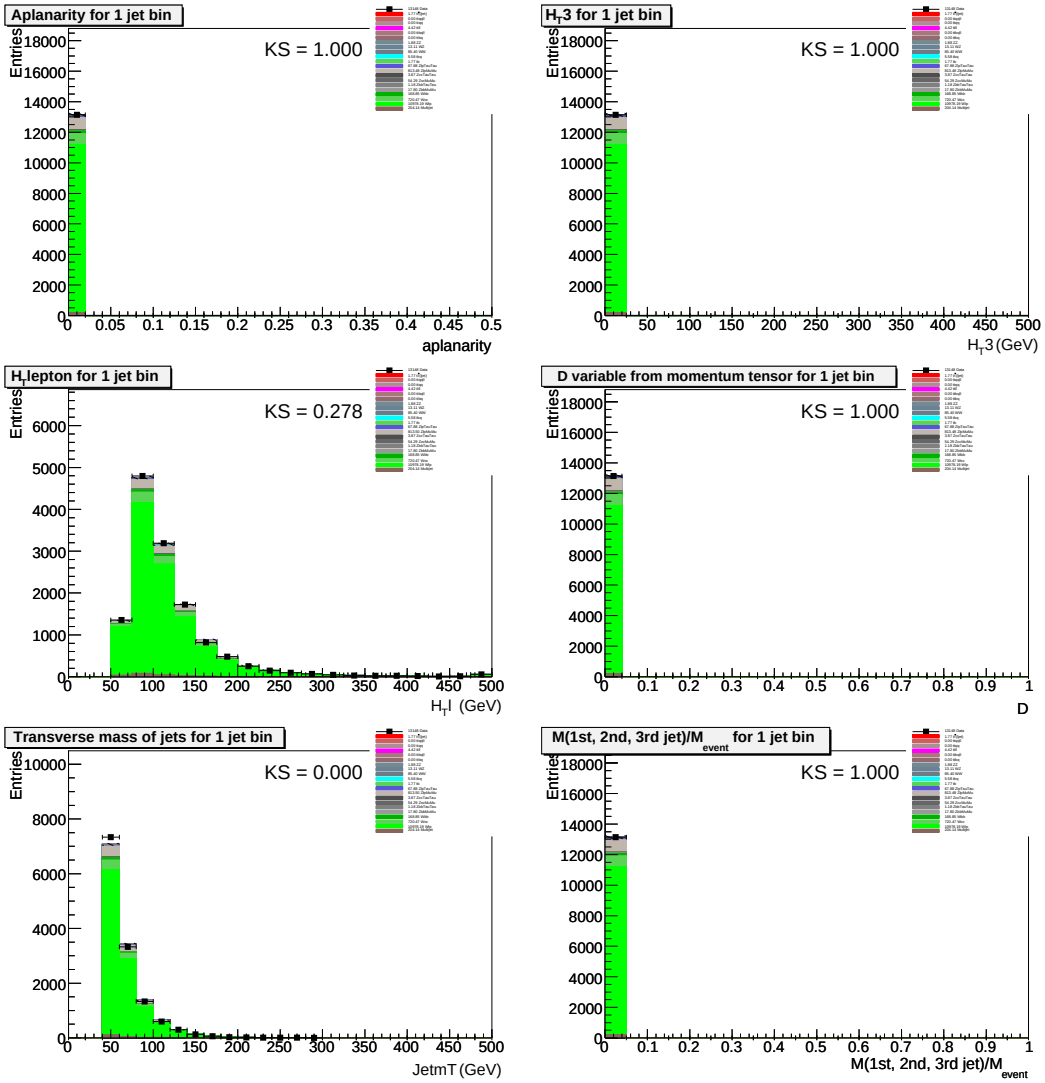

Figure D.5.: Data to Monte Carlo comparisons for the input variables to the topological discriminant function in the 0 b-tagged sample. For the μ+jets channel and $= 1$ jet.

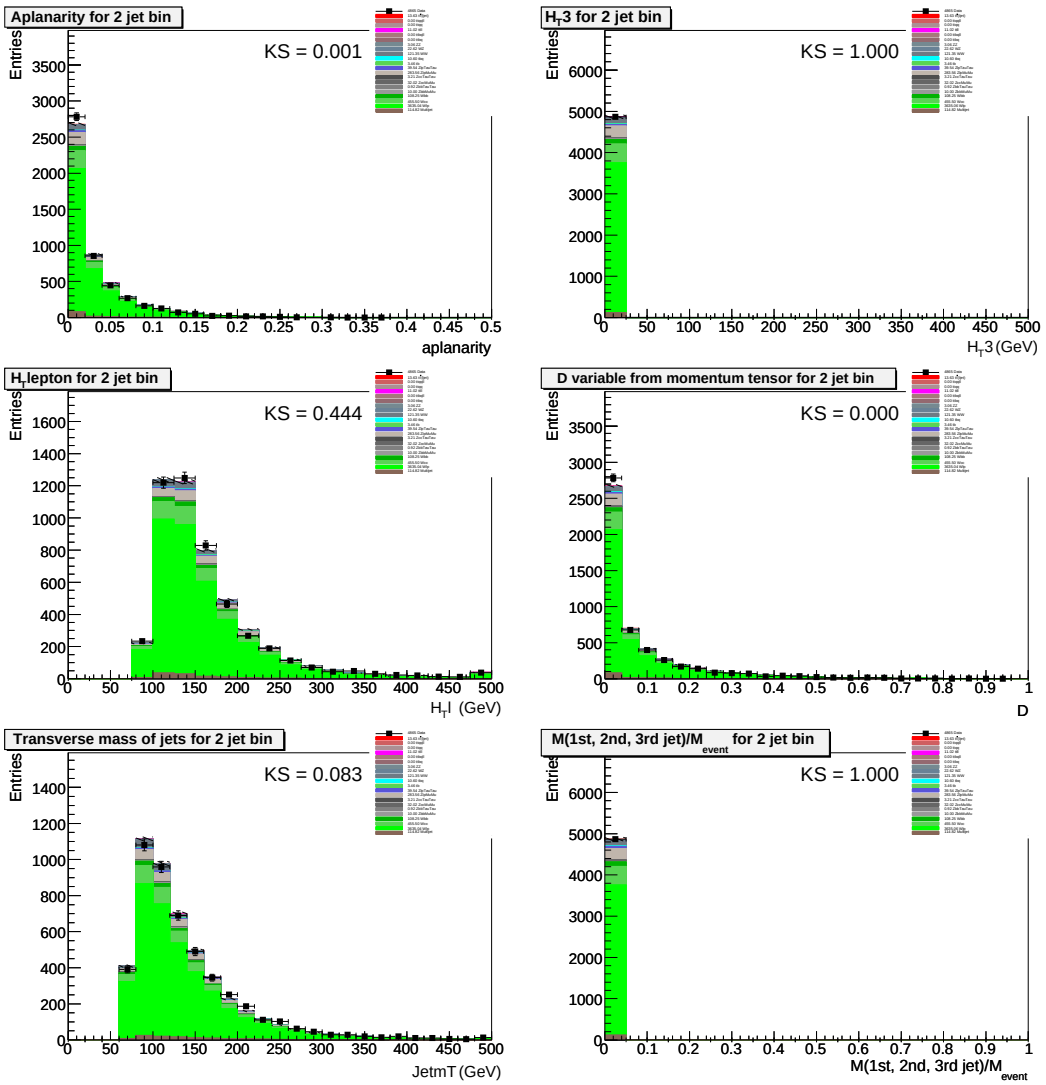

Figure D.6.: Data to Monte Carlo comparisons for the input variables to the topological discriminant function in the 0 b-tagged sample. For the μ+jets channel and $=$ 2 jets.

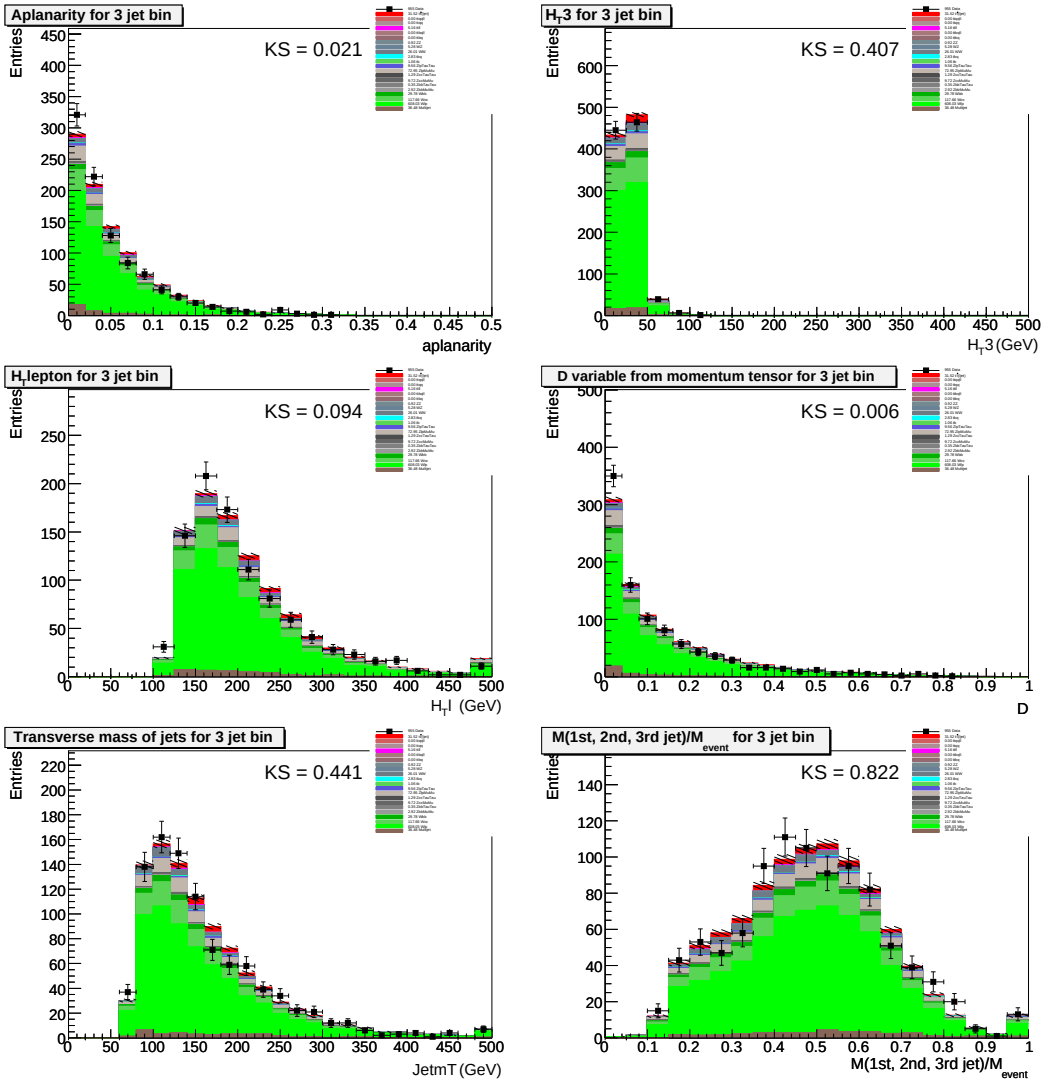

Figure D.7.: Data to Monte Carlo comparisons for the input variables to the topological discriminant function in the 0 b-tagged sample. For the μ+jets channel and $=$ 3 jets.

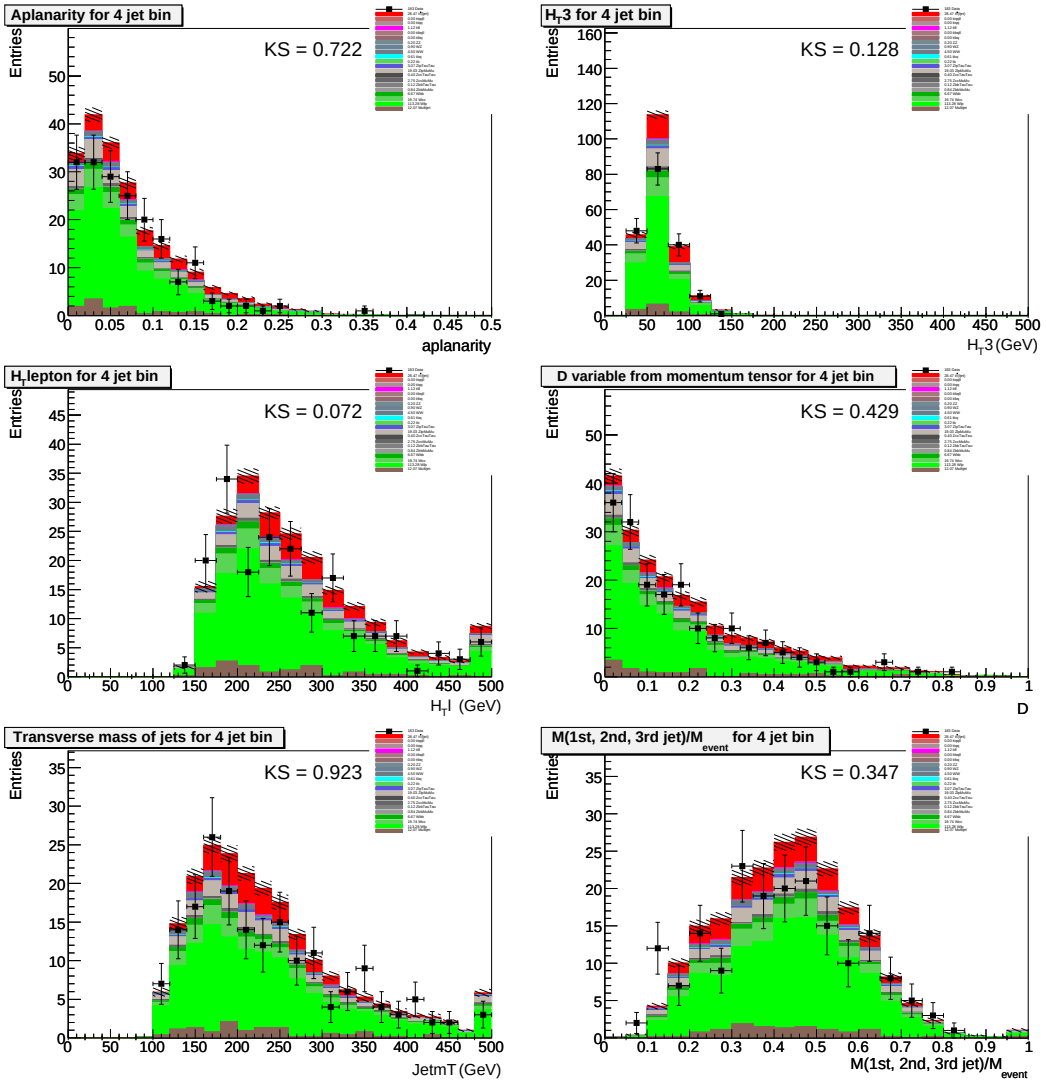

Figure D.8.: Data to Monte Carlo comparisons for the input variables to the topological discriminant function in the 0 b-tagged sample. For the μ+jets channel and $\geq$ 4 jets.

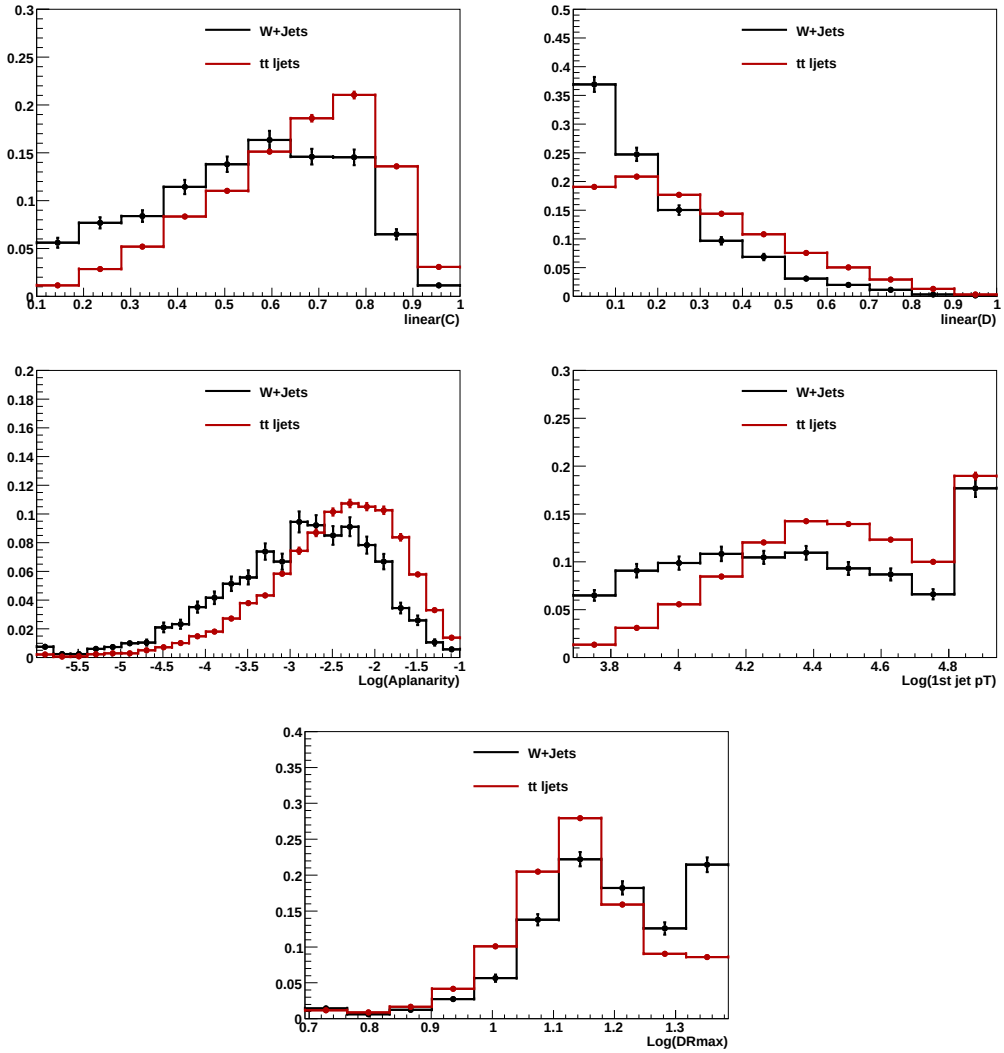

Figure D.9.: Normalised distributions of the transformed input variables to the topological discriminant for Wlp+Jets and $t\bar{t} \rightarrow l + jets$ in the e+jets channel.

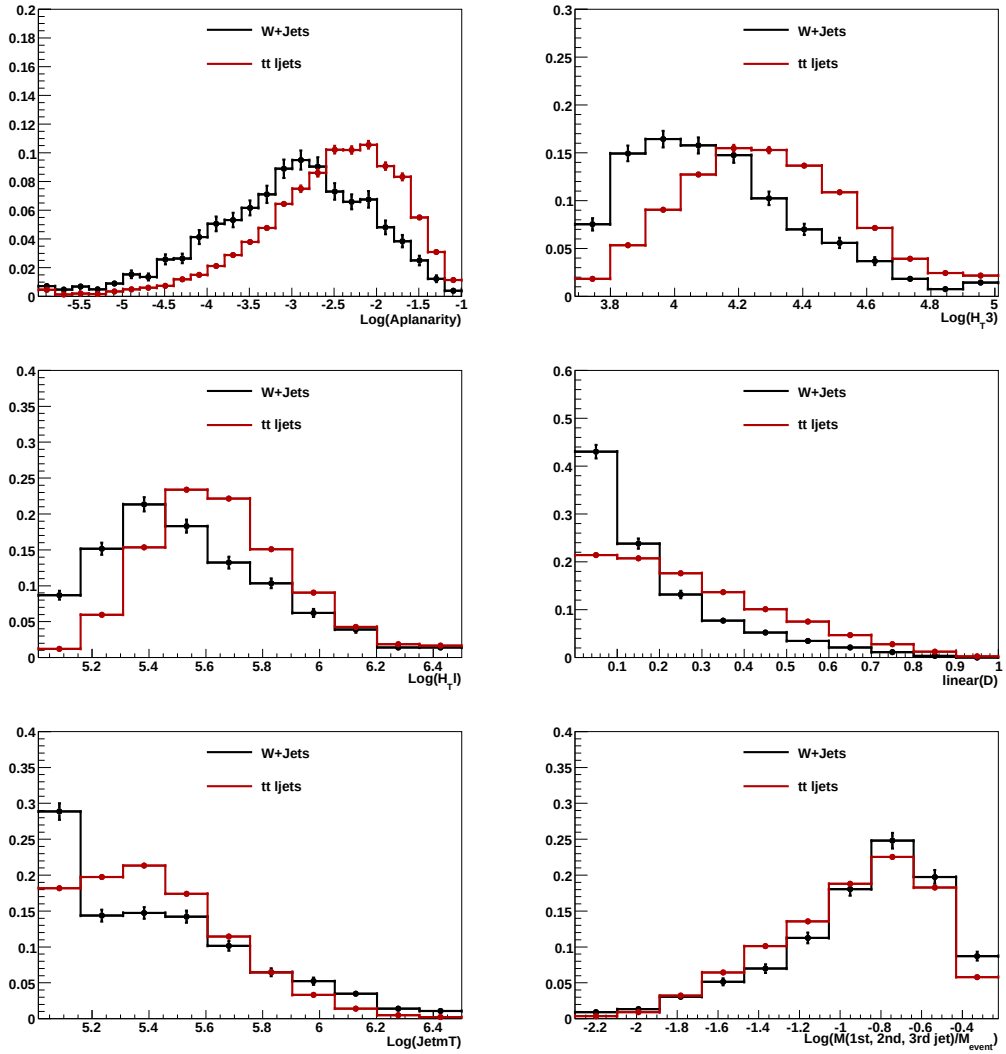

Figure D.10.: Normalised distributions of the transformed input variables to the topological discriminant for Wlp+Jets and $t\bar{t} \rightarrow l + jets$ in the μ+jets channel.

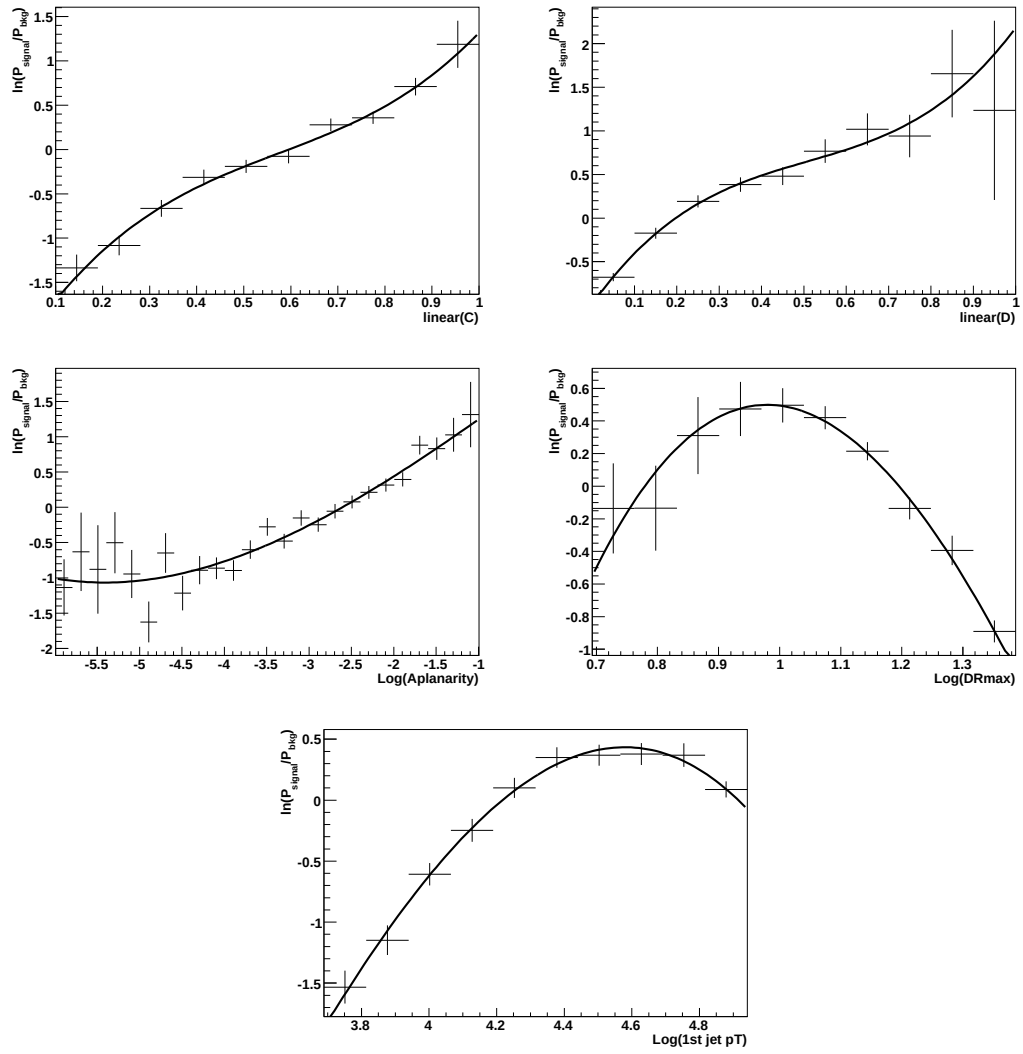

Figure D.11.: Fit to the logarithm of the probability density function for signal ($t\bar{t} \rightarrow l + jets$) over background ($W$+jets) for all transformed input variables to the discriminant function in the e+jets channel.

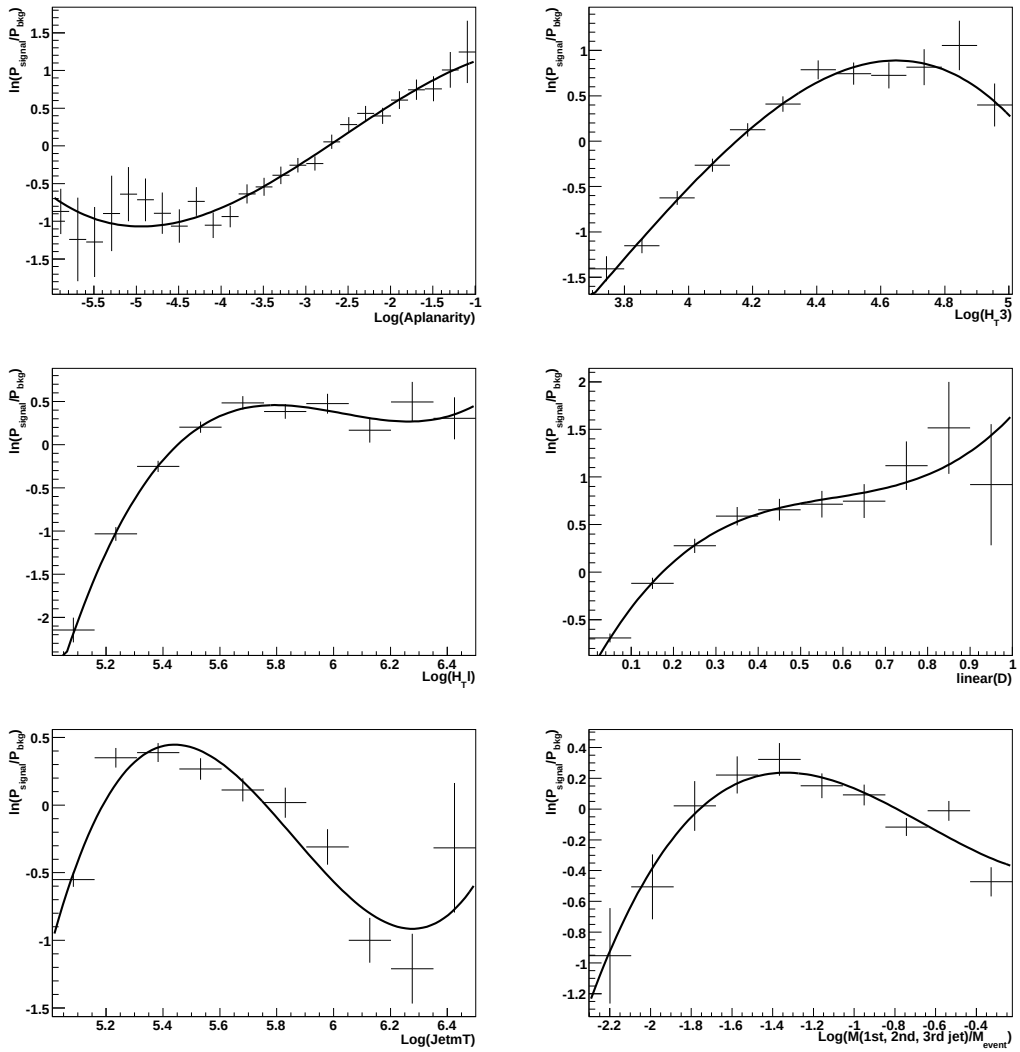

Figure D.12.: Fit to the logarithm of the probability density function for signal ($t\bar{t} \rightarrow l + jets$) over background ($W$+jets) for all transformed input variables to the discriminant function in the μ+jets channel.

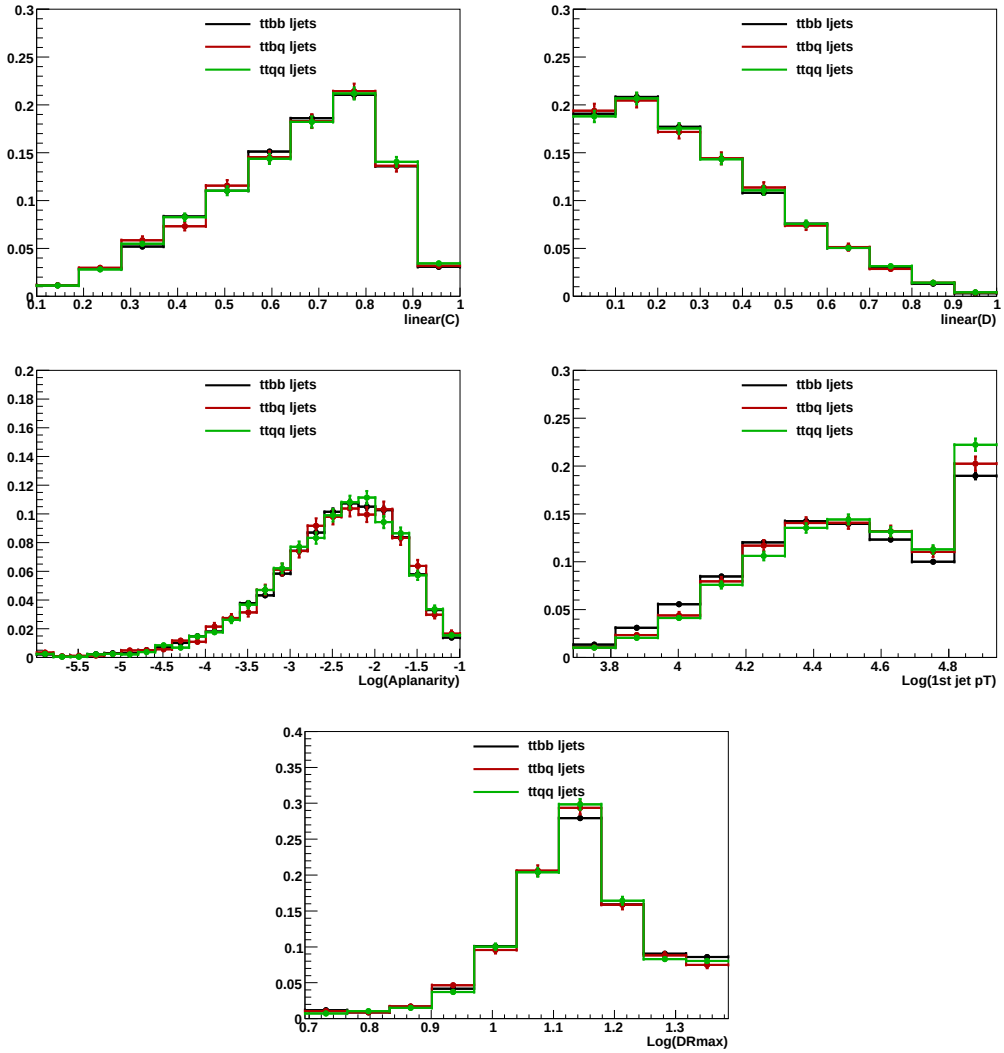

Figure D.13.: Normalised distributions of the transformed input variables to the topological discriminant for $t\bar{t} \to WbWb$, $t\bar{t} \to WbWq$ and $t\bar{t} \to WqWq$ in the e+jets channel.

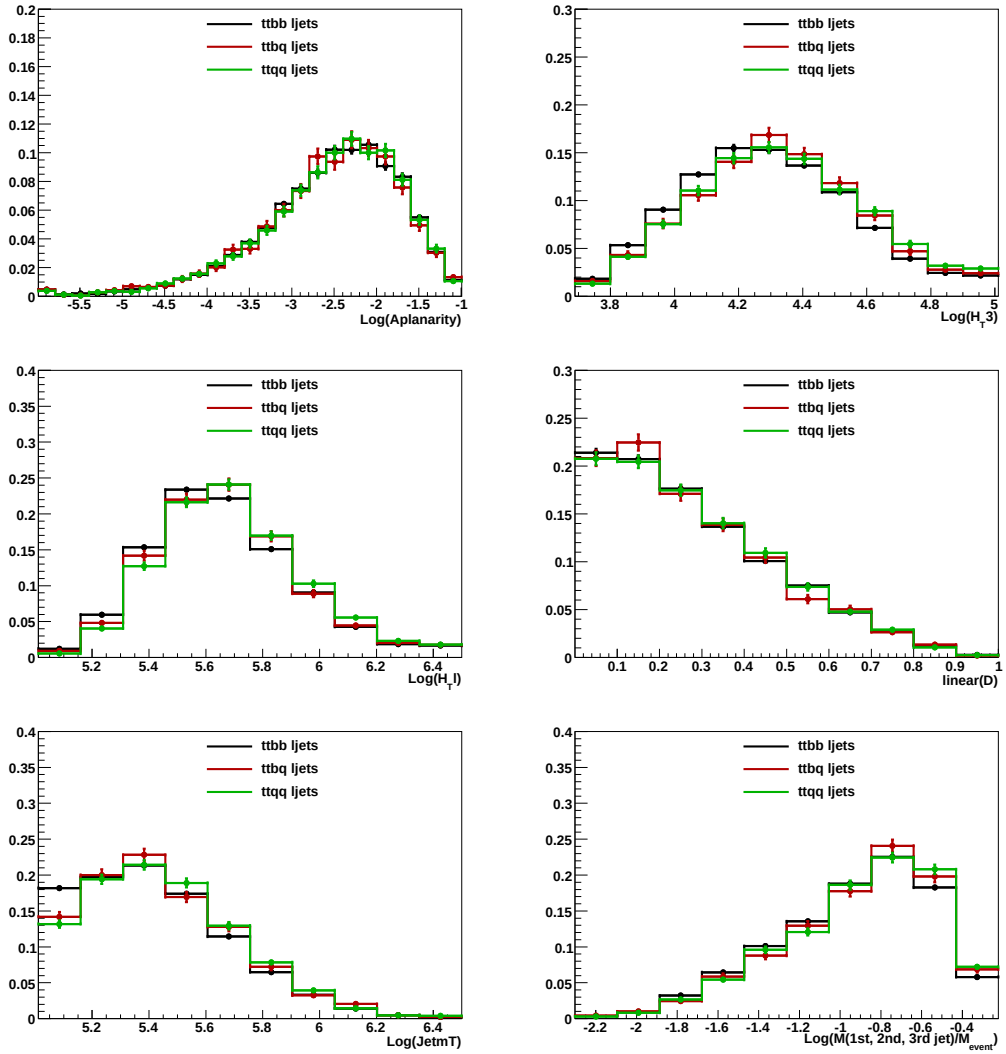

Figure D.14.: Normalised distributions of the transformed input variables to the topological discriminant for $t\bar{t} \to WbWb$, $t\bar{t} \to WbWq$ and $t\bar{t} \to WqWq$ in the μ+jets channel.

E. Ensemble tests for the simultaneous measurement of R and the top quark pair production cross section

In order to check the procedure to determine the $t\bar{t}$ cross section and R, a variety of tests with pseudo-data – so-called ensemble tests – are performed.

Two kinds of ensemble tests are used: For the first kind, only the number of expected signal and background events are varied within the Poisson statistics for a given R and $\sigma \cdot B^2$. That sort of ensembles is referred to as yield-only ensembles. In the second kind the ensembles are generated by simulating the different composition of the pseudo-data sample by picking events from the corresponding signal and background samples. As every single event in this approach is selected from the pool of available events in a particular Monte Carlo sample, the latter ensembles are in the following referred to as event-by-event ensembles or event-by-event pseudo-experiments, in order to distinguish them from the first kind of ensemble test.

While the yield-only ensembles do not take into account differences in the composition of the ensembles, the advantage is the easy implementation of systematic uncertainties. The variation of the systematic uncertainties can be done by varying the corresponding nuisance parameters randomly according to the Gaussian distributions of mean 0 and standard deviation 1. The event-by-event ensembles are implemented in order to check if both types of ensembles give consistent results.

E.0.1. Generation of yield-only pseudo-experiments

The yield-only ensembles are generated by using the event selection and b-tagging efficiencies for signal and Monte Carlo backgrounds.

For every chosen value of R and $\sigma \cdot B^2$ the expected yield for all Monte Carlo backgrounds and signal samples in the 0, 1 and ≥ 2 b-tag samples for tight (denoted $T0$, $T1$ and $T2$) and "loose-tight" (denoted $LT0$, $LT1$ and $LT2$) events are calculated, using the corresponding b-tag probability, event selection efficiency, luminosity and branching ratios. The total number of $t\bar{t}$ events is composed of three contributions: $t\bar{t} \to WbWb$, $t\bar{t} \to WbWq$ and $t\bar{t} \to WqWq$ based on the value of R. The Monte Carlo background and the multijet background predictions do not depend on R and $\sigma \cdot B^2$. The number of multijet events is calculated with the Matrix Method in the samples $T0$, $T1$ and $T2$. The number of multijet events in the "loose-tight" samples $LT0$, $LT1$ and $LT2$ can be derived from the tight samples as:

$$N_{QCD}^{LT0} = \frac{N_{QCD}^{T0}}{\epsilon_{qcd}} - N_{QCD}^{T0} \tag{E.1}$$

$$N_{QCD}^{LT1} = \frac{N_{QCD}^{T1}}{\epsilon_{qcd}} - N_{QCD}^{T1} \tag{E.2}$$

$$N_{QCD}^{LT2} = \frac{N_{QCD}^{T2}}{\epsilon_{qcd}} - N_{QCD}^{T2}. \tag{E.3}$$

In order to predict the number of Monte Carlo background events in the "loose-tight" samples, the calculated prediction in $T0$, $T1$ and $T2$ can be used:

$$N_{MC}^{LT0} = \frac{N_{MC}^{T0}}{\epsilon_{sig}} - N_{MC}^{T0} \tag{E.4}$$

$$N_{MC}^{LT1} = \frac{N_{MC}^{T1}}{\epsilon_{sig}} - N_{MC}^{T1} \tag{E.5}$$

$$N_{MC}^{LT2} = \frac{N_{MC}^{T2}}{\epsilon_{sig}} - N_{MC}^{T2} \tag{E.6}$$

For the prediction of the W+jets background, the number of true isolated leptons from the Matrix Method is calculated. By calculating the number of signal, multijet and Monte Carlo background before b-tagging at a given value of R and $\sigma \cdot B^2$, using the corresponding event selection efficiency, luminosity and branching ratio, the number of W+jets events in the tight sample can be extracted as the difference to the observed number of events. The number of W+jets events in the tight 1 and ≥ 2 b-tagged samples are derived by application of the corresponding b-tag probabilities. In the zero b-tagged sample the number of W+jets events is the difference between the predicted number of events in the pretagged minus the prediction in the one and two b-tagged samples. To get the number of W+jets events in the "loose-tight" sample the following equations are applied:

$$N_{W+jets}^{LT0} = \frac{N_{W+jets}^{T0}}{\epsilon_{sig}} - N_{W+jets}^{T0} \tag{E.7}$$

$$N_{W+jets}^{LT1} = \frac{N_{W+jets}^{T1}}{\epsilon_{sig}} - N_{W+jets}^{T1} \tag{E.8}$$

$$N_{W+jets}^{LT2} = \frac{N_{W+jets}^{T2}}{\epsilon_{sig}} - N_{W+jets}^{T2} \tag{E.9}$$

Each of the contributions in the different samples $T1$, $T2$, $LT0$, $LT1$ and $LT2$ are then varied independently according to a Poisson distribution. In the tight zero b-tagged sample $T0$ an additional step has to be done due to the topological discriminant. Each of the templates is normalised to the predicted number of events in $T0$. For the W+jets template the normalisation from W+jets and Monte Carlo background events is used. After the normalisation, a random number in each bin of the topological discriminant is drawn, according to a Poisson distribution.

E.0.2. Generation of event-by-event pseudo-experiments

In order to generate event-by-event ensembles or pseudo-experiments, for each Monte Carlo sample all events passing the tight event selection for exactly three and four or more jets are stored with their corresponding event weight, the probability to have 0-, 1- or at least 2 b-tags in the event and the value of the topological discriminant. The three and four jet events are treated separately for the ensemble creation, as well as the e+jets and μ+jets channels.

For every chosen R and $\sigma \cdot B^2$, the expected yield for all Monte Carlo backgrounds and signal samples before b-tagging are calculated, using the corresponding event selection efficiency, luminosity and branching ratio. The number of multijet events is calculated with the matrix method from the tight and "loose-tight" data sample before b-tagging. The expected number of events in the W+jets sample before tagging is calculated as the difference between the number of data events and the sum of the signal, multijet and Monte Carlo background yields.

In every sample, random numbers distributed according to a Poissonian around the expected yields are drawn. For each Monte Carlo sample of the signal, Monte Carlo backgrounds and W+jets, a loop over the predicted number of events for this contribution is performed. In each iteration of the loop a uniformly distributed random number is used to choose one event from the available pool. Furthermore, another uniformly distributed random number rn between 0 and the maximum event weight of that particular sample is calculated. If the event weight for the chosen event is larger than the random number rn the event is kept, and dropped otherwise. If the event is dropped the procedure to select an event is repeated. If the event is accepted, a new random number tn, uniformly distributed between 0 and 1, is calculated, in order to select the b-tag for the chosen event. For this purpose, the probabilities to have 0, 1 and ≥ 2 b-tags ($w0$, $w1$ and $w2$) are compared to the random value tn for the chosen event. If $tn \leq w0$, the event is assumed to have no b-tagged jets, for $w0 < tn \leq w0 + w1$ the event is assumed to have exactly one b-tag, and otherwise it is chosen to have at least two b-tags.

With this procedure all the samples with zero, one and at least two b-tags (T0, T1 and T2) for all different contributions except multijet background are created. For events with four or more jets and 0 b-tags the likelihood discriminant value for each event of the chosen ensemble is used to create the likelihood discriminant for a particular pseudo-experiment.

The number of events in the "loose-tight" samples are estimated by applying the b-tagging to data and using the Matrix Method in the subsamples with zero, one and at least two b-tags. The corresponding number of multijet events in the "loose-tight" sample is calculated as given in Eq. E.1. For the Monte Carlo backgrounds and the W+jets background the contribution in the "loose-tight" samples are calculated according to Eq. E.4 and Eq. E.7, respectively.

All multijet contributions in the tight and "loose-tight" samples, for the different b-tag subsamples, are then varied according to the Poisson distribution. For the events with at least four jets and 0-tags the topological discriminant is constructed by normalising the multijet background template obtained from the "loose-tight" sample to the number of estimated multijet events in the tight 0 b-tag sample, and adding the distribution to the total pseudo-experiment discriminant.

E.0.3. Test of the fitting procedure

In order to test if the fitting procedure causes a bias, the two types of ensembles are applied to the fit of R and $\sigma \cdot B^2$. Besides the bias check this is also a check on the yield-only ensembles, which are needed for the limit setting on R as described in section 8.6.5.

In the event-by-event ensembles, a limited pool size and oversampling of events have to be taken into account by applying a correction factor according to [185], where the correction factor was derived for signal-only samples. Since the event-by-event ensembles are only used to check the bias on the fitted value and its uncertainty, but not to extract the uncertainty from the pseudo-experiments, an estimate is used without the correction factor. Especially since randomised distributions are used for determining the b-tag subsample, and since signal and background events are used to create the ensembles, the correction due to reusing events is expected to be small.

Fitted versus true R

A check for possible biases in extracting R is performed, by using yield-only ensembles. The true values of R are varied in steps of 0.1 between 0 and 1.0 while $\sigma \cdot B^2$ is kept at a value of 7 pb. For each R, 1000 ensembles are generated. For each ensemble, R is fitted simultaneously with the top pair production cross section.

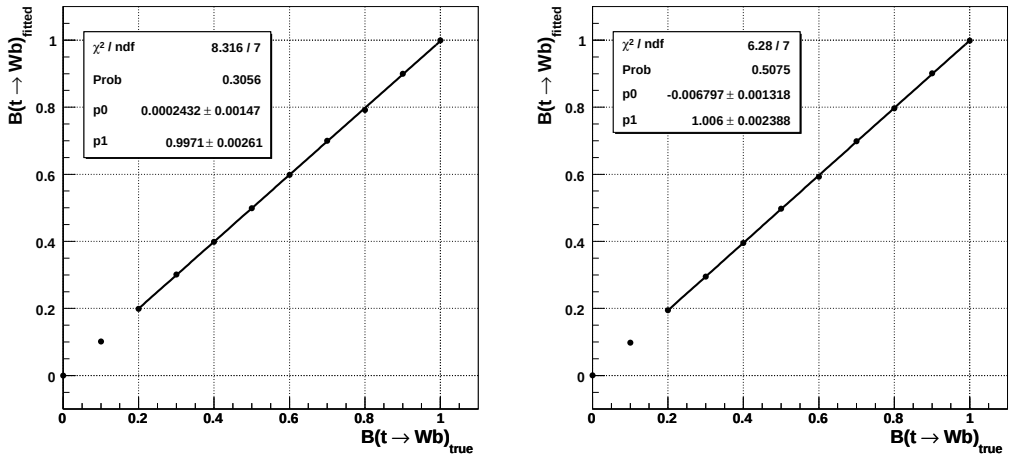

Figure E.1.: Mean value of the fitted R as a function of the true R. The Medium NN Tagger and the dependency of the topological discriminant on R are used. Left: yield-only ensembles. Right: event-by-event ensembles.

The distributions of the fitted R for each true value of R are fitted with a Gaussian distribution, The mean values of each Gaussian fit are plotted in Fig. E.1 (left) as a function of true R. No bias can be observed on the curves.

Figure E.2 (left) shows the fitted $\sigma \cdot B^2$ as a function of R. The fitted cross section does not depend on R and is approximately 2% larger than the true value of $\sigma \cdot B^2 = 7$ pb.

Figure E.3 (left) shows the pull width of the fitted R versus true R. The pull is defined as the fitted minus the true value divided by the uncertainty of the fitted value, as returned by the likelihood maximisation procedure. Figure E.4 (left) shows the pull width of the fitted $\sigma \cdot B^2$ versus true R. The pull width is ~ 2 % and ~ 5 % smaller than 1 for both cases, showing that the uncertainty is overestimated or that the ensembles are missing an additional fluctuation.

The same procedure is repeated with the event-by-event ensembles. Figure E.1 (right) shows the mean values of the Gaussian fits versus the true value of R. A very small bias in the slope can be observed. For fitted values of R close to 1 no significant bias can be seen.

In Fig. E.2 (right) the fitted $\sigma \cdot B^2$ is shown as function of R. The fitted value of $\sigma \cdot B^2$ comes out a bit larger than the input value for low R. The pull, shown in Fig. E.3 (right) for fitted versus true R, and in Fig. E.4 (right) for the fitted $\sigma \cdot B^2$ versus true R, comes out with a width smaller than one, by about 8 %. This indicates a small overestimation of the uncertainty.

Fitted versus true $\sigma(p\bar{p} \rightarrow t\bar{t}) \times B^2(t \rightarrow Wq)$

Possible biases of the fitting procedure on $\sigma \cdot B^2$ are checked with yield-only and event-by-event ensembles. The input value of $\sigma \cdot B^2$ is varied in steps of 1.0 between 0 and 15.0, while R is fixed to 1. For each true $t\bar{t}$ cross section 1000 ensembles are generated. For each set of ensemble $\sigma \cdot B^2$ is fitted simultaneously with R.

The distribution of measured cross section is fitted with a Gaussian distribution for every set of ensembles. The mean values of each Gaussian fit are shown in Fig. E.5 (left) as a function of the true $\sigma \cdot B^2$. Figure E.6 (left) shows the fitted R as a function of true $\sigma \cdot B^2$. No significant bias is observed.

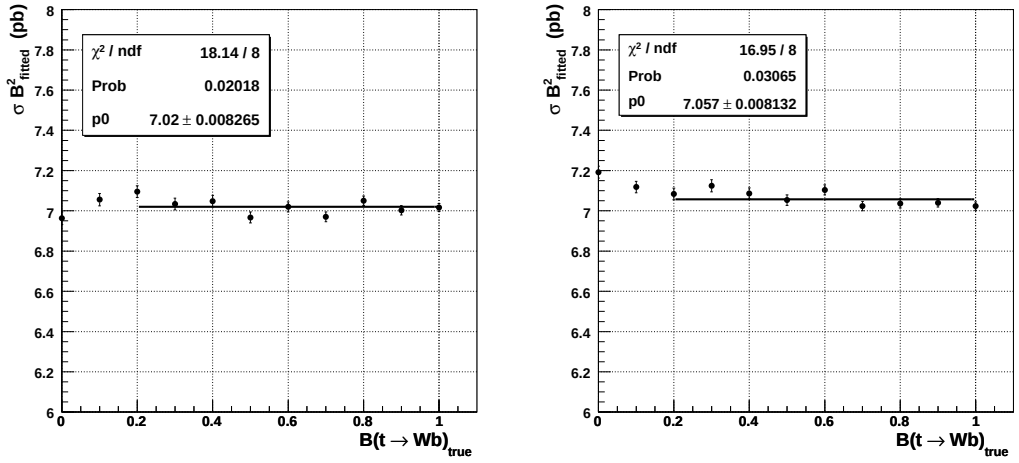

Figure E.2.: Mean value of the fitted $\sigma \cdot B^2$ as a function of the true R. The Medium NN Tagger and the dependency of the topological discriminant on R are used. Left: yield-only ensembles. Right: event-by-event ensembles.

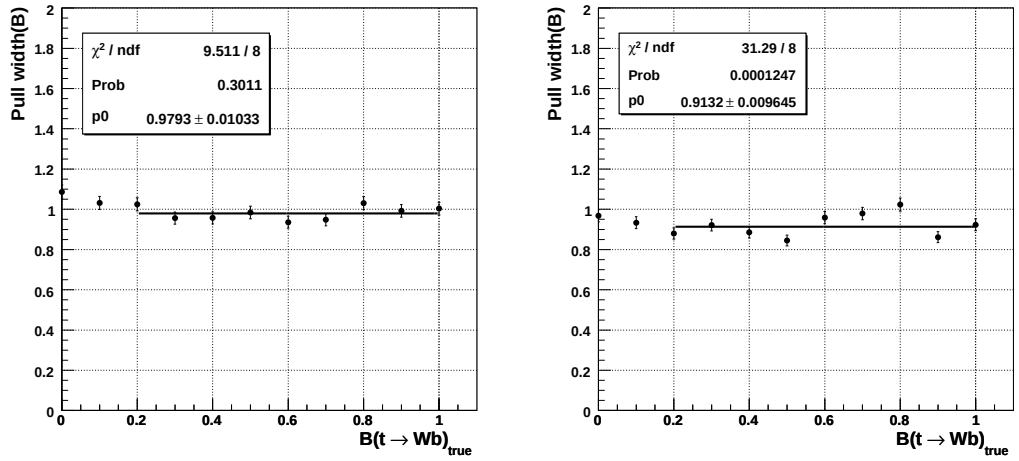

Figure E.3.: Distribution of the fitted pull width for R versus true R. A Gaussian fit is performed to get the mean value for each distribution of $(\text{fitted} - \text{true})/\sigma_{\text{fitted}}$. The Medium NN Tagger and the dependency of the topological discriminant on R are used. Left: yield-only ensembles. Right: event-by-event ensembles.

Figure E.7 (left) shows the pull width of the fitted versus true $\sigma \cdot B^2$, and Fig. E.8 (left) shows the pull width of the fitted R versus true $\sigma \cdot B^2$.

For the event-by-event ensembles, the distribution of the mean values of the Gaussian fits to the distribution of fitted $\sigma \cdot B^2$ are presented in Fig. E.5 (right) as a function of the true value of $\sigma \cdot B^2$. No significant bias is observed. The same plot for R versus $\sigma \cdot B^2$, as shown in Fig. E.6 (right), also shows no significant deviation from 1, i. e. no bias is seen.

In Figure E.7 (right) the pull width of the fitted versus true $\sigma \cdot B^2$, resulting from the event-by-event ensembles, is shown. Figure E.8 (right) shows the pull width of the fitted R versus

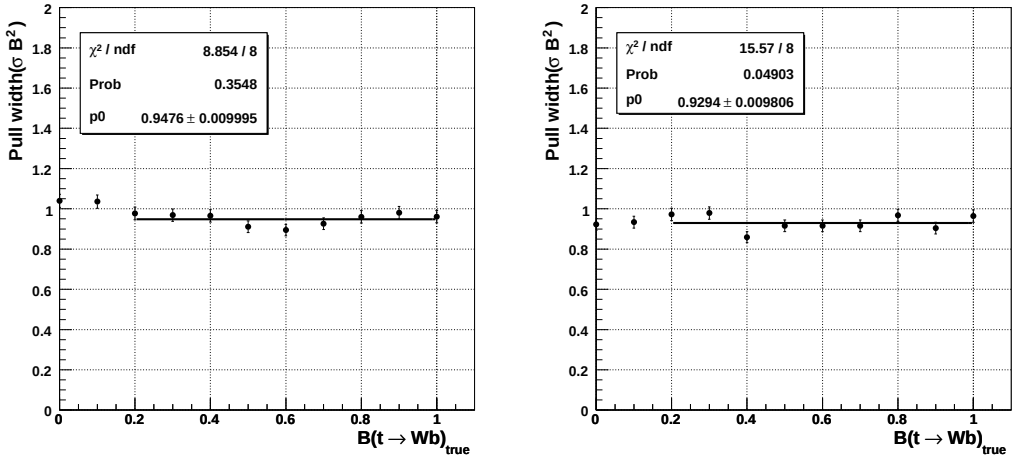

Figure E.4.: Distribution of the fitted pull width for $\sigma \cdot B^2$ versus true R. A Gaussian fit is performed to get the mean value for each distribution of $(\text{fitted} - \text{true})/\sigma_{\text{fitted}}$. The Medium NN Tagger and the dependency of the topological discriminant on R are used. Left: yield-only ensembles. Right: event-by-event ensembles.

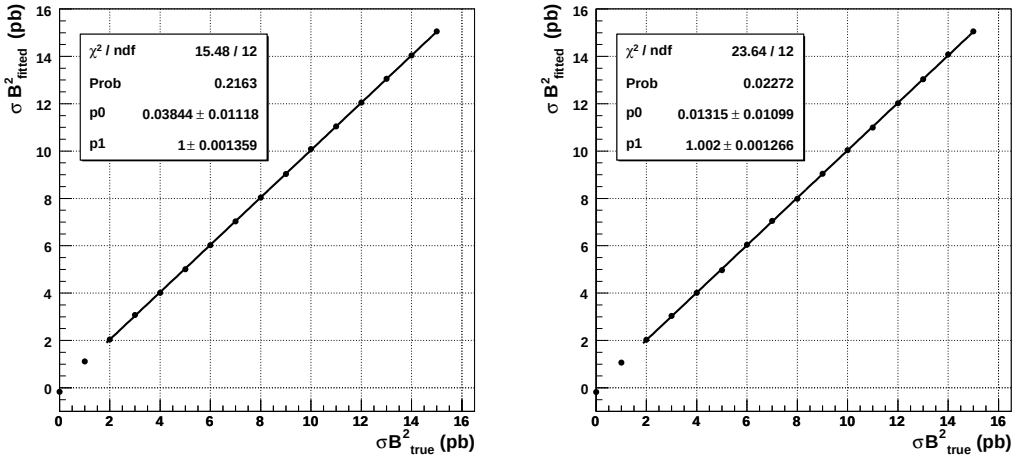

Figure E.5.: Mean value of the fitted $\sigma \cdot B^2$ as a function of the true $\sigma \cdot B^2$. The Medium NN Tagger and the dependency of the topological discriminant on $\sigma \cdot B^2$ are used. Left: yield-only ensembles. Right: event-by-event ensembles.

true $\sigma \cdot B^2$. In both cases the test indicates that the statistical uncertainty is overestimated by ~ 6 %.

E.0.4. Expected statistical uncertainties

The expected statistical uncertainty on the fitted R and $\sigma \cdot B^2$ can be extracted from the pseudo-experiments with the yield-only and event-by-event ensembles. For each of the pseudo-experiments the uncertainties on R and $\sigma \cdot B^2$ are computed with MINOS.

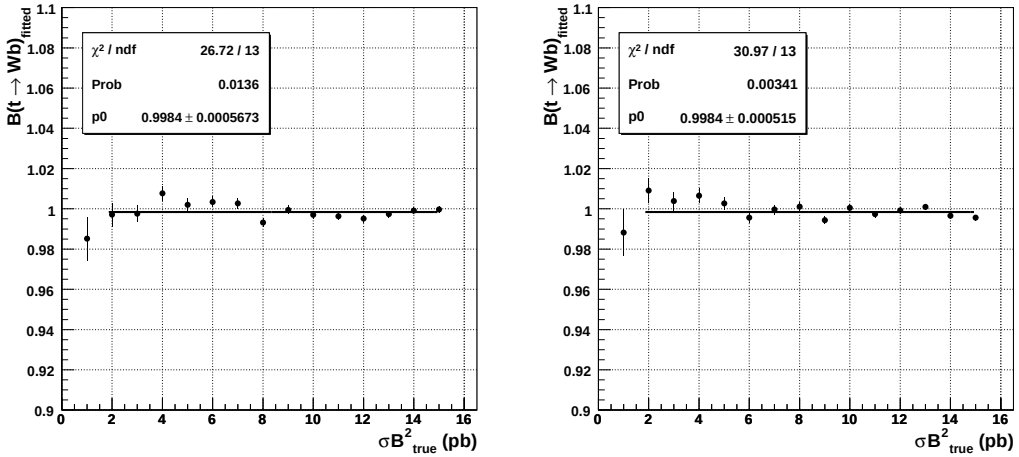

Figure E.6.: Mean value of the fitted R as a function of the true $\sigma \cdot B^2$. The Medium NN Tagger and the dependency of the topological discriminant on $\sigma \cdot B^2$ are used. Left: yield-only ensembles. Right: event-by-event ensembles.

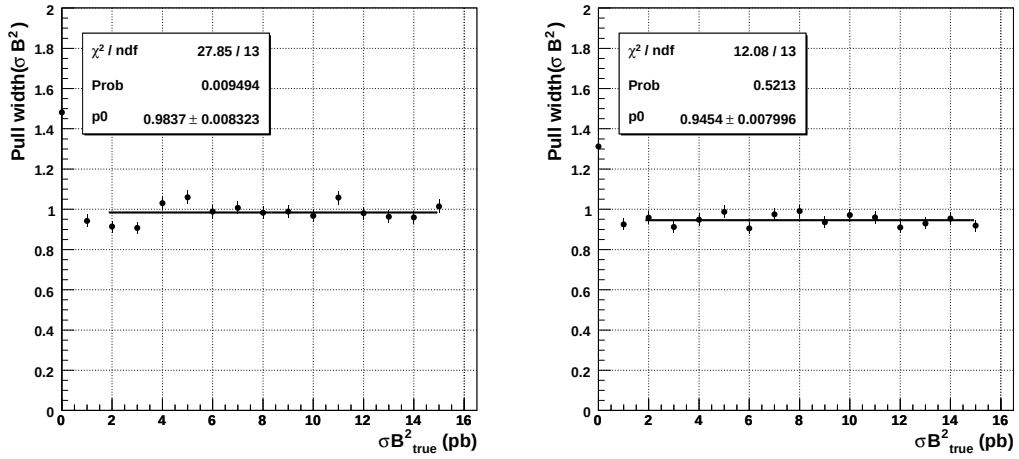

Figure E.7.: Distribution of the fitted pull width for $\sigma \cdot B^2$ versus true $\sigma \cdot B^2$. A Gaussian fit is performed to get the mean value for each distribution of $(\text{fitted} - \text{true})/\sigma_{\text{fitted}}$. The Medium NN Tagger and the dependency of the topological discriminant on R are used. Left: yield-only ensembles. Right: event-by-event ensembles.

Figure E.9 shows the most probable relative statistical upward and downward uncertainty on R as a function of true R for $\sigma \cdot B^2 = 7$ pb in the yield-only ensembles and the event-by-event ensembles, respectively.

In Fig. E.10 the expected statistical upward and downward uncertainty on R as a function of true $\sigma \cdot B^2$ for the yield-only and the event-by-event ensembles are shown, respectively. For $\sigma \cdot B^2 = 7$ pb the relative statistical upward and downward uncertainty on R is ~ 0.08.

The results of similar tests for $\sigma \cdot B^2$ are presented in Figure E.11, where the most probable relative upward and downward uncertainties on $\sigma \cdot B^2$ as a function of true $\sigma \cdot B^2$ are shown.

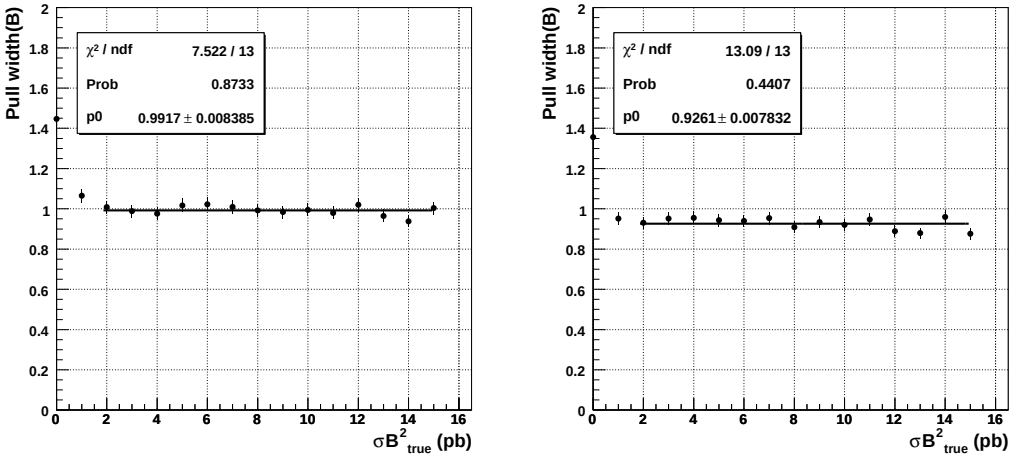

Figure E.8.: Distribution of the fitted pull width for R versus true $\sigma \cdot B^2$. A Gaussian fit is performed to get the mean value for each distribution of $(\text{fitted} - \text{true})/\sigma_{\text{fitted}}$. The Medium NN Tagger and the dependency of the topological discriminant on R are used. Left: yield-only ensembles. Right: event-by-event ensembles.

For $R = 1$ and $\sigma \cdot B^2 = 7$ pb the relative statistical upward uncertainty on $\sigma \cdot B^2$ is ~ 10 %, and downward uncertainty of ~ 9 %.

In Fig. E.12 the relative uncertainties on $\sigma \cdot B^2$ as a function of true R are demonstrated.

By comparing the relative statistical uncertainty on R for different b-tag working points, the medium NN tagger turns out to be the optimal choice.

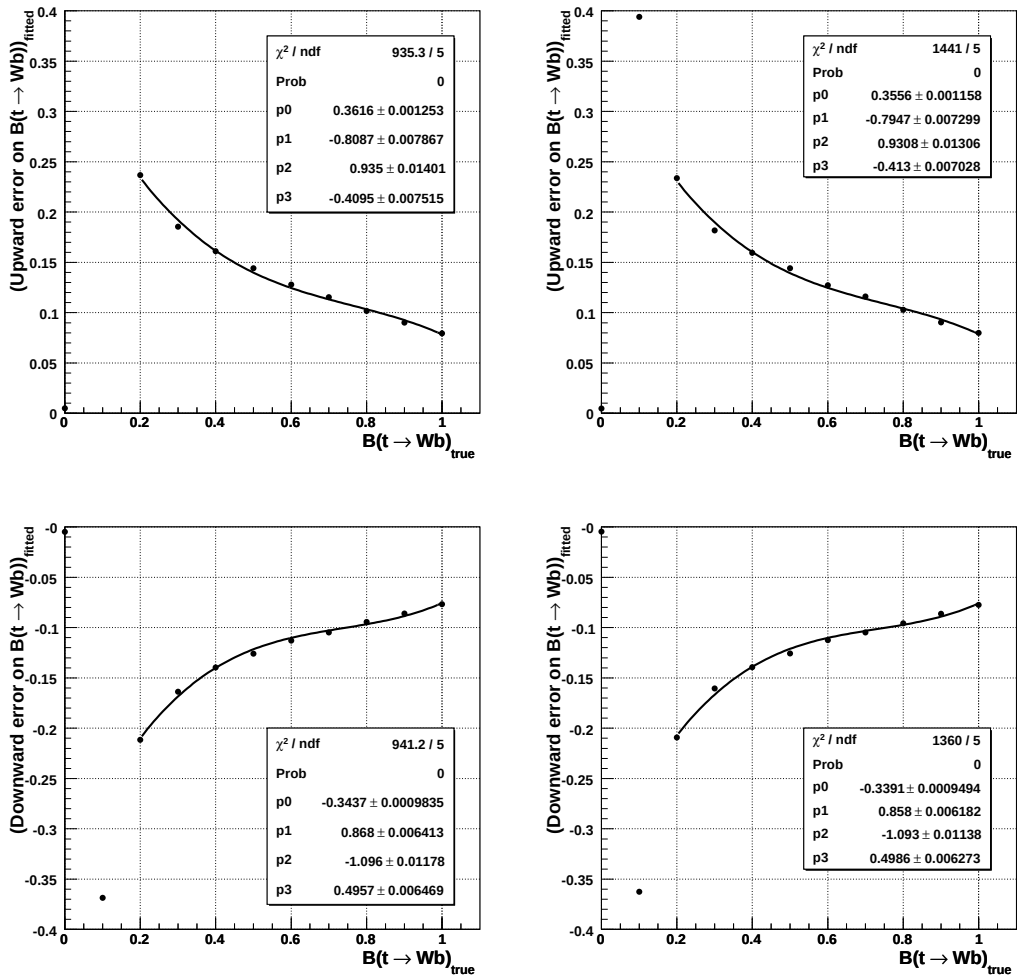

Figure E.9.: Expected relative statistical upward (top) and downward (bottom) error on R as a function of the true R. The Medium NN Tagger and the dependency of the topological discriminant on R are used. Left: yield-only ensembles. Right: event-by-event ensembles.

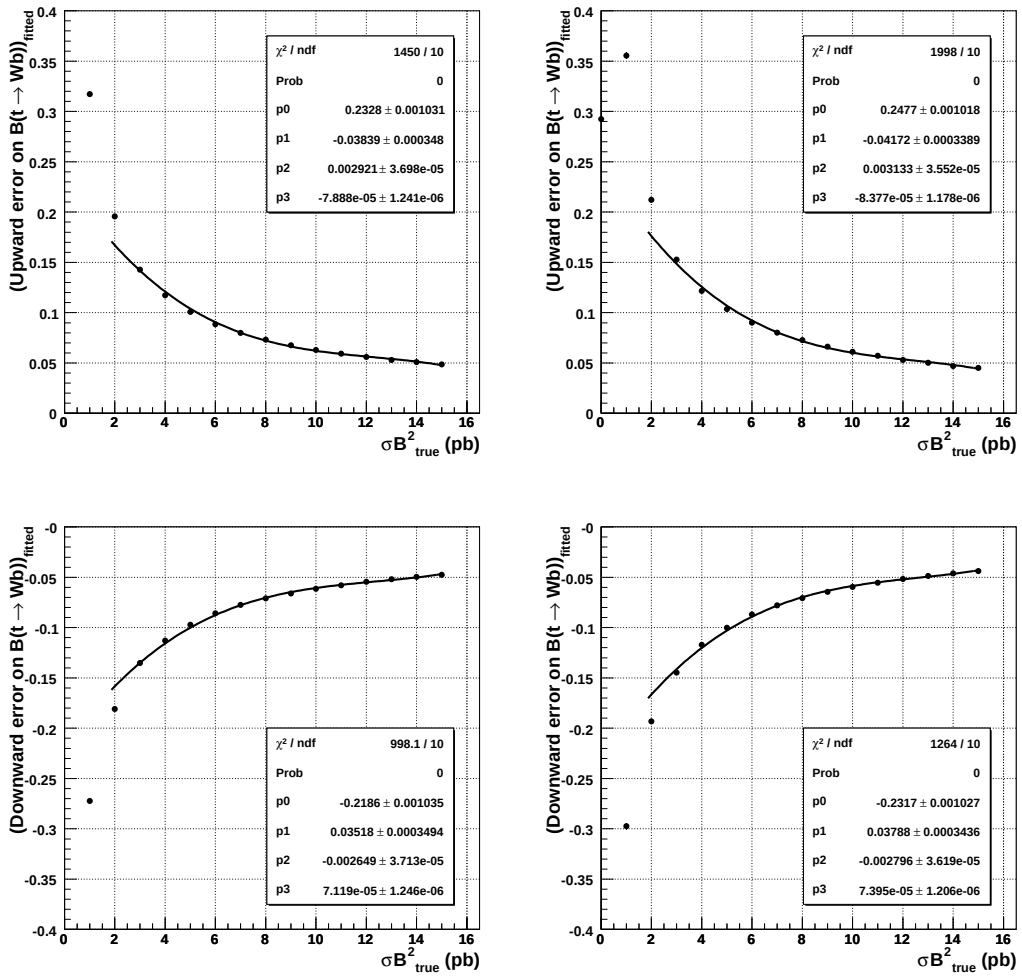

Figure E.10.: Expected relative statistical upward (top) and downward (bottom) error on R as a function of the true $\sigma \cdot B^2$. The Medium NN Tagger and the dependency of the topological discriminant on R are used. Left: yield-only ensembles. Right: event-by-event ensembles.

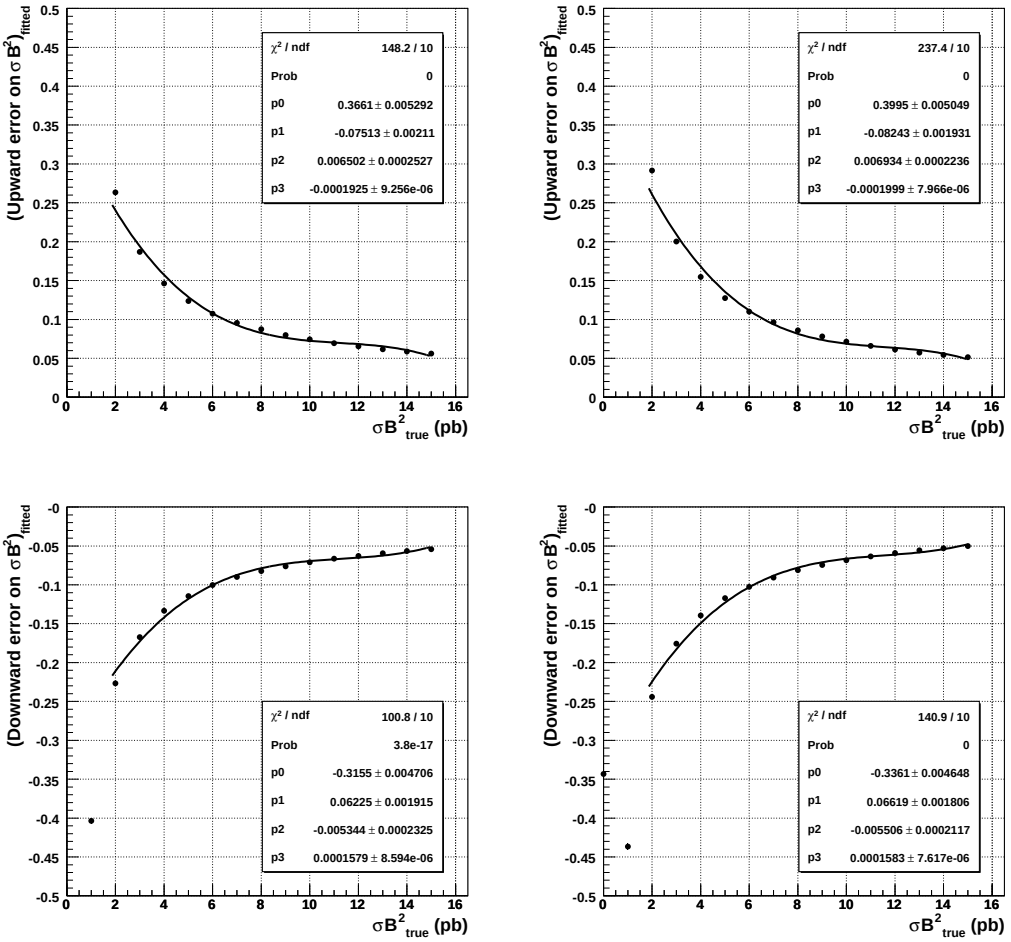

Figure E.11.: Expected relative statistical upward (top) and downward (bottom) error on $\sigma \cdot B^2$ as a function of the true $\sigma \cdot B^2$. The Medium NN Tagger and the dependency of the topological discriminant on R are used. Left: yield-only ensembles. Right: event-by-event ensembles.

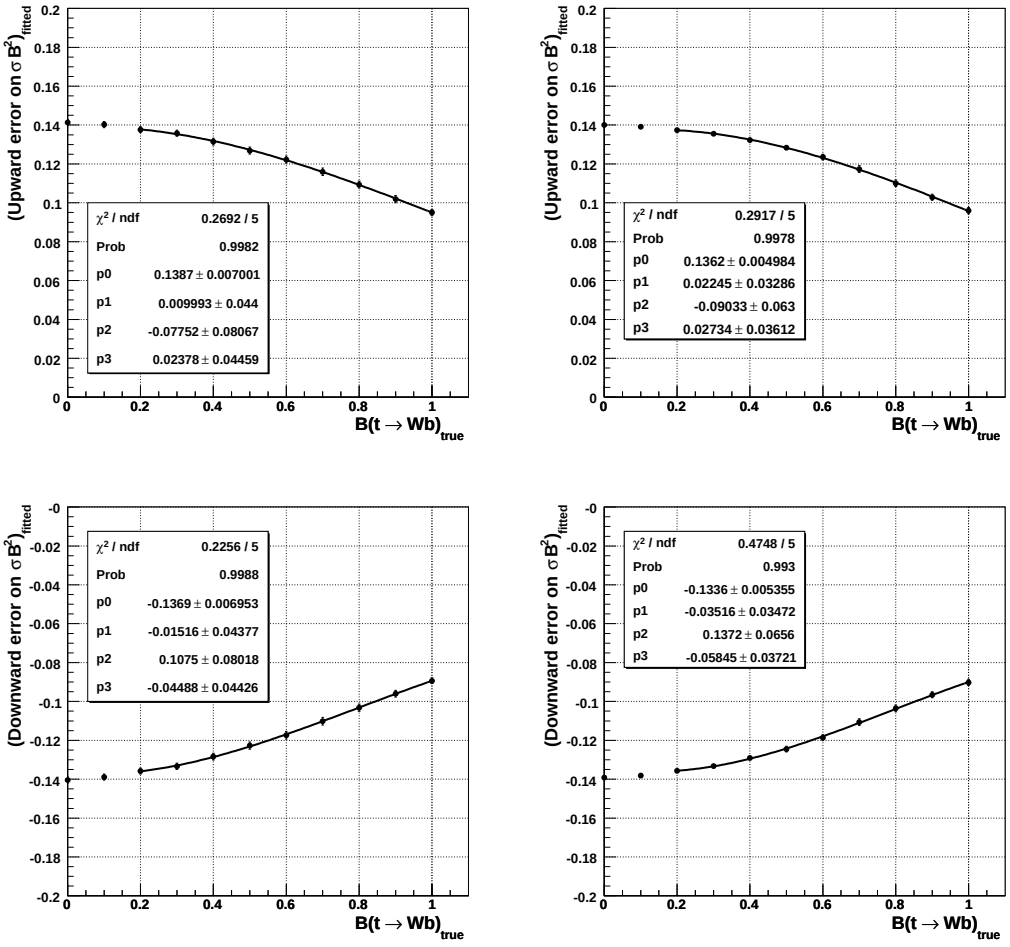

Figure E.12.: Expected relative statistical upward (top) and downward (bottom) error on $\sigma \cdot B^2$ as a function of the true R. The Medium NN Tagger and the dependency of the topological discriminant on R are used. Left: yield-only ensembles. Right: event-by-event ensembles.

F. Fit of $B(t \longrightarrow H^+b)$ for fixed $\sigma_{t\bar{t}}$ with part of all final states

In order to check the significance of individual channels contributing to the total limit on $B(t \rightarrow H^+b)$, as presented in section 11.2, the limit calculation for the tauonic decaying charged Higgs is repeated for the l+jets channel only and the l+jets channel combined with the dilepton final states. In case of leptophobic decaying charged Higgs the combined l+jets and dilepton channel are considered, as no appearance channel is used that can change the behaviour of the limits significantly. The limit calculation is done with the Feldman Cousins method. The $t\bar{t}$ cross section is set to 7.3 ± 0.7 pb.

The expected and observed limits on $B(t \rightarrow H^+b)$ in the tauonic model for the l+jets channel only are shown in Fig. F.1. Figure F.2 shows the corresponding expected and observed limits for the combined l+jets and dilepton channels. It can be observed that the limits get better with increasing charged Higgs mass, whereas the limits for high charged Higgs masses get worse for the full combination as shown in Fig. 11.5. The l+jets and dilepton channels represent disappearance channels, i. e. the less events containing charged Higgs pass the selection, the better the limits. For high mass charged Higgs the b-jets have a smaller momentum, resulting in smaller jet p_T. This makes it more unlikely that the event passes the selection cuts and leads to the improving limits with higher mass. The τ+lepton channel only represents an appearance channel for low charged Higgs masses, where it significantly improves the limits compared to not including this final state. For high charged Higgs mass τ+lepton does not contribute significant information, and thus does not improve the limits with respect to not using τ+lepton.

Besides showing the improvement of the limit itself, the l+jets only limits show a large discrepancy between expected and observed limit. Due to the $t\bar{t}$ cross section being fixed to 7.3 pb for the search for charged Higgs, but the observed cross section in the l+jets channel being measured as 8.46 pb (see Table 11.5 in section 11.1), the large difference between observed and expected limit shows again how sensitive the measurement of $B(t \rightarrow H^+b)$ is on the cross section. For only l+jets channels, $B(t \rightarrow H^+b)$ and $\sigma_{t\bar{t}}$ are almost 100 % correlated, making the limit setting highly dependent on the assumed $t\bar{t}$ production model.

Figure F.3 shows the expected and observed limits on $B(t \rightarrow H^+b)$ for leptophobic decaying H^+ in the combined l+jets and dilepton channel. Due to all channels, including τ+lepton – as shown in Fig. 11.6 –, being disappearance channels in the leptophobic model, the inclusion of τ+lepton does not contribute much to the significance.

These studies show again how important the inclusion of disappearance and appearance channels is. Although the τ+lepton final state has low statistics it can improve the limits on the tauonic model significantly for low mass charged Higgs. The same behaviour is expected for the leptophobic model, if an appearance channel would be included.

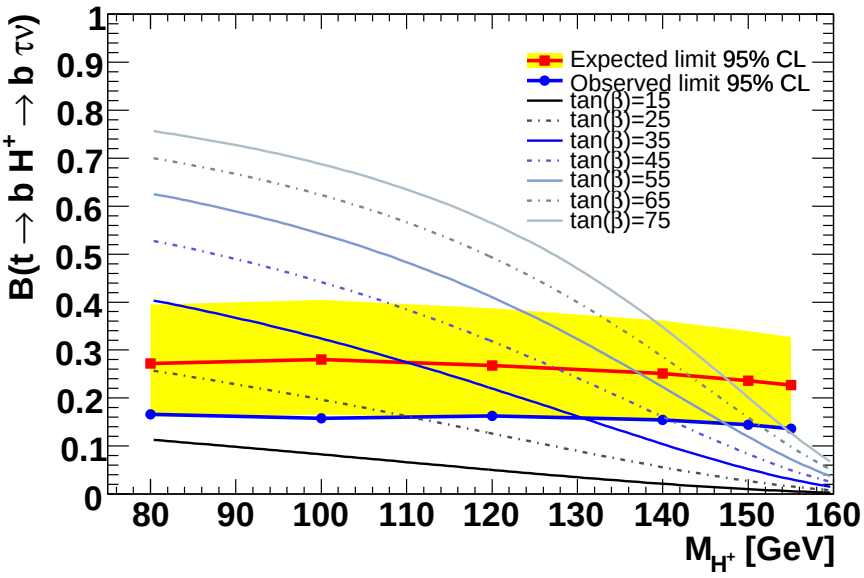

Figure F.1.: Expected (red) and observed (blue) limits for $B(t \to H^+b)$ versus H^+ mass for the l+jets channels. Only the tauonic charged Higgs decays are considered.

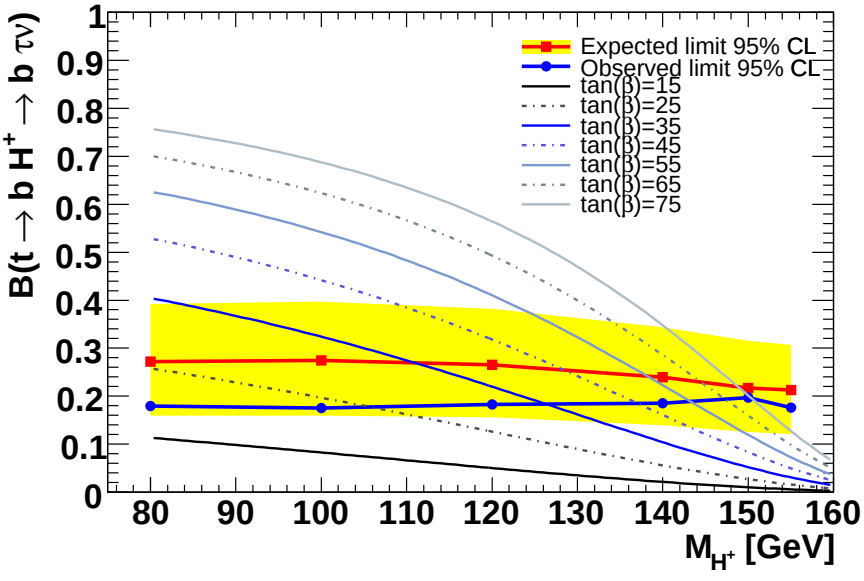

Figure F.2.: Expected (red) and observed (blue) limits for $B(t \to H^+b)$ versus H^+ mass for the combined l+jets and dilepton channels. Only the tauonic charged Higgs decays are considered.

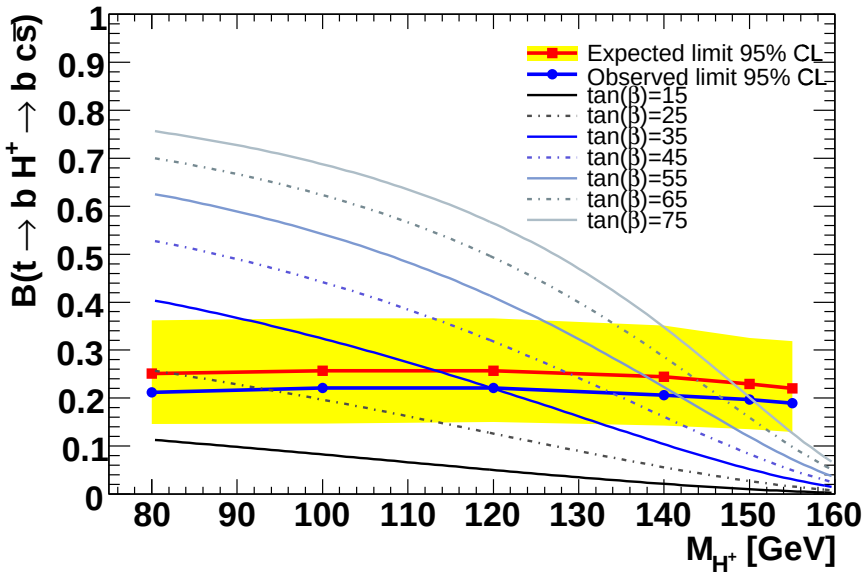

Figure F.3.: Expected (red) and observed (blue) limits for $B(t \to H^+ b)$ versus H^+ mass for the combined l+jets and dilepton channels. Only the leptophobic charged Higgs decays are considered.

G. Bayesian limits on $B(t \to H^+b)$

Different limit setting procedures may lead to different answers. While the frequentist methods sometimes overcover, Bayesian methods suffer from a subjective choice of the prior. The limit setting on $B(t \to H^+b)$, as presented in section 11.2, is performed with a frequentistic method from Feldman and Cousins. In this section the limits on the tauonic and leptophobic model for a Bayesian approach are presented. The incorporation of systematic uncertainties into the Bayesian limit setting is done by means of Monte Carlo integration. The $t\bar{t}$ cross section is fixed to 7.3 ± 0.7 pb for the Bayesian limits.

The Monte Carlo integration is performed for each physically allowed point of a grid in $B(t \to H^+b)$, i. e. in the region from zero to one. For each $B(t \to H^+b)$ the posterior probability is calculated. The prior on tauonic and leptophobic decaying charged Higgs is set to one in the physically allowed region and zero otherwise.

Figure G.1 shows the expected and observed posterior probability densities for tauonic decaying charged Higgs bosons in the combined l+jets, dilepton and τ+lepton channel for several charged Higgs masses. Figure G.2 shows the expected and observed limits on $B(t \to H^+b)$ for tauonic decaying H^+ as a function of the charged Higgs mass, derived with the Bayesian approach.

Table G.1 lists the expected and observed limit on $B(t \to H^+b)$ versus the charged Higgs mass.

H^+ mass [GeV]	expected	observed
80	0.13	0.11
100	0.13	0.11
120	0.14	0.12
140	0.14	0.14
150	0.15	0.15
155	0.14	0.15

Table G.1.: Bayesian upper limits on the branching ratio $B(t \to H^+b)$ for each generated H^+ mass point in the tauonic model.

Figure G.3 shows the expected and observed posterior probability densities for leptophobic decaying charged Higgs bosons for six different m_{H^+}.

In Fig. G.4 the expected and observed limits on $B(t \to H^+b)$ for leptophobic decaying H^+ are shown as a function of the charged Higgs mass derived with the Bayesian approach.

Table G.2 lists the expected and observed limit on $B(t \to H^+b)$ versus the charged Higgs mass.

For both models, tauonic and leptophobic, the Bayesian limits come out a bit better than the frequentist limits. For both procedures the observed limit is better than the expected limit by about the same amount.

H^+ mass [GeV]	expected	observed
80	0.18	0.14
100	0.18	0.14
120	0.18	0.14
140	0.18	0.15
150	0.16	0.15
155	0.16	0.14

Table G.2.: Bayesian upper limits on the branching ratio $B(t \to H^+b)$ for each generated H^+ mass point in the leptophobic model.

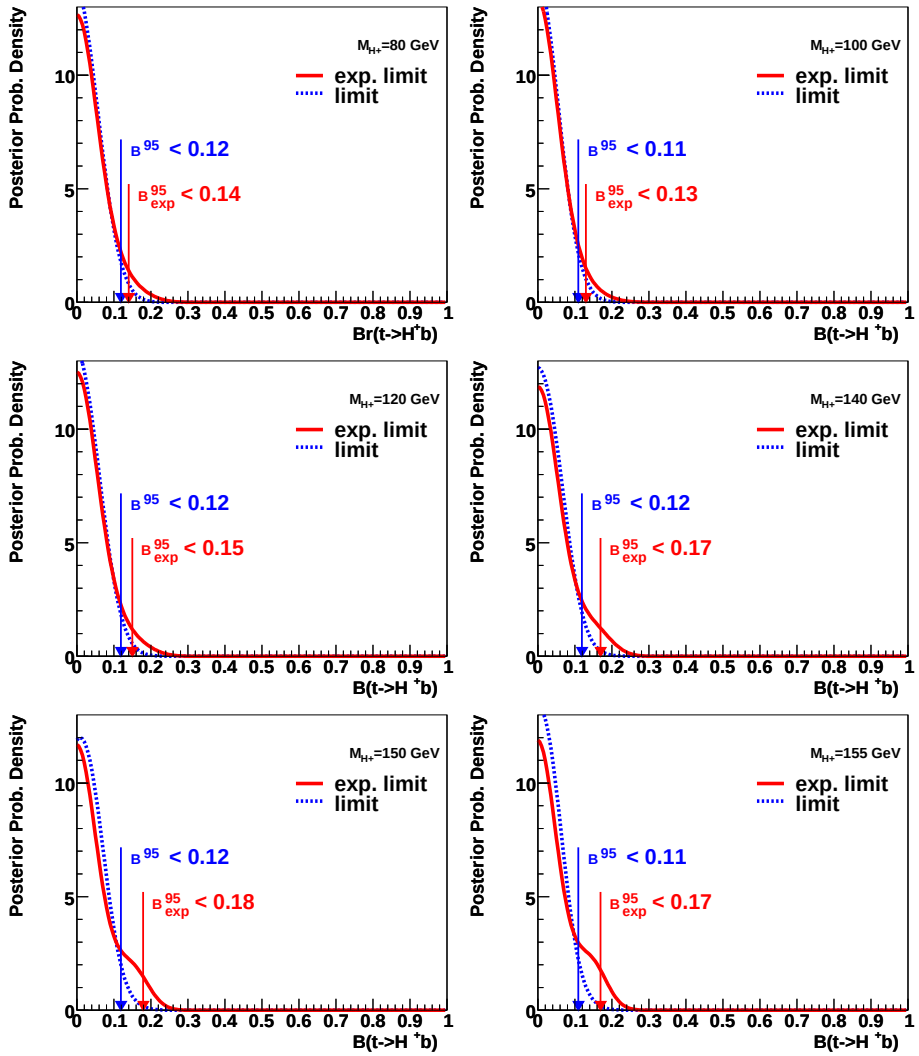

Figure G.1.: Bayesian posterior probabilities for $B(t \to H^+b)$. For the combined l+jets, τ+lepton and dilepton channels and tauonic decaying charged Higgs.

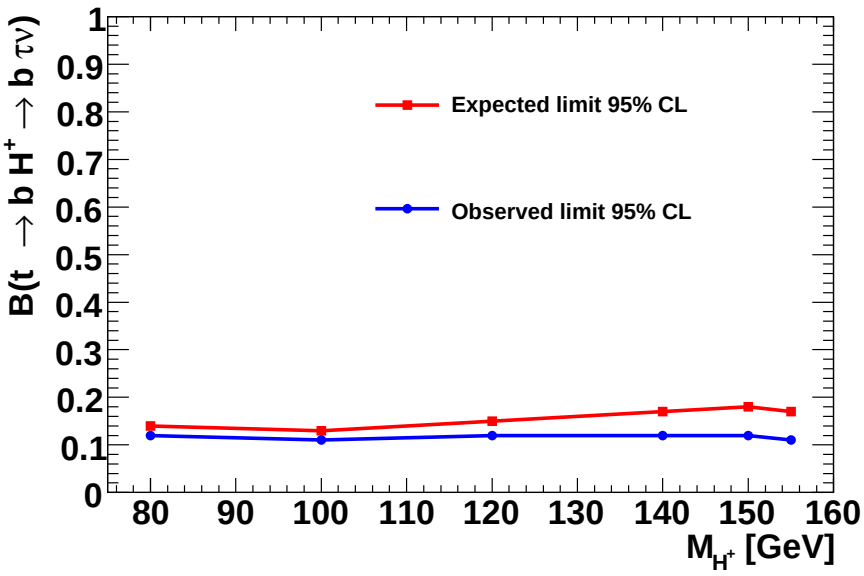

Figure G.2.: Bayesian expected (red) and observed (blue) limits for $B(t \to H^+b)$ versus H^+ mass for the combined l+jets, τ+lepton and dilepton channels. Only the tauonic charged Higgs decays are considered.

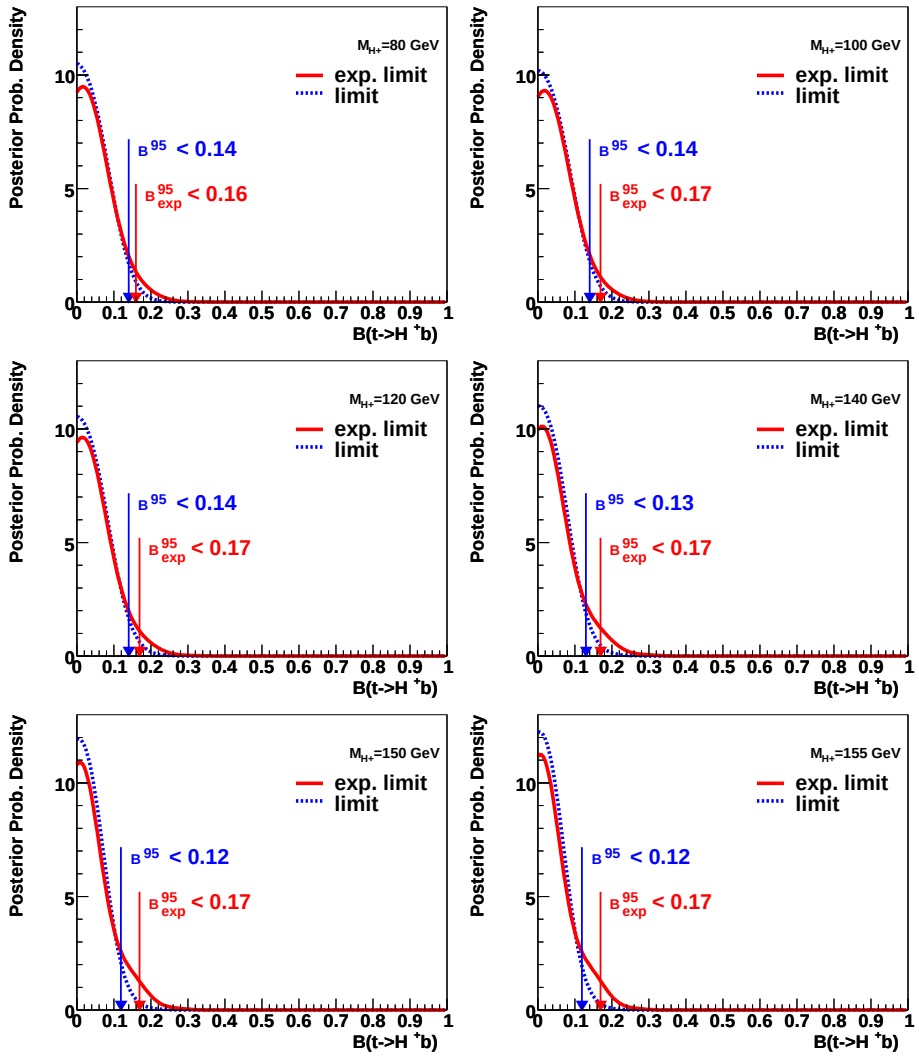

Figure G.3.: Bayesian posterior probabilities for $B(t \to H^+ b)$. For the combined l+jets, τ+lepton and dilepton channels and leptophobic decaying charged Higgs.

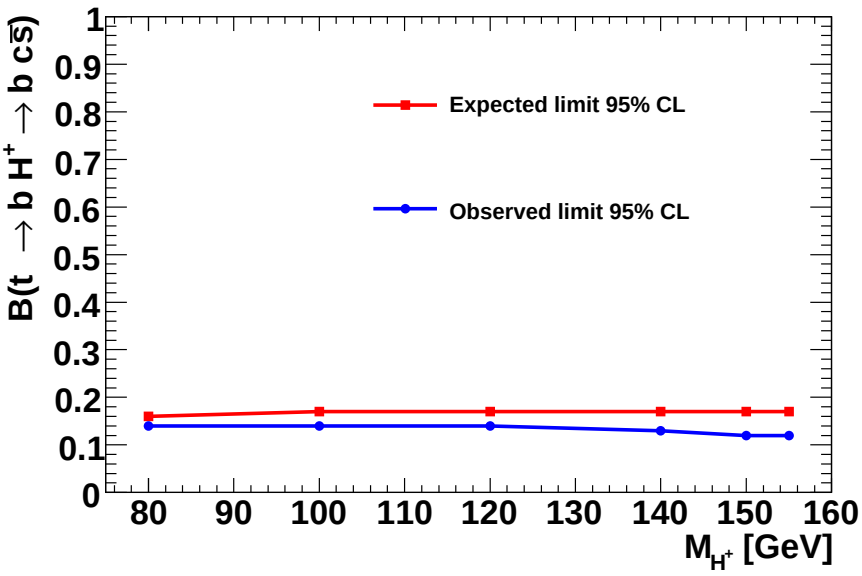

Figure G.4.: Bayesian expected (red) and observed (blue) limits for $B(t \to H^+ b)$ versus H^+ mass for combined l+jets, τ+lepton and dilepton channels. Only the leptophobic charged Higgs decays are considered.

List of Figures

List of Tables

Bibliography

[1] R. K. Ellis, W. J. Stirling, B. R. Webber. *QCD and collider physics*. Cambridge Univ. Press, 2003.

[2] F. Halzen, A. D. Martin. *Quarks and Leptons*. Wiley, 1984.

[3] W.-M. Yao et al. *Review of Particle Physics*. 2006. Journal of Physics G **33**, 1.

[4] P. W. Higgs. 1964. Phys. Rev. Lett. **12**.

[5] J. F. Gunion et al. *The Higgs Hunter's Guide*. Addison-Wesley, 1990.

[6] P. Raimond. *Journeys beyond the Standard Model*. Perseus Books, 1999.

[7] Z. Maki, M. Nakagawa, S. Sakata. 1962. Prog. Theor. Phys. **28**, 870.

[8] The Tevatron Electroweak Working Group. 2008. arxiv:0808.1089.

[9] The Tevatron Electroweak Working Group. 2008. FERMILAB-TM-2403-E.

[10] DØ Collaboration. 2007. DØ note 5459-CONF.

[11] V. M. Abazov. 2008. Phys. Rev. Lett. **100**, 192004.

[12] V. M. Abazov et al. 2007. Phys. Rev. Lett. **98**, 181802.

[13] `http://durpdg.dur.ac.uk/hepdata/pdf3.html`.

[14] A. Quadt. *Top quark physics at Hadron Colliders*. 2006. Eur. POhys.J. **C48**, 835-1000.

[15] N. Kidonakis, R. Vogt. 2003. Phys. Rev. D **68**, 114014.

[16] J. Pumplin et al. *New Generation of Parton Distributions with Uncertainties from Global QCD Analysis*. 2002. JHEPO207, 012.

[17] M. Cacciari et al. 2004. JHEP **404**, 68.

[18] S. Moch, P. Uwer. *Theoretical status and prospectes for top-quark pair production at hadron colliders*. 2008. hep-ph/0804.1476.

[19] S. Moch, P. Uwer. *Heyva-quark pair production at two loops in QCD*. 2008. hep-ph/0807.2794.

[20] P. M. Nadolsky et al. 2008. arXiv:0802.0007.

[21] `http://www-d0.fnal.gov/Run2Physics/top/top_public_web_pages/top_public.html`.

[22] T. Hahn et al. 2006. hep-ph/0607308.

[23] S. P. Martin. *A Supersymmetry Primer*. 1999. hep-ph/9709356.

[24] I. Aitchison. *Supersymmetry in Particle Physics*. Cambridge University Press, 2007.

[25] S. Eidelmann et. al. *Review of Particle Physics*. 2004. Phys. Lett. **B 592**,1.

[26] S. Glashow, S. Weinberg. 1977. Phys. Rev. **D 15**, 1958.

[27] M. Carena, H. E. Haber. *Higgs Boson Theory and Phenomenology*. 2002. arxiv:hep-ph/0208209.

[28] Y. Grossman. 1994. Nucl. Phys. **B 426**,355.

[29] A. K. Akeroyd. 1995. hep-ph/9509203.

[30] M. Carena et al. *Report of the Tevatron Higgs Working Group*. 2000. hep-ph/0010338.

[31] A. Czarnecki, S. Davidson. 1993. Phys. Rev. **D 48**, 4183.

[32] J. Guasch, R. A. Jimenez, J. Sola. 1995. Phys. Lett **B 360**,47.

[33] J. S. Lee et al. *CPsuperH*. 2004. Comput. Phys. Commun. 156, 283.

[34] R. Eusebi. *Search for Charged Higgs in $t\bar{t}$ Decay Products from Proton-Antiproton Collisions at $\sqrt{s} = 1.96$ TeV*. 2005. FERMILAB-THESIS-2005-33.

[35] M. S. Carena, S. Mrenna, C. E. M. Wagner. 2000. Phys. Rev. **D 62**, 055008.

[36] H. B. Prosper et al. *Limits using a Bayesian approach in the package "top_statistics"*. 2006. DØ note 5123.

[37] G. Feldman, R. Cousins. 1998. Phys. Rev. **D 57**, 3873.

[38] T. Junk. 1999. Nucl. Instrum. Meth. **A 434**,435.

[39] V. Buescher et al. *Recommendation of the Ad-Hoc Committee on Limit-Setting Procedures to be Used by D0 in Run II*. 2004. DØ note 4629.

[40] J. Neyman. 1937. Phil. Trans. Royal Soc. London, Series A, 236 333-80.

[41] Y. Peters et al. *Calculation of confidence regions with the Cousins and Feldman method*. 2007. DØ note 5526.

[42] W. Fisher. *Systematics and Limit Calculation*. 2006. DØ note 5309.

[43] W. Fisher. *Calculating Limits for Combined Analyses*. 2005. DØ note 4975.

[44] Visual Media Service Photo Database. `http://www-visualmedia.fnal.gov/VMS_Site/active.html`.

[45] Fermilab's Chain of Accelerators. `http://www-bd.fnal.gov/public/index.html`.

[46] Run II Handbook. `http://www-ad.fnal.gov/runII/index.html`.

[47] `http://www-d0.fnal.gov/Run2Physics/displays/presentations/`.

[48] S. Abachi et al. *The DØ Detector*. 1994. FERMILAB-Pub-93/179-E.

[49] S. Abachi et al. *The DØ Upgrade, The Detector and Its Physics*. 1996. FERMILAB-Pub-96/357-E.

[50] V. M. Abazov et al. *The Upgraded DØ Detector*. 2006. Nucl. Instrum. Meth. A 565, 463.

[51] `http://www-d0.fnal.gov/Run2Physics/WWW/drawings/d0det_tracking_ah.eps`.

[52] M. Weber. `http://d0server1.fnal.gov/projects/Silicon/www/SMT_files/talks/`.

[53] D. Chapin et al. *Measurement of $Z \rightarrow ee$ and $W \rightarrow e\nu$ Production Cross Sections using one tight central Electron*. 2005. DØ note 4897.

[54] M. Voutilainen, C. Royon. *Jet p_T resolution using JetCorr v7.1*. 2007. DØ note 5381.

[55] `http://www-d0.fnal.gov/phys_id/luminosity/`.

[56] M. Begel. `http://www-d0.fnal.gov/phys_id/luminosity/presentations/tutorial.ps` .

[57] T. Andeen et. al. *The DØ Experiment's Integrated Luminosity for Tevatron Run IIa*. 2007. FERMILAB-TM-2365.

[58] T. Edwards et. al. *Determination of the effective inelastic p anti-p cross-section for the DØ Run II luminosity measurement*. 2004. FERMILAB-TM-2278-E.

[59] S. Klimenko, J. Konigsberg, T. M. Liss. *Averaging of the inelastic cross sections measured by the CDF and the E811 experiments*. 2003. FERMILAB-FN-0741.

[60] `http://d0server1.fnal.gov/Projects/Operations/D0RunII_DataTaking_files/`.

[61] `http://www-d0online.fnal.gov/www/groups/tm/tm_main.html`.

[62] G. C. Blazey. *The DØ Run II Trigger*. 1997. FERMILAB-CONF-97-395-E.

[63] `http://www-d0.fnal.gov/runcoor/run2best.html`.

[64] `http://www-d0.fnal.gov/d0dist/dist/packages/coor/devel/doc/coorover.ps`.

[65] R. van Kooten et al. *Tracking Algorithm Recommendation Committee (TARC) Report II*. 2003. `http://d0server1.fnal.gov/www/Computing/Web/Meeting/Reviews/TARC/TARC2Recom.pdf`.

[66] A. Khanov. *HTF: histogramming method for finding tracks. The algorithm description.* 2000. DØ note 3778.

[67] G. Borissov. *Ordering a Chaos or...Technical Details of AA Tracking*. 2003. `http://www-d0.fnal.gov/atwork/adm/d0_private/2003-02-28/adm_talk.ps`.

[68] H. Greenlee. *The D0 Kalman Track Fit*. 2004. DØ note 4303.

[69] H. Greenlee. *The DØ Interaction Propagator*. 2003. DØ note 4293.

[70] A. Schwartzman, C. Tully. *Primary vertex reconstruction my means of adaptive vertex fitting*. 2005. DØ note 4918.

[71] A. Schwartzman, M. Narain. *Vertex Fitting by means of the Kallman Filter technique*. 2001. DØ note 3907.

[72] A. Garcia-Belido et al. *Primary vertex certification in p14*. 2004. DØ note 4320.

[73] Y. Peters, A. Schwartzman, M. Strauss. *Certification of the adaptive primary vertex in p17*. 2006. DØ note 5192.

[74] A. Schwartzman, M. Narain. *Probabilistic Primary Vertex Selection*. 2002. DØ note 4042.

[75] A. Schwartzman, M. Narain. *Secondary Vertex Reconstruction using the Kalman Filter*. 2001. DØ note 3908.

[76] A. Schwartzman, M. Narain. *Secondary b tagging using the Kalman Filter Algorithm*. 2001. DØ note 3909.

[77] A. Schwartzman, M. Narain. *b quark jet identification via Secondary Vertex Reconstruction*. 2003. DØ note 4080.

[78] A. Schwartzman. *Measurement of the $B^{\pm}$ Lifetime and Top Quark Identification using Secondary Vertex b-tagging*. 2004. FERMILAB-THESIS-2004-21.

[79] I. Anghel, C. Gerber, E. Shabalina, T. Ten. *Studies of Taggabilty versus number of Primary Vertices for p17 data*. 2006. DØ note 5240.

[80] D. Boline, L. Feligioni, M. Narain. *Update on b-quark jet identification with Secondary Vertex Reconstruction using DØ reco version p14-Pass2 Samples*. 2005. DØ note 4796.

[81] Y. Peters, H. Greenlee, A. Haas, A. Schwartzman. *Optimization of the Secondary Vertex Tagger in p17*. 2006. DØ note 5265.

[82] J. Kozminski et al. *Electron Likelihood in p14*. 2004. DØ note 4449.

[83] L. Wang et al. *Electron Likelihood Efficiency in p17*. 2006. DØ note 5114.

[84] P. Calfayan et al. *Muon Identification Certification for p17 data*. 2007. DØ note 5157.

[85] `http://www-d0.fnal.gov/computing/algorithms/muon/p17/muonId_quality_type.html`.

[86] S. Catani, Y. L. Dokshitzer, B. R. Webber. *The $k_{\perp}$-Clustering Algorithm for Jets in Deep Inelastic Scattering and Hadron Collisions*. 1992. Phys.Lett. **B285** 291-299.

[87] G. C. Blazey, J. R. Dittmann et al. *Run II Jet Physics*. 2000. hep-ex/0005012.

[88] E. Busato, B. Andrieu. *JetAlgorithms in the DØ Run II Software: Description and User's Guide*. 2004. DØ note 4457.

[89] G. Bernardi, E. Busato, J.-R. Vlimant. *Improvements from the T42 Algorithm on Calorimeter Object Reconstruction*. 2004. DØ note 4335.

[90] A. Harel. *Jet ID Optimization*. 2005. DØ note 4919.

[91] A. Harel, R. Wagner. *Improved L1 Confirmation*. 2005. DØ note 4932.

[92] Jet Energy Scale Working Group. *Jet Energy Scale Determination at DØ Run II (final p17 version)*. 2007. DØ note 5382.

[93] `http://www-d0.fnal.gov/phys_id/jes/public/plots_v7.1/`.

[94] M. Voutelainen, C. Royon. *Jet p_T resolution using JetCorr v7.1*. 2006. DØ note 5381.

[95] N. Makovec, J.-F. Grivaz. *Shifting, Smearing and Removing Simulated Jets*. 2005. DØ note 4914.

[96] C. Orchando, J.-F. Grivaz. *SSR for p17*. 2008. DØ note 5609.

[97] S. Calvet, P. Verdier, E. Kajfasz. *Towards MissingET Certification and Unclustered Energy Studies*. 2005. DØ note 4927.

[98] C. Gerber, E. Shabaline, G. Otero y Garcon. *Taggability in p14 pass2 data*. 2006. DØ note 4995.

[99] K. Hanagaki, J. Kasper. *Identification of b-jets by Soft Muon*. 2005. DØ note 4867.

[100] R. Demina, A. Khanov, F. Rizatdinova, E. Shabalina. *Measurement of b-tagging efficiency and mis-tagging rates with CSIP method*. 2004. DØ note 4432.

[101] D. Bloch, B. Clement. *Update of the JLIP b-tagger Performance in p14/pass2 with JES 5.3*. 2005. DØ note 4824.

[102] A. Schwartzman, M. Narain. *b quark jet identification via Secondary Vertex reconstruction in DØ reco p13 software*. 2003. DØ note 4081.

[103] T. Scanlon. *A Neural Nwtwork b-tagging Tool*. 2005. DØ note 4889.

[104] M. Anastasoaie, S. Robinson, T. Scanlon. *Performance of the NN b-tagging Tool in p17 Data*. 2006. DØ note 5213.

[105] B. Clement et al. *SystemD or how to get signal, backgrounds and their efficiences with real data*. 2001. DØ note 4159.

[106] V. Abazov et al. *Measurement of the $t\bar{t}$ production cross section in $p\bar{p}$ collisions at $\sqrt{s} =$ 1.96 TeV using secondary vertex b tagging*. 2006. Phys. Rev. D **74**, 112004.

[107] Y. Peters et al. *Study of the W+jets heavy flavor scale factor in p17*. 2007. DØ note 5406.

[108] S.-J. Park, M. Begel. *Efficiency of the Data Quality Calorimeter Flags*. 2007. DØ note 5324.

[109] `http://www-d0.fnal.gov/Run2Physics/top/d0\_private/wg/triggers/triggers.html`.

[110] S. Gieseke. *Event Generators – New Developments*. 2002. hep-ph/0210294.

[111] B. Andersson. Cambridge University Press, 1998.

[112] G. Corcella, I. G. Knowles, G. Marchesini, S. Moretti, K. Odagiri, P. Richardson, M. H. Seymor, B. R. Webber. *HERWIG 6.5*.

[113] T. Sjöstrand, L. Lönnblad, S. Mrenna, P. Skands. *Pythia 6.3: Physics and Manual*, 2003. hep-ph/0308153(2003).

[114] M. L. Mangano et al. *ALPGEN, an generator for hard multiparton processes in hadronic collisions*. 2002. CERN-TH/2002-129, FTN-T-2002-06, hep-ph/0206293.

[115] E. E. Boos et al. *Method for simulating electroweak top-quark production events in the NLO approximation: Single Top event generator*. 2006. Phys. Atom. Nucl. 69, 1317.

[116] M. R. Whally et al. *The les houches accord pdfs (lhapdf) and lhaglue*. 2007. `http://projects.hepforge.org/lhapdf/`.

[117] S. Höche et al. *Matching Parton Showers and Matrix Elements*. 2006. hep-ph/0602031.

[118] M. Begel, L. Christofek, E. Shabalina. *Determination of Weighting Factors for Alpgen Monte Carlo Signal and Background Samples*. 2006. DØ note 5016.

[119] Y. Fisyak, J. Womersley. *D0 GEANT Simulation of the Total Apparatus Response*. 1997. DØ note 3191.

[120] S. Agostinelli et al. *GEANT4: A simulation toolkit*. 2003. Nucl. Instrum. Meth. **A 506**, 250.

[121] DØ Collaboration. *D0SIM User Manual*. 1986. 407.

[122] `http://www-d0.fnal.gov/computing/MonteCarlo/MonteCarlo.html`.

[123] The ALEPH Collaboration. *Study of the fragmentation of b quarks into B mesons at the Z peak*. 2001. CERN-EP/2001-039.

[124] DELPHI Collaboration. *A Study of the b-quark Fragmentation Function with the DELPHI Detector at LEP I*. 2003.

[125] The OPAL Collaboration. *Inclusive Analysis of the b Quark Fragmentation Function in Z Decays at LEP*. 2002. CERN-EP/2002-051.

[126] The SLD Collaboration. *Measurement of the b-Quark Fragmentation Function in Z° DEcays*. 2002. SLAC-PUB-0987.

[127] M. G. Bowler. *e^+e^- Production of Heavy Quarks in the String Model*. 1981. Z. Phys. **C11** 169.

[128] Y. Peters, K. Hamacher, D. Wicke. *Improving the tuning of the b fragmentation in the DØ Monte Carlo*. 2006. DØ note 4968.

[129] Y. Peters, K. Hamacher, D. Wicke. *Precise tuning of the b fragmentation for the DØ Monte Carlo*. 2006. DØ note 5229.

[130] Y. Peters, M. Begel, K. Hamacher, D. Wicke. *Reweighting of the fragmentation function for the DØ Monte Carlo*. 2007. 5325.

[131] J. Hays et al. *Single Electron Efficiencies in p17 Data and Monte Carlo Using p18.05.00 d0correctEfficiency of the Data Quality Calorimeter Flags*. 2006. DØ note 5105.

[132] H. Schellman. *The longitudinal shape of the luminosity region*. 2006. DØ note 5142.

[133] B. Martin dit Latour. *Z p_T reweighting procedure for p17 Alpgen Monte Carlo*. 2008. DØ note 5571.

[134] M.-A. Pleier. *Measurement of the Electron and Muon Fake Rates in Lepton+Jets Datasets*. 2007. DØ note 5469.

[135] E. Barberis et al. *The Matrix Method and its Error Calculation*. 2004. DØ note 4564.

[136] J. Campbell, R. K. Ellis. *MCFM – Monte Carlo for FeMtobarn processes*. `http://mcfm.fnal.gov`.

[137] V. M. Abazov et al. 2008. Phys. Rev. Lett. **100**, 192003.

[138] Y. Peters, E. Shabalina, D. Wicke. *Simultaneous measurement of $B(t \to Wb)/B(t \to Wq)$ and $\sigma_{t\bar{t}} \times B(t \to Wq)$ at DØ*. 2007. DØ note 5437.

[139] S. Eidelman et al.

[140] F. James, M. Roos. *MINUIT: A System for Function Minimization and Analysis of the Parameter Errors and Correaltion*. 1975. Comput. Phys. Commun. **10**, 343-367.

[141] V. M. Abazov et al. *Measurement of the $t\bar{t}$ production cross section in $p\bar{p}$ collisions at $\sqrt{s} =$ 1.96 TeV using kinematic characteristics of lepton+jets events*. 2007. Phys. Rev. D **76**, 092007.

[142] top_cafe package. `http://www-d0.fnal.gov/Run2Physics/top/d0\_private/wg/top\_cafe/doxydoc/html`.

[143] S. Fu, A. Haas. *A search for $ZH(\to e^+e^-b\bar{b})$ Production with the DØ Detector in $p\bar{p}$ Collisions at $\sqrt{s} = 1.96TeV$*. 2006. DØ note 5275.

[144] K. Johns, J. Leveque, E. Varnes. *Measurement of the W Boson Helicity in Top Quark Decays using 1fb-1 of RunII Data*. 2007. DØ note 5313.

[145] M. Arthaud et al. *Measurement of the ttbar Production Cross-section at sqrts=1.96TeV in Electron Muon Final States using p17 data set*. 2007. DØ note 5360.

[146] B. Martin et al. *Measurement of the ttbar production cross section at sqrt(s)=1.96TeV in the ee final state using p17 data set*. 2007. DØ note 5386.

[147] E. Aguilo et al. *Search for Single Top Quark Production in 1 fb $^{-1}$ of Data*. 2006. DØ note 5285.

[148] J. Brunelle et al. *Measurement of the top-antitop quark pair production cross section in proton-antiproton collisions at $\sqrt{s} = 1.96$ TeV in the lepton+jets final state using event kinematics on 900 pb^{-1} of DØ data*. 2007. DØ note 5354.

[149] K. Harder. PDF systematics in CAF.
`http://www-d0.hef.kun.nl//askArchive.php?base=agenda&categ=a061130&id=a061130s1t3/transparencies/harder_060621_printversion.pdf`.

[150] V. Buescher et al. *Conclusions of Mini-Workshop on PDF uncertainties and related topics*. 2004. DØ note 4618.

[151] V. M. Abazov et al. 2006. Phys. Lett. B **639**,616.

[152] C. Clement andA. Juste, F. Rizetdinova, J. Strandberg. *Simultaneous measurement of $B(t \to Wb)/B(t \to Wq)$ and $\sigma(p\bar{p} \to t\bar{t}) * B(t \to Wq)^2$*. 2006. DØ note 4823.

[153] T. Affolder et al. CDF Collaboration. 2001. Phys. Rev. Lett. **86**, 3233.

[154] T. Affolder et al. CDF Collaboration. 2005. Phys. Rev. Lett. **95**, 102002.

[155] J. Alwall et al. 2007. Eur. Phys. J. C **49**, 791.

[156] V. Abazov et al. DØ Collaboration. 2007. DØ note 5466-CONF.

[157] V. Abazov et al. DØ Collaboration. 2007. DØ note 5371-CONF.

[158] K. Bloom. 2004. FERMILAB-CONF-04-071-E, hep-ex/0405020.

[159] N. Gray, D. J. Broadhurst, W. Grafe, K. Schilcher. *Three Loop Relation Of Quark (Modified) Ms And Pole Masses*. 1990. Z. Phys. C **48**, 673.

[160] K. Melnikov, T. v. Ritbergen. *About the three-loop relation between the MS-bar and the pole quark masses*. 2000. Phys. Lett. B **482**, 99.

[161] K. G. Chetyrkin, M. Steinhauser. *Short distance mass of a heavy quark at order $\alpha(s)^3$*. 1999. Phys. Rev. Lett. **83**, 4001.

[162] The DØ Collaboration. *Top Quark Mass Extraction from $t\bar{t}$ Cross Section Measurements*. 2008. DØ note 5742-CONF.

[163] M. Cacciari et al. 2008. hep-ph/0804.2800v1.

[164] S. Chevalier-Thery et al. *Top Quark Mass Extraction from $t\bar{t}$ Cross Section Measurements*. 2008. DØ note 5700.

[165] J. Cammin, Y. Peters, M. Owen, C. Schwanenberger, E. Shabalina, Z. Ye. *Search for the Standard Model Higgs boson in the $t\bar{t}H \to t\bar{t}b\bar{b}$ channel*. 2008. DØ note 5711.

[166] DØ Collaboration. *Search for the Standard Model Higgs boson in the $t\bar{t}H \to t\bar{t}b\bar{b}$ channel*. 2008. DØ note 5739.

[167] The LEP Higgs working group. 2003. Phys. Lett. **B 565** 61.

[168] J. A. Aguilar-Saaveda. 2006. JHEP **0612**, 033 [arXiv:hep-ph/0603200].

[169] J. Cammin. *Study of a light standard model Higgs boson in the t anti-t H0 channel with ATLAS at LHC and decay mode independent searches for neutral Higgs bosons with OPAL at LEP*. 2004. BONN-IR-2004-06.

[170] J. Drohan. *An investigation of the Higgs Boson production channel $t\bar{t}H$, $H \rightarrow b\bar{b}$ with the ATLAS detector at the LHC*. 2006. Ph.D. Thesis.

[171] B. Martin et al. *Measurement of the ttbar production cross section at sqrt(s)=1.96TeV in the ee final state using p17 data set*. 2008. DØ note 5579.

[172] J.-P. Konrath et al. *Measurement of the ttbar production cross section at sqrt(s)=1.96TeV in the $\mu\mu$ final state using p17 data set*. 2008. DØ note 5581.

[173] M. Arthaud et al. *Measurement of the ttbar Production Cross-section at sqrts=1.96TeV in Electron Muon Final States using p17 data set*. 2008. DØ note 5580.

[174] T. Adams, Y. Peters, S. Sumowidago. *Measurement of the ttbar production cross section at sqrt(s)=1.96TeV in the τ+lepton final state with 1 fb^{-1} of Run II data*. 2008. DØ note 5735.

[175] Y. Peters et al. *Combination of the top quark pair production cross section and search for Charged Higgs Bosons from top quark pair decay in the dilepton, τ+lepton and lepton+jets final states at $\sqrt{s} = 1.96$ TeV*. 2008. DØ note 5597.

[176] DØ Collaboration. *Top quark pair production cross section combination and search for charged Higgs bosons*. 2008. DØ note 5715-CONF.

[177] Y. Peters. *Combined ttbar cross section in the dilepton final state*. 2008. DØ note 5685.

[178] The Tevatron Electroweak Working Group. 2007. FERMILAB-TM-2380-E.

[179] D. Chakraborty et al. *Reconstruction of τ leptons in hadronic final states at DØ Run II*. 2003. DØ note 4210.

[180] J. A. Coarasa et al. 1998. Eur. Phys. J. C **2**, 373, arXiv:hep-ph/9607485.

[181] A. Abulencia et al. 2008. CDF note 9322.

[182] B. Abott et al. 2002. Phys. Rev. Lett. **88**, 151803.

[183] B. Abott et al. 1999. Phys. Rev. Lett. **82**, 4975.

[184] A. Abulencia et al. 2006. Phys. Rev. Lett. **96**, 042003, hep-ex/0510065.

[185] M. Mulders. *Ensemble testing for the Top Mass measurement*. 2004. DØ note 4460.

Acknowledgement

During the three years of my PhD thesis many people supported me, whom I would like to thank. First of all I would like to thank Peter Mättig for giving me the opportunity to work on interesting subjects in high energy physics, for giving me a lot of freedom and for the possibility to stay at Fermilab for two years. Then I would like to thank my supervisor Daniel Wicke, especially for our more or less peaceful, but always fruitful, discussions. Also I would like to thank Klaus Hamacher for many entertaining discussion (even for listeners) and regular advice.

While being in Wuppertal, but also during my time abroad, the group in Wuppertal helped me with technical and formal issues, kept me awake during owl shifts or just raised up my mood - thank you all very much. Foremost I would like to thank my DØ colleagues from Wuppertal, Maren Vaupel, Hendrik Hoeth and Thorsten Schliephake, for funny times at Fermilab and Wuppertal. Then I would like to mention Torsten Harenberg (especially for his computer support), Marisa Sandhoff, Tatjana Lenz, Anca Siebel, Andreas Kootz and Markus Mechtel for advice, coffee and their company. And of course not to forget Henning, Britta, Florian and Christa, my companions my undergraduate, but also during my PhD time.

The two years at Fermilab had the largest impact on my professional and personal life in the last three years. Thanks to my apartment mate Björn for his company, his admin support and our loud discussions about everything one wanted to know (or not). Thanks to Alexander for numerous discussions and sharing our analysis successes and failures. Thanks to Su-Jung for her cakes, her company and cheering me up when getting depressed. Furthermore I would like to thank Jörg, Isa, Philippe, Jens, Olav, Matthias, Marc-Andre, Thorsten Kuhl from our German "ghetto", and all the more or less Germans Krisztian, Maiko, Shannon and her husband Fred, Marcelle, Marcel, Iris, Stefan and whomever I forgot from our regular Pizza meetings.

I'd like to thank the whole top group for working in collaboration with me, for their education and discussions. Thanks to Amnon Harel for his support and our lengthy but fruitful discussions, mainly those about statistics issues. Furthermore, I would like to thank Ariel Schwarzman, who showed me the world of vertexing during the first month of my stay at Fermilab and made my service work very enjoyable and effective.

Every single result in this thesis is based on a fitting code originally written by Christophe Clement - thanks for tens of thousands of lines of for loops and if statements. And thanks to Jonas Strandberg who took his time to explain to me the most important parts of that code, without this I wouldn't have been able to understand it and find out where to start cutting out things and building up my stuff. Furthermore I'd like to thank Jochen Cammin, especially for creating his great ROC-tree framework on which everything I did was based upon, and for his help with running all the hundreds of samples we needed and for taking over the book-keeping part.

Out of everybody at Fermilab I am especially grateful to three people, without whom my whole work would not have been possible the way it was. First of all thanks to Michael Begel, for his long term support, hours of discussions, pushing me to give talks in the right moments and all his advice, especially during my first year at DØ. Then I would like to thank Lisa Shabalina for all her support, help with the analyses in more than technical issues, and not to forget her farewell party where everybody learned about Christian's impersonator's talent.

Of course I also want to thank Christian Schwanenberger for his support, but especially for the great ideas leading to the presented interpretations. These would not have been possible without our meetings on Sundays in the office and brainstorming possibilities about cross section ratios or what to make out of our ttH analysis skeleton.

Many thanks to the German Academic Exchange Service (DAAD) for the financial support of my first year's visit at Fermilab.

Last but not least I would like to thank my brother Marcel, my sister Anna and my parents and grandmother for their long-term support - since more than 27 years.